Etude de la maurocalcine comme peptide de pénétration cellulaire

Cathy Poillot

UNIVERSITÉ DE GRENOBLE

THÈSE

Pour obtenir le grade de

DOCTEUR DE L'UNIVERSITÉ DE GRENOBLE

Spécialité : **Biotechnologie**

Arrêté ministériel : 7 août 2006

Présentée par

Cathy POILLOT

Thèse dirigée par **Michel De Waard**

Préparée au sein du laboratoire **Canaux Calciques Fonctions et Pathologies**
Dans **l'École Doctorale Chimie et Sciences du Vivant**

Etude de la maurocalcine comme peptide de pénétration cellulaire

Thèse soutenue publiquement le **20 juin 2011,**
Devant le jury composé de :

Mr Jean-Luc LENORMAND,
Professeur, Université Joseph Fourier, TIMC-IMAG, Président
Mr Bernard LEBLEU,
Professeur, Université Montpellier 2, Rapporteur
Mr Alain JOLIOT
DR2, Collège de France, Rapporteur
Mr Denis CHURCH
Docteur, The Toxinomics Foundation, Examinateur
Mr Michel DE WAARD
DR1, Institut des Neurosciences de Grenoble, Directeur de thèse

A mes parents, sans qui je n'en serais pas là aujourd'hui…,

SUMMARY

Maurocalcine (MCa) is a 33 mer toxin initially identified from a tunisian scorpion venom, *scorpio maurus palmatus*. This peptide initially triggered our interest for its pharmacological activity on Ryanodine Receptor type 1 (RyR1) of skeletal muscles. In studying how this toxin reaches the intracellular RyR1, it has been shown that MCa could be placed in the growing family of cell penetrating peptides. Since the discovery that MCa can act as a transport agent for the intracellular delivery of fluorescent streptavidine, data have accumulated to illustrate the amazing biotechnological properties of this toxin. Several new analogs have been produced that keep cell penetration properties and lose pharmacological activity of the native molecule. This is the case for a linear analog of MCa synthesized by replacing internal cysteine residues by aminobutyric acid, or by the synthesis of a MCa analog with all its amino acid in D conformation. MCa proved efficient for the intracellular delivery of nanoparticles leading to a myriad of hi-tech applications. Finally, MCa has been grafted on an anti-tumor agent, doxorubicin, to made chemo-resistant tumor cells chemo-sensitive. So it seems that MCa begins its career as a biotechnological tool, and that this toxin will be helpful to see the light on the mechanistic aspects of RyR function.

RESUME

La maurocalcine (MCa) est une toxine de 33 acides aminés issus du venin de scorpion *Scorpio maurus palmatus*. Ce peptide a initialement été étudié pour son activité pharmacologique en tant qu'activateur du récepteur à la ryanodine (RyR1) des muscles squelettiques. En étudiant comment cette toxine pouvait atteindre le RyR qui est localisé à l'intérieur des cellules, il a été montré que la maurocalcine pouvait être classé dans la liste croissante des peptides de pénétration cellulaire. Depuis la découverte que la maurocalcine peut servir de vecteur à la délivrance intracellulaire de streptavidine fluorescente, les données se sont accumulées pour illustrer l'incroyable valeur biotechnologique de cette toxine. Plusieurs nouveaux analogues ont été produits qui séparent les propriétés pharmacologiques et de pénétration cellulaire du peptide comme une maurocalcine sans ponts disulfulres, synthétisée en remplaçant les résidus cystéine par des acides aminobutyriques, ou en remplaçant tous les acides aminés par leur isomère de conformation D. La maurocalcine s'est avérée efficace pour la délivrance cellulaire de nanoparticules ouvrant ainsi une myriade possible d'applications high-tech. Enfin, la maurocalcine a été couplé à la doxorubicine, un agent anti-tumoral, pour rendre chimio-sensibles des cellules cancéreuses devenues chimio-résistantes. Il semble donc que la maurocalcine débute sa carrière comme outil biotechnologique, mais aussi que cette toxine s'avèrera utile pour déchiffrer finement les détails mécanistiques du fonctionnement du récepteur à la ryanodine.

TABLE DES MATIERES

LISTE DES FIGURES

LISTE DES TABLEAUX

LISTE DES ABREVIATIONS

AC	Agent de contraste
Antp	Antennapedia
AP	Assembly proteins
CaCCs	Calcium-activated chlorid currents
CHO	Chinese hamster ovary
DTP	Domaines de transduction protéique
GAG	Glycosaminoglycane
GFP	Green fluorescent protein
GPI	Glycosyl phosphatidylinositol
GTP	Guanosine triphosphate
GUV	Giant unilamellar vesicles
HEK	Human embryonic kidney
HPV16	Papillovirus 16
HS	Héparane sulfate
HSPG	Héparane sulfate protéoglycanes
KDa	Kilo dalton
LUV	Large unilamellar vesicles
MCa	Maurocalcine
miRNA	Micro ARN
MDCK	Madin-Darby canine kidney
MLV	Multi lamellar vesicles

PC	Phosphatidylcholine
PE	Phosphatidylethanolamine
PG	Protéoglycane
PNA	Acide polynucléaire
PPC	Peptide de pénétration cellulaire
PS	Phosphatidylsérine
PTD	Protein transduction domain
PTRF	Polymerase I and transcript release factor
RNA	Ribonucleique acide
RMN	Résonnance magnétique nucléaire
RRM	Réponse de réparation membranaire
RTK	Récepteurs aux tyrosines kinases
RyR	Récepteur à la ryanodine
siRNA	Small interfering RNA
SDPR	Serum deprivation protein response
SM	Sphingomyéline
SUV	Small unilamellar vesicles
SV40	Virus simien 40
TEM	Tertaspin-enriched microdomain
VIH-1	Virus 1 de l’immunodéficience humaine

Introduction

I. Introduction

L'intérêt de la communauté scientifique pour les peptides de pénétration cellulaire est croissant depuis quelques années. En effet, l'obstacle majeur à l'administration de drogues ou de molécules d'intérêt est le passage de la membrane plasmique. La membrane cellulaire constitue une barrière pour une majorité de composés hydrophiles. Un bon passage dans la cellule nécessite donc l'administration de très fortes quantités de composé actif dans le but d'obtenir la quantité nécessaire à un effet biologique. C'est pourquoi les peptides de pénétration cellulaire s'imposent peu à peu dans le rôle de vecteur thérapeutique pour l'administration de molécules actives dans les cellules.

Cette thèse porte sur l'étude d'un de ces peptides prometteurs, la maurocalcine (MCa) qui est issue du venin d'un scorpion. J'ai tout d'abord travaillé à l'amélioration de la MCa pour trouver des analogues sans « effets secondaires » et qui seraient plus simples à synthétiser, mais en conservant toujours comme but premier la non altération des propriétés de pénétration cellulaire. Je me suis ensuite intéressée à la distribution *in vivo* de la MCa, ainsi qu'à sa clairance, données indispensables en cas de future utilisation en clinique. Puis, j'ai utilisé la MCa pour ses propriétés de vecteur, en internalisant dans les cellules des nanoparticules et des agents de contraste pour l'imagerie par résonnance magnétique.

Rappels bibliographiques

II. Rappels bibliographiques

1. Les toxines de venin

a. Introduction

Le venin est un mélange toxique produit par des animaux et destiné à tuer ou paralyser leur proies ou prédateurs. Les venins sont constitués de plusieurs dizaines ou centaines de protéines dont quelques-unes seulement sont toxiques. La composition du venin varie selon l'espèce et l'origine géographique du spécimen.

Une toxine est une substance toxique élaborée par un organisme vivant (bactérie, champignon, animal ou végétal) auquel elle confère son pouvoir pathogène. Les animaux possèdent ces toxines, soit par expression de gènes (produisant directement une toxine protéique ou peptidique), soit par synthèse métabolique (métabolites secondaires qui demandent de nombreuses réactions chimiques, catalysées par des enzymes, pour donner une activité aux toxiques), ou par assimilation (stockage de séquestration de toxines produites par d'autres organismes unicellulaires, les plantes ou d'autres animaux).

Les toxines présentes dans les venins sont des petits peptides de moins de 120 acides aminés, avec un nombre important de ponts disulfures. Ces molécules sont stables face aux conditions dénaturantes et aux attaques enzymatiques (Gilquin, Bourgoin et al. 2003). La nature possède une grande diversité de toxines, qu'elles soient animales ou végétales. Elles sont utilisées le plus souvent dans un but défensif mais aussi offensif (production de neurotoxines par les serpents pour l'immobilisation d'une proie). Les systèmes les plus souvent « atteins » par les toxines sont le système neuromusculaire, le système nerveux et le système cardiovasculaire. Au sein de ces systèmes, les toxines ciblent un grand nombre de macromolécules, comme les canaux ioniques, les récepteurs hormonaux, les enzymes et les transporteurs. Du fait de leurs caractéristiques, les toxines peuvent jouer un rôle important dans la découverte de médicaments, cette ressource encore peu exploitée à un potentiel énorme en tant que future molécules pharmacologiquement actives (Escoubas and King 2009).

Parmi les organismes capables de produire de telles toxines, les scorpions ont été l'objet d'une attention particulière à cause des nombreux cas d'envenimement constatés dans certains

pays africains et américains, ainsi que pour le remarquable potentiel pharmacologique de leurs venins.

b. Les scorpions

Les scorpions font partis de l'ordre des arthropodes et de la classe des arachnides. Il en existe environ 1500 espèces à travers le monde, cependant, les plus dangereux pour l'homme sont regroupés dans la famille des buthidés (Martin-Eauclaire and Bougis 2007). La famille des scorpionidaes possède plusieurs genres dont *Scorpio* auquel l'espèce *maurus* (sous espèce *palmatus*) appartient.

i. Le venin de scorpion

Les venins de scorpions contiennent des mucploysaccharides, des hyaluronidases, des phospholipases, de la sérotonine, de l'histamine, des inhibiteurs d'enzymes et des protéines appelées peptides neurotoxiques (Gwee, Nirthanan et al. 2002; Petricevich 2010). A la différence des venins de serpents et d'araignées, beaucoup de venins de scorpions sont dépourvus d'enzymes, ou bien possèdent des taux vraiment bas d'activités enzymatiques (Gwee, Nirthanan et al. 2002). Les principes actifs des venins de buthidés sont des protéines basiques constituées d'une trentaine à une soixantaine d'acides aminés (Martin-Eauclaire and Bougis 2007). Les toxines de scorpions sont toutes structurées avec trois à quatre ponts disulfures et deux brins de feuillets β antiparallèles reliés à une hélice α par deux ponts disulfures, référencé comme « plate-forme α-β » (Martin-Eauclaire and Bougis 2007).

Les venins de scorpions peuvent être classés en 4 catégories : 1) la famille 1 contient les peptides de 60 à 70 acides aminés liés par 4 ponts disulfures et qui font varier l'activité des canaux sodiques (Catterall 1980), 2) la famille 2 comprend des peptides court et long (30-40 acides aminés ou 60-64 acides aminés) avec 3 ou 4 ponts disulfures et qui bloquent les canaux potassiques (Legros, Ceard et al. 1998; Tytgat, Chandy et al. 1999), 3) la famille 3 est composé de petites chaines de peptides insectotoxine-like d'à peu près 36 acides aminés avec 4 ponts disulfures qui inhiberaient les canaux chlores (Tytgat, Debont et al. 1998), et 4) la

famille 4 comprend les peptides qui modulent les canaux calciques sensibles à la ryanodine (Valdivia, Kirby et al. 1992).

ii. Pharmacologie des toxines de scorpions

L'activité d'une toxine dépend de l'affinité de sa fixation sur un site spécifique d'un canal particulier, et de la réponse pharmacologique et électrophysiologique qui en découle (Martin-Eauclaire and Bougis 2007). Le venin contient des peptides neurotoxiques responsables des symptômes présents lors de l'envenimation par interaction avec des canaux ioniques et qui ont la faculté de causer des détériorations sérieuses sur le système nerveux (Mebs 2002). Les toxines de scorpions présentent une spécificité, une haute affinité et ont été utilisées comme outils pharmaceutiques pour caractériser différents récepteurs protéiques impliqués dans le fonctionnement des canaux ioniques (Lecomte, Sabatier et al. 1998). D'autre part, les peptides neurotoxiques ainsi que de petites protéines des venins de scorpions mènent à des disfonctionnements et provoquent des processus pathophysiologiques, comme des déstabilisations de la membrane, le blocage du système nerveux central et périphérique ou altèrent l'activité des muscles lisses et squelettiques (Tytgat, Chandy et al. 1999). Les toxines de scorpions ont pour cible potentielle les canaux ioniques des cellules excitables, dont elles altèrent le fonctionnement, ce qui conduit en général à une perturbation de la conduction nerveuse qui modifie le potentiel d'action et de libération des neurotransmetteurs (Martin-Eauclaire and Bougis 2007). Les toxines de scorpion ont des actions sur les canaux 1) sodium, environ 230 structures primaires de toxines actives sur les canaux sodiques ont été déterminées (Srinivasan, Gopalakrishnakone et al. 2002), 2) les canaux potassiques, en fonction de leur poids moléculaire et de la position du résidu cystéine, les toxines actives sur les canaux potassiques sont classifiées en trois familles : α-KTx, β-KTx et γ-KTx (Tytgat, Chandy et al. 1999), 3) les canaux chlores, notamment la chlorotoxine, qui est issue du scorpion *Leiurus quinquestriatus* et qui bloque le canal dans l'épithélium de souris et se fixe spécifiquement au canal chlore dans les cellules gliales (Mamelak and Jacoby 2007) et 3) les canaux calciques comme la maurocalcine qui se fixe sur un canal intracellulaire, le récepteur à la ryanodine [RyR] (Fajloun, Kharrat et al. 2000).

2. Les voies d'entrées dans la cellule

Le mécanisme d'accumulation des CPP dans le cytoplasme des cellules n'est pas encore clairement identifié. Ce qui semble être acquis est le fait que deux types d'internalisation cellulaire coexistent mais qui diffèrent drastiquement en terme d'accumulation cytoplasmique et donc d'applications possibles. D'une part, la translocation directe au travers de la bicouche lipidique et qui présente l'avantage d'un accès direct et rapide des CPP au cytoplasme des cellules. Et d'autre part l'endocytose, mais qui présente l'inconvénient d'une accumulation cytoplasmique lente et limitée des CPP ***(Figure 1)***. La part contributive des mécanismes d'entrée des CPP (translocation *versus* endocytose) varie selon la nature du CPP utilisé, sa concentration ainsi qu'en fonction du cargo transporté.

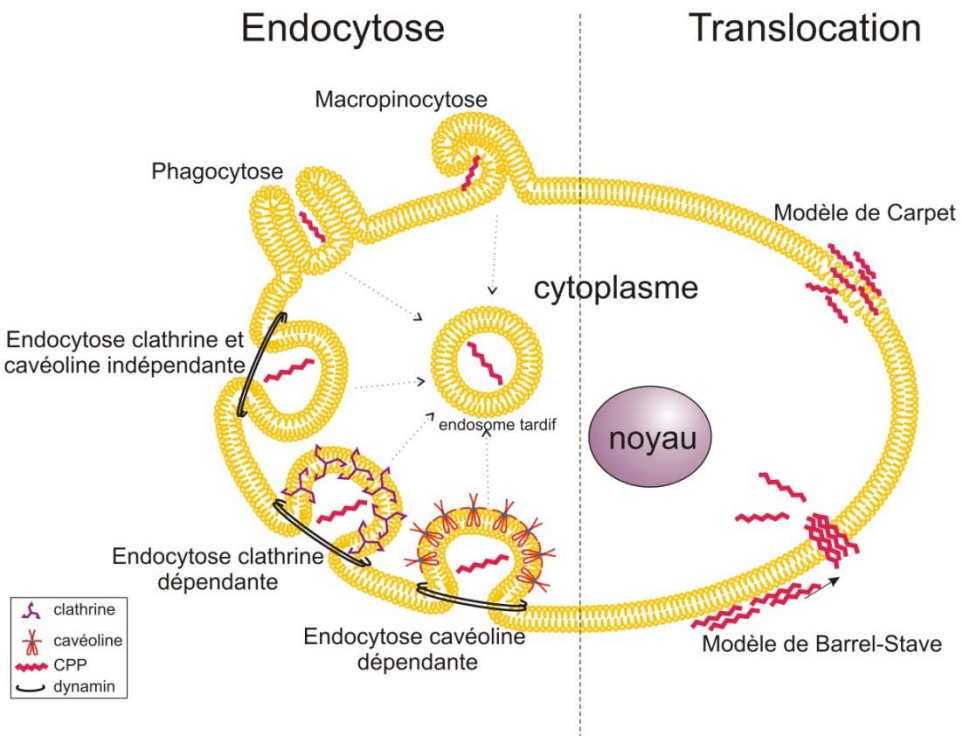

Figure 1: Les différentes voies d'entrée dans la cellule

a. La translocation

La translocation est un processus énergie-indépendant (Pooga, Hallbrink et al. 1998). Elle peut suivre différents schémas, les modèles de Barrel-Stave et Carpet étant les plus connus (Yeaman and Yount 2003; Herbig, Weller et al. 2005). Ces deux modèles ont été empruntés à l'étude des interactions des peptides antimicrobiens avec les bicouches lipidiques et la translocation des peptides est basée sur le concept de perturbation locale de la bicouche lipidique par des agrégats peptidiques.

i. Le modèle de Barrel-Stave

Le terme barrel-stave décrit la topologie des canaux membranaires formés lors de ce mécanisme. Dans ce modèle, un nombre variable de peptides formants des canaux sont positionnés « dans un cylindre » ayant une forme de tonneau autour d'un pore aqueux. Dans ce mécanisme, les surfaces hydrophobes des hélices α ou des feuillets β sont faces extérieures, vers les chaines acyles de la membrane, alors que les surfaces hydrophiles forment le « revêtement » du pore (Ehrenstein and Lecar 1977; Breukink and De Kruijff 1999) (Shai and Oren 2001; Yeaman and Yount 2003). La première étape de la formation des pores de barrel-stave implique la liaison du peptide à la surface membranaire, le plus souvent sous forme monomérique. Au moment de la liaison, le peptide peut entrer dans une phase de transition conformationnelle, forçant les têtes polaires des phospholipides à induire un amincissement localisé de la membrane. A ce stade, la partie hydrophobe du peptide s'insère dans la membrane en concordance avec l'hydrophobicité du feuillet externe de celle-ci. Quand le peptide lié atteint un certain niveau de concentration, les peptides monomériques s'auto-assemblent et s'insèrent dans le noyau hydrophobe de la membrane. Après la translocation du pore, les peptides sont transportés à l'intérieur du feuillet membranaire du fait du gradient de concentration des peptides liés à la surface (Yeaman and Yount 2003).

ii. Le modèle de Carpet

Dans le modèle de carpet, les peptides se lient d'abord à la membrane plasmique et la couvrent à la façon d'un tapis. Contrairement au modèle de barrel-stave, dans le model de

carpet, les peptides sont en contact avec la membrane par toute la longueur du peptide et ne sont pas insérés dans le cœur de la membrane. Lors de ce mécanisme d'internalisation, les peptides sont en contact avec les têtes des phospholipides tout au long du processus de pénétration membranaire. Le mécanisme de ce modèle se déroule en quatre étapes 1) les peptides établissent des liaisons électrostatiques avec les têtes des phospholipides, 2) Les monomères de peptides s'alignent sur la surface de la membrane de manière à ce que leur surface hydrophile soit en contact avec les têtes des phospholipides, 3) il se produit une rotation des molécules menant à la réorientation des résidus hydrophobes dans la direction du cœur hydrophobe de la membrane et 4) il s'ensuit une désintégration de la membrane du fait de la perturbation de la courbure de la bicouche. Les peptides qui agissent selon le mécanisme de carpet doivent posséder une charge nette fortement positive et présente le long de la chaine peptidique (Shai and Oren 2001; Yeaman and Yount 2003).

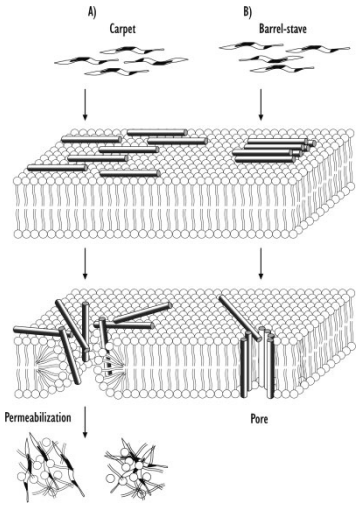

Figure 2: Représentation du mode d'entrée des peptides dans la cellule dans le cas du modèle de Carpet et de Barrel-Stave (Lundberg and Langel 2003)

iii. Le mécanisme de « Toroid Pore » ou « Wormhole »

Une première différence entre le modèle de toroid pore et le modèle de Barrel-stave est que dans le premier, les lipides sont intercalés avec les peptides dans le canal transmembranaire (Yeaman and Yount 2003). Pour cette raison, cette structure est référencée comme un complexe supramoléculaire et représente un pore recouvrant la membrane tapissée avec des

peptides polaires et avec des têtes phospholipidiques (Yeaman and Yount 2003). Ce modèle a été observé principalement avec des peptides possédant une structure en hélice α. Les peptides s'orientent avec leur hélice α parallèle à la surface membranaire et interagissent avec celle-ci grâce à son hydrophobicité et au fait qu'elle soit chargée. Les résidus hydrophobes des peptides déplacent les têtes polaires, créant une faille dans la région hydrophobe et induisant une courbure de la membrane (Hara, Mitani et al. 2001). L'introduction de cette tension et l'affinement de la membrane qui en découle altèrent l'intégrité de la surface membranaire, la rendant vulnérable aux interactions qui s'ensuivent avec les peptides. A un certain ratio peptides/lipides, les peptides s'orientent perpendiculairement à la membrane. A ce stade, les hélices commencent à s'auto assembler, de telle sorte que leurs résidus polaires ne soient plus exposés aux chaines hydrocarbonés de la membrane. Ce transitoire forme le complexe de toroid pore (Yang, Harroun et al. 2001; Yeaman and Yount 2003). Lors de la désintégration de ce pore, les peptides transloquent dans le cytoplasme (Uematsu and Matsuzaki 2000).

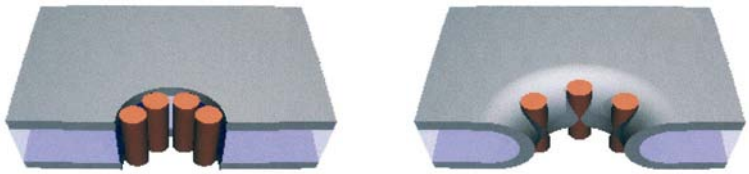

Figure 3: Représentation schématique des modèles de Barrel-Stave (gauche) et de « Wormhole » (droite). Les têtes des phospholipides sont représentés en gris et les cylindres représentent les peptides (Yang, Harroun et al. 2001)

A ces trois modèles, il est utile de mentionner l'existence de mécanismes supplémentaires :

- Le modèle de pore transitoire, dans lequel les CPP intégrés dans la bicouche lipidique génèrent un courant ionique par formation de pore transmembranaire (Deshayes, Plenat et al. 2006)
- Le modèle de fusion membranaire, dans lequel les CPP, en s'insérant dans le feuillet externe de la bicouche lipidique, promeuvent une fusion locale et transitoire de deux régions membranaires, rapprochant les surfaces cationiques des CPP du feuillet interne anionique de la membrane et le transfert intracellulaire du CPP (Henriques and Castanho 2004)

- Un modèle d'électroporation, dans lequel la fixation de CPP cationiques aux lipides anioniques de surface de la membrane plasmique crée un champ électrique transmembranaire qui altère les tensions latérales et de courbure de la membrane, et les conditions favorables à une électroporation membranaire permettant l'internalisation des peptides par la formation de structures membranaires atypiques et transitoires (Binder and Lindblom 2003)
- Le modèle de la micelle inversée, qui commence par l'interaction des charges positives des peptides avec les phospholipides chargés négativement suivi par des interactions des acides aminés hydrophobes avec la membrane, ce qui conduit à la formation de micelles inversées (Derossi, Calvet et al. 1996).

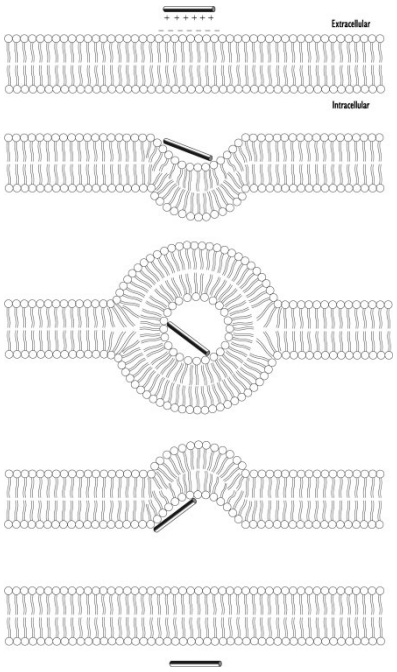

Figure 4: Modèle de la micelle inversée, les charges positives des peptides interagissent avec les charges négatives des phospholipides induisant la formation de micelles inversées (Lundberg and Langel 2003)

b. L'endocytose

L'endocytose est un processus énergie-dépendant (Watkins, Schmaljohann et al. 2009) utilisé par les cellules pour internaliser une large variété de composés. L'endocytose regroupe la phagocytose pour les grosses particules et la pinocytose pour les solutés. Quatre types de

pinocytose existent, la macropinocytose, l'endocytose dépendante de la cavéoline ou de la clathrine et l'endocytose clathrine et cavéoline indépendante (Conner and Schmid 2003).

i. La phagocytose

La phagocytose est un mécanisme par lequel des particules volumineuses sont « ingérées » puis détruites par des cellules spécialisées comme les macrophages, les neutrophiles et les cellules dendritiques (Tollis, Dart et al. ; Vercauteren, Piest et al.). Ce procédé implique la reconnaissance et la fixation aux récepteurs situés à la surface de la membrane (Tollis, Dart et al.), suivi d'une cascade de signalisation aboutissant au réarrangement du cytosquelette et à plusieurs remodelages de la membrane (Desjardins 2003). La première étape de la phagocytose est l'attachement de la particule aux récepteurs présents à la surface de la cellule. Les molécules de lectines font parties des récepteurs qui participent au processus d'internalisation. L'activation des récepteurs phagocytiques génère une transduction du signal qui conduit à une importante réorganisation de la surface cellulaire aux points d'internalisation (Desjardins 2003) conduisant à une croissance de la membrane autour de la particule pour former un phagosome (Swanson 2008). Après l'internalisation, le phagosome fusionne avec des vésicules contenant des enzymes (Silva, Au-Yeung et al. 2007; Yu, Lu et al. 2008), des acides (Kinchen and Ravichandran 2008) et des radicaux d'oxygène (Hampton, Kettle et al. 1998; Segal 2005) ce qui conduit à la destruction de la particule (Tollis, Dart et al.).

ii. La macropinocytose

La macropinocytose est une forme d'endocytose responsable de la majorité des internalisations de fluides dans différents types cellulaires (Gold, Monaghan et al.). La macropinocytose diffère des autres types de pinocytose par le fait qu'elle est précédée par de forts mouvements de la membrane plasmique, conduisant à la formation de vésicules hétérogènes de grande taille appelés macropinosomes (Kerr and Teasdale 2009; Mercer and Helenius 2009). Ce processus est le plus souvent induit par des facteurs de croissance, qui déclenchent l'activation des récepteurs aux tyrosines kinases (RTK), ce qui induit une

réorganisation des filaments d'actine présents à la surface de la membrane plasmique ainsi qu'une excroissance et repliement de la membrane plasmique (Kerr and Teasdale 2009; Mercer and Helenius 2009). La persistance des macropinosomes dans le cytoplasme dépend du type cellulaire. Dans les macrophages, ils se déplacent vers le centre de la cellule, et se rétrécissent à cause de la perte d'eau et de l'acidité en 15 mn. Au cours de ce processus, ils se modifient en endosomes tardifs puis se fondent complètement dans les compartiments lysosomaux (Swanson and Watts 1995).

iii. L'endocytose dépendante de la clathrine

L'endocytose dépendante de la clathrine intervient dans toutes les cellules et est impliquée par exemple dans la capture de composés essentiels comme les lipoprotéines chargés en cholestérol ou la transferrine chargée en fer via leur récepteur respectif (Sahay, Alakhova et al. 2010).

La clathrine est une protéine qui a donné son nom à une voie d'endocytose car elle est le constituant majeur des puits recouverts de clathrine, structures membranaires spécialisées responsables de l'internalisation des molécules dans cette voie de transport (Benmerah and Lamaze 2002). La clathrine est un trimère d'hétérodimères, chaque unité étant constitué d'une chaîne lourde et d'une chaîne légère. Cet assemblage est appelé triskèle (Kumari, Mg et al. 2010). *In vitro* (dans des conditions non physiologiques : salinité faible et concentration en calcium élevée), les triskèles s'auto-assemblent spontanément pour former des structures polygonales (pentagones ou hexagones) très régulières appelées « cages » (Conner and Schmid 2003). Sous conditions physiologiques, l'assemblage de cages nécessite un autre constituant du « manteau », les complexes AP (assembly proteins). Deux classes d'AP ont été identifiées, le monomère AP180 et quatre hétérotétramères AP1-4, tous impliqués dans la formation de vésicules, mais uniquement AP2 est engagé dans la formation des vésicules recouvertes de clathrine (Conner and Schmid 2003). Ces complexes sont formés de quatre sous unités, deux de haut poids moléculaire appelés α- et β-adaptines, une sous unité de taille moyenne, μ2, et une petite sous unité,σ2 (Conner and Schmid 2003). Cette structure est appelée « tête de Mickey » ***(Figure 5)***. Le complexe AP2 est localisé uniquement dans la membrane plasmique (Benmerah and Lamaze 2002).

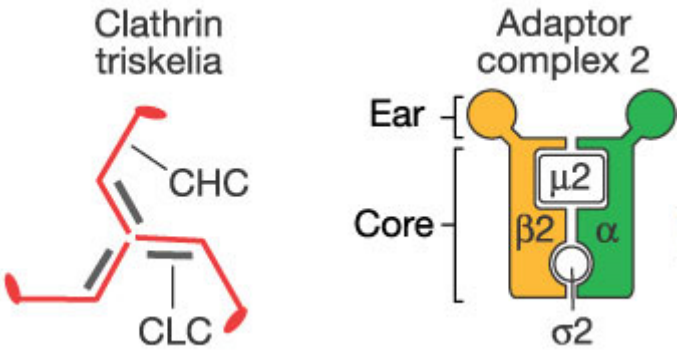

Figure 5: (gauche) Représentation du triskèle de clathrine CHC : chaîne lourde et CLD : chaîne légère (droite) Complexe hétérotétramérique AP2.

Du fait de sa capacité à s'auto-assembler en structure grillagée formant une cage, il a été suggéré que la clathrine est le moteur responsable de la déformation de la membrane et de la formation de vésicules (Benmerah and Lamaze 2002; Conner and Schmid 2003). La clathrine forme une coque dans laquelle sont piégés les complexes AP2, ce qui laisse penser que les complexes AP2 serviraient de lien entre la membrane plasmique, les récepteurs et la clathrine (Benmerah and Lamaze 2002). Une fois réunis, la clathrine, les complexes AP2 et AP180 semblent être suffisants pour sélectionner les cargos et former des vésicules (Conner and Schmid 2003).

La dynamine est une protéine faisant partie de la classe d'enzyme GTPase qui lient et hydrolysent la guanosine triphosphate (GTP). Dans le modèle d'endocytose dépendante de la clathrine, le puits recouvert de clathrine s'invagine et juste avant le détachement d'une vésicule, la dynamine est recrutée au niveau du col. L'activation de sa fonction GTPasique entraîne ensuite la libération d'une vésicule (Benmerah and Lamaze 2002). La clathrine retourne ensuite à la membrane plasmique ou elle est réutilisée, puis les vésicules fusionnent avec les endosomes précoces.

iv. L'endocytose dépendante de la cavéoline

La cavéole a initialement été décrite dans les années 1950 comme une invagination de la membrane plasmique de 50 à 100 nm en forme de flacon (Parkar, Akpa et al. 2009). Les

cavéoles sont recouvertes d'une protéine transmembranaire, la cavéoline, et elles sont riches en cholestérol et en sphingolipides ***(Figure 6)*** (Pelkmans and Helenius 2002; Kiss and Botos 2009). Les cavéoles sont présentes dans de nombreux types cellulaires et tissus comme les muscles lisses, les fibroblastes, les cellules endothéliales et les adipocytes (Lajoie and Nabi 2010). Trois isoformes de la cavéoline ont été identifiés, la cavéoline 1 et la cavéoline 3 sont majoritairement exprimées dans la membrane plasmique, alors que la cavéoline 2 est localisée dans l'appareil de Golgi (Lajoie and Nabi 2010). L'association cavéoline/lipides conduit à des structures résistantes aux détergents appelées raft lipidiques (Kiss and Botos 2009). La formation des cavéoles est dépendante du cholestérol, la perte membranaire de cholestérol conduit à une annulation des structures cavéoles (Kumari, Mg et al. 2010).

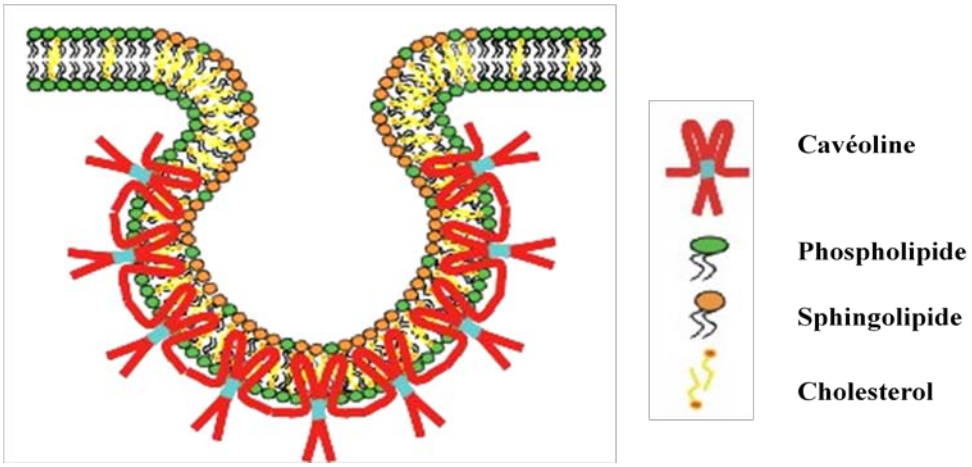

Figure 6: Représentation d'une cavéole, constituée de cavéoline, de phospholipides, de sphingolipides et de cholestérol (Galbiati, Razani et al. 2001)

De récentes études ont identifié d'autres facteurs du manteau de la cavéole, la protéine SDPR (serum deprivation protein response) et la protéine cavin ou PTRF (polymerase I and transcript release factor) (Hill, Bastiani et al. 2008; Hansen, Bright et al. 2009). Ces molécules semblent faire partie du manteau de la cavéole et sont nécessaires à l'assemblage de celle-ci (Kumari, Mg et al. 2010).

L'endocytose dépendante de la cavéoline est responsable de l'internalisation de l'albumine (Schnitzer, Oh et al. 1994), de la toxine du tétanos (Herreros, Ng et al. 2001), de la toxine du choléra (Shogomori and Futerman 2001) et l'acide folique (Rothberg, Ying et al. 1990) pour n'en citer que quelques-uns. Le virus simien 40 (SV40) est un composé rentrant dans les cellules par cette voie d'endocytose, il a d'ailleurs été utilisé comme modèle afin de mieux

comprendre le mécanisme ***(Figure 7)*** (Pelkmans, Kartenbeck et al. 2001). Le virus se lie à la membrane plasmique via l'antigen de classe I du complexe d'histocompatibilité (Breau, Atwood et al. 1992), puis il se diffuse le long de la membrane jusqu'à ce qu'il soit « pris au piège » dans une cavéole (Pelkmans, Kartenbeck et al. 2001). Dans la cavéole, SV40 déclenche une cascade de signalisation menant à la polymérisation de l'actine corticale. Des monomères d'actine sont recrutés à la cavéole contenant le virus et il se forme une « plaque » d'actine sur le pourtour de la cavéole. Simultanément, de la dynamine s'assemble au « col » de la cavéole et une impulsion de polymérisation d'actine s'y produit. La vésicule de cavéole se détache de la membrane et se déplace dans le cytoplasme, l'actine corticale retournant ensuite à sa position normale (Pelkmans and Helenius 2002).

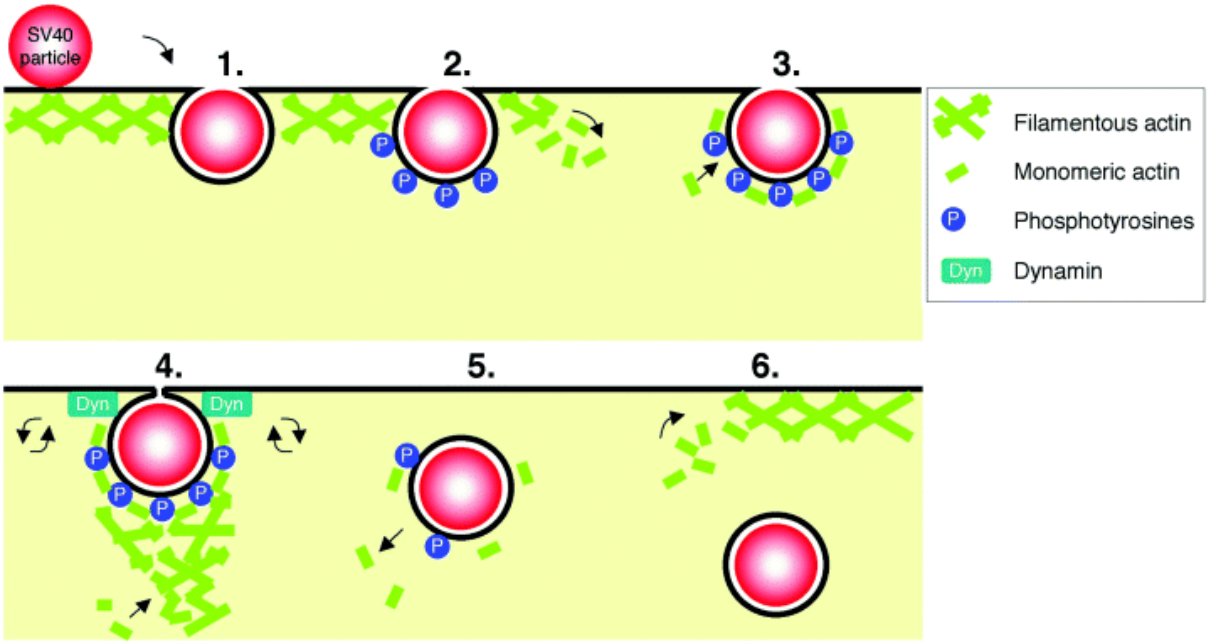

Figure 7: Mécanisme d'internalisation du virus SV40 par les cavéoles

v. L'endocytose indépendante de la clathrine et de la cavéoline

Les cavéoles représentent seulement un type de microdomaine riche en cholestérol à la membrane plasmique, les autres sont nommés « raft » (Conner and Schmid 2003). Ce sont des petites structures de 40 à 50 nm de diamètre présentes le long de la surface cellulaire (Edidin 2001) riches en cholestérol, sphyngomyéline et glycolipides (Anderson and Jacobson 2002). Comme nous l'avons dis plus haut, le virus simien 40 rentre dans les cellules hôtes par

endocytose dépendante de la cavéoline. Cependant, SV40 parvient tout de même à pénétrer dans des cellules déficientes en cavéoline-1 (hépatomes humain et fibroblastes embryonnaires venant d'une souris cavéoline-1 KO). SV40 entre donc par une voie indépendante de la cavéoline et de la dynamine. L'internalisation est rapide (20 mn) et dépendante du cholestérol et des tyrosines kinases (Damm, Pelkmans et al. 2005).

Les flotillines sont des protéines localisées dans le domaine lipidique de la membrane plasmique ainsi que dans le compartiment intracellulaire (Pust, Dyve et al. 2010). Il existe deux molécules de flotilline, la flotilline-1 et la flotilline-2. Les flotillines ont été découvertes grâce à une méthode de purification des endosomes afin d'identifier les protéines présentes dans ceux-ci (Glebov, Bright et al. 2006). Après oligomérisation, les flotillines sont associés à la membrane cellulaire à des clusters d'une taille de 50 à 100 nm, différents des cavéoles (Rajendran, Le Lay et al. 2007; Pust, Dyve et al. 2010). La flotilline est localisée dans des petites structures à l'intérieur de la membrane plasmique, dans une population spécifique d'intermédiaires d'endocytose. Ces intermédiaires accumulent la protéine GPI (glycosyl phosphatidylinositol) et la sous-unité B de la toxine du choléra. Il a été vu par microscopie que des régions de la membrane plasmique contenant de la flotilline bourgeonnaient à l'intérieur de la cellule, et que ces régions étaient diférentes des puits recouverts de clathrine et des cavéoles contenant de la cavéoline (Glebov, Bright et al. 2006). Il a été trouvé que des siRNA (small interfering RNA) contre la Flotillin-1 inhibaient l'internalisation de la toxine du choléra et de la protéine GPI (Glebov, Bright et al. 2006).

Une autre famille de protéine servant de « plateforme » pour l'endocytose est la famille des tétraspanins. Les tétraspanins sont des protéines qui contiennent quatre domaines transmembranaires (Yanez-Mo, Barreiro et al. 2009). Elles possèdent la propriété de s'associer avec différents récepteurs transmembranaires, formant ainsi une classe de domaines membranaires, les TEMs (tetraspin-enriched microdomains) (Hemler 2005). Le papillovirus 16 (HPV16) rentre dans les cellules par les domaines tetraspanins (CD63 et CD151) de la membrane plasmique, et l'extinction de CD151 dans les cellules bloque l'entrée du HPV16 (Spoden, Freitag et al. 2008). Ce mode d'endocytose est différent des autres types d'endocytose indépendant de la dynamine car il n'est pas perturbé par le niveau de cholestérol dans les cellules (Spoden, Freitag et al. 2008). Cependant, les étapes exactes de ce type d'endocytose, ainsi que les acteurs mis en jeu ne sont pas encore complètement définis.

3. Les peptides de pénétration cellulaire

a. Introduction

La membrane cellulaire constitue une barrière imperméable à la plupart des macromolécules. La découverte des peptides de pénétration cellulaire (CPP pour cell penetrating peptide en anglais) aussi appelés domaines de transduction protéique (PTD pour protein transduction domaine en anglais) il y a maintenant une vingtaine d'année a suscité un grand intérêt car ils sont capable de traverser la membrane cellulaire et ainsi de faire pénétrer dans la cellule des cargos auxquels ils seraient attachés. Les CPP sont de petits peptides d'une taille variant entre 10 et une trentaine d'acides aminés et ayant une charge positive nette due aux lysines et aux arginines.

Ils sont capables de rentrer dans les cellules par différents mécanismes, dont certains ne nécessitent pas d'apport énergétique cellulaire (Thoren, Persson et al. 2000), ce qui est le cas quand ces CPP sont toujours capables d'être internalisé dans les cellules lorsque celles-ci sont maintenues à 4°C (Esteve, Mabrouk et al. 2005; Jiao, Delaroche et al. 2009) ou lorsqu'ils sont incubés en présence de différents inhibiteurs d'endocytose (Poillot, Dridi et al. ; Vives, Richard et al. 2003). En règle générale, les CPP n'ont pas de récepteurs cellulaires connus, mais il existe un certain nombre d'exception notable en raison du fait que certains CPP sont issus de protéines fonctionnelles plus large. Les peptides n'ayant pas de récepteurs interagissent cependant avec des molécules de la face externe de la membrane plasmique. Les CPP et ces composés interagissent entre eux par liaisons électrostatiques, notamment par les lipides chargés négativement (Console, Marty et al. 2003; Ziegler and Seelig 2004) mais aussi avec les glycoaminoglycanes (Ram, Aroui et al. 2008).

De nombreuses molécules voient leur utilisation en clinique limitée par le fait qu'elles ne peuvent pas atteindre le milieu intracellulaire. *In vitro* et *in vivo*, une large gamme de cargo a pu être internalisée dans les cellules grâce aux peptides de pénétration cellulaire. L'objectif est maintenant de réussir à transposer ces résultats pour le diagnostique et le traitement des maladies.

La faiblesse des CPP est leur manque de sélectivité (Vives, Schmidt et al. 2008). Ils peuvent entrer dans des types cellulaires très variés, bien que leur efficacité de pénétration puisse varier d'un type cellulaire à un autre.

Mon travail de thèse à porté sur l'étude de la maurocalcine (MCa), un peptide de pénétration cellulaire extrait du venin d'un scorpion tunisien. Nous avons étudié sa biodistribution, puis nous avons voulu améliorer l'efficacité de la MCa par deux techniques différentes : i) en remplaçant lors de la synthèse tous les acides aminés par leur isomère de conformation D, et ii) en déterminant la séquence d'acides aminés responsables des propriétés de pénétration de la MCa. Nous avons aussi montré que la MCa agit comme un agent de rétention au sein des cellules, lorsqu'elle est couplée à un composé qui peut rentrer et sortir des cellules par lui-même.

b. Origines des peptides de pénétration cellulaire

i. Tat

Alors qu'ils étudiaient l'activité de la protéine Tat du virus 1 de l'immunodéficience humaine (VIH-1), Frankel et Pabo découvrirent en 1988 que celle-ci était capable de pénétrer dans les cellules et se localisait dans le noyau. La protéine Tat VIH-1 est composée de 86 acides aminés et possède une région fortement basique grâce à 2 résidus lysines et 6 arginines (Arya, Guo et al. 1985; Sodroski, Patarca et al. 1985). En 1994, deux fragments de Tat (1-72 et 32-72) ont été chimiquement couplés à de la β-galactosidase et injectés dans des souris par voie intraveineuse. Le complexe a été retrouvé dans le foie, la rate et le cœur, et en quantité moindre, dans les muscles squelettiques, dans les poumons et dans les reins (Fawell, Seery et al. 1994). La séquence minimale de la protéine nécessaire à la pénétration cellulaire a été révélée en 1997. Elle contient les acides aminés 47 à 60 qui font parti du cluster basique de la protéine (Vives, Brodin et al. 1997). Une série de mutations a permis de mettre en évidence le rôle important des résidus arginines pour la translocation cellulaire du peptide Tat (Vives, Granier et al. 1997). Initialement, il a été montré que Tat pouvait entrer dans les cellules par voie non endocytaire, car la pénétration de ce peptide marqué à la fluorescéine n'était pas bloquée lorsque les cellules étaient incubées à 4°C (Vives, Brodin et al. 1997). Cependant, à l'heure actuelle, il reste des données divergentes sur l'internalisation du peptide Tat_{48-60} et de ses cargos (Said Hassane, Saleh et al.). Les groupes guanidiums présents sur les arginines sont connus pour former des liaisons hydrogènes bidentates avec les anions comme les sulfates ou les groupes phosphates (Said Hassane, Saleh et al.). D'importantes études sur les

structures/fonctions du peptide Tat ont établi que ces groupes guanidiums et donc les arginines, jouaient un rôle clé dans l'internalisation cellulaire et a donné lieu à des CPP oligo-arginines, et à des dérivés peptoidiques oligoguanidines (Goun, Pillow et al. 2006). Le mode d'entrée du peptide Tat tagué fluorescent couplé à un PNA à été étudié en utilisant différents inhibiteurs d'endocytose et des marqueurs spécifiques de ces voies. L'endocytose dépendante de la clathrine s'est révélée être la voie d'entrée majoritaire pour Tat et le complexe Tat-PNA dans des cellules HeLa. Une co-localisation entre Tat et la transferrine, un marqueur des vésicules cytoplasmiques acides dans l'endocytose par puits de clathrines a aussi été observé (Richard, Melikov et al. 2005). Une autre étude a cependant conduit à des conclusions différentes. Il s'est révélé qu'une protéine de fusion Tat-GFP a co-localisé avec de la cavéoline-1 dans des cellules exprimant cette protéine, mais pas avec les marqueurs de l'endocytose clathrine dépendante (Fittipaldi, Ferrari et al. 2003). De plus, l'internalisation de Tat-GFP était inhibée en cas de réduction du cholestérol et en cas de traitement par la cyclodextrine ou le cytochalasin D qui altèrent la formation des puits lipidiques et gênent l'ancrage des cavéoles dans le cytosquelette d'actine (Fittipaldi, Ferrari et al. 2003). Il a aussi été montré que le peptide Tat entrait dans les cellules par macropinocytose (Wadia, Stan et al. 2004; Kaplan, Wadia et al. 2005). Le mode d'internalisation de Tat est comme pour les autres CPP dépendant du cargo auquel il est attaché et de la concentration appliquée sur les cellules (Brooks, Lebleu et al. 2005).

Tat a été utilisé pour internaliser différents composés comme des agents de contraste au gadolinium pour l'imagerie par résonnance magnétique (Bhorade, Weissleder et al. 2000; Mishra, Su et al. 2009), des quantums dots et nanoparticules pour l'imagerie des cellules par microscopie confocale ou par cytométrie en flux, ainsi que pour l'imagerie *in vivo* (Santra, Yang et al. 2005; Ruan, Agrawal et al. 2007; Xue, Chen et al. 2007; Chen, Liu et al. 2008; Rao, Reddy et al. 2008) mais aussi des siRNA (Endoh, Sisido et al. 2008) ou des molécules anticancéreuses comme le paclitaxel (Niu, Zhao et al. ; Zhao, Wang et al. ; Sawant and Torchilin 2009).

ii. Pénétratine

L'homéodomaine codé par le gêne *Antennapedia* (Antp) de la drosophile consiste en un résidu de 60 acides aminés localisés près du C-terminal de la protéine Antp (Qian, Billeter et al. 1989). Cette protéine est structurée en trois hélices α avec un brin β entre les hélices 2 et 3 (Qian, Billeter et al. 1989). Il s'avère que cette protéine est capable de pénétrer dans les neurones différentiés, s'accumule dans le noyau et stimule la croissance neuritique (Joliot, Pernelle et al. 1991). L'internalisation de cette protéine a lieu à 37°C ainsi qu'à 4°C, ce qui indique qu'elle rentre dans les cellules par une voie différente de l'endocytose. Plusieurs mutants de la protéine homéodomaine ont été synthétisés dont un délété d'un tryptophane et d'une phénylalanine contenus dans la 3ème hélice α. Ce mutant a perdu sa capacité à pénétrer dans les cellules, suggérant que la troisième hélice α est essentielle à la pénétration cellulaire (Le Roux, Joliot et al. 1993). Un peptide de 16 acides aminés correspondant à la troisième hélice α a ensuite été synthétisé. Il conserve les propriétés de pénétration cellulaire de la protéine homéodomaine et son mode d'entrée est énergie indépendante (Derossi, Joliot et al. 1994). Ce peptide appelé pénétratine est le premier peptide de pénétration cellulaire à avoir été décrit. La pénétratine possède une forte proportion d'acides aminés basiques comme les peptides Tat et oligoarginine. Par contre, une caractéristique unique de la pénétratine est la présence de résidus hydrophobes, en particulier de tryptophanes, qui sont critiques pour le processus d'internalisation (Derossi, Joliot et al. 1994). Comme la pénétratine composée d'acides aminés D ainsi que la forme retro-inverso du peptide sont internalisés dans les cellules aussi efficacement que la pénétratine, il en a été conclu qu'un récepteur membranaire chiral n'est pas requis pour la pénétration cellulaire (Derossi, Calvet et al. 1996). Des études suggèrent que la pénétratine se lie aux têtes lipidiques (Fragneto, Bellet-Amalric et al. 2000; Fragneto, Graner et al. 2000). D'autres études ont montré que la pénétratine traversait effectivement la bicouche lipidique, soit lors d'une application d'un gradient de pH (Magzoub, Pramanik et al. 2005; Bjorklund, Biverstahl et al. 2006), soit en réponse à une auto production de potentiel résultant de l'agrégation de peptide d'un côté de la bicouche (Binder and Lindblom 2003). Des mutations ont confirmé la nécessité des propriétés hydrophobes et électrostatiques pour la translocation de la pénétratine (Dupont, Prochiantz et al.). Des mutations des résidus basiques favorisent l'insertion du peptide dans les chaines acyles, mais déstabilisent la bicouche (Christiaens, Grooten et al. 2004). L'ajout de sonde fluorescente sur la pénétratine augmente ainsi son hydrophobicité (Esbjorner, Lincoln et al. 2007), et induit

une déstabilisation de la membrane plasmique dans les cellules vivantes (Dupont, Prochiantz et al. 2007). De plus, de petites modifications, comme la substitution de deux résidus tryptophanes par deux résidus phénylalanines modifie les interactions peptides/lipides et diminue la translocation dans les cellules vivantes (Derossi, Joliot et al. 1994; Magzoub, Eriksson et al. 2003; Zhang and Smith 2005; Esbjorner, Lincoln et al. 2007). Comme la protéine, la pénétratine peut être internalisée à 4°C et à 37°C dans les cellules, donc par un mécanisme énergétiquement indépendant et est localisée dans le cytoplasme et le noyau (Derossi, Joliot et al. 1994), mais des études ultérieures montrent également la présence d'un processus endocytaire pour ce peptide notamment à concentration élevée (Alves, Jiao et al. ; Maiolo, Ferrer et al. 2005; Duchardt, Fotin-Mleczek et al. 2007).

La pénétratine a eu de nombreuses applications en tant que vecteur de composés actifs au sein des cellules comme par exemple la délivrance de peptides (Khafagy el, Morishita et al. 2009) ou d'agents anti-tumoraux (Aroui, Mili et al. ; Yang, Liu et al.). Mais elle a aussi été utilisée pour ces propriétés de pénétration cellulaire, mais sans forcément transporter de cargo. Lors du passage de la pénétratine à travers la membrane plasmique, il se met en place un autre mécanisme: la réponse de réparation membranaire (RRM) (Palm-Apergi, Lorents et al. 2009). Quand la membrane plasmique des cellules est abimée, le calcium extracellulaire s'infiltre dans le cytoplasme et active la RRM (Palm-Apergi, Lorents et al. 2009). Les auteurs ont montré que la pénétratine provoquait une augmentation de calcium intracellulaire dans les cellules HeLa et CHO-K1 en culture (Palm-Apergi, Lorents et al. 2009). Les canaux chlores activés par le calcium (CaCCs pour Calcium-activated chloride currents) sont nécessaires pour la sécrétion des fluides, la fécondation, la transduction sensorielle et l'excitabilité des neurones et des muscles lisses (Kanjhan and Bellingham). L'identification de la pénétratine comme potentialisateur des CaCCs endogènes est donc susceptible de stimuler les recherches sur les CaCCs dans les cellules (Kanjhan and Bellingham).

iii. Transportan

Le transportan fait partie de la classe des peptides chimères, c'est-à-dire qu'il est constitué de deux fragments de peptides, reliés entre eux par un acide aminé ou un linker. Le transportan contient 12 acides aminés du groupe amine-terminal du neuropeptide galanin, et les 14 acides

aminés du peptide mastoparan issu du venin de guêpe. Ces deux peptides sont reliés entre eux par une lysine (Pooga, Hallbrink et al. 1998). Le transportan pénètre rapidement dans différents types cellulaires (HeLa, HEK293, SAOS-1, CaSki, U937, COS-7, Jurkat, Rinm5F et des cellules de mélanome de Bowes), et rentre dans les cellules à 4°C, donc, il peut rentrer dans les cellules par un mode indépendant de l'énergie (Pooga, Hallbrink et al. 1998). L'endocytose peut être inhibée par une solution de sucrose hyperosmolaire, qui bloque la formation des puits recouverts de clathrines (Heuser and Anderson 1989), ou par un traitement à l'oxyde de phénylsarine, qui lie entre eux les groupements thiols des protéines à la surface membranaire (Frost and Lane 1985). Le mode d'entrée du transportan a été étudié en couplant le peptide à des nanoparticules d'or, il est alors apparu que le transportan pénétrait dans les cellules par endocytose et par translocation (Padari, Saalik et al. 2005). Dans les plantes, le prétraitement de protoplastes par des inhibiteurs d'endocytose comme le nocodazole et l'azide de sodium n'altère pas l'internalisation du transportan dans les protoplastes (Chugh and Eudes 2008).

Des siRNA ont pu être délivrés efficacement dans le cytoplasme lorsqu'ils étaient couplés par un pont disulfure au transportan. L'environnement réducteur du cytoplasme rend les siRNA libres et actifs (Muratovska and Eccles 2004). Le transportan a aussi été utilisé pour transporter dans les cellules des PNA (Kilk, Elmquist et al. 2004; Chaubey, Tripathi et al. 2005) et des protéines de masses allant de 30 kDa à 150 kDa (Pooga, Kut et al. 2001). Le transportan biotinylé a efficacement délivré de la streptavidine dans les cellules. La streptavidine ainsi acheminée est retrouvée dans un premier temps à proximité de la membrane plasmique, puis est distribuée dans la région périnucléaire. La plupart de la streptavidine internalisée est confinée dans des vésicules, mais une fraction significative de la protéine est localisée dans le cytoplasme (Pooga, Kut et al. 2001).

iv. MPG et Pep

MPG est également un peptide chimère de 27 acides aminés. Il est composé d'un domaine hydrophobe dérivé de la glycoprotéine 41 du VIH et d'un domaine hydrophile dérivé de la séquence nucléaire de la protéine SV40 T-antigen (Morris, Vidal et al. 1997). MPG forme des

complexes stables avec les acides nucléiques, et permet une délivrance rapide (moins d'une heure) et efficace d'oligonucléotides dans les cellules en culture (Morris, Vidal et al. 1997).

Pep-1est un peptide de 21 acides aminés composé de 3 domaines : un domaine hydrophobe (5 résidus tryptophanes), un domaine hydrophile (4 lysines) dérivé de la séquence nucléaire de l'antigen T du virus simien 40 et un spacer composé d'une sérine, d'une glutamine et d'une proline (Morris, Depollier et al. 2001). Pep-1 pénètre dans les cellules rapidement (10 min) et se localise dans le noyau (Morris, Depollier et al. 2001). Pep-1 forme des complexes non covalents stables avec les peptides et protéines et est capable de les faire pénétrer très efficacement dans le noyau des cellules (fibroblastes humains) (Morris, Depollier et al. 2001).

MPG comme Pep-1 rentre dans les cellules par un processus qui semble non endocytaire (Morris, Vidal et al. 1997; Morris, Depollier et al. 2001). Pep-1a été utilisé pour la délivrance de protéines *in vivo* dans différents modèles animaux par différentes méthodes d'administrations (Kim, Kim et al. ; Aoshiba, Yokohori et al. 2003).

v. CADY

CADY est un peptide amphipathique de 20 acides aminés construit par design à partir du peptide PPTG1, lui-même dérivé du peptide de fusion JTS1 (Crombez, Aldrian-Herrada et al. 2009). CADY se structure en hélice au sein des membranes cellulaires avec les résidus chargés sur une face et tryptophanes sur l'autre face et semble pénétrer dans les cellules par une voie indépendante de l'endocytose (Crombez, Aldrian-Herrada et al. 2009). L'insertion de CADY dans la membrane implique des contacts hydrophobes et électrostatiques (Konate, Crombez et al.). Les interactions sont majoritairement initiées par l'hydrophobicité de CADY, suivies par des interactions entre les charges cationiques des quatre résidus arginines et du résidu lysine de CADY et des têtes polaires des lipides anioniques, qui stabilisent sa conformation dans la membrane (Konate, Crombez et al.). En se liant aux phospholipides, CADY passe d'une conformation aléatoire à une conformation en hélice α, induisant la ségrégation le long de l'axe hélicoïdal des résidus chargés, des résidus aromatiques et des résidus hydrophobes (Konate, Crombez et al.).

CADY forme des complexes électrostatiques stables avec des siRNA par interactions entre les résidus arginines et lysine de CADY avec les groupes phosphates des siRNA, puis par l'implication des résidus tryptophanes dans la stabilisation du complexe CADY/siRNA (Konate, Crombez et al.). Ce complexe augmente la stabilité des siRNA et améliore leur délivrance dans différents types cellulaires (Crombez, Aldrian-Herrada et al. 2009). Les complexes composés avec CADY et les siRNA forment des liaisons électrostatiques avec les protéoglycanes et les phospholipides présents à la surface de la cellule (Konate, Crombez et al.). Ce mécanisme est dépendant du ratio molaire CADY/siRNA ce qui suggère la présence d'une particule de cœur contenant des molécules de CADY en contact avec des siRNA couverte par une couche de molécules de CADY qui forme les interactions peptide/peptide et qui interagit avec les glycosaminoglycanes et les phospholipides (Konate, Crombez et al.). Les complexes CADY/siRNA interagissent donc avec les phospholipides de la membrane et entrainent une désorganisation de la membrane, qui conduit à l'internalisation dans les cellules du siRNA indépendamment des voies endocytaires (Konate, Crombez et al.).

vi. La crotamine

La crotamine est peptide issu du venin d'un serpent sud Américain : *Crotalus durissus terrificus*. La crotamine possède 42 acides aminés dont 11 basiques. Sa séquence compte 6 cystéines impliquées dans 3 ponts disulfures (Kerkis, Kerkis et al. 2004). Ce peptide pénètre rapidement dans les cellules (5min) et se localise dans le noyau. Le mode d'entrée dans les cellules de la crotamine est un processus endocytaire comme le montre l'inhibition de la pénétration à des températures d'incubation faibles (Kerkis, Kerkis et al. 2004). La crotamine forme des complexes électrostatiques stables avec des plasmides qui pénètrent efficacement dans différents types cellulaires *in vitro* et *in vivo* (Nascimento, Hayashi et al. 2007). Marquée à l'^{125}I, la crotamine se retrouve principalement dans les reins et le foie, et à plus faibles doses dans le cerveau (Boni-Mitake, Costa et al. 2006). Différents analogues tronqués de la crotamine ont été synthétisés : 1) un peptide contenant les résidus 1 à 9 liés aux résidus 38 à 42, 2) un peptide de même séquence que 1 mais avec un acide 6-aminohexanoique servant de jonction entre les fragments 1-9 et 38-42 et 3) un peptide comprenant les acides aminés 42 à 38 liés aux acides aminés 9 à 1 avec une mutation d'une histidine par une isoleucine. Ces 3 peptides ont conservé les propriétés de pénétration cellulaire de la crotamine mais ont une

localisation différente du peptide d'origine, ils sont situés dans les nucléoles (Radis-Baptista, de la Torre et al. 2008).

Séquence	Résidus impliqués	Références
Crotamine		
YKQCHKKGGHCFPKEKICLPPSSDFGKMDCRWRWKCCKKGS-G	1-42	(Kerkis, Kerkis et al. 2004)
1		
YKQCHKKGGKKGSG	(1-9)-(38-42)	(Radis-Baptista, de la Torre et al. 2008)
2		
YKQCHKKGG-Ahx-KKGSG	(1-9)-Ahx-(38-42)	(Radis-Baptista, de la Torre et al. 2008)
3		
GSGKKGGKKICQKY	(42-38)-(9-1) H10I	(Radis-Baptista, de la Torre et al. 2008)

Tableau 1. Séquences de la crotamine et de ses analogues.

c. La maurocalcine (MCa)

i. Historique de la découverte

La maurocalcine est un CPP original (Esteve, Mabrouk et al. 2005) car issue du venin d'un scorpion tunisien *Scorpio maurus palmatus*. Ce peptide de 33 acides aminés fut identifié grâce à son activité pharmacologique en tant qu'activateur du récepteur à la ryanodine (RyR1) des muscles squelettiques. La cible est particulièrement originale puisqu'il s'agit d'un canal calcique intracellulaire impliqué dans le couplage excitation-contraction (Fajloun, Kharrat et al. 2000). Ces observations avaient laissé entrevoir la possibilité que la maurocalcine devait traverser la bicouche lipidique des cellules afin d'exercer sa fonction d'activateur de canal calcique. Cette hypothèse était largement renforcée par le fait que le site d'interaction de la maurocalcine sur RyR1 est localisé dans une zone du cytoplasme (Altafaj, Cheng et al. 2005). La démonstration que la maurocalcine était bel et bien un CPP vient des observations suivantes : i) l'application extracellulaire du peptide à des myotubes induit une libération calcique quasi-instantanée (Esteve, Smida-Rezgui et al. 2003), et ii) le greffage d'une

protéine, la streptavidine fluorescente, à la maurocalcine biotinylée induit sa translocation intracellulaire (Esteve, Mabrouk et al. 2005). Par ailleurs, la maurocalcine partage en commun avec les autres CPP la propriété d'être un peptide basique dont de nombreux acides aminés sont chargés positivement (11 sur 33). De plus, la plupart des acides aminés basiques sont localisés sur une même face de la molécule en accord avec la distribution asymétrique observée sur des molécules telles que Tat et pénétratine (Ram, Weiss et al. 2008).

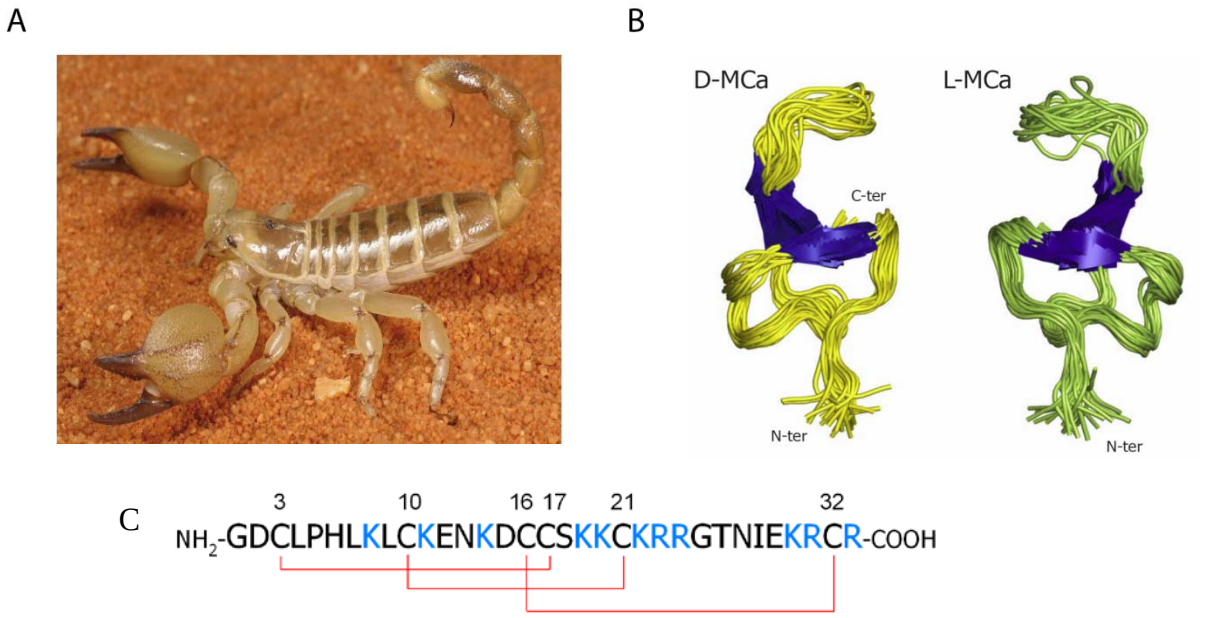

***Figure 8:** (A) Scorpio maurus palmatus, (B) Structure 3-D de la MCa à gauche la MCa sous sa conformation D et à droite la MCa sous la conformation L, (C) Séquence de la MCa avec ses trois ponts disulfures.*

ii. Propriétés pharmacologiques

Le récepteur à la ryanodine (RyR) est un canal calcique qui permet au calcium de sortir du réticulum endoplasmique. Il existe trois isoformes du RyR : 1) le RyR1 qui est présent dans les muscles squelettiques, 2) le RyR2 présent dans les muscles cardiaques et 3) le RyR3 qui est ubiquitaire. RyR1 est un homotétramère de poids moléculaire de 2260 kDa. Cette protéine est impliquée dans le couplage excitation contraction qui est le processus par lequel la dépolarisation de la membrane plasmique entraîne le relâchement du calcium stocké dans les citernes du réticulum sarcoplasmique. Les toxines issues de venins sont depuis longtemps une source de composés biologiquement actifs sur les canaux ioniques. La maurocalcine a trois effets sur le RyR1 :

Elle augmente fortement la liaison de [^{3}H]-ryanodine sur des vésicules de réticulum sarcoplasmique ainsi que sur RyR1 purifié, ce qui se traduit par la transformation de sites de liaison de la [^{3}H]-ryanodine de faible affinité en sites de forte affinité (Esteve, Smida-Rezgui et al. 2003).

Elle induit un relâchement de calcium mesuré à partir de vésicules de membrane de réticulum sarcoplasmique.

La fixation de la maurocalcine sur RyR1 entraine une importante modification de ses propriétés de canal calcique. Cela se traduit par une augmentation de la probabilité d'ouverture du canal, ainsi que par l'apparition de longues périodes, pendant lesquelles le canal reste ouvert, dans un état caractérisé par une conductance inférieure à la conductance maximale de RyR1 mesurée en absence de maurocalcine (Fajloun, Kharrat et al. 2000; Chen, Esteve et al. 2003; Esteve, Smida-Rezgui et al. 2003).

Nom	Séquence en acides aminés	Origines	Cargos
PTD			
Tat_{48-60}	GRKKRRQRRRPPQ	HIV-1	ADN, peptide (Johnson, Lowell et al. ; Vives, Brodin et al. 1997; Perea, Reyes et al. 2004)
Penetratin	RQIKIWFQNRRMKWKK	*Drosophila Antennapedia homeodomain*	Peptide (Khafagy el, Morishita et al. ; Derossi, Joliot et al. 1994)
Peptides chimères			
Transportan	GWTLNSAGYLLGKINLKALAALAKKIL	Galanin + Mastoparan	Protéine, PNA (Pooga, Hallbrink et al. 1998; Pooga, Kut et al. 2001; Chaubey, Tripathi et al. 2005)
Pep-1	KETWWETWWTEWSQPKKKRKV	Domaine riche en tryptophane + spacer + domaine dérivé de la séquence de localisation nucléaire de l'antigène de virus SV40	Enzymes (Morris, Depollier et al. 2001; Kim, Jeong et al. 2009)
MPG	GALFLGFLGAAGSTMGAWSQPKKKRKV	Motif hydrophobe dérivé	siRNA, oligo-nucléotides

		de VIH-1 gp41 + linker + domaine dérivé de la séquence de localisation nucléaire de l'antigène de virus SV40	(Morris, Vidal et al. 1997; Crombez, Charnet et al. 2007)
CADY	GLWRALWRLLRSLWRLL WRA	Dérivé de PPTG11, variante de la protéine de fusion JTS1	siRNA (Konate, Crombez et al. ; Crombez, Aldrian-Herrada et al. 2009)
Peptides modèles			
$(Arg)_x$	(RRRRR)x	Peptide de synthèse	siRNA (Zhang, Tang et al. 2006)
MAP	KLALKLALKALKAALKA	Peptide de synthèse	Peptide (Hallbrink, Floren et al. 2001)
CPP naturels			
Maurocalcine	GDCLPHLKLCKENKDCCS KKCKRRGTNIEKRCR	*Scorpio maurus palmatus*	Doxorubicine (Fajloun, Kharrat et al. 2000; Aroui, Ram et al. 2009)

Tableau 2. Quelques peptides de pénétration cellulaire et leurs cargos

d. Internalisation des peptides de pénétration cellulaire

Les mécanismes d'entrée dans les cellules des CPP n'est pas encore totalement défini. Dans la majorité des cas, les CPP interagissent avec la membrane plasmique avant de transloquer ou d'endocyter dans les cellules. De plus, le mode d'entrée peut varier pour un même peptide en fonction de la température, de sa concentration, du cargo auquel il est attaché, ou du type cellulaire utilisé.

Il existe de nombreuses techniques pour évaluer l'internalisation d'un complexe CPP-cargo, comme la microscopie (électronique, confocale, biphotonique), la chromatographie liquide, la cytométrie en flux, ou la spectrométrie de masse (Holm, Andaloussi et al. 2011).

i. Composition de la membrane plasmique

La membrane plasmique est une bicouche lipidique, composée de phosphatidylethanolamine (PE), de phosphatidylcholine (PC), de sphingomyéline (SM) qui sont tous trois neutres et de phosphatidylsérine (PS) qui est quand à lui chargé négativement (Cahill 2009). Dans les

cellules vivantes, la PE et la PS sont pour la plus part dans la couche cytosolique, alors que la PC et la SM sont situés dans la couche externe (Cahill 2009).

La matrice extracellulaire est composée de collagène, de protéoglycanes (PGs), d'élastine et de glycoprotéines non collagéneuses (Wilson 2010). Un protéoglycane est composé d'une protéine et d'un glycosaminoglycane (GAG). Les GAGs possédent plusieurs charges négatives dues aux nombreux acides les composants. Ils sont en effet constitués de longues chaînes linéaires, de sulfates et de sucres. Il existe quatre classes de GAGs : 1) le sulfate de chondroïtine et le dermatan sulfate, 2) l'héparane sulfate (HS) et l'héparine, 3) le kératan sulfate et 4) l'acide hyaluronique (qui n'est pas classifiée comme une composante des PGs) (Yanagishita, Podyma-Inoue et al. 2009).

Les PGs jouent un rôle important dans la régulation des microdomaines de la surface cellulaire (Heitz, Morris et al. 2009). L'héparane sulfate protéoglycane (HSPG) et le syndecane font parti des composants majoritaires de la matrice extracellulaire, leur regroupement déclenche une modification du cytosquelette avec l'activation de protéine kinase C et des GTPases Rho/Rac. Ces dernières contrôlent les microdomaines riches en cholestérol et donc la fixation des ligands et l'internalisation dans les cellules (Couchman 2003; Beauvais and Rapraeger 2004).

ii. Interaction des CPP avec la matrice extracellulaire

Le premier contact entre les CPP et la surface cellulaire se déroule par interactions électrostatiques avec les GAGs présents à la surface cellulaire (Heitz, Morris et al. 2009). Il a été montré que la protéine TAT se liait à l'héparine et à l'HS (Rusnati, Coltrini et al. 1997) et que l'internalisation de cette protéine nécessitait la présence d'HSPG (Tyagi, Rusnati et al. 2001). Quelques années plus tard, une expérience à montré que TAT pouvait efficacement transloquer dans des cellules déficientes en HS, cependant en quantité plus faible qu'avec des cellules non dépourvues d'HS (Gump, June et al.). De la même façon, MCa interagit avec l'héparine et l'HS et un analogue de la MCa a subi une diminution de 50% de sa pénétration lorsqu'il était utilisé avec des cellules déficientes en GAGs (Ram, Aroui et al. 2008). Un analogue de la pénétratine ou les résidus arginines ont été substitués par des lysines montre une très faible affinité pour la surface cellulaire, indiquant que les arginines jouent un rôle

important dans l'internalisation des CPP dans les cellules, bien qu'une telle substitution ne modifie pas la charge du peptide (Thoren, Persson et al. 2005). Il a été montré que les peptides polyarginines, une fois en interaction avec les PGs de la surface cellulaire, activaient la protéine Rac-1, induisant un signal menant à la réorganisation des filaments d'actines présents à la surface de la cellule et qui aboutit à la macropinocytose (Nakase, Tadokoro et al. 2007) ainsi que pour MPG (Gerbal-Chaloin, Gondeau et al. 2007). La crotamine se lie aussi à l'HSPG et présente une forte affinité uniquement pour l'HSPG (Nascimento, Hayashi et al. 2007). La pénétratine n'interagit pas avec les lipides zwitterioniques comme la palmitoylphosphatidylcholine (Ghibaudi, Boscolo et al. 2005) mais seulement avec les membranes contenant des lipides anioniques ou de l'HS (Binder and Lindblom 2003).

Des études biophysiques, basées sur l'utilisation de petite et grande vésicules unilamellaires (small unilamellar vesicles (SUV), large unilamellar vesicles (LUV) et giant unilamellar vesicles (GUV)) donnent des renseignements précieux concernant les interactions peptide-membrane sans avoir de perturbations induites par les autres composantes de la membrane (Holm, Andaloussi et al. 2011). Les différences notoires entre ces trois types de vésicules sont leur taille et donc la courbure et la tension de la membrane (Lamaziere, Maniti et al.). Une étude par microscopie cryo-électronique sur des LUV et des vésicules multilamellaires (multilamellar vesicles (MLV)) a permis de mettre en évidence un mécanisme d'action de la pénétratine. 1) la pénétratine se lie aux têtes des phospholipides, 2) en fonction des affinités entre la pénétratine et les différents phospholipides, la pénétratine provoque une séparation et un épaississement de la membrane, 3) puis, une augmentation de la concentration locale de pénétratine sur des domaines séparés de la membrane mène à une courbure de la membrane, conduisant à des ondulations, des vésiculations et/ou à la formation de tubes et éventuellement à des micelle inversées ***(Figure 9)*** (Lamaziere, Maniti et al.). La pénétratine ne modifie pas le signal RMN des SUV composées de PC/PS (4/1) (Berlose, Convert et al. 1996) et ne change pas la turbidité des lipides LUVs zwitterioniques des LUVs, elle perturbe considérablement les lipides anioniques démontrant que la pénétratine conduit à des agrégations des liposomes chargés négativement (Lamaziere, Burlina et al. 2007; Alves, Goasdoue et al. 2008)

Après la première étape de contact entre les CPP et la membrane, une réorganisation des lipides a lieu pour permettre l'entrée des peptides, par endocytose ou par translocation directe à travers la membrane (Alves, Jiao et al.).

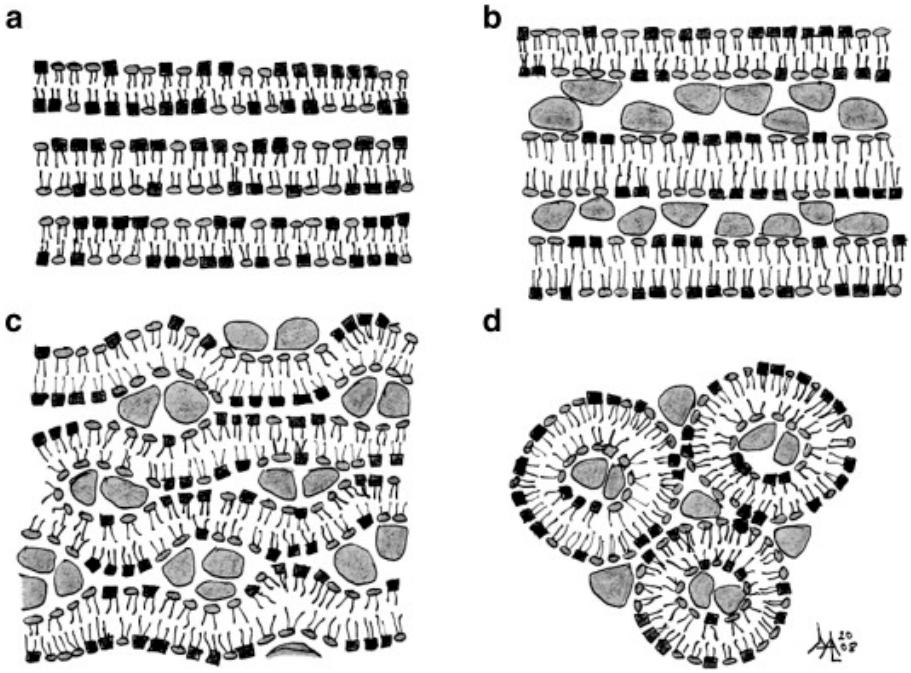

Figure 9: ***Modèle de perturbation membranaire et de translocation par la pénétratine.*** *(a) Membrane composée de différents lipides (cercles gris et carrés noirs). (b) Au contact de la pénétratine, la membrane se sépare en fonction de la nature des lipides, et elle s'épaissit. (c) Après la séparation en différents domaines membranaires, l'augmentation de la concentration en pénétratine provoque des courbures et des ondulations dans la membrane. (d) Il en résulte un formation de petites vésicules (Lamaziere, Maniti et al.).*

e. Passage de la membrane plasmique

Le mécanisme d'entrée des CPP dans les cellules est une clé essentielle pour le développement et l'optimisation de stratégies appropriées pour l'administration de molécules thérapeutiques *in vivo* (Heitz, Morris et al. 2009). Bien que l'internalisation cellulaire des CPP a été étudié dans différents types cellulaires, les mécanismes d'entrée ont été longtemps inconnus et décrits comme indépendant de l'endocytose, de l'énergie et de récepteurs spécifiques (Heitz, Morris et al. 2009). Bien qu'il est difficile d'établir un schéma général

décrivant le mécanisme d'entrée des CPP, il est accepté que le premier contact entre les CPP et la surface cellulaire à lieu par liaisons électrostatiques avec les protéoglycanes et que la voie de passage dans la cellule est dictée par plusieurs paramètres dont : 1) la nature et la structure secondaire du CPP, 2) son aptitude à interagir avec la surface cellulaire et les lipides composant la membrane, 3) la nature, le type et la concentration du cargo et 4) le type cellulaire et la composition de la membrane (Heitz, Morris et al. 2009). De plus, la différence majeure entre les CPP réside en leur mode d'interaction avec les composants de surface cellulaire (Heitz, Morris et al. 2009). Les interactions de Tat, pénétratine et des polyarginines avec la matrice extracellulaire ont été montré comme étant électrostatique, avec une induction de la pénétration via un processus endocytaire dépendant de l'énergie (Rusnati, Tulipano et al. 1999; Console, Marty et al. 2003; Nakase, Niwa et al. 2004; Murriel and Dowdy 2006; Nakase, Tadokoro et al. 2007). Bien que la macropinocitose a été décrite comme la voie principale d'internalisation dans les cellules des CPP cationiques, d'autres voies d'endocytose comme l'endocytose dépendante de la clatrine et de la cavéoline ont été décrite pour les CPP (Wadia, Stan et al. 2004; Kaplan, Wadia et al. 2005; Richard, Melikov et al. 2005). De plus, plusieurs mécanismes de translocation et d'endocytose peuvent intervenir simultanément pour la plus part des CPP, ce qui est spécialement vrai pour les peptides amphipathiques, qui interagissent avec les lipides et adoptent des structures secondaires dans la membrane, ce qui modifie l'intégrité de celle-ci (Heitz, Morris et al. 2009). Dans le cas de la pénétratine et du transportan, il a été suggéré que la translocation et l'endocytose intervenaient simultanément (Letoha, Gaal et al. 2003; Saalik, Elmquist et al. 2004). Pour des concentrations supérieures à 40 µM, le peptide antennapedia pénètre dans les cellules par au moins trois mécanismes différents : la macropinocitose, l'endocytose dépendante de la clathrine et l'endocytose dépendante de la cavéoline sans qu'aucune de ces trois voies prennent l'avantage (Duchardt, Fotin-Mleczek et al. 2007). La crotamine entre dans les cellules par voie endocytaire comme le montrent différentes expériences. L'incubation à 4°C de la crotamine diminue drastiquement la pénétration de celle-ci. D'autre part, dans les cellules, un marqueur de vésicules acides (LysoTracker) indique que la crotamine s'accumule dans les vésicules lysosomales et co-localise avec la transferrine, un ligand spécifique de l'endocytose dépendante de la chlatrine (Nascimento, Hayashi et al. 2007; Kerkis, Silva Fde et al. 2010). La MCa synthétisée uniquement avec des acides aminés de conformation dextrogyre (MCa-D) pénètre dans les cellules avec la même efficacité que la MCa native, ce qui indique que les

interactions entre les lipides et la MCa sont insensibles à la conformation et que la MCa ne pénètre pas dans les cellules par une voie dépendante d'un récepteur (Poillot, Dridi et al.).

f. Devenir des peptides de pénétration cellulaire au sein de la cellule

Dès lors que les CPP entrent dans les cellules par endocytose, il est nécessaire qu'ils puissent être relargués des vésicules jusqu'au cytoplasme afin d'atteindre leur cible. Une petite fraction des CPP est capable de sortir des endosomes, soit du fait de leur capacité à « détruire » les endosomes, soit du fait de la faible « solidité » de la vésicule de macropinocytose (Heitz, Morris et al. 2009). Différentes études ont montré que les CPP pouvaient passer à travers le réticulum endoplasmique et le réseau de Golgi via un chemin rétrograde qui implique le relarguage cytosolique (Fischer, Fotin-Mleczek et al. 2005). Des endosomes précoces et tardifs chargés de protéines Tat et d'autres marqueurs de protéines ont été purifiés à partir de cellules de Jurkat et l'expérience à été réalisée dans un système sans cellules. Il a été montré que la protéine chaperone Hsp90 est nécessaire à la sortie de l'endosome de la protéine Tat (Vendeville, Rayne et al. 2004). L'acidification des endosomes apparait comme étant nécessaire pour la sortie des CPP des vésicules endosomales (Potocky, Menon et al. 2003; Fischer, Kohler et al. 2004). La chloroquine est un réactif chimique qui perturbe les endosomes en inhibant leur acidification (Endoh and Ohtsuki 2009) et qui peut mener au gonflement et à l'éclatement des endosomes. Par addition de chloroquine dans le milieu de culture cellulaire, des études ont montré une amélioration de l'activité du cargo délivré par les CPP (Wadia, Stan et al. 2004; Veldhoen, Laufer et al. 2006; Shaw, Catchpole et al. 2008). Des quantum-dots couplés à un CPP polyarginine via des liaisons non covalentes sont restés « emprisonnés » intacts dans les vésicules endosomales durant trois jours en culture (Delehanty, Bradburne et al. 2010). Nous pouvons prendre l'exemple de la crotamine, qui s'accumule dans les endosomes ou lysosomes, ces vésicules sont déstabilisées et leur contenu est relâché dans le cytosol. Cette perte du contenu lysosomal provoque la distribution de la crotamine dans le compartiment cytoplasmique, qui est l'étape précédant le passage de la crotamine dans le noyau (Nascimento, Hayashi et al. 2007; Kerkis, Silva Fde et al. 2010).

g. Stabilité des CPP dans la cellule

Un aspect crucial de l'administration de drogues est, bien sur, le transport efficace de l'agent pharmaceutique à son site d'action, mais aussi la vitesse de dégradation du CPP qui est utilisé comme vecteur cellulaire. Les CPP ont besoin de transporter leur cargo avant la dégradation extracellulaire de celui-ci, cependant, quand il se trouve dans la cellule, il doit être éliminé dans le but de ne pas causer de toxicité à la cellule (Palm, Jayamanne et al. 2007). Peu d'études se sont focalisées sur la dégradation des CPP au sein des endosomes ou dans le cytoplasme. Du fait que l'endocytose soit la voie majoritaire d'entrée des CPP dans les cellules et avec plus de 40 enzymes hydrolysantes caractérisées dans les lysosomes, il existe une probabilité importante que les CPP entrent en contact avec des voies de dégradation des lysosomes. La stabilité de la transportan, du TP10 et de la pénétratine ont été testée dans des cellules Caco-2. Il s'est avéré que le transportan est plus stable que TP10, qui est plus stable que la pénétratine. La pénétratine est rapidement dégradée, probablement du fait de ses nombreux sites de clivage dibasiques. Cependant, après 4 hrs d'incubation, du peptide intact est toujours détectable dans le lysat cellulaire, montrant que la pénétratine n'a été dégradée que partiellement (Lindgren, Hallbrink et al. 2004). Une autre étude réalisée avec Tat et pénétratine dans trois types de cellules épithéliales a révélé d'importantes différences de stabilité entre les deux peptides. Dans des cellules MDCK, Tat a une stabilité de plus de 100 hrs et pénétratine de plus de 34 hrs. Dans des cellules Calu-3, Tat a une durée de vie de 9 hrs et pénétratine de 45 min. Et dans des cellules TR146, Tat est stable durant 8 hrs et pénétratine pendant pratiquement 3 hrs (Trehin, Nielsen et al. 2004). La résistance protéolytique du CPP hCT(9-32) a été augmentée dans du plasma sanguin humain et dans du surnageant de culture cellulaire HEK293T en remplaçant les acides aminés en position 12 et 16 par un groupement N-méthylphénylalanine ou par une D-phénylalanine (Rennert, Wespe et al. 2006). Dans le cas de la N-méthylation, l'augmentation de résistance protéolytique est due à la diminution de l'accessibilité stérique pour les enzymes protéolytique. En utilisant un acide aminé de conformation non physiologique D, il y a une incompatibilité avec les enzymes natifs (Rennert, Wespe et al. 2006). De la même manière, la D-MCa est totalement résistante à l'action de la trypsine et de l'endoprotéinase Asp-N, alors que la L-MCa est significativement dégradée (Poillot, Dridi et al.).

h. Les inhibiteurs de l'endocytose

L'endocytose est un processus énergétiquement dépendant. La dépendance énergétique du mécanisme d'internalisation est unique, car toutes les voies endocytaires sont inhibées à faible température. De plus, à cette température, la fluidité membranaire est aussi affectée. Vu que la transduction directe commence par des interactions entre les CPP et la membrane cellulaire, il est concevable que l'inhibition de la fluidité membranaire bloque aussi les voies d'internalisation non endocytaires. Ceci a été testé pour l'oligo-arginine à 4°C, 16°C et 37°C dans des cellules CHO. Les résultats montrent clairement que l'inhibition de la fluidité membranaire à 4°C peut affecter l'endocytose et la translocation directe à travers la membrane (Zaro and Shen 2003; Zaro, Rajapaksa et al. 2006).

Il existe différents composés chimiques ou naturels qui peuvent inhiber les différentes voies d'endocytose (***Tableau 3)***. L'amiloride bloque la macropinocytose, le nocodazole inhibe la formation des microtubules, le cytochalasin D empêche l'élongation des F-actines et le méthyl-β-cyclodextrine supprime l'endocytose dépendante des lipides raft par réduction du cholestérol (Poillot, Dridi et al.). Les voies d'entrée de la MCa ont été étudiées par co-incubation de ces différents inhibiteurs d'endocytose. Le nocodazole entraîne une réduction de 50% de la pénétration cellulaire, le cytochalasin D provoque 59% de perte de pénétration. L'amiloride inhibe l'entrée de MCa dans les cellules de 53% et le méthyl-β-cyclodextrine de 15.8% (Poillot, Dridi et al.) ce qui n'est pas observé quand le cargo est la streptavidine (Ram, Aroui et al. 2008). La chlorpromazine inhibe la formation des puits recouverts de clathrine à la membrane plasmique (Vendeville, Rayne et al. 2004) et comme mentionné ci-dessus, la chloroquine perturbe les endosomes. Le prétraitement des cellules CHO avec de la chloroquine empêche l'endocytose de la crotamine d'environ 92%. La pré-incubation des cellules avec de la chlorpromazine inhibe de 65% l'internalisation de la crotamine (Nascimento, Hayashi et al. 2007).

Macropinocytose

Cytochalasin D
Amiloride
Toxine B
Inhibiteur de PI_3K
Mutant GTPase ARF_6
Domaine autoinhibiteur PAK_1

Famille des inhibiteurs mutants Rho

Clathrine dépendante

Anticorps anti-clathrine
Choc à faible pH
Réduction en potassium
Brefeldin A
Chlorpromazine
Mutant dynamine dominant négatif
Mutant Eps15 dominant négatif
Domaine clathrine hub
Sous unité AP-2 µ2

Cavéoline dépendante

Drogues de liant au stérol
Mutant cavéoline dominant négatif

Endosomes

Mutants GTPase Rab
Mutants GTPase de la famille Rho
Inhibiteurs de PI_3K
Inhibiteurs de PKC

Tableau 3. Liste de réactifs ciblant les voies endocytaires *(Sieczkarski and Whittaker 2002)*

i. Toxicité des peptides de pénétration cellulaire

Du fait de l'utilisation croissante des CPP, une investigation approfondie sur leur toxicité *in vitro* est la première étape vers la sélection de ceux-ci comme agents d'administration en clinique (Lundin, Andaloussi et al. 2011). Les CPP ont montré des effets tels qu'une diminution de la viabilité cellulaire à de fortes concentrations (Mueller, Kretzschmar et al. 2008) et peuvent provoquer une hémolyse (Saar, Lindgren et al. 2005). Ces effets sont souvent associés à de la formation de pores, des perturbations (Saar, Lindgren et al. 2005) et pertes membranaires (étudié par perte de la calcéine dans des LUVs) (Magzoub, Oglecka et al. 2005; Barany-Wallje, Gaur et al. 2007). Différents tests de toxicité existent ***(Figure 10)***, le test à l'iodure de propidium, basé sur l'exclusion de l'agent intercalant de l'ADN fluorescent.

Le test MTT évalue l'activité déhydrogénase mitochondriale par le biais de la conversion enzymatique du tétrazole en formazan, comme indicateur de viabilité cellulaire. Le test d'hémolyse quantifie les propriétés hémolytiques des CPP (Lundin, Andaloussi et al. 2011). Le test au déoxyglucose donne une indication sur l'intégrité de la membrane plasmique, il est basé sur les « fuites » de déoxyglucose, radiomarqué, phosphorylé intracellulairement, par la membrane plasmique lésée (Walum and Peterson 1982).

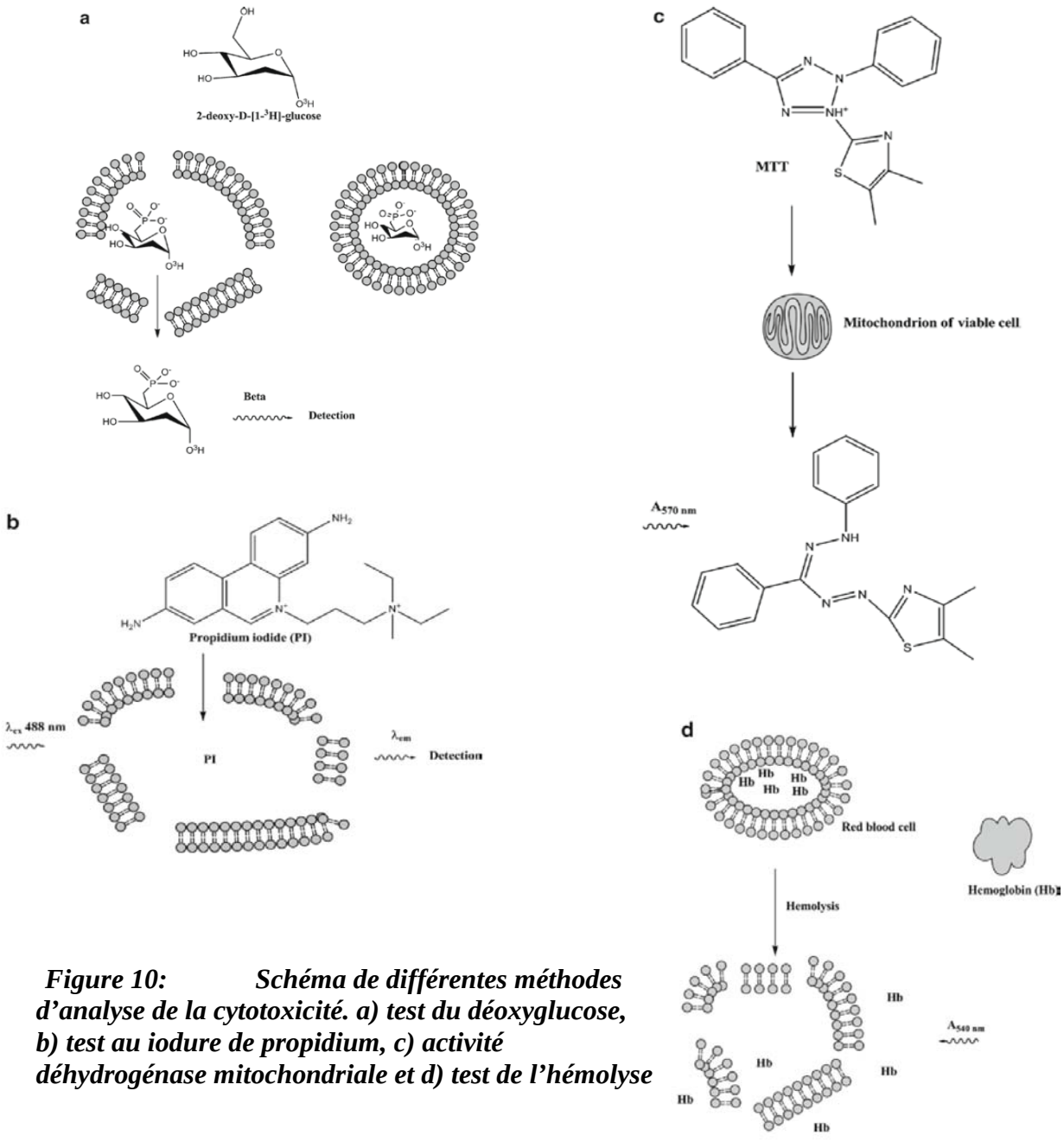

Figure 10: Schéma de différentes méthodes d'analyse de la cytotoxicité. a) test du déoxyglucose, b) test au iodure de propidium, c) activité déhydrogénase mitochondriale et d) test de l'hémolyse

Grâce à un test MTT, il a pu être montré que la L-MCa et la D-MCa ne sont pas cytotoxiques (Poillot, Dridi et al.). Par le même test, le peptide SAP a été révélé non cytotoxique même à 500 µM durant 24 hrs dans des cellules HeLa, ni dans des cellules endothéliales microvasculaires de cerveau bovin (Martin, Teixido et al. 2011). La crotamine est inoffensive pour les cellules HeLa à plus de 100 µM (Radis-Baptista, de la Torre et al. 2008).

4. Application des peptides de pénétration cellulaire

L'atout majeur des CPP consiste à pouvoir transporter des cargos qui sans eux ne pourraient pas accéder aux compartiments intracellulaires de la cellule (endosomes, noyaux et cytoplasme). Les CPP peuvent être couplés à des cargos de nature très diverses. A titre d'exemple, les CPP ont permis avec succès un transport intracellulaire efficace de i) peptides, ii) protéines , iii) acides nucléiques (oligonucléotides, cDNA, RNA, siRNA, PNA), iv) fluorochromes, v) nanoparticules, vi) agents de contraste IRM, et vii) drogues (Brasseur and Divita).

a. Méthode de couplage aux cargos

Le couplage entre les CPP et les cargos peut se faire de différentes manières selon la nature du cargo et les fonctions chimiques présentes sur celui-ci ***(Figure 11)***.

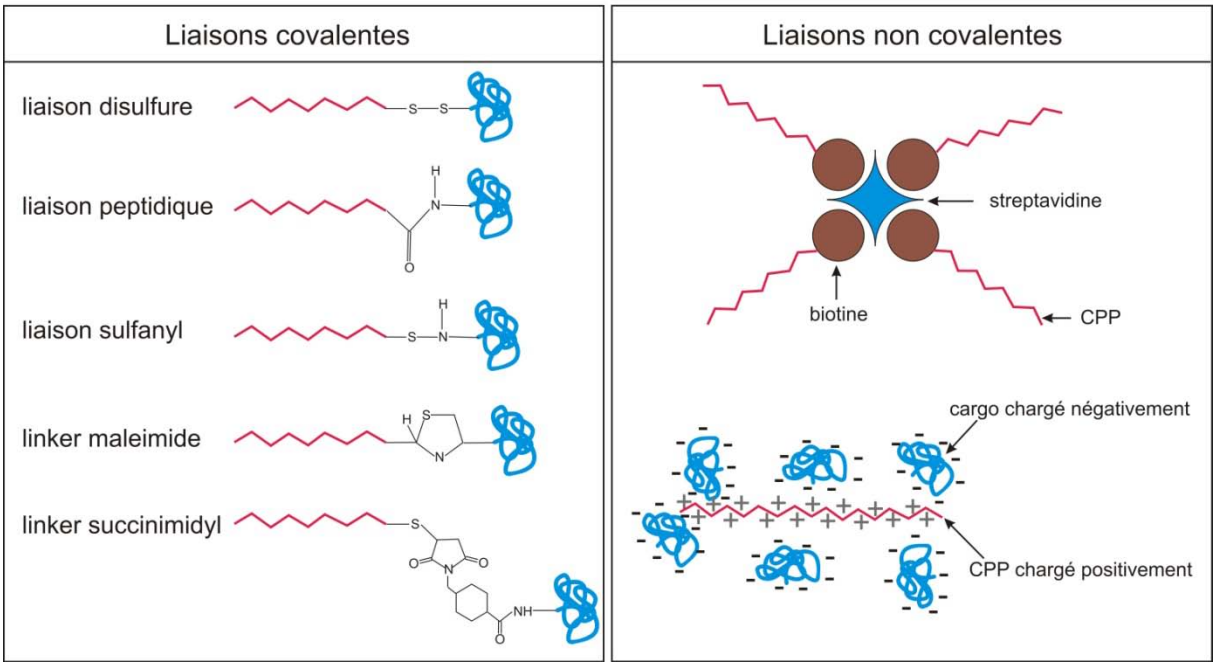

Figure 11: Illustration des différentes méthodes pour attacher les cargos aux CPP

Il existe plusieurs types de liaison chimique, dont deux sont utilisés pour attacher des cargos à internaliser dans les cellules à des peptides de pénétration cellulaire : la liaison covalente et la liaison électrostatique.

Les siRNAs sont le plus souvent liés aux CPP par des liaisons électrostatiques (Simeoni, Morris et al. 2003; Crombez, Charnet et al. 2007; Lundberg, El-Andaloussi et al. 2007; Meade and Dowdy 2007). Il y a attraction de charges opposées entre les siRNAs chargés négativement et les CPP chargés positivement. Cette réaction de couplage est simple, rapide et efficace (Lundberg, El-Andaloussi et al. 2007). Une fois le complexe CPP/siRNA internalisé dans les cellules, l'activité du siRNA n'est pas inhibé, et le gêne ciblé peut être éteint ***(Figure 12)*** (Crombez, Aldrian-Herrada et al. 2009).

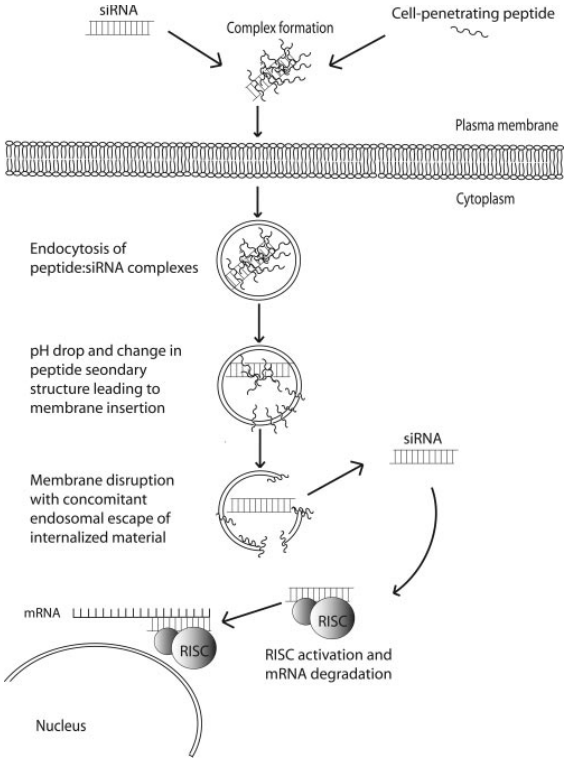

Figure 12: Schéma de l'internalisation de siRNA par les CPP.
Le complexe CPP/siRNA interagit en premier lieu avec les charges positives des glycosaminoglycanes de la membrane plasmique, s'ensuit l'endocytose. Après l'acidification des endosomes, une protonation a lieu, menant au changement de la structure secondaire des peptides. Le changement de la structure secondaire conduit à l'insertion de peptides dans la membrane endosomale, induisant une lyse des endosomes et la sortie du siRNA dans le cytosol (Lundberg, El-Andaloussi et al. 2007)

Le deuxième type de liaison électrostatique implique l'utilisation de biotine et de streptavidine. Le CPP et le cargo doivent donc être modifiés chimiquement. L'affinité entre la biotine et la streptavidine est extrêmement forte, ce qui rend le complexe CPP/cargo très stable (Ram, Weiss et al. 2008).

Les cargos peuvent être directement couplés aux CPP durant la synthèse, il y aura donc une liaison peptidique entre le peptide et son cargo. Cependant, dans certains cas, la modification chimique du cargo et/ou le couplage directe sur le CPP peut faire perdre au cargo son activité biologique (Temsamani and Vidal 2004).

Dans la majorité des liaisons covalentes, le CPP est attaché à son cargo par liaison disulfure. Dans ce cas, la liaison entre le cargo et le CPP est coupée une fois le complexe internalisé dans la cellule, relâchant ainsi le cargo dans le cytoplasme (Muratovska and Eccles 2004). Les

autres types de couplage électrostatique, mettent tous en jeu un linker auquel est lié le CPP et le cargo.

b. Délivrance de peptides et de protéines

Nombreux sont les peptides et protéines exogènes qui possèdent des activités biologiques importantes (Sato, Viswanathan et al. 2006) et qui pourraient être utilisés en thérapeutique humaine pour le traitement de diverses pathologies. Ce qui limite l'utilisation thérapeutique des peptides est leur faible biodisponibilité en raison des difficultés d'absorption et des faibles perméabilités au travers de la muqueuse intestinale, puis des membranes cellulaires. Des solutions satisfaisantes ont pu être établies en couplant des peptides bioactifs à des CPP. Cette augmentation du transport favorise très largement la biodisponibilité de ces peptides thérapeutiques. Ainsi, le groupe de Takayama a établi récemment que le glucagon-like peptide-1 (GLP-1) et l'exendin-4, deux peptides pour le traitement du diabète de type 2, peuvent être transportés efficacement au travers de la muqueuse nasale s'ils sont couplés à la pénétratine (Khafagy el, Morishita et al. 2009). Dans ce cas-là, le peptide glucagon-like et l'exendin-4 ont été incubés avec la pénétratine afin de créer un complexe électrostatique. La pénétratine à été utilisée sous sa forme L, ainsi que sous sa forme D, afin de comparer la stabilité des deux isomères. Les peptides contenant des acides aminés L sont plus instables métaboliquement dans la cavité nasale que ceux contenant des acides aminés D, mais l'absorption de GLP-1 est renforcée lorsqu'il est complexé avec la pénétratine L. A contrario, la pénétratine D est plus efficace que la forme L pour l'absorption de l'interferon-β (INF-β) (Khafagy el, Morishita et al. 2009). Le facteur de transcription p53 régule des fonctions cellulaires importantes comme la mitose ou l'apoptose. Dans la moitié des tumeurs, p53 est mutée, et la perte des fonctions normales de p53 augmente la résistance des cellules cancéreuses face à la thérapie (Sherr and McCormick 2002). Tat a été utilisé pour délivrer un peptide p53 modifié (p53C') dans des souris porteuses de tumeurs aux ovaires (Snyder, Meade et al. 2004). Des injections de TAT-p53C' pendant 12 jours ont abouti à une réduction significative de la croissance tumorale et une durée de vie multipliée par six (Snyder, Meade et al. 2004). Le facteur de croissance hépatocytaire (FCH) et son récepteur Met sont responsables de différentes réponses cellulaires, durant le développement embryonnaire, durant l'homéostasie des tissus et durant la croissance tumorale. Dans le cancer, Met peut agir

comme un oncogène sur les cellules tumorales aussi bien que comme un facteur pro-angiogénique activant les cellules endothéliales et induisant la formation de nouveaux vaisseaux (Cantelmo, Cammarota et al. 2010). Un peptide aux propriétés anti-angiogéniques imitant le site d'accueil de la partie C ter de Met à été couplé à Tat par fusion et délivré dans les cellules. Le peptide TAT-Met inhibe la prolifération des cellules endothéliales, la propagation et la morphogénèse *in vitro* (Cantelmo, Cammarota et al. 2010). *In vivo*, TAT-Met inhibe l'angiogénèse induite par FCH dans l'essai de l'éponge matrigel et altère la croissance des tumeurs xénogreffées et la vascularisation dans le sarcome de Kaposi (Cantelmo, Cammarota et al. 2010).

De la même façon que pour les peptides, de nombreuses protéines ont été couplées à des peptides de pénétration cellulaire de manière à être efficacement internalisées dans les cellules. La neuroglobine (Ngb) est une globine présente dans le cerveau, capable de le protéger contre les dommages ischémiques induits par l'hypoxie (Cai, Lin et al. 2010). Cependant, en raison de sa grande taille, Ngb est incapable de passer la barrière hémato-encéphalique (BHE) ce qui limite les applications dans les lésions du cerveau (Cai, Lin et al. 2010). La protéine Ngb à été greffée à TAT par fusion, injecté par voie intra-veineuse, ce complexe à ainsi été capable de passer la BHE et de protéger le cerveau des ischémies cérébrales (Cai, Lin et al. 2010). Le cancer du poumon non à petites cellules (CPNPC) représente 80% des cas de cancer du poumon. Le dysfonctionnement de p53 et l'hypoxie sont les signes biologiques caractéristiques des tumeurs solides comme la CPNPC (Zhao, Wu et al. 2011). Une protéine de fusion p53 à été couplé avec le motif minimum du domaine dépendant de la dégradation de l'oxygène (DDDO) et TAT. Le complexe a été testé dans des cellules délaitées de p53 (Zhao, Wu et al. 2011). Le complexe TAT-DDDO-p53 induit significativement le blocage du cycle cellulaire et/ou l'apoptose *in vitro* (Zhao, Wu et al. 2011). Les résultats *in vivo* montrent que le complexe s'accumule sélectivement dans les régions de faible oxygénation des tissus contenant les tumeurs solides, inhibant ainsi la croissance tumorale (Zhao, Wu et al. 2011). L'anticorps humain simple chaine (HuScFv) est spécifique de la protéine matrice (M1) du virus influenza A. M1 joue un rôle important dans la réplication du virus. Pour interférer avec M1, il est nécessaire que HuScFv soit capable d'accéder à sa cible intracellulaire (Poungpair, Pootong et al. 2010). Une séquence du gêne codant pour HuScFv (*huscfv*) à été couplé à la pénétratine. Le complexe Pen-huscfv à été efficacement internalisé dans des cellules infectées A/H5N1 et s'est lié à M1 (Poungpair,

Pootong et al. 2010). En traitant les cellules infectées par le virus de l'influenza avec Penhuscfv, on observe une réduction du nombre de virus libéré des cellules (Poungpair, Pootong et al. 2010).

CPP utilisé	Cargo	Cible/Effet	Référence
Pénétratine	Glucagon-like peptide-1 et endexin-4	Traitement du diabète	(Khafagy el, Morishita et al. 2009)
Tat	p53 modifiée	Réduction de la croissance tumorale	(Snyder, Meade et al. 2004)
Tat	Peptide anti-angiogénique	*in vitro* : inhibe la prolifération des cellules endothéliales, la propagation et la morphogénèse *in vivo* : altère la croissance tumorale et la vascularisation dans le sarcome de Kaposi	(Cantelmo, Cammarota et al. 2010)
Tat	Neuroglobine	Passage de la BHE, protection contre les ischémies	(Cai, Lin et al. 2010)
Tat	p53	Inhibition de la croissance tumorale	(Zhao, Wu et al. 2011)
Pénétratine	*huscfv*	Diminue la réplication du virus de l'influenza	(Poungpair, Pootong et al. 2010)
MCa	Streptavidine	Etude de l'internalisation de la MCa	(Ram, Weiss et al. 2008)

Tableau 4. Exemples de peptides/protéines internalisés grâce à des CPP

c. Délivrance d'oligonucléotides/siRNA

Pour contrôler l'expression des gênes ou pour éteindre l'activité de certaines protéines, les oligonucléotides (ONs), les siRNAs, les plasmides ou leurs analogues comme les PNAs (peptide nucleic acid) ont été largement utilisés ces dernières années.

Les micros ARN (miRNAs) sont des ARN simple brin long de 22 nucléotides environ. Ils sont impliqués dans la régulation de l'expression des gênes au niveau post transcriptionnel (Fu, Chen et al. 2011), et dans des processus biologiques, comme la différentiation, la prolifération, l'apoptose et le métabolisme (Zhou and Verne 2011). Les acides nucléiques peptidiques (PNA) sont des molécules aux bases similaires à l'ADN ou à l'ARN mais qui se différentie par son squelette. Le squelette du PNA ne comporte pas de groupement phosphate,

ce qui lui confère une liaison plus forte avec l'ADN ou l'ARN qu'une liaison ADN/ADN du fait de l'absence de répulsion électrostatique. Les PNAs ont été développés pour améliorer la spécificité et l'affinité pour les miRNAs cibles (Oh, Ju et al. 2010). Onze CPP ont été couplés avec un PNA afin d'étudier la translocation des PNA dans les cellules ainsi que l'inhibition du miRNA cible. Sur les onze peptides, quatre n'ont pas amélioré l'internalisation du PNA (Cationic, C-myc tag, H region, et PTD-4). Le peptide conduisant à l'inhibition la plus efficace du miRNA cible est un peptide Tat modifié (Oh, Ju et al. 2010).

L'encéphalite Japonaise est une maladie virale transmise par les piqures de moustique. Elle est la cause principale des encéphalites chez l'homme. Un PNA ciblé contre une partie de l'ARN du génome du virus à été couplé covalament à Tat. Le complexe Tat-PNA a ainsi pu empêcher la prolifération du virus de l'encéphalite Japonaise en bloquant les interactions ARN-protéines ou ARN-ARN essentielles à la production d'une infection virale (Yoo, Kim et al. 2009).

L'exposition à des UV entraine la formation de cancers cutanés causés par des lésions de l'ADN. Les lésions majoritairement provoquées par les UV sont les dimères de cyclobuatne pyrimidine (DCPs). Les mécanismes pour réparer les DCPs, sont la voie de réparation par excision nucléotidique (REN) et la voie de réparation par excision de base (REB). Bien que les humains possèdent une voie REB, il leur manque une glycosilase qui initie la catalyse de REB en réponse aux dégâts causés par l'exposition aux UV. L'hypothèse qu'une administration exogène de l'enzyme initialisant la voie REB pourrait favoriser la réparation précise des DCPs à été émise (Johnson, Lowell et al. 2010). En effet, le bactériophage T4-pyrimidine dimer-specific DNA glycosylase (T4-pdg) améliore la réparation des DCPs (Johnson, Lowell et al. 2010). T4-pdg a été couplé à une séquence de localisation nucléaire (NLS) pour favoriser le ciblage au noyau et à Tat. Le complexe T4-pdg-NLS-Tat a efficacement pénétré dans les cellules et rapidement et significativement augmenté le taux d'initiation de la réparation des DCPs sur des cellules épithéliales ayant subi une exposition aux UV (Johnson, Lowell et al. 2010).

Les siRNA sont des petits ARN double brin d'environ 19-21 nucléotides qui, après une prise en charge par le système RISC (RNA-inducing silencing complex), et hybridation spécifique à l'ARNm ciblé, induit une coupure au sein de l'ARNm, rendant celui-ci indisponible à la traduction protéique (Elbashir, Harborth et al. 2001). La découverte des siRNA a valu à leurs

auteurs (Prs. Melo et Fire) le prix Nobel de Physiologie et Médecine en 2006. Bien que le potentiel thérapeutique des siRNA soit immense, leur utilisation en clinique est limitée du fait d'une mauvaise délivrance cellulaire. C'est pourquoi de nombreuses études portent sur le couplage des siRNA avec des CPP (Choi, Lee et al. ; Konate, Crombez et al. ; Simeoni, Morris et al. 2005; Lundberg, El-Andaloussi et al. 2007; Medarova, Pham et al. 2007). La plupart des stratégies ont porté sur des liaisons non-covalentes entre CPP et siRNA ; liaisons rendues possibles grâce à la complémentarité de charges électrostatiques entre ces deux ligands (charges positives pour le CPP et charges négatives pour le siRNA). Ce couplage s'est avéré approprié dans le cas du CPP MPG pour la délivrance des siRNA en raison d'une très bonne affinité avec les acides nucléiques et la formation de complexes stables avec les siRNA par liaisons électrostatiques (Choi, Lee et al. ; Crombez, Charnet et al. 2007). Ainsi complexés, les siRNA ont pu être délivrés dans différents types cellulaires, comprenant celles en suspension ou adhérentes, les cellules primaires ou les cellules souches embryonnaires (Simeoni, Morris et al. 2005). L'autre alternative à cette méthodologie repose sur un couplage par pont disulfure entre un brin du siRNA et le CPP (Muratovska and Eccles 2004). Autour de cette technique, des variantes sont possibles reposant sur l'utilisation de siRNA fluorescents. C'est ainsi que cette technique a été utilisé avec succès *in vitro*, en utilisant la pénétratine, pour la répression de l'expression de SOD1 et caspase-3 dans les neurones sympathiques et d'hippocampes (Davidson, Harel et al. 2004). Sur des modèles animaux de cancer xénogreffé avec des cellules de carcinome, le CPP dérivé de la protamine supprime la croissance tumorale en inhibant l'expression de VEGF grâce aux siRNA adéquats (Choi, Lee et al.). La même stratégie s'avère payante par injection intra-tumorale avec le CPP MPG-8 en ciblant les RNA de la cycline B1 avec un siRNA dirigé contre cette cycline des cellules tumorales PC3 ou SCK3-Her2 (Crombez, Morris et al. 2009). Ces résultats très prometteurs sur des modèles animaux laissent entrevoir une utilisation prochaine des CPP couplés aux siRNA en clinique.

CPP	**Oligonucléotide**	**Cible/effet attendu**	**Référence**
MPG-8	siRNA	Empêcher la croissance des tumeurs en ciblant la cycline B1	(Crombez, Morris et al. 2009)
Pénétratine	siRNA	Caspase-3, extinction de la superoxide dismutase 1	(Davidson, Harel et al. 2004)
Tat	PNA	dsRed	(Su, Mishra et al. 2007)
Tat et Pénétratine	siRNA	Extinction de p38	(Moschos, Williams et

		MAPK (Mitogen-Activated Protéine Kinase)	al. 2007)
Crotamine	ADN plasmidique	Etude de l'internalisation du complexe dans les cellules	(Nascimento, Hayashi et al. 2007)
Protamine	siRNA	Protéine luciférase et Facteur de croissance de l'endothélium vasculaire	(Choi, Lee et al.)
CADY	siRNA	Etude de l'internalisation du complexe dans les cellules	(Konate, Crombez et al.)
Transportan 10	PNA	Etude du rôle des sous-types Cav1.2 et Cav1.3 des canaux L voltage-dépendant dans les douleurs neuropathiques chroniques	(Fossat, Dobremez et al. 2010)

Tableau 5. Récents exemples d'utilisation des CPP pour la délivrance d'oligonucléotides

d. Délivrance de nanoparticules

Les nanoparticules sont de plus en plus étudiées comme plateformes multimodales à la fois pour la possibilité de greffer des molécules bioactives et comme outil de diagnostique (fluorescence, magnétisme) ou de traitement thérapeutique (production d'énergie). Leur incapacité à traverser les membranes lipidiques des cellules limite cependant grandement leur utilisation *in vitro* et *in vivo*. De ce fait, les nanoparticules sont souvent utilisées en complexe avec des CPP afin de contourner cet écueil de pénétration cellulaire. Plusieurs ligands ont pu être fixés sur une même nanoparticule. Ainsi, des nanoparticules de fer super paramagnétiques, conjuguées à Tat, ont pu être internalisées dans des lymphocytes avec une efficacité 100 fois supérieure à celle des nanoparticules seules. Ce complexe est localisé dans le noyau et le cytoplasme des cellules (Josephson, Tung et al. 1999). Les cellules sont magnétiques et deviennent détectables par IRM. Cette technique permet le tracking cellulaire *in vivo* par IRM et la récupération des cellules des organes en raison de leurs propriétés magnétiques. D'autres applications reposent sur l'utilisation de nanocristaux semi-

conducteurs luminescents (encore appelés quantum dots), une classe de sondes fluorescentes ayants des propriétés optiques qui les rendent supérieures aux colorants organiques pour les applications biologiques. Selon la nature des nanocristaux ou leurs diamètres, les longueurs d'onde d'émissions diffèrent permettant de créer tout un panel de couleurs. Cette propriété a été utilisée avec des quantums dots fonctionnalisés avec la maurocalcine pour marquer avec des codes de couleurs différents des monocytes/macrophages et des lymphocytes T (Jayagopal, Su et al. 2009). La réinjection *in vivo* des cellules ainsi marquées dans un modèle d'athérosclérose (souris ApoE$^{-/-}$) permet de marquer des aires de lésion aortique. Les nanoparticules de platine (Pt-np) sont des mimes des superoxides dismutases/catalases et ont une activité similaire à celle du complexe I de transport d'électron mitochondrial (Sakaue, Kim et al. 2010). Afin d'étudier l'efficacité de ce complexe I-like *in vivo*, Tat à été couplé à un peptide de haute affinité pour le platine, ainsi qu'aux Pt-np (Tat-PtBP-Pt). Les auteurs ont ensuite étudié l'effet de Tat-PtBP-Pt sur un complexe mitochondrial I-deficient du mutant neo-1 de *Caenorhabditis elegans* (LB25). Le complexe à été testé sur des larves maintenues dans un milieu contenant le complexe Tat-PtBP-Pt (Sakaue, Kim et al. 2010). Le complexe a été internalisé dans les mitochondries ainsi que dans le cytosol et présente une activité NADH oxydase. Les larves traitées avec Tat-PtBp-Pt ont vu leur durée de vie allongée (moyenne maximale : 24% d'augmentation) (Sakaue, Kim et al. 2010).

e. Délivrance d'agents anti-tumoraux

Une des applications prometteuses des CPP semble être la délivrance efficace d'agents anti-tumoraux *in vivo*. La doxorubicine est un agent intercalant fréquemment utilisé en chimiothérapie des cancers solides. Après une période d'administration de cet agent, les cellules tumorales développent généralement un mécanisme de résistance à la doxorubicine appelé « multidrug resistance» (MDR) (Sawicka, Kalinowska et al. 2004) qui conduit à l'expulsion des molécules administrées des cellules. Aroui *et al* ont démontré en 2009 que l'administration à des cellules chimio-résistantes MDA-MB-231 d'un complexe moléculaire formé par une liaison chimique entre un analogue de la maurocalcine (CPP sans activité pharmacologique) et la doxorubicine (Aroui, Ram et al. 2009), permettait de contrer ce phénomène de résistance. Il semblerait que le complexe moléculaire soit moins susceptible à l'expulsion cellulaire par le MDR que la doxorubicine. Inversement, sur les cellules chimio-

sensibles MCF-7, l'efficacité de la doxorubicine est diminuée par le couplage à la maurocalcine, probablement en raison d'une différence de distribution subcellulaire du complexe (localisation essentiellement cytoplasmique pour la maurocalcine-doxorubicine *versus* une distribution nucléaire prédominante pour la doxorubicine). Il apparaît que le couplage de la doxorubicine à un CPP favoriserait en réalité plutôt des mécanismes d'apoptose, différant en ce point du mécanisme traditionnel de mort induite par la doxorubicine seule. Ces résultats obtenus avec la maurocalcine ont pu être généralisés à d'autres CPP (Liang and Yang 2005; Aroui 2009), voire à d'autres agents tumoraux comme le methotrexate (Lindgren, Rosenthal-Aizman et al. 2006). D'autres stratégies ont été utilisées avec succès. Citons à titre d'exemple, l'encapsulation de paclitaxel, un agent anti-tumoral inhibiteur de la mitose, au sein de liposomes fonctionnalisés avec des CPP. Ce type de complexe s'est avéré prometteur sur un modèle animal xenogreffé avec des cellules cancéreuses KB (lignée cellulaire humaine KB d'un carcinome d'épiderme naso-pharynx) (Niu, Zhao et al.).

f. Délivrance d'agent de contraste pour l'imagerie

Pouvoir visualiser *in vivo* des molécules, des cellules, des organes ou des tumeurs et coupler à ces agents de détection des fonctions thérapeutiques serait un atout considérable pour la médecine moderne. L'imagerie intracellulaire s'est jusqu'à présent heurtée à un écueil considérable, celui du passage des agents d'imagerie au travers de la membrane plasmique. De nombreuses applications pour l'imagerie *in vivo* fleurissent aujourd'hui avec l'apport des CPP à ce passage membranaire, que ce soit pour la délivrance de molécules fluorescentes ou des agents de contrastes pour l'imagerie par résonnance magnétique (Olson, Jiang et al. ; Medarova, Pham et al. 2007; Kersemans, Kersemans et al. 2008). L'institut de veille sanitaire estime à plus de 347 000 les nouveaux cas de cancer diagnostiqués en 2009 en France. Le principal moyen de traitement des tumeurs solides est la chirurgie. La réussite d'une telle opération dépend de l'aptitude du chirurgien à différencier la tumeur du tissu sain. Le groupe du Pr. Roger Tsien de l'Institut Médical Howard Hughes de San Diego a développé une méthode permettant de visualiser la tumeur durant la chirurgie grâce à un CPP couplé à un fluorochrome : la Cy5. Ce peptide de pénétration cellulaire est couplé à un peptide neutralisateur de la pénétration (peptide chargé négativement) *via* un linker protéase-sensible.

Ce complexe a une pénétration cellulaire inefficace au sein des cellules non-tumorales, mais après clivage du linker par des protéases spécifiques de la tumeur, le CPP-Cy5 est libéré et pénètre dans les cellules tumorales, marquant ainsi très efficacement la tumeur *in vivo*. Ils ont ainsi pu montré que quand la chirurgie est effectuée avec ce complexe de pénétration cellulaire, il y a 10 fois moins de cellules tumorales résiduelles que durant une chirurgie classique (Nguyen, Olson et al.). Le Pr. Tsien a obtenu lui aussi le prix Nobel de chimie en 2008 pour l'ensemble de ses travaux sur le design de molécules fluorescentes et photo-labiles. Cette même approche a été généralisée à l'utilisation de nanoparticules de gadolinium, ce qui permet, outre une détection de la fluorescence, une imagerie de la tumeur par IRM (Olson, Jiang et al.). D'autres efforts sont en cours de réalisation pour la détection d'ARNm cellulaire par la délivrance de PNA (peptide nucléique acide), aux séquences complémentaires à ces ARNm, grâce à des CPP couplés à des agents de contraste IRM, tel le DOTA (Su, Mishra et al. 2007). Cette stratégie se heurte cependant encore à l'absence de spécificité cellulaire quand à la pénétration des CPP, mais nul doute qu'elle présage de manière ambitieuse de l'avenir de l'imagerie moléculaire *in vivo*.

Résultats

III. Résultats

1. Revues 1 et 2

Administration de molécules actives dans les cellules : Le potentiel des peptides de pénétration cellulaire

Cathy Poillot, Michel De Waard

Médecine/Sciences 2011 ; 27 :261-8

Use of maurocalcine analogues as biotechnological tools for the penetration of cell-impermeable compounds

Cathy Poillot, Michel De Waard

Toxines et Signalisation, Rencontres en Toxinologie, 2009, Editions de la SFET

a. Introduction

L'administration de molécules actives, comme les peptides, les protéines ou les acides nucléiques, se heurtent à la difficulté pour de tels composés de traverser la membrane plasmique. Les peptides de pénétration cellulaire (CPP pour Cell Penetrating Peptide) sont une classe de peptides possédants la faculté prometteuse de traverser la membrane cellulaire. Ces peptides sont utilisés de façon exponentielle depuis quelques années. Ils peuvent faire rentrer dans différents types cellulaires toutes sortes de cargos de façon très rapide.

Cette revue fait un balayage des CPP les plus utilisés, de leur origine et de leurs caractéristiques. Ainsi que des cargos qui peuvent être délivrés dans les cellules via les CPP et les différentes techniques de couplage de ces cargos aux CPP.

médecine/sciences 2011 ; 27 : 527-34

Administration de molécules actives dans les cellules

Le potentiel des peptides de pénétration cellulaire

Cathy Poillot, Michel De Waard

› L'intérêt de la communauté scientifique pour les peptides de pénétration cellulaire (CPP) s'accroît depuis quelques années et leur nombre ne cesse d'augmenter. Ces peptides sont des outils puissants pour l'acheminement des molécules actives jusqu'à leur site d'action. En effet, de nombreuses drogues qui ne peuvent franchir les membranes cellulaires ont, en revanche, pu être efficacement transportées dans les cellules lorsqu'elles étaient couplées à un peptide de pénétration cellulaire. De nombreux *cargos* ont ainsi pu être fixés sur des peptides de pénétration cellulaire : oligonucléotides, molécules aux activités pharmacologiques connues, agents de contraste pour l'imagerie, nanoparticules agissant comme des plates-formes aux fonctionnalités multimodales, etc. Cette revue montre le formidable potentiel des peptides de pénétration cellulaire et leur large diversité d'usage, mais surtout, elle envisage leur future destinée dans les applications cliniques et le traitement des maladies. ‹

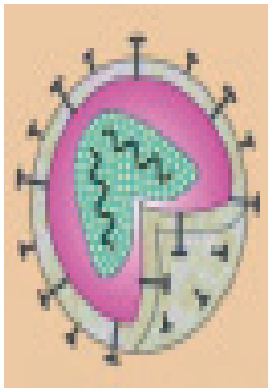

Équipe canaux calciques, fonctions et pathologies, Institut des neurosciences de Grenoble, Inserm U836 ; Université Joseph Fourier, site Santé de La Tronche, BP 170, 38042 Grenoble Cedex 9, France.
cathy.poillot@ujf-grenoble.fr
michel.dewaard@ujf-grenoble.fr

Les premiers peptides de pénétration cellulaire : historique et définition

Le principal obstacle à l'administration de molécules actives dans l'organisme vient du blocage qu'oppose la membrane plasmique à l'entrée dans les cellules des molécules hydrophiles. Un accès intracellulaire pour ces composés s'effectue donc au prix de leur administration répétée et massive ou par le biais de stratégies de formulation adéquates. Une méthode permettant de pallier ce problème se développe à vitesse exponentielle. Il s'agit de l'utilisation de peptides de pénétration cellulaire (CPP pour *cell penetrating peptide*). Ce sont de petits peptides d'une taille variant de 10 à 30 acides aminés, et qui ont une charge nette positive, essentiellement apportée par des résidus lysines et arginines. Ils peuvent être internalisés dans les cellules par un ou plusieurs mécanismes, dont certains ne nécessitent pas d'apport énergétique cellulaire. En règle générale, les CPP n'ont pas de récepteurs cellulaires connus, à l'exception notable de certains d'entre eux issus de protéines fonctionnelles plus larges.

Ce sont Frankel et Pabo qui les premiers en 1988, en étudiant l'activité de la protéine Tat du virus de l'immunodéficience humaine (VIH), se sont aperçus que cette protéine purifiée était capable de pénétrer dans les cellules [1]. Par la suite, Joliot *et al.* ont montré en 1991 que la protéine *Drosophila antennapedia homeodomain* pénètre dans les cellules neuronales et qu'elle a la capacité de s'accumuler dans les noyaux cellulaires [2]. À l'issue de ces travaux, le tout premier CPP à être décrit, la pénétratine, encore appelée Antp, d'une longueur de 16 acides aminés, fut dérivé de la troisième hélice de *Drosophila antennapedia homeodomain* [3]. Cette étude démontrait pour la première fois que les propriétés de pénétration cellulaire d'une protéine sont dues à des séquences minimales au sein de ces protéines également appelées *protein transduction domain* (PTD). En 1998, Vives *et al.* [4] ont adopté la même approche d'étude pour les domaines tronqués de la protéine Tat et identifié une séquence minimale de la protéine capable d'entrer dans les cellules. Ce peptide a été appelé Tat également en référence à la protéine et ses utilisations ont connu un succès grandissant. Ces deux peptides, pénétratine et Tat,

sont devenus les premiers CPP d'une longue liste de peptides capables de se distribuer au sein des cellules. Parmi ces nouveaux peptides, la maurocalcine est un CPP original [5] car issu du venin d'un scorpion tunisien *Scorpio maurus palmatus*. Ce peptide de 33 acides aminés fut identifié grâce à son activité pharmacologique en tant qu'activateur du récepteur à la ryanodine (RyR1) des muscles squelettiques. La cible est particulièrement originale puisqu'il s'agit d'un canal calcique intracellulaire impliqué dans le couplage excitation-contraction [6]. Ces observations avaient laissé entrevoir la possibilité que la maurocalcine devait traverser la bicouche lipidique des cellules afin d'exercer sa fonction d'activateur de canal calcique. Cette hypothèse était largement renforcée par le fait que le site d'interaction de la maurocalcine sur RyR1 est localisé dans une zone du cytoplasme [7]. La démonstration que la maurocalcine était effectivement un CPP est venue des observations suivantes : (1) l'application extracellulaire du peptide à des myotubes induit une libération calcique quasi instantanée [8] ; et (2) la greffe d'une protéine streptavidine fluorescente sur la maurocalcine biotinylée permet sa translocation intracellulaire [5]. Par ailleurs, la maurocalcine partage en commun avec les autres CPP la propriété d'être un peptide basique dont de nombreux acides aminés sont chargés positivement (11 sur 33). De plus, la plupart des acides aminés basiques sont localisés sur une même face de la molécule en accord avec la distribution asymétrique observée sur des molécules telles que Tat et pénétratine [9].

Le *Tableau I* recense des exemples de divers peptides de pénétration cellulaire, et la *Figure 1* illustre l'origine de quelques-uns d'entre eux. Ces peptides peuvent être *a priori* séparés en quatre classes distinctes. À la classe des PTD découverts à l'origine (Tat et pénétratine) s'ajoutent donc trois classes supplémentaires : (1) la classe des peptides chimères, comprenant CADY [10], MPG [11], Pep-1 [12] et transportan [13] ; (2) la classe des peptides modèles, dont les plus connus sont les peptides polyarginine [14] ; et (3) la classe des CPP naturels comme les toxines de venins dont font partie la maurocalcine et la crotamine [15]. Les peptides chimères sont souvent issus d'une protéine plus large (transportan et CADY). Les peptides comme les polyarginines ou MAP (*model amphipathic peptide*) sont, eux, totalement artificiels et leur conception *de novo* a été inspirée des propriétés de certains acides aminés (basiques et hydrophobes) nécessaires à la pénétration cellulaire des peptides.

Peptides de pénétration cellulaire et mécanisme d'entrée cellulaire

Le mécanisme d'accumulation des CPP dans le cytoplasme des cellules n'est pas encore clairement identifié. Il semble acquis que deux types d'internalisation cellulaire coexistent mais diffèrent drastiquement en termes d'efficacité d'accumulation cytoplasmique des CPP et donc d'applications possibles : d'une part, la translocation directe au travers de la bicouche lipidique, qui présente l'avantage d'un accès direct et rapide des CPP au cytoplasme des cellules ; d'autre part l'endocytose qui, en revanche, présente l'inconvénient d'une accumulation cytoplasmique lente et limitée des CPP *(Figure 2)*. La translocation peut suivre plusieurs

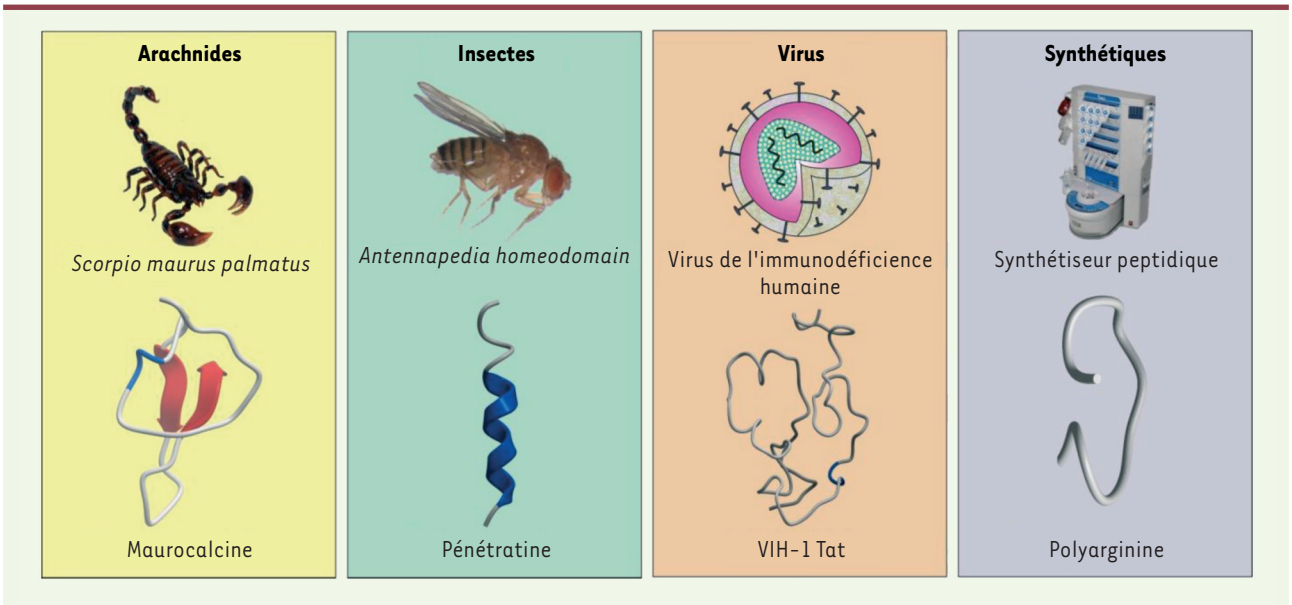

Figure 1. ***Origine de quelques CPP.*** Exemple de l'origine de quatre CPP : la maurocalcine, la pénétratine, Tat et la polyarginine. La maurocalcine, la pénétratine et Tat sont dérivés de séquences naturelles, alors que la polyarginine a été produite par conception *de novo* pour avoir une bonne pénétration cellulaire.

Nom	Séquence en acides aminés	Origines	Cargos
PTD			
Tat_{48-60}	GRKKRRQRRRPPQ	VIH-1	ADN, peptide [4, 46, 47]
Pénétratine	RQIKIWFQNRRMKWKK	*Drosophila Antennapedia homeodomain*	Peptide [3, 48]
Peptides chimères			
Transportan	GWTLNSAGYLLGKINLKALAALAKKIL	Galanin + Mastoparan	Protéine, PNA [13, 49, 50]
Pep-1	KETWWETWWTEWSQPKKKRKV	Domaine riche en tryptophane + *spacer* + domaine dérivé de la séquence de localisation nucléaire de l'antigène du virus SV40	Enzyme [12, 51]
MPG	GALFLGFLGAAGSTMGAWSQPKKKRKV	Motif hydrophobe dérivé de VIH-1 gp41 + *linker* + domaine dérivé de la séquence de localisation nucléaire de l'antigène T du virus SV40	siARN, oligo-nucléotides [11, 52]
CADY	GLWRALWRLLRSLWRLLWRA	Dérivé de PPTG11, variante de la protéine de fusion JTS1	siARN [10, 53]
Peptides modèles			
$(Arg)_x$	(RRRRR)x	Peptide de synthèse	siARN [14]
MAP	KLALKLALKALKAALKA	Peptide de synthèse	Peptide [54]
CPP naturels			
Maurocalcine	GDCLPHLKLCKENKDCCSKKCKRRGT-NIEKRCR	*Scorpio maurus palmatus*	Doxorubicine [6, 36]

Tableau I ***Exemples de quatre classes de peptides de pénétration cellulaires et exemples de cargos transportés.*** La liste des *cargos* utilisés n'est pas exhaustive et est simplement donnée à titre d'illustration. x = 7, 8 ou 9 résidus arginine.

schémas, les modèles de Barrel-Stave et Carpet étant les plus connus [16, 17]. Ces deux modèles ont été empruntés à l'étude des interactions des peptides antimicrobiens avec les bicouches lipidiques et la translocation des peptides est basée sur le concept de perturbation locale de la bicouche lipidique par des agrégats peptidiques. Il est utile de mentionner l'existence de trois modèles supplémentaires : (1) le modèle de pore transitoire, dans lequel les CPP intégrés dans la bicouche lipidique génèrent un courant ionique par formation de pore transmembranaire [18] ; (2) le modèle de fusion membranaire, dans lequel les CPP, en s'insérant dans le feuillet externe de la bicouche lipidique, promeuvent une fusion locale et transitoire de deux régions membranaires, rapprochant ainsi les surfaces cationiques des CPP du feuillet interne anionique de la membrane et facilitant le transfert intracellulaire du CPP [19] ; et (3) un modèle d'électroporation, dans lequel la fixation de CPP cationiques aux lipides anioniques de surface de la membrane plasmique crée un champ électrique transmembranaire. Ceci altère les tensions latérales et de courbure de la membrane et crée les conditions favorables à une électroporation membranaire permettant l'internalisation des peptides par la formation de structures membranaires atypiques et transitoires [20]. Le terme endocytose représente la phagocytose pour les grosses particules et la pinocytose pour les solutés. Quatre types de pinocytose existent : la macropinocytose, l'endocytose dépendante de la cavéoline ou de la clathrine et l'endocytose indépendante de la clathrine et de la cavéoline [21]. Selon le type de CPP et de *cargo* utilisé, chacun de ces mécanismes d'endocytose a été impliqué dans l'internalisation des CPP. La contribution respective des mécanismes d'entrée des CPP (translocation *versus* endocytose) varie selon la nature du CPP utilisé, sa concentration ainsi qu'en fonction du *cargo* transporté.

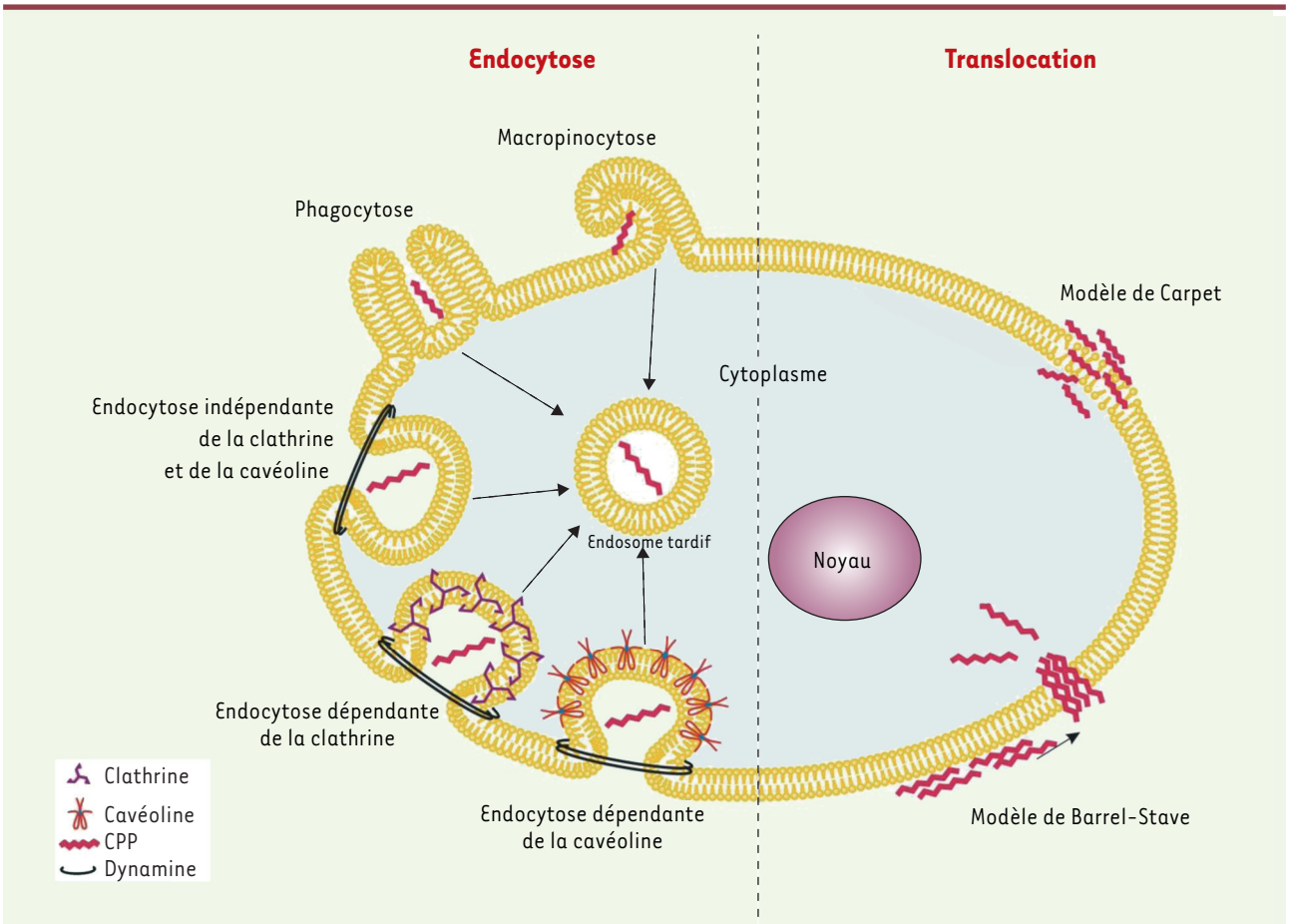

Figure 2. ***Mécanismes d'entrée dans la cellule.*** Deux modes d'entrée des molécules dans la cellule existent : l'endocytose et la translocation. L'endocytose regroupe la macropinocytose, la phagocytose, l'endocytose dépendante de la clathrine, l'endocytose dépendante de la cavéoline et l'endocytose indépendante de la clathrine et de la cavéoline. La translocation se décline en deux modèles : le modèle de Carpet et le modèle de Barrel-Stave.

Peptides de pénétration cellulaire et fonction de transport des cargos

L'atout majeur des CPP consiste à pouvoir transporter des *cargos* qui, sans eux, ne pourraient pas accéder aux compartiments intracellulaires de la cellule (endosomes, noyau et cytoplasme). Les CPP peuvent être couplés à des *cargos* de natures très diverses. À titre d'exemple, les CPP ont permis avec succès un transport intracellulaire efficace de : peptides, protéines, acides nucléiques (oligonucléotides, ADNc, ARN, siARN, PNA [peptide nucléique acide]), fluorochromes, nanoparticules, agents de contraste pour l'imagerie à résonance magnétique, et drogues [22]. Le couplage des CPP avec les *cargos* peut se faire de manière covalente ou non afin de permettre une distribution des molécules d'intérêt dans les cellules. La *Figure 3* illustre différentes méthodes de couplage de ces peptides aux *cargos*. Nous illustrons ci-dessous quelques applications à visée thérapeutique ayant un potentiel de développement clinique.

Peptides de pénétration cellulaire : objectifs thérapeutiques

Délivrer des peptides thérapeutiques

Nombreux sont les peptides et protéines exogènes qui possèdent des activités biologiques importantes et qui pourraient être utilisés en thérapeutique humaine pour le traitement de diverses pathologies. Ce qui peut limiter l'utilisation thérapeutique des peptides, ce sont leur faible biodisponibilité en raison des difficultés d'absorption, et les faibles perméabilités au travers de la muqueuse intestinale. Des solutions satisfaisantes ont pu être établies en couplant des peptides bioactifs à des CPP. Ainsi, le groupe de Takayama a établi récemment que le *glucagon-like peptide-1* (GLP-1) et l'*exendin-4*, deux peptides utilisés pour le traitement du diabète de type 2, peuvent être transportés efficacement au travers de la muqueuse nasale s'ils sont couplés à la pénétratine [23]. Cette augmentation du transport favorise très largement la biodisponibilité de ces peptides thérapeutiques.

Délivrer des siARN

Les siARN (*short interfering RNA*), découverts par Fire et Mello [55], sont des petits ARN double-brin d'environ 19-21 nucléotides qui, après une prise en charge par le système RISC (*RNA-inducing silencing complex*), et hybridation spécifique à un ARNm cible, induisent une coupure au sein de l'ARNm, rendant celui-ci indisponible pour sa traduction en protéine [24]. Bien que le potentiel thérapeutique des siARN soit immense, leur utilisation en clinique est limitée par leur mauvaise pénétration cellulaire. C'est pourquoi de nombreuses études portent sur le couplage des siARN à des CPP [10, 25-28]. La plupart des stratégies impliquent la formation de liaisons non covalentes entre CPP et siARN, liaisons rendues possibles grâce à la complémentarité de charges électrostatiques entre ces deux ligands (charges positives pour le CPP et charges négatives pour le siARN). Ce couplage s'est avéré approprié dans le cas du CPP MPG pour délivrer des siARN, en raison d'une très bonne affinité avec les acides nucléiques et la formation de complexes stables avec les siARN par liaisons électrostatiques [11, 28]. Ainsi complexés, les siARN ont pu être délivrés dans des cellules en suspension, adhérentes, ou en cultures primaires, ou dans les cellules souches embryonnaires [25]. L'autre alternative à cette méthodologie repose sur un couplage par pont disulfure entre un brin du siARN et le CPP [29]. Des variantes de cette technique sont possibles, elles reposent sur l'utilisation de siARN fluorescents. Cette méthode a été appliquée avec succès *in vitro*, en utilisant la pénétratine, pour la répression de l'expression de SOD1 (*superoxide dismutase*) et caspase-3 dans les neurones sympathiques et d'hippocampes [30]. Dans des modèles animaux de cancer établis par xénogreffe avec des cellules de carcinome, le CPP dérivé de la protamine couplé aux siARN adéquats supprime la croissance tumorale en inhibant l'expression du VEGF (*vascular endothelial growth factor*) [31]. La même stratégie s'avère efficace après injection intratumorale (cellules tumorales PC3 ou SCK3-Her2) de CPP MPG-8 ciblant les ARN de la cycline B1 grâce à un siARN dirigé contre cette cycline [32]. Ces résultats très prometteurs obtenus dans des modèles animaux laissent entrevoir une utilisation possible des CPP couplés aux siARN en clinique.

Délivrer des nanoparticules

Les nanoparticules sont de plus en plus étudiées comme plateformes multimodales, à la fois parce qu'elles permettent de greffer des molécules bioactives et comme outil diagnostique (fluorescence, magnétisme) ou thérapeutique (production d'énergie) [56]. Leur incapacité à traverser les membranes lipidiques des cellules peut limiter cependant grandement leur utilisation *in vitro* et *in vivo*. De ce fait, les nanoparticules sont souvent utilisées en complexe avec des CPP afin de contourner cet écueil de pénétration cellulaire. Plusieurs ligands ont pu être fixés sur une même nanoparticule. Ainsi, des nanoparticules de fer superparamagnétiques, conjuguées à Tat, ont ainsi pu être internalisées dans des lymphocytes avec une efficacité 100 fois supérieure à celle des nanoparticules seules. Ce complexe est localisé dans le noyau et le cytoplasme des cellules [33]. Les cellules sont magnétiques et deviennent détectables par IRM. Cette technique permet le suivi cellulaire *in vivo* par IRM et l'extraction des cellules des organes en raison de leurs propriétés magnétiques. D'autres applications reposent sur l'utilisation de nanocristaux semi-conducteurs luminescents (encore appelés *quantum dots*), une classe de sondes fluorescentes ayant des propriétés optiques qui les rendent supérieures aux colorants organiques pour les applications biologiques. Selon la nature des nanocristaux ou leurs diamètres, les longueurs d'onde d'émission diffèrent, ce qui permet de créer toute une série de couleurs. Cette propriété a été utilisée avec des *quantum dots* fonctionnalisés avec la maurocalcine pour marquer avec des codes couleurs différents des monocytes/macrophages et des lymphocytes T [34]. La réinjection *in vivo* des cellules ainsi marquées dans un modèle d'athérosclérose (souris *ApoE*$^{-/-}$) permet de marquer des aires de lésion aortique.

Délivrer des agents antitumoraux

Une des applications prometteuses des CPP semble être la délivrance efficace d'agents antitumoraux *in vivo*. La doxorubicine est un agent intercalant fréquemment utilisé en chimiothérapie des cancers solides. Après une période d'administration de cet agent, les cellules tumorales développent généralement un mécanisme de résistance à la doxorubicine appelé *multidrug resistance* (MDR) [35] qui conduit à l'expulsion par les cellules des molécules administrées. Aroui *et al.* ont démontré en 2009 que l'exposition de cellules chimiorésistantes MDA-MB-231 à un complexe moléculaire formé par une liaison chimique entre un analogue de la maurocalcine (CPP sans activité pharmacologique) et la doxorubicine [36] permettait de contrer ce phénomène de résistance. Il semblerait que le complexe moléculaire soit moins susceptible à l'expulsion cellulaire par le MDR que la doxorubicine. Inversement, si l'on utilise des cellules chimiosensibles MCF-7, l'efficacité de la doxorubine est diminuée par le couplage à la maurocalcine, probablement en raison d'une différence de distribution subcellulaire du complexe (localisation essentiellement cytoplasmique pour la maurocalcine-doxorubicine *versus* une distribution nucléaire prédominante pour la doxorubicine). Il apparaît que le couplage de la doxorubicine à un CPP favoriserait en réalité plutôt des mécanismes d'apoptose, différant en ce point du mécanisme traditionnel de mort induite par la doxorubicine seule. Ces résultats obtenus avec la maurocalcine ont pu être généralisés à d'autres CPP [37, 38], voire à d'autres agents antitumoraux comme le méthotrexate [39]. D'autres stratégies ont été utilisées

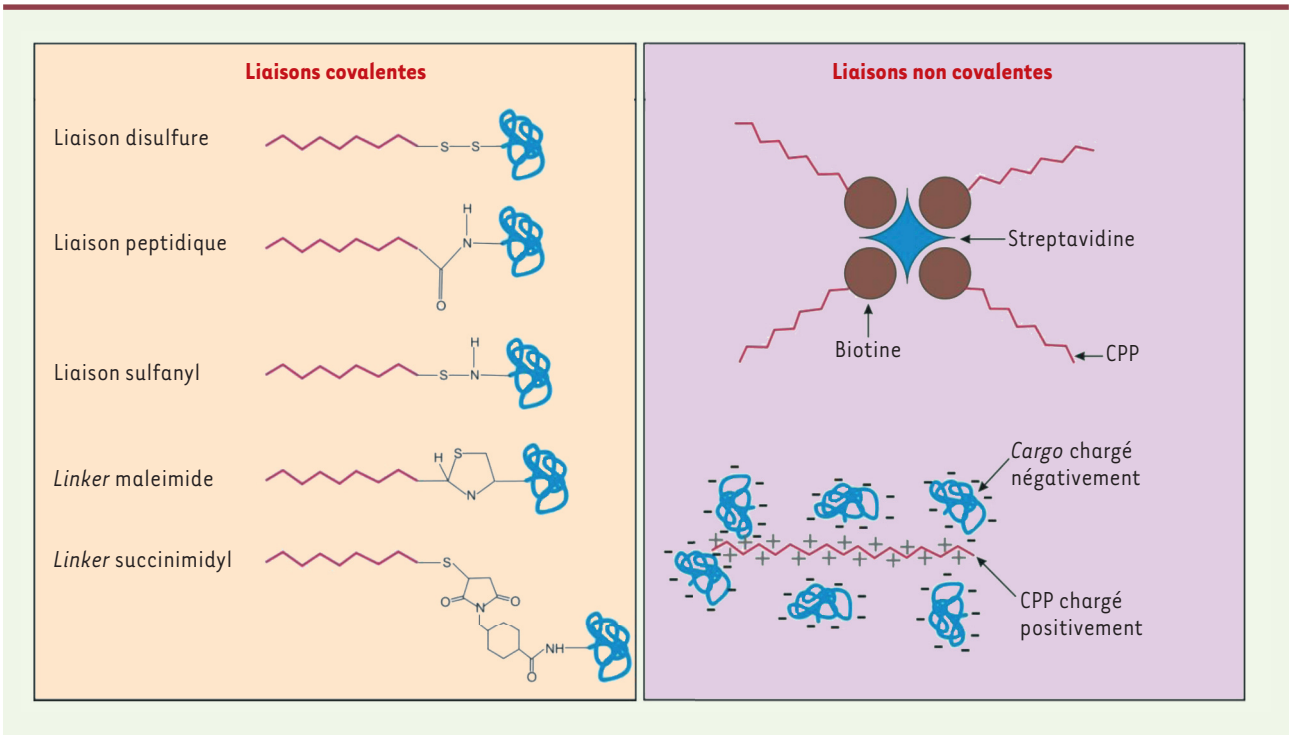

Figure 3. ***Les différents types de couplage des CPP aux cargos à internaliser.*** Les *cargos* peuvent être fixés aux CPP de façon non covalente ou par réaction chimique *via* un *linker*, sauf dans le cas du pont disulfure.

avec succès. Citons à titre d'exemple l'encapsulation du paclitaxel, un agent antitumoral inhibiteur de la mitose, au sein de liposomes fonctionnalisés avec des CPP. Ce type de complexe s'est avéré prometteur dans un modèle animal établi par xénogreffe de cellules cancéreuses KB (lignée cellulaire humaine issue d'un carcinome du nasopharynx) [40].

Peptides de pénétration cellulaire et imagerie cellulaire *in vivo*

Pouvoir visualiser *in vivo* des molécules, des cellules, des organes ou des tumeurs et coupler à ces agents de détection des fonctions thérapeutiques serait un atout considérable pour la médecine moderne. Les méthodes d'imagerie intracellulaire se sont jusqu'à présent heurtées à un écueil considérable, celui du passage des agents d'imagerie au travers de la membrane plasmique. De nombreuses applications d'imagerie *in vivo* utilisant les CPP pour ce passage membranaire fleurissent aujourd'hui, que ce soit pour la délivrance de molécules fluorescentes ou d'agents de contraste pour l'imagerie par résonance magnétique [27, 41, 42]. L'Institut de veille sanitaire estime à plus de 347 000 les nouveaux cas de cancer diagnostiqués en 2009 en France. Le principal moyen de traitement des tumeurs solides est la chirurgie. Or, la réussite d'une telle opération dépend de l'aptitude du chirurgien à différencier la tumeur du tissu sain. Le groupe de Tsien de l'Institut médical Howard Hughes de San Diego a développé une méthode qui permet de visualiser la tumeur durant la chirurgie grâce à un CPP couplé à un fluorochrome : la Cy5. Ce peptide de pénétration cellulaire est couplé à un peptide neutralisant la pénétration (peptide chargé négativement) *via* un agent de liaison (*linker*) sensible aux protéases. Ce complexe ne pénètre pas efficacement dans les cellules non tumorales, mais le clivage du *linker* par des protéases spécifiques de la tumeur libère le CPP-Cy5 qui pénètre dans les cellules tumorales, marquant ainsi très efficacement la tumeur *in vivo*. L'équipe a ainsi pu montrer que quand la chirurgie est effectuée en présence de ce complexe de pénétration cellulaire, il y a dix fois moins de cellules tumorales résiduelles que lors d'une chirurgie classique [43]. Tsien a obtenu le prix Nobel de chimie en 2008 pour l'ensemble de ses travaux sur la conception de molécules fluorescentes et photolabiles [57]. Cette même approche a été généralisée à l'utilisation de nanoparticules de gadolinium, ce qui permet, outre une détection de la fluorescence, une imagerie de la tumeur par IRM [41]. D'autres efforts sont en cours de réalisation pour la détection d'ARNm cellulaires par la délivrance de PNA aux séquences complémentaires à ces ARNm, grâce à des CPP couplés à des agents de contraste IRM, tel le DOTA [44]. Cette stratégie se heurte cependant encore à l'absence de spécificité cellulaire quant à la pénétration des CPP, mais elle présage de manière ambitieuse de l'avenir de l'imagerie moléculaire *in vivo*.

Les différents exemples d'applications décrits ici prouvent tout le potentiel clinique des CPP et prédisent un brillant avenir à ces peptides pour l'amélioration de l'internalisation de drogues d'intérêt clinique. Cette stratégie d'administration possède plusieurs avantages, comme par exemple une délivrance rapide des *cargos* dans les cellules, une bonne stabilité et une absence de toxicité avérée [45]. ◊

SUMMARY

Potential of cell penetrating peptides for cell drug delivery

The interest of the scientific community for cell penetrating peptides (CPP) has been growing exponentially for these last years, and the list of novel CPP is increasing. These peptides are powerful tools for the delivery of cargoes to their site of action. Indeed, several drugs that cannot translocate through the cell plasma membrane have been successfully delivered into cells when grafted to a CPP. Various cargoes have been linked to CPP, such as oligonucleotides, pharmacologically active drugs, contrast agents for imaging, or nanoparticles as platforms for multigrafting purposes... This review illustrates the fabulous potential of CPP and the diversity of their use, but that most interesting appears their future clinical application for the treatment of various pathological conditions. ◊

CONFLIT D'INTÉRÊTS

Les auteurs déclarent n'avoir aucun conflit d'intérêts concernant les données publiées dans cet article.

RÉFÉRENCES

1. Frankel AD, Pabo CO. Cellular uptake of the tat protein from human immunodeficiency virus. *Cell* 1988 ; 55 : 1189-93.
2. Joliot A, Pernelle C, Deagostini-Bazin H, Prochiantz A. Antennapedia homeobox peptide regulates neural morphogenesis. *Proc Natl Acad Sci USA* 1991 ; 88 : 1864-8.
3. Derossi D, Joliot AH, Chassaing G, Prochiantz A. The third helix of the antennapedia homeodomain translocates through biological membranes. *J Biol Chem* 1994 ; 269 : 10444-50.
4. Vives E, Brodin P, Lebleu B. A truncated HIV-1 Tat protein basic domain rapidly translocates through the plasma membrane and accumulates in the cell nucleus. *J Biol Chem* 1997 ; 272 : 16010-7.
5. Esteve E, Mabrouk K, Dupuis A, *et al*. Transduction of the scorpion toxin maurocalcine into cells. Evidence that the toxin crosses the plasma membrane. *J Biol Chem* 2005 ; 280 : 12833-9.
6. Fajloun Z, Kharrat R, Chen L, *et al*. Chemical synthesis and characterization of maurocalcine, a scorpion toxin that activates Ca^{2+} release channel/ryanodine receptors. *FEBS Lett* 2000 ; 469 : 179-85.
7. Altafaj X, Cheng W, Esteve E, *et al*. Maurocalcine and domain A of the II-III loop of the dihydropyridine receptor Cav 1.1 subunit share common binding sites on the skeletal ryanodine receptor. *J Biol Chem* 2005 ; 280 : 4013-6.
8. Esteve E, Smida-Rezgui S, Sarkozi S, *et al*. Critical amino acid residues determine the binding affinity and the Ca^{2+} release efficacy of maurocalcine in skeletal muscle cells. *J Biol Chem* 2003 ; 278 : 37822-31.
9. Ram N, Weiss N, Texier-Nogues I, *et al*. Design of a disulfide-less, pharmacologically inert, and chemically competent analog of maurocalcine for the efficient transport of impermeant compounds into cells. *J Biol Chem* 2008 ; 283 : 27048-56.
10. Konate K, Crombez L, Deshayes S, *et al*. Insight into the cellular uptake mechanism of a secondary amphipathic cell-penetrating peptide for siRNA delivery. *Biochemistry* 2010 ; 49 : 3393-402.
11. Crombez L, Charnet A, Morris MC, *et al*. A non-covalent peptide-based strategy for siRNA delivery. *Biochem Soc Trans* 2007 ; 35 : 44-6.
12. Morris MC, Depollier J, Mery J, *et al*. A peptide carrier for the delivery of biologically active proteins into mammalian cells. *Nat Biotechnol* 2001 ; 19 : 1173-6.
13. Pooga M, Hallbrink M, Zorko M, Langel U. Cell penetration by transportan. *FASEB J* 1998 ; 12 : 67-77.
14. Zhang C, Tang N, Liu X, *et al*. siRNA-containing liposomes modified with polyarginine effectively silence the targeted gene. *J Control Release* 2006 ; 112 : 229-39.
15. Radis-Baptista G, de la Torre BG, Andreu D. A novel cell-penetrating peptide sequence derived by structural minimization of a snake toxin exhibits preferential nucleolar localization. *J Med Chem* 2008 ; 51 : 7041-4.
16. Herbig ME, Weller K, Krauss U, *et al*. Membrane surface-associated helices promote lipid interactions and cellular uptake of human calcitonin-derived cell penetrating peptides. *Biophys J* 2005 ; 89 : 4056-66.
17. Yeaman MR, Yount NY. Mechanisms of antimicrobial peptide action and resistance. *Pharmacol Rev* 2003 ; 55 : 27-55.
18. Deshayes S, Plenat T, Charnet P, *et al*. Formation of transmembrane ionic channels of primary amphipathic cell-penetrating peptides. Consequences on the mechanism of cell penetration. *Biochim Biophys Acta* 2006 ; 1758 : 1846-51.
19. Henriques ST, Castanho MA. Consequences of nonlytic membrane perturbation to the translocation of the cell penetrating peptide pep-1 in lipidic vesicles. *Biochemistry* 2004 ; 43 : 9716-24.
20. Binder H, Lindblom G. Charge-dependent translocation of the Trojan peptide penetratin across lipid membranes. *Biophys J* 2003 ; 85 : 982-95.
21. Conner SD, Schmid SL. Regulated portals of entry into the cell. *Nature* 2003 ; 422 : 37-44.
22. Brasseur R, Divita G. Happy birthday cell penetrating peptides: already 20 years. *Biochim Biophys Acta* 2010 ; 1798 : 2177-8.
23. Khafagy el S, Morishita M, Kamei N, *et al*. Efficiency of cell-penetrating peptides on the nasal and intestinal absorption of therapeutic peptides and proteins. *Int J Pharm* 2009 ; 381 : 49-55.
24. Elbashir SM, Harborth J, Lendeckel W, *et al*. Duplexes of 21-nucleotide RNAs mediate RNA interference in cultured mammalian cells. *Nature* 2001 ; 411 : 494-8.
25. Simeoni F, Morris MC, Heitz F, Divita G. Peptide-based strategy for siRNA delivery into mammalian cells. *Methods Mol Biol* 2005 ; 309 : 251-60.
26. Lundberg P, El-Andaloussi S, Sutlu T, *et al*. Delivery of short interfering RNA using endosomolytic cell-penetrating peptides. *FASEB J* 2007 ; 21 : 2664-71.
27. Medarova Z, Pham W, Farrar C, *et al*. *In vivo* imaging of siRNA delivery and silencing in tumors. *Nat Med* 2007 ; 13 : 372-7.
28. Choi YS, Lee JY, Suh JS, *et al*. The systemic delivery of siRNAs by a cell penetrating peptide, low molecular weight protamine. *Biomaterials* 2011 (sous presse).
29. Muratovska A, Eccles MR. Conjugate for efficient delivery of short interfering RNA (siRNA) into mammalian cells. *FEBS Lett* 2004 ; 558 : 63-8.
30. Davidson TJ, Harel S, Arboleda VA, *et al*. Highly efficient small interfering RNA delivery to primary mammalian neurons induces MicroRNA-like effects before mRNA degradation. *J Neurosci* 2004 ; 24 : 10040-6.
31. Choi Y-S, Lee JY, Suh JS, *et al*. The systemic delivery of siRNAs by a cell penetrating peptide, low molecular weight protamine. *Biomaterials* 2010 ; 31 : 1429-43.
32. Crombez L, Morris MC, Dufort S, *et al*. Targeting cyclin B1 through peptide-based delivery of siRNA prevents tumour growth. *Nucleic Acids Res* 2009 ; 37 : 4559-69.
33. Josephson L, Tung CH, Moore A, Weissleder R. High-efficiency intracellular magnetic labeling with novel superparamagnetic-Tat peptide conjugates. *Bioconjug Chem* 1999 ; 10 : 186-91.
34. Jayagopal A, Su YR, Blakemore JL, *et al*. Quantum dot mediated imaging of atherosclerosis. *Nanotechnology* 2009 ; 20 : 165102.
35. Sawicka M, Kalinowska M, Skierski J, Lewandowski W. A review of selected anti-tumour therapeutic agents and reasons for multidrug resistance occurrence. *J Pharm Pharmacol* 2004 ; 56 : 1067-81.
36. Aroui S, Ram N, Appaix F, *et al*. Maurocalcine as a non toxic drug carrier overcomes doxorubicin resistance in the cancer cell line MDA-MB 231. *Pharm Res* 2009 ; 26 : 836-45.
37. Aroui S. Maurocalcine as a non toxic drug carrier overcomes doxorubicin resistance in the cancer cell line MDA-MB 231. *Pharm Res* 2009 ; 26 : 836-45.
38. Liang JF, Yang VC. Synthesis of doxorubicin-peptide conjugate with multidrug resistant tumor cell killing activity. *Bioorg Med Chem Lett* 2005 ; 15 : 5071-5.
39. Lindgren M, Rosenthal-Aizman K, Saar K, *et al*. Overcoming methotrexate resistance in breast cancer tumour cells by the use of a new cell-penetrating peptide. *Biochem Pharmacol* 2006 ; 71 : 416-25.
40. Niu R, Zhao P, Wang H, *et al*. Preparation, characterization, and antitumor activity of paclitaxel-loaded folic acid modified and TAT peptide conjugated PEGylated polymeric liposomes. *J Drug Target* 2011 (sous presse).
41. Olson ES, Jiang T, Aguilera TA, *et al*. Activatable cell penetrating peptides linked to nanoparticles as dual probes for *in vivo* fluorescence and MR imaging of proteases. *Proc Natl Acad Sci USA* ; 107 : 4311-6.
42. Kersemans V, Kersemans K, Cornelissen B. Cell penetrating peptides for *in vivo* molecular imaging applications. *Curr Pharm Des* 2008 ; 14 : 2415-47.
43. Nguyen QT, Olson ES, Aguilera TA, *et al*. Surgery with molecular fluorescence imaging using activatable cell-penetrating peptides decreases residual cancer and improves survival. *Proc Natl Acad Sci USA* ; 107 : 4317-22.

RÉFÉRENCES

44. Su W, Mishra R, Pfeuffer J, *et al*. Synthesis and cellular uptake of a MR contrast agent coupled to an antisense peptide nucleic acid: cell-penetrating peptide conjugate. *Contrast Media Mol Imaging* 2007 ; 2 : 42-9.

45. Heitz F, Morris MC, Divita G. Twenty years of cell-penetrating peptides: from molecular mechanisms to therapeutics. *Br J Pharmacol* 2009 ; 157 : 195-206.

46. Johnson JL, Lowell BC, Ryabinina OP, *et al*. TAT-mediated delivery of a DNA repair enzyme to skin cells rapidly initiates repair of UV-induced DNA damage. *J Invest Dermatol* 2011 ; 131 : 753-61.

47. Perea SE, Reyes O, Puchades Y, *et al*. Antitumor effect of a novel proapoptotic peptide that impairs the phosphorylation by the protein kinase 2 (casein kinase 2). *Cancer Res* 2004 ; 64 : 7127-9.

48. Khafagy el S, Morishita M, Takayama K. The role of intermolecular interactions with penetratin and its analogue on the enhancement of absorption of nasal therapeutic peptides. *Int J Pharm* 2010 ; 388 : 209-12.

49. Pooga M, Kut C, Kihlmark M, *et al*. Cellular translocation of proteins by transportan. *FASEB J* 2001 ; 15 : 1451-3.

50. Chaubey B, Tripathi S, Ganguly S, *et al*. A PNA-transportan conjugate targeted to the TAR region of the HIV-1 genome exhibits both antiviral and virucidal properties. *Virology* 2005 ; 331 : 418-28.

51. Kim DW, Jeong HJ, Kang HW, *et al*. Transduced human PEP-1-catalase fusion protein attenuates ischemic neuronal damage. *Free Radic Biol Med* 2009 ; 47 : 941-52.

52. Morris MC, Vidal P, Chaloin L, *et al*. A new peptide vector for efficient delivery of oligonucleotides into mammalian cells. *Nucleic Acids Res* 1997 ; 25 : 2730-6.

53. Crombez L, Aldrian-Herrada G, Konate K, *et al*. A new potent secondary amphipathic cell-penetrating peptide for siRNA delivery into mammalian cells. *Mol Ther* 2009 ; 17 : 95-103.

54. Hallbrink M, Floren A, Elmquist A, *et al*. Cargo delivery kinetics of cell-penetrating peptides. *Biochim Biophys Acta* 2001 ; 1515 : 101-9.

55. Harel-Bellan A. Prix Nobel de médecine 2006. Andrew Z. Fire et Craig C. Mello : silence, on désactive les gènes. *Med Sci (Paris)* 2006 ; 22 : 993-4.

56. Horcajada P, Serre C, Férey G, *et al*. Des nanovecteurs hybrides pour la restitution retard de médicaments antitumoraux et antiviraux. *Med Sci (Paris)* 2010 ; 26 : 761-7.

57. Nicolas MR, Moreau M. Prix Nobel de chimie 2008 (osumo Shimomura, Martin Chalfie et Roger Y. Tsien). Med Sci (Paris) 2008 ; 24 : 983-4.

TIRÉS À PART

C. Poillot

Toxines et Signalisation – Toxins and Signalling
Rencontres en Toxinologie – Meeting on Toxinology, 2009
Editions de la SFET – SFET Editions
Accès libre en ligne sur le site – Free access on line on the site : http://www.sfet.asso.fr

Use of maurocalcine analogues as biotechnological tools for the penetration of cell-impermeable compounds

Cathy POILLOT[1,2], Michel DE WAARD[1,2*]

[1] *Inserm U836, Grenoble Neuroscience Institute, Site Santé Tronche, Chemin Fortuné Ferrini, BP 170, 38042 Grenoble cedex 09 ;* [2] *Université Joseph Fourier, Grenoble, France*

** Corresponding author ; Tel : +33 (0) 456520563 ; Fax : +33 (0) 456520637 ;*
E-mail : michel.dewaard@ujf-grenoble.fr

Abstract

Maurocalcine is unique in the sense that its natural molecular target, the ryanodine receptor, is localized inside cells. While studying how this toxin could reach its target, it was found that it represents a new member of a family of cell penetrating peptides. Indeed, maurocalcine is a highly basic peptide and most of the positively charged amino-acids are located on one face of the molecule according to a distribution that resembles that seen in Tat and penetratin. Since the initial discovery that maurocalcine can serve as a vector for the intracellular delivery of fluorescent streptavidin, accumulating data highlight the incredible biotechnological value of this toxin. Several new analogues have been designed that segregate the pharmacological and cell penetrating properties of the peptide. Maurocalcine was shown to be efficient for the cell delivery of nanoparticles opening a wealth of possible high tech applications. Also, maurocalcine has been covalently coupled to doxorubicine, an anti-tumour agent, to reverse chemo-resistance of cancer cells. It appears that this toxin is only at the start of his career as biotechnological tool, but also that it may still prove useful for deciphering fine mechanistic details of the functioning of the ryanodine receptor.

Utilisation d'analogues de la maurocalcine comme outils biotechnologiques de la pénétration cellulaire de composés non perméables

La maurocalcine est une toxine unique en ce sens que sa cible moléculaire naturelle, le récepteur à la ryanodine, est localisée à l'intérieur des cellules. En étudiant comment cette toxine pouvait atteindre sa cible, nous avons montré qu'elle représente un nouveau membre d'une famille de peptides de pénétration cellulaire. En effet, la maurocalcine est un peptide hautement basique et la plupart des acides aminés chargés positivement sont localisés sur une face de la molécule en accord avec la distribution observée sur des molécules telles que Tat et pénétratine. Depuis la découverte que la maurocalcine peut servir de vecteur à la délivrance intracellulaire de streptavidine fluorescente, les données se sont accumulées pour illustrer l'incroyable valeur biotechnologique de cette toxine. Plusieurs nouveaux analogues ont été produits qui séparent les propriétés pharmacologiques et de pénétration cellulaire du peptide. La maurocalcine s'est avérée efficace pour la délivrance cellulaire de nanoparticules ouvrant ainsi une myriade d'applications high tech. Enfin, la maurocalcine a été couplée à la doxorubicine, un agent anti-tumoral, pour rendre chimio-sensibles des cellules cancéreuses devenues chimio-résistantes. Il semble donc que la maurocalcine débute sa carrière comme outil biotechnologique, mais aussi que cette toxine s'avèrera utile pour déchiffrer finement les détails mécanistiques du fonctionnement du récepteur à la ryanodine.

Keywords : *Acetylcholine, pathogenicity, embryotoxicity, pain,* Cerastes cerastes.

Introduction

Maurocalcine initially triggered the interest of our research group based on the finding that it has strong sequence homology with imperatoxin A, an activator of the ryanodine receptor (el-Hayek *et al.*, 1995). The first characterization of maurocalcine dates back to 2000, date at which it was first chemically synthesized by peptide chemistry by the group of Dr. Jean-Marc Sabatier in Marseille, France. The toxin however originates from the group led by Pr. Mohamed El Ayeb at the Institut Pasteur of Tunis (Tunisia) where it was purified from the venom of the scorpion *Scorpio maurus palmatus*. Maurocalcine is a 33-mer basic peptide cross-linked by three disulfide bridges with the following pairing: Cys^{3}-Cys^{17}, Cys^{10}-Cys^{21}, and Cys^{16}-Cys^{32}. The solution structure of the peptide was determined by ^{1}H-NMR (Mosbah *et al.*, 2000). Its three dimensional structure consists of a double-stranded antiparallel beta-sheet comprising residues 20-23 and 30-33, and a third

extended strand from residues 9 to 11 that is perpendicular to the beta-sheet. Interestingly, this was the first description of a scorpion toxin folding according to an Inhibitor Cystine Knot fold (ICK), a motif previously described for various protease inhibitors. *In vivo*, maurocalcine was lethal to mice only upon intracerebroventricular inoculation (LD_{50} of 20 µg/mouse).

Maurocalcine is a member of a growing family of toxins

Maurocalcine is the second discovered member of an increasing family of new calcin toxins active on ryanodine receptors. The first member of this family, imperatoxin A, was isolated in 1995 from the venom of scorpion *Pandinus imperator* (el-Hayek *et al.*, 1995). Since that time, five more analogous peptides were subsequently discovered, first maurocalcine in 2000 from the scorpion *Scorpio maurus palmatus* (Mosbah *et al.*, 2000), followed by both opicalcine 1 and 2 from the scorpion *Opistophthalmus carinatus* in 2003 (Zhu *et al.*, 2003), hemicalcin from the scorpion *Hemiscorpius* lepturus in 2007 (Shahbazzadeh *et al.*, 2007), and finally hadrucalcin in 2009 from the scorpion *Hadrurus gertschi* (Schwartz *et al.*, 2009). The homology between these peptides ranges from 76 to 91%. All these peptides share common features that include a length of 33 to 35 amino acids, three disulfide bridges paired according to the motif Cys^1-Cys^4, Cys^2-Cys^5 and Cys^3-Cys^6 (see *Figure 1*). Hadrucalcin is a quite interesting new member in the sense that it is significantly divergent from the five other members. With this member, the number of variable amino acids rises from 7 to 12 and demonstration is made that the toxin can accommodate 13 positively charged amino acids instead of 12 and that the sequence can be extended at its N-terminus (the sequence length goes from a constant value of 33 for all other members to 35 with this analogue). This finding suggests that the calcin family will probably be soon incremented with new members from other scorpion sources. Also, it provides interesting new clues on how to design novel calcin toxins that would conserve activity on RyR and penetrate into cells.

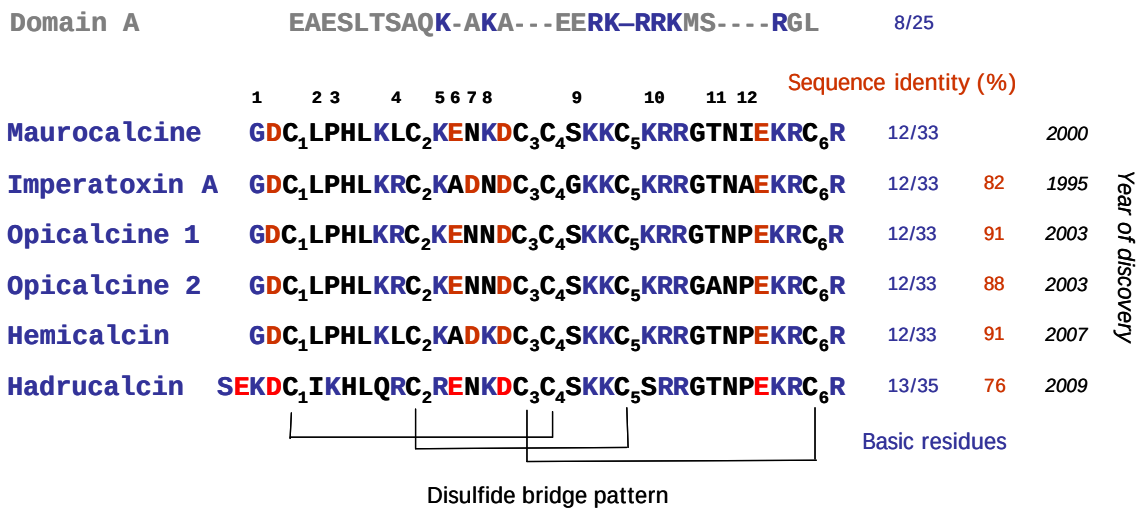

Fig. 1. Maurocalcine-like scorpion toxins. Sequence alignment of maurocalcine with five analogous toxins, imperatoxin A, opicalcine 1, opicalcine 2, hemicalcin and hadrucalcin. Maurocalcine, imperatoxin A, hemicalcin and hadrucalcin have all shown to be active on the ryanodine receptor. Opicalcine 1 and 2 have not been tested for pharmacological activity. Toxins have between 12 and 13 positively charged amino acid residues (the N-terminal residue, six or seven lysine residues, and four to six arginine residues as indicated in blue). Negatively charged amino acids are represented in red as well as sequence identities with maurocalcine. Highlighted residues (twelve possible positions) indicate variable amino acids among toxins. The year of discovery of each toxin is also provided in italics. Sequence alignment with domain A of the L-type calcium channel is also illustrated.

Fig. 1. *Toxines de scorpion du type maurocalcine. Alignement de séquence de la maurocalcine avec 5 toxines analogues, l'imperatoxine A, l'opicalcine 1, l'opicalcine 2, l'hemicalcine et l'hadrucalcine. Maurocalcine, imperatoxine A, hemicalcine et hadrucalcine sont tous connus pour être actif sur le récepteur à la ryanodine. Les opicalcines 1 et 2 n'ont pas été testé pour leurs activités pharmacologiques. Les toxines possèdent entre 12 et 13 acides aminés chargés positivement (le résidu N-terminal, 6 ou 7 résidus lysine, 4 à 6 résidus arginine, indiqués en bleu). Les acides aminés chargés négativement sont en rouge ainsi que les identités de séquence avec la maurocalcine. Les résidus surlignés (12 positions possibles) indiquent les acides aminés variables entre toxines. L'année de découverte de chaque toxine est aussi indiquée en italique. L'alignement de séquence avec le domaine A du canal calcique de type L est aussi montré.*

Calcin toxins are active on the ryanodine receptor

Ryanodine receptors are calcium channels that allow calcium cations to exit the lumen of endoplasmic reticulum. They contribute therefore to calcium signalling events in the cell cytoplasm. These channels are present therefore within the membrane of the endoplasmic reticulum and are constituted of an ion pore and a large cytoplasmic bulk. None of the sequence of the channel is integrated in the plasma membrane or present at the extracellular surface. For this reason, the ryanodine receptor is an unusual target for a toxin. Three genes encode for ryanodine receptor type I, II and III. The type I ryanodine receptor is mainly expressed in skeletal muscles, the type II is mostly cardiac and cerebral, whereas the type III is predominantly neuronal. Most calcin toxins have been tested on type I ryanodine receptor, essentially because this type is easier to

purify from the skeletal muscle, a rich source of that type of channel. Calcin toxins induce similar effects on the ryanodine receptor that can be summarized as follows. (i) Application of a calcin toxin to purified sarcoplasmic reticulum induces Ca^{2+} release, suggesting that one effect of the toxin is channel activation. (ii) Calcin toxins converts low affinity [^{3}H]-ryanodine binding sites to high affinity ones (el-Hayek *et al.*, 1995 ; Esteve *et al.*, 2003). High affinity [^{3}H]-ryanodine binding has been interpreted to a change of channel conformation compatible with the open state conformation of the channel. Using this assay, it was estimated that calcin toxins should bind to ryanodine receptors with an affinity in the 10 to 50 nM range (Zamudio *et al.*, 1997 ; Esteve *et al.*, 2003 ; Schwartz *et al.*, 2009). (iii) Calcin toxins have complex effects on channel activity recorded from ryanodine receptors incorporated into lipid bilayers. The first effect observed is generally an increase in open-state probability, followed by the appearance of a long-lasting subconductance state, which is rarely reversible. Higher concentration of toxins induce complete channel block meaning that calcin toxins are considered as activators at low concentrations and blockers at high concentrations. This complex set of effects is probably due to the fact that ryanodine receptor are organized as homo-tetramers, implying that toxins can occupy one to at least four potential sites on the channel. Multi-site occupancy likely triggers different channel behaviours (Chen *et al.*, 2003). The interaction of calcin toxin with the ryanodine receptor is direct since a biotinylated derivative of maurocalcine bound to streptavidin-coated beads pulls down purified skeletal muscle RyR (Altafaj *et al.*, 2005). Also, it was shown that maurocalcine directly binds onto a cytoplasmic domain of the ryanodine receptor. This domain is of functional importance for increased [^{3}H]-ryanodine binding in the presence of maurocalcine. The cytoplasmic nature of the calcin toxin binding site on the ryanodine receptor is confirmed by the observation that maurocalcine alters the activity of channels reconstituted into lipid bilayers only when applied to the cytoplasmic face of the channel (Fajloun *et al.*, 2000). Altogether, these data demonstrate that calcin toxins are pharmacological modulators of the ryanodine receptors by directly binding onto a site located in the cytoplasm.

Existence of a curious sequence homology between calcin toxins and a voltage-dependent calcium channel domain

One amazing property of calcin toxins is their limited sequence homology with a voltage-dependent calcium channels. Skeletal muscle L-type channel come as a complex of four subunits: the pore-forming and voltage-sensing subunit $Ca_v1.1$, associated to three auxiliary subunits β, $\alpha_2\delta$ and γ. This channel type is peculiar in the sense that it transmits changes in membrane potential directly to the ryanodine receptor. This process termed excitation-contraction coupling ensures that action potentials trigger enough calcium elevation in the cytoplasm to produce muscle contraction. Since most of the calcium originates from the sarcoplasmic reticulum through opening of the ryanodine receptor, the voltage-dependent calcium channel transmits the necessary information to the ryanodine receptor directly by changes in conformation. This entire chain of events is still poorly understood at the mechanistic level, but several channel determinants have been identified that serve as lead in the understanding of the process. One such determinant is called domain A, a small 20 amino acid sequence of $Ca_v1.1$ that is located in the cytoplasmic II-III loop of the channel. Sequence homology of domain A with calcin toxins is restricted to a basic patch of amino acids, but it was found that both domain A and calcin toxins share structural homology (Green *et al.*, 2003), they similarly induce an increase in [^{3}H]-ryanodine binding, activate channel activity (Gurrola *et al.*, 1999), and finally they bind onto identical sites (Lee *et al.*, 2004 ; Altafaj *et al.*, 2005). The finding that calcin toxins bind to the ryanodine receptor with higher affinity than domain A (20 nM versus 1 µM) indicates that these toxins may be used as interesting molecular tools to dissect the functional role of domain A in excitation-contraction coupling. This goal has been partially reached by the demonstration that maurocalcine induces a default in the closure of the ryanodine-sensitive calcium channel following activation by membrane depolarisation (Szappanos *et al.*, 2005). These data seem to imply that maurocalcine is able to substitute to domain A while the ryanodine receptor is activated by membrane depolarization. During repolarisation, ryanodine receptor closure is slowed presumably because of the greater affinity of maurocalcine for the binding site it shares in common with domain A. Obviously, calcin toxins still have to reveal many intimate mechanistic details on the process of excitation-contraction coupling.

Firsts evidences that maurocalcine penetrates into cells

The location of the pharmacological target of calcin toxins (intracellular) and the position of maurocalcine binding site on the ryanodine receptor with regard to the channel topology (cytoplasm) are strong evidences that calcin toxins need to cross the plasma membrane before reaching their target. For a long period, criticisms had been formulated with regard to the pharmacological target of imperatoxin A, the first discovered calcin toxin. It was estimated that peptides could not cross the plasma membrane, and therefore doubts were expressed about the pharmacological reality of the ryanodine receptor as target for calcin toxins. To sort this question out, two sorts of experiments were performed. On one hand, it was observed that extracellular application of 100 nM maurocalcine to myotubes produces a rapid rise (within a few seconds) of intracellular calcium (Esteve *et al.*, 2003). Similarly, it was shown that hadrucalcin elicits discharges of internal calcium stores within seconds in ventricular myocytes (Schwartz *et al.*, 2009). On the other hand, we evidenced that a biotinylated derivative of maurocalcine had the ability to trigger cell entry of fluorescent streptavidine (Esteve *et al.*, 2005). The cell entry of this vector / cargo couple was unique in the history of toxinology, and the first demonstration that (i) maurocalcine enters into cells, and (ii) can be used for the cell entry of cargoes that would otherwise not enter the cell. These data illustrate the succession of molecular events undergone by calcin toxins until calcium release from the lumen of the endoplasmic reticulum: (i) very rapid plasma membrane crossing, (ii) elevation of the cytoplasm concentration of the toxin to a level close or above 10 nM to reach the K_D value for RyR, (iii) binding onto the RyR site, (iv) opening of RyR channels, and (v) calcium release from internal stores.

Separating the pharmacological properties from the cell penetration properties

The discovery that maurocalcine may serve as a vector for the cell penetration of various cargoes turns out of great interest. Contrary to many cell penetrating peptides whose sequences have been derived from larger proteins, maurocalcine is a functional entity on its own. More importantly, a functional readout of the effects of maurocalcine can easily be measured (calcium release or alteration in excitation-contraction coupling). Since these effects all require the presence of the toxin in the cytoplasm, these functional readouts ensure that cell entry of maurocalcine coincides with cytoplasmic localization. This issue is essential since the fate of cell penetrating peptides is diverse. Two modes of cell entry exist: direct translocation through the plasma membrane through a mechanism(s) still unexplained, but that results in accumulation in the cytoplasm, or endocytosis, generally macropinocytosis, with significant accumulation in endosomes and little escapes from there into the cytoplasm. In that sense, maurocalcine presents an incredible advantage over other cell penetrating peptides in that complicated cell assays don't need to be developed alongside with chemical modification of the cell penetrating peptide.

This being stated, it is also obvious that the cell penetrating peptide virtue of maurocalcine is an advantage provided that pharmacological effects of the peptide are not obscuring the beneficial technological effects. This implies that structural analogues of maurocalcine ought to be designed that conserve cell penetration properties but are significantly impaired with regard to the pharmacological activation of the ryanodine receptor. This aim has been reached by different methods. A first approach consisted by site directed mutagenesis of maurocalcine (Mabrouk *et al.*, 2007). This approached taught us that it was possible to drastically reduce the pharmacological activity of maurocalcine while largely preserving the cell penetration of fluorescent streptavidin. For instance ; the R24A-maurocalcine mutant totally lost its effect on the ryanodine receptor (both stimulation of [^{3}H]-ryanodine binding and activation of channel activity (Lukacs *et al.*, 2008)), while keeping more than half the cell penetration properties of the peptide. The advantage of this approach was that it precisely maps the amino acid residues involved in the pharmacological action or in the cell penetrating one. Conclusions were that pharmacology has more stringent structural requirements than cell penetration. This was good news because it suggested that alternative strategies could be envisioned. Finally, this approach also yielded a novel analogue E12A-maurocalcine that possesses better cell penetration properties than the wild-type sequence. A second approach was based on two observations: i) other cell penetrating peptides are disulfide-less, and ii) disulfide bridges contribute to the fold of toxins and thus presumably to pharmacological activity. We therefore assumed that removing the disulfide bridges of maurocalcine would alter its 3D structure and consequently its functional effects, but possibly without inhibiting cell penetration. This is indeed what we observed by synthesizing an analogue in which all internal cysteine residues were substituted by Abu derivatives. The peptide was unfolded as assessed by circular dichroism and lost the ability to regulate ryanodine receptor activity (Ram *et al.*, 2008b). The added advantage of this approach was the possibility to add a cysteine residue at the N-terminus of the sequence to chemically couple cargoes through thiol chemistry. Unfolded MCa was slightly less efficient for cell penetration than its folded counterpart suggesting that folding is an advantage in maurocalcine over other cell penetrating peptides such as Tat or penetratin. Nevertheless, in a comparative study, we found that this unfolded analogue is as potent as other cell penetrating peptides demonstrating that it represents a good vector for biotechnical applications (unpublished observations). From there, we start to investigate shorter maurocalcine sequences to determine the minimal structural requirement for cell penetration. Preliminary results indicate that the basic region of maurocalcine is responsible for its cell penetration, in agreement with the data obtained by single amino acid substitution (Ram *et al.*, 2008b). The third approach that is currently in development in our laboratory is the production of a D-maurocalcine, synthesized with D-amino acids instead of L-amino acids. The synthesis is a challenge because this new analogue should fold according to the motif observed in L-maurocalcine. Our preliminary results indicate that we are successful in the production of this analogue that is a mirror structure of L-maurocalcine. Peptides produced this way lose target recognition and binding, and preserve cell penetration, again because the structural requirements for pharmacology and cell penetration are significantly different. D-maurocalcine is indeed unable to activate the ryanodine receptor, yet still penetrates into cells.

How does maurocalcine enter cells ?

There is no trivial answer to that question. Let's simply emphasize that the mechanism of cell entry of cell penetrating peptides is crucial for the application that is programmed. By definition, a "real" cell penetrating peptide is one that accumulates in the cytoplasm and not into endosomes! Yet, most manuscripts dealing about cell penetrating peptides relate to peptide accumulation into endosomes. To be honest, the fate of the peptide into cells does not simply rely on the nature of the cell penetrating peptide itself, but also frequently to the nature of the cargo being transported or the type of cell under consideration. It is interesting to observe that maurocalcine can adopt both types of cell entry: translocation for cytoplasmic accumulation or endocytosis for endosome localization. When streptavidine is the cargo, we observed mainly punctuate distribution coinciding with endosomes (Boisseau *et al.*, 2006). Now, we also observed a predominant cytoplasmic localization with other cargoes such as fluorescent peptides, doxorubicine or quantum dots (Ram et al., 2008b ; Aroui et al., 2009). It is difficult to decide in advance what type of cell distribution to expect with a given cargo and no general rule seem to emerge. It is possible that cargo size may be a factor as membrane translocation may accommodate only small cargoes. But it would be reductionist to limit this differential distribution to this sole factor. One way to better understand by which mechanism maurocalcine enters into cells is to determine the nature of the molecular partner that takes maurocalcine in charge at the surface of the cell and to analyze how it may contribute to the cell penetration. We found two types of interacting molecules: glycoaminoglycans (Ram *et al.*, 2008a) and several negatively charged lipids (Boisseau *et al.*, 2006). Maurocalcine interacts with

heparin, heparin sulphate, and chondroitin sulphate. Incubating maurocalcine with soluble GAGs can inhibit up to 80 % of the cell uptake of maurocalcine for two reasons: (i) soluble GAGs screen the positive charges of maurocalcine required for cell entry, and (ii) they compete for the interaction of maurocalcine with cell surface bounds GAGs. Interactions with GAGs are however not totally required for cell entry of maurocalcine since penetration is partially preserved in GAG-deficient CHO cells. In these same cells, the mode of penetration is not modified suggesting that membrane receptors of maurocalcine are not associated with a particular type of cell penetration. We assume that GAGs contribute to cell penetration of maurocalcine at the quantitative level by favoring local accumulation of the peptide at the cell membrane. It is possible that it acts as a reservoir of peptide for delivery to membrane lipids. In that sense, it is interesting that the affinity of maurocalcine for GAGs (1-2 µM) is lower than for lipids. For instance, maurocalcine interacts with GD3 (disialoganglioside NeuAca2-8NeuAca2-3Galß1-4Glcß1-Cer) at an affinity in the 100 nM range (Boisseau *et al.*, 2006). This is an affinity that is more in agreement with the concentration-dependence of cell penetration of maurocalcine, suggesting that lipids may well represent the final/true penetrating partners of maurocalcine. It makes sense for the translocation process through the plasma membrane. However, considerably more work is required at the biophysical level to determine how the complex of maurocalcine / lipids evolves during the translocation process. Also, because of the multiplicity of intervening partners, it would be highly desirable to identify what lipid, if there a specific one, is responsible for the cell entry of maurocalcine. Knowledge of this information would be of tremendous help in the design of more efficient analogues of maurocalcine for cell penetration.

Examples of biotechnological applications

Doxorubicine-maurocalcine : a chimera molecule to treat chemo resistance of tumor cells

Although it is of conceptual interest to develop novel analogues of cell penetrating peptides and to understand their mode of cell entry, the main interest of these peptides resides in the applications that can be envisioned. We therefore sought to develop a novel therapeutic application using our pharmacologically inert, but still efficient cell penetrating Abu-derivative maurocalcine analogue. Doxorubicine is an anti-tumor agent but that also induces chemo-resistance in cancer cells. One mechanism of chemo-resistance is the over-expression of multidrug resistance protein in cells that expels efficiently doxorubicine that is normally capable to enter freely into cells. We therefore investigated whether coupling doxorubicine to maurocalcine could oppose cell resistance presumably by inhibiting this expulsion process. To that purpose, we used two cancer cell lines, MCF7 and MDA-MB-231, described as having a different sensitivity/resistance for doxorubicine and tested doxorubicine itself and various cell penetrating peptides coupled to doxorubicine, such as Tat and penetratin besides the Abu-derivative maurocalcine analogue. All peptides were synthesized with a cysteine residue at the N-terminus to couple them to doxorubicine via SMCC (succinimidyl-4-(*N*-maléimidomethyl)cyclohexane-1-carboxylate, according to the method of Liang and Yang (Liang and Yang, 2005). Two parameters were investigated at short and long-term in culture: cell penetration and cell survival (Aroui *et al.*, 2009). Because doxorubicine has intrinsic fluorescent properties, the subcellular localization of the complexes could be followed by confocal microscopy and FACS analyses allowed the quantification of the entry of the complexes. We demonstrated that doxorubicine, coupled to cell penetrating peptides, is mainly localized in the cytoplasm of the cells, while it is predominantly concentrated in the nucleus when it is uncoupled. FACS analyses demonstrate that evident cell penetration of doxorubicine is detected at 0.5 µM and saturates at 10 µM for both the free form and cell penetrating coupled forms. We observed a clear accumulation of doxorubicine in MDA-MB-231 cells only when it is coupled to cell penetrating peptides, suggesting that the coupling process blocks doxorubicine expulsion in this chemo-resistant cell line. Accordingly, we observed that the conjugation of doxorubicine to cell penetrating peptides greatly enhances MDA-MB-231 cell death, even at very low concentrations, while it reduces cell death of MCF7 cells (see *Figure 2*). The reduced doxorubicine distribution in the nucleus is correlated with reduced toxicity in MCF7 cells, while the enhanced cell accumulation of the drug in MDA-MB-231 cells is associated with enhanced cell death. It has been shown that the toxic action of doxorubicine depends of its DNA intercalating properties and of the modifications in activity and expression levels of its target topoisomerase II. The toxicity induced by cell penetrating peptide coupled doxorubicine, while the drug is mostly present in the cytoplasm, appears to occur through different mechanisms, namely the induction of apoptosis. What our data have shown is that the Abu-derivative maurocalcine analogue is at least as efficient as other cell penetrating peptides for the cell penetration and retention of doxorubicine. The drug remains highly toxic in spite of chemical conjugation to cell penetrating peptides and of altered subcellular distribution. This approach suggests that cell penetrating peptides may constitute a significant progress when it comes to re-sensitize cancer cells to doxorubicine. We hope to complement these analyses by *in vivo* studies demonstrating the usefulness of maurocalcine for cancer therapy.

Coupling maurocalcine to nanoparticles : new diagnostic and therapeutic applications in perspective

Semiconductor quantum dots are new classes of fluorescent probes with a large surface to volume ratio. This property can be exploited to graft new functional entities at their surface, such as peptides, proteins, nucleic acids, antibodies and drugs. They possess excellent photo stability, far exceeding that of conventional organic fluorophores, and high emission quantum yield, which leads to increased fluorescence detection sensitivity. Quantum dots consist of a core of semi-conducting material, typically cadmium-telluride (CdTe) or cadmium-selenium (CdSe) for emission in the visible to the near infrared domain, for which tissue auto-fluorescence and absorption are reduced.

This core is generally covered by a shell composed of zinc sulfide (ZnS), in order to improve the chemical stability and emission quantum yield of the quantum dot (Lim *et al.*, 2003 ; Michalet *et al.*, 2005). These

nanocrystals are surface-modified for their stabilization in aqueous media and biological functionalization. In particular, coating of nanoparticles by a polyethylene glycol polymer (PEGylation) improves colloidal stability (Lee *et al.*, 2008) and blood circulation time (Ballou *et al.*, 2004).

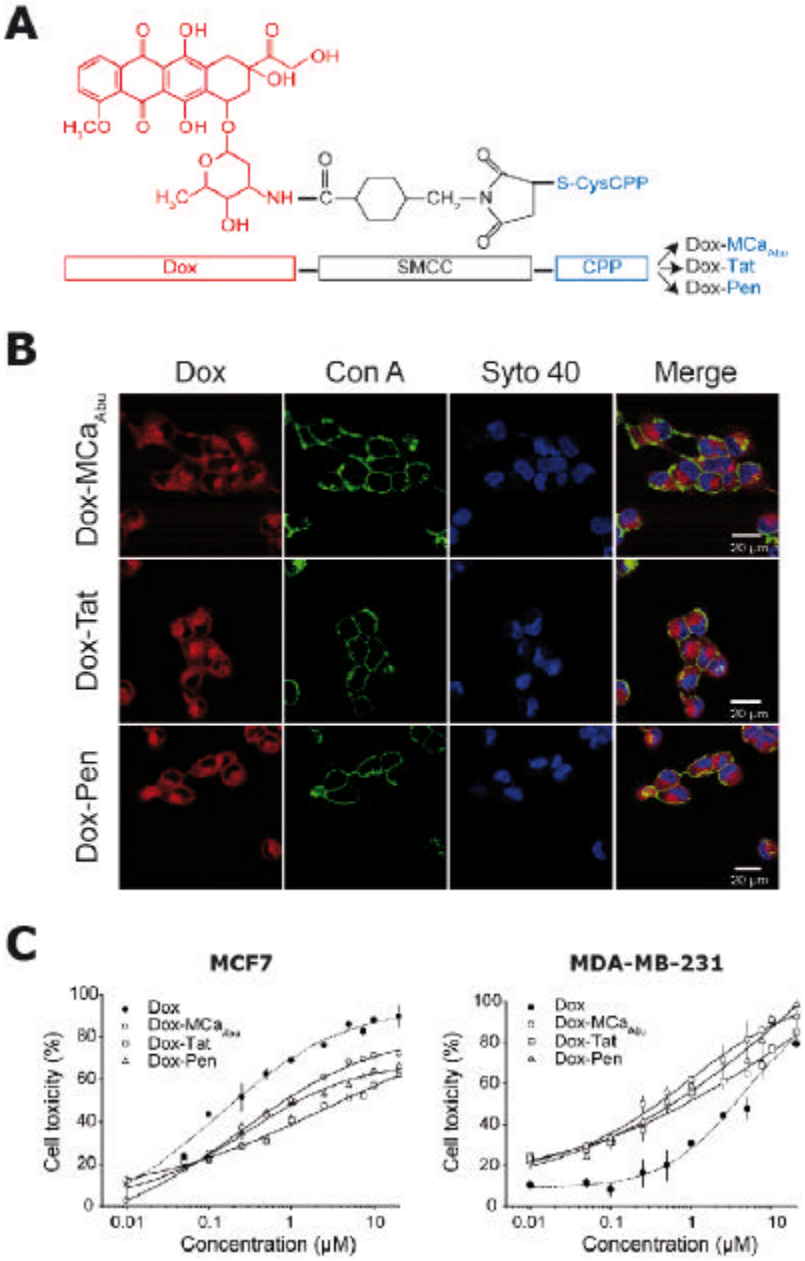

Fig. 2. (**A**) Structure of doxorubicine-cell penetrating peptide (CPP) complexes. (**B**) Cell distribution of doxorubicine conjugates in MDA-MB-231 cells showing the predominant presence in the cytoplasm. (**C**) Cell death induction by 24 hrs exposure to doxorubicine or doxorubicine-conjugates in MCF7 or MDA-MB-231 cells.

Fig. 2. *(**A**) Structures des complexes doxorubicine / peptide de pénétration cellulaire. (**B**) Distribution cellulaire des conjugués de doxorubicine dans les cellules MDA-MB-231 démontrant leurs présences prédominantes dans le cytoplasme. (**C**) Induction de la mort cellulaire après une exposition de 24 heures à la doxorubicine ou les conjugués de doxorubicine dans les cellules MCF7 ou MDA-MB-231.*

The emission spectra of quantum dots is size-tunable which enables their simultaneous excitation and tracking with the same excitation source (Biju *et al.*, 2008). Their properties are so useful that they have been used in several biological applications. In particular, quantum dots have proven useful for immunostaining of membrane proteins (Sukhanova *et al.*, 2004) and staining of organelles like mitochondria or nuclei (Hoshino *et al.*, 2004) in fixed cells, and for tracking single molecules in living cells by videomicroscopy (Dahan *et al.*, 2003 ; Lidke *et al.*, 2004 ; Mansson *et al.*, 2004). *In vivo* imaging applications have also been reported (Akerman *et al.*, 2002 ; Dubertret *et al.*, 2002 ; Gao *et al.*, 2004 ; Michalet *et al.*, 2005 ; Choi *et al.*, 2007).

Peptides have been used to improve quantum dot solubility in aqueous solution and for targeting cell surface proteins of interest *(Pinaud et al.*, 2004). Nevertheless, the use of quantum dots for intracellular applications *in vitro* or *in vivo* has been hampered by their inability to cross the plasma membrane. Several experimental strategies have been developed to physically deliver quantum dots, including direct microinjection, but this limits the number of cells that can be studied, or electroporation (Chen, 2004 ; Derfus, 2004 ; Voura *et al.*, 2004). Cell delivery of quantum dots using lipofectamine results in the formation of aggregates (Voura *et al.*, 2004). None of these delivery systems seem promising for *in vivo* applications because of their limited cell penetration efficiencies. Recently, the cell penetrating peptides, polyarginine (Silver and Ou, 2005) or TAT (Santra *et al.*, 2005), have been used for the delivery of quantum dots into living cells *in vitro* or across the blood brain barrier *in vivo*. This delivery approach appears very promising because many applications rely on the efficient cell delivery of cargoes such as peptides, proteins, siRNA, peptide nucleic acids, cDNA or drugs (Wadia and Dowdy, 2002).

Using biotinylated maurocalcine, we were the first group to report that streptavidine-coated quantum dots can be physically delivered within cells (see *Figure 3*).

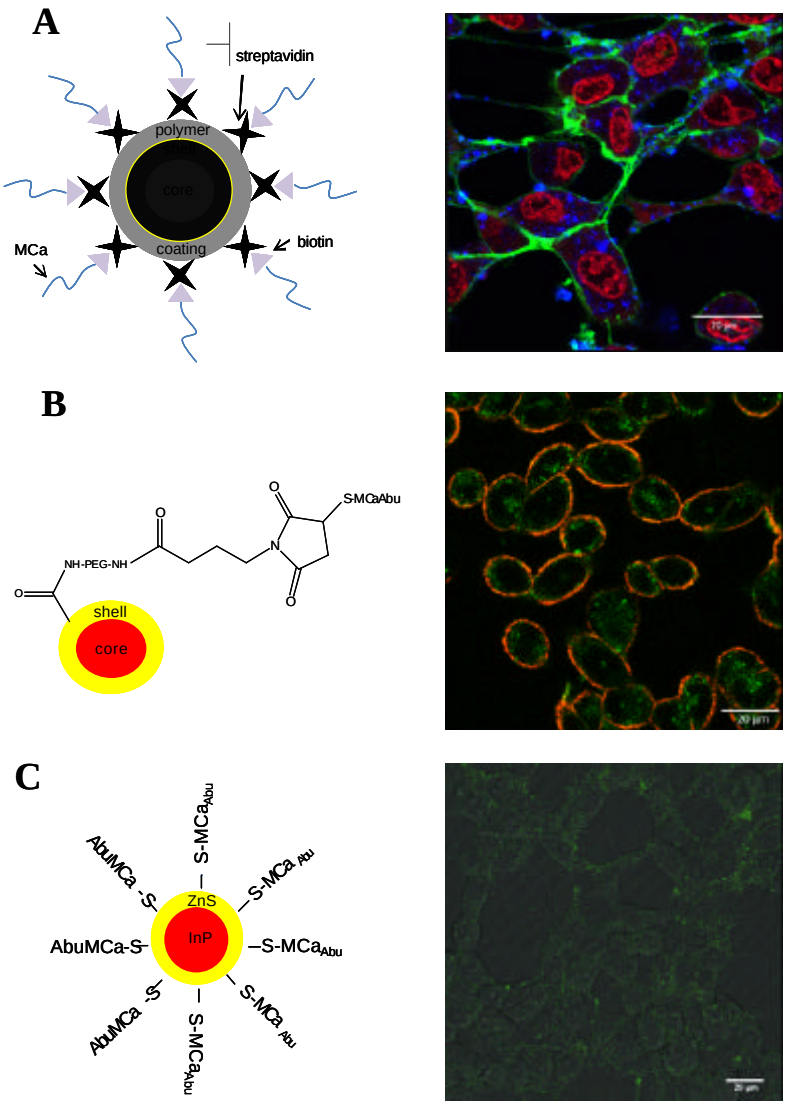

Fig. 3. Maurocalcine is an efficient vector for the entry of nanoparticles into CHO cells. (**A**) Cell delivery of streptavidine-coated CdSe/ZnS quantum dots by biotinylated folded maurocalcine. Punctate distribution is indicative of endosomal localization. (**B**) Cell delivery of CdSe/ZnS quantum dots directly coupled to Abu-derivative unfolded maurocalcine. Localization is predominantly cytoplasmic. (**C**) Cell delivery of InP/ZnS nanoparticles directly coupled to Abu-derivative unfolded maurocalcine.

Fig. 3. *Maurocalcine est un vecteur efficace pour la pénétration cellulaire de nanoparticules dans les cellules CHO. (**A**) Délivrance cellulaire de quantum dots CdSe/ZnS recouverts de streptavidine par une maurocalcine foldée biotinylée. La distribution ponctiforme est indicative d'une localisation endosomale. (**B**) Délivrance cellulaire de quantum dots CdSe/ZnS directement couplé à un analogue non foldé de la maurocalcine. La localisation est essentiellement cytoplasmique. (**C**) Délivrance cellulaire de nanoparticules InP/ZnS directement couplé à un analogue non foldé de la maurocalcine.*

One peculiar property of these quantum dots is that the maurocalcine / streptavidine linkage automatically is always associated with endosomal localization. Using a different chemical linkage, that makes abstraction of streptavidin, and using the Abu-derivative maurocalcine as cell penetrating peptide, we found a very different subcellular distribution of the quantum dots. Most of the nanoparticles were found in the cytoplasm suggesting that membrane translocation of peptide / quantum dots complexes is possible. More recently, through a targeted collaboration with Drs. Peter Reiss and Isabelle Texier of the CEA Grenoble, we successfully produced nanoparticules of InP/ZnS, functionalized with penicillamin, which have beeen coupled to our abu-derivative maurocalcine analogue. The data demonstrate the efficient cell penetration of this new generation of nanoparticles that present three decisive advantages for *in vivo* applications: i) preliminary data indicate that, owing to their relatively small size, these nanoparticles can be eliminated *in vivo* by urine secretion (unpublished data), ii) none of the materials used present the known cell toxicity of free cadmium, and iii) these nanoparticules emit at near infrared wavelengths indicating their good suitability for imaging across tissues.

In one specific applications, the ability of maurocalcine to deliver quantum dots to cells were used for imaging of atherosclerosis (Jayagopal *et al.*, 2009). In this application, the authors used biotinylated maurocalcine to deliver streptavidine coated CdSe/ZnS quantum dots *in vitro* to isolated monocytes and T-lymphocytes. Quantum dot labeled cells were then injected into ApoE-/- mice, a model of atherosclerosis. It was shown that cells incorporated aortic lesions and that quantum dots were present in atherosclerotic plaques 2 days after injection. This fluorescence could be monitored for up to four weeks demonstrating the remarkable stability of these quantum dots *in vivo*. During that study, it was confirmed that maurocalcine / quantum dots complexes present no toxicity for the cells, similarly to what was observed for streptavidine alone (Boisseau *et al.*, 2006).

Nanotechnology is destined to a fabulous future and many of the applications will require intracellular delivery of active compounds. Maurocalcine is one of the promising cell delivery peptide vector that holds great promises for these applications. Although it is more complex to synthesize than other cell penetrating peptides, it has some competitive advantages such as a cell penetration at lower concentration, absence of cell toxicity, greater resistance to protease degradation.

Acknowledgements. *We acknowledge financial support from CEA (Program TIMOMA2), ANR PNANO (Program SYNERGY), and from Inserm.*

References

Akerman ME, Chan WC, Laakkonen P, Bhatia SN, Ruoslahti E (2002) Nanocrystal targeting *in vivo*. *Proc Natl Acad Sci USA* **99**: 12617-12621

Altafaj X, Cheng W, Esteve E, Urbani J, Grunwald D, Sabatier JM, Coronado R, De Waard M, Ronjat M (2005) Maurocalcine and domain A of the II-III loop of the dihydropyridine receptor Cav 1.1 subunit share common binding sites on the skeletal ryanodine receptor. *J Biol Chem* **280**: 4013-4016

Arou S, Ram N, Appaix F, Ronjat M, Kenani A, Pirollet F, De Waard M (2009) Maurocalcine as a Non Toxic Drug Carrier Overcomes Doxorubicin Resistance in the Cancer Cell Line MDA-MB 231. *Pharm Res* **26**: 836-845

Ballou B, Lagerholm BC, Ernst LA, Bruchez MP, Waggoner AS (2004) Noninvasive imaging of quantum dots in mice. *Bioconjug Chem* **15**: 79-86

Biju V, Itoh T, Anas A, Sujith A, Ishikawa M (2008) Semiconductor quantum dots and metal nanoparticles: syntheses, optical properties, and biological applications. *Anal Bioanal Chem* **391**: 2469-2495

Boisseau S, Mabrouk K, Ram N, Garmy N, Collin V, Tadmouri A, Mikati M, Sabatier JM, Ronjat M, Fantini J*, et al.* (2006) Cell penetration properties of maurocalcine, a natural venom peptide active on the intracellular ryanodine receptor. *Biochim Biophys Acta* **1758**: 308-319

Chen F, Gerion D (2004) Fluorescent CdSe/ZnS nanocrystal-peptide conjugates for long-term, nontoxic imaging and nuclear targeting in living cells. *Nano Lett* **4**: 1827-1832

Chen L, Esteve E, Sabatier JM, Ronjat M, De Waard M, Allen PD, Pessah IN (2003) Maurocalcine and peptide A stabilize distinct subconductance states of ryanodine receptor type 1, revealing a proportional gating mechanism. *J Biol Chem* **278**: 16095-16106

Choi HS, Liu W, Misra P, Tanaka E, Zimmer JP, Itty Ipe B, Bawendi MG, Frangioni JV (2007) Renal clearance of quantum dots. *Nat Biotechnol* **25**: 1165-1170

Dahan M, Levi S, Luccardini C, Rostaing P, Riveau B, Triller A (2003) Diffusion dynamics of glycine receptors revealed by single-quantum dot tracking. *Science* **302**: 442-445

Derfus AM, Chen WCW, Bhatia SN (2004) Intracellular delivery of quantum dots for live cell labeling and organelle tracking. *Adv Mater* **16**: 961-966

Dubertret B, Skourides P, Norris DJ, Noireaux V, Brivanlou AH, Libchaber A (2002) In vivo imaging of quantum dots encapsulated in phospholipid micelles. *Science* **298**: 1759-1762

el-Hayek R, Lokuta AJ, Arevalo C, Valdivia HH (1995) Peptide probe of ryanodine receptor function. Imperatoxin A, a peptide from the venom of the scorpion Pandinus imperator, selectively activates skeletal-type ryanodine receptor isoforms. *J Biol Chem* **270**: 28696-28704

Esteve E, Mabrouk K, Dupuis A, Smida-Rezgui S, Altafaj X, Grunwald D, Platel JC, Andreotti N, Marty I, Sabatier J**M***, et al.* (2005) Transduction of the scorpion toxin maurocalcine into cells. Evidence that the toxin crosses the plasma membrane. *J Biol Chem* **280**: 12833-12839

Esteve E, Smida-Rezgui S, Sarkozi S, Szegedi C, Regaya I, Chen L, Altafaj X, Rochat H, Allen P, Pessah IN*, et al.* (2003) Critical amino acid residues determine the binding affinity and the Ca^{2+} release efficacy of maurocalcine in skeletal muscle cells. *J Biol Chem* **278**: 37822-37831

Fajloun Z, Kharrat R, Chen L, Lecomte C, Di Luccio E, Bichet D, El Ayeb M, Rochat H, Allen PD, Pessah **N***, et al.* (2000)

Chemical synthesis and characterization of maurocalcine, a scorpion toxin that activates Ca(2+) release channel/ryanodine receptors. *FEBS Lett* **469**: 179-185

Gao X, Cui Y, Levenson RM, Chung LW, Nie S (2004) In vivo cancer targeting and imaging with semiconductor quantum dots. *Nat Biotechnol* **22**: 969-976

Green D, Pace S, Curtis SM, Sakowska M, Lamb GD, Dulhunty AF, Casarotto MG (2003) The three-dimensional structural surface of two beta-sheet scorpion toxins mimics that of an alpha-helical dihydropyridine receptor segment. *Biochem J* **370**: 517-527

Gurrola GB, Arevalo C, Sreekumar R, Lokuta AJ, Walker JW, Valdivia HH (1999) Activation of ryanodine receptors by imperatoxin A and a peptide segment of the II-III loop of the dihydropyridine receptor. *J Biol Chem* **274**: 7879-7886

Hoshino A, Fujioka K, Oku T, Nakamura S, Suga M, Yamaguchi Y, Suzuki K, Yasuhara M, Yamamoto K (2004) Quantum dots targeted to the assigned organelle in living cells. *Microbiol Immunol* **48**: 985-994

Jayagopal A, Su YR, Blakemore JL, Linton MF, Fazio S, Haselton FR (2009) Quantum dot mediated imaging of atherosclerosis. *Nanotechnology* **20**: 165102

Lee CW, Lee EH, Takeuchi K, Takahashi H, Shimada I, Sato K, Shin SY, Kim do H, Kim JI (2004) Molecular basis of the high-affinity activation of type 1 ryanodine receptors by imperatoxin A. *Biochem J* **377**: 385-394

Lee J, Kim J, Park E, Jo S, Song R (2008) PEG-ylated cationic CdSe/ZnS QDs as an efficient intracellular labeling agent. *Phys Chem Chem Phys* **10**: 1739-1742

Liang JF, Yang VC (2005) Synthesis of doxorubicin-peptide conjugate with multidrug resistant tumor cell killing activity. *Bioorganic & medicinal chemistry letters* **15**: 5071-5075

Lidke DS, Nagy P, Heintzmann R, Arndt-Jovin DJ, Post JN, Grecco HE, Jares-Erijman EA, Jovin TM (2004) Quantum dot ligands provide new insights into erbB/HER receptor-mediated signal transduction. *Nat Biotechnol* **22**: 198-203

Lim YT, Kim S, Nakayama A, Stott NE, Bawendi MG, Frangioni JV (2003) Selection of quantum dot wavelengths for biomedical assays and imaging. *Mol Imaging* **2**: 50-64

Lukacs B, Sztretye M, Almassy J, Sarkozi S, Dienes B, Mabrouk K, Simut C, Szabo L, Szentesi P, De Waard M*, et al.* (2008) Charged surface area of maurocalcine determines its interaction with the skeletal ryanodine receptor. *Biophys J* **95**: 3497-3509

Mabrouk K, Ram N, Boisseau S, Strappazzon F, Rehaim A, Sadoul R, Darbon H, Ronjat M, De Waard M (2007) Critical amino acid residues of maurocalcine involved in pharmacology, lipid interaction and cell penetration. *Biochim Biophys Acta* **1768**: 2528-2540

Mansson, A., Sundberg, M., Balaz, M., Bunk, R., Nicholls, I.A., Omling, P., Tagerud, S., and Montelius, L. (2004). In vitro sliding of actin filaments labelled with single quantum dots. B*iochem Biophys Res Commun* **314**: 529-534

Michalet X, Pinaud FF, Bentolila LA, Tsay JM, Doose S, Li JJ, Sundaresan G, Wu AM, Gambhir SS, Weiss S (2005) Quantum dots for live cells, in vivo imaging, and diagnostics. *Science* **307**: 538-544

Mosbah A, Kharrat R, Fajloun Z, Renisio JG, Blanc E, Sabatier JM, El Ayeb M, Darbon H (2000) A new fold in the scorpion toxin family, associated with an activity on a ryanodine-sensitive calcium channel. *Proteins* **40**: 436-442

Pinaud F, King D, Moore HP, Weiss S (2004) Bioactivation and cell targeting of semiconductor CdSe/ZnS nanocrystals with phytochelatin-related peptides. *J Am Chem Soc* **126**: 6115-6123

Ram N, Aroui S, Jaumain E, Bichraoui H, Mabrouk K, Ronjat M, Lortat-Jacob H, De Waard M (2008a) Direct Peptide Interaction with Surface Glycosaminoglycans Contributes to the Cell Penetration of Maurocalcine. *J Biol Chem* **283**: 24274-24284

Ram N, Weiss N, Texier-Nogues I, Aroui S, Andreotti N, Pirollet F, Ronjat M, Sabatier JM, Darbon H, Jacquemond V*, et al.* (2008b) Design of a disulfide-less, pharmacologically-inert and chemically-competent analog of maurocalcine for the efficient transport of impermeant compounds into cells. *J Biol Chem*. **283**: 27048-27056

Santra S, Yang H, Stanley JT, Holloway PH, Moudgil BM, Walter G, Mericle RA (2005) Rapid and effective labeling of brain tissue using TAT-conjugated CdS:Mn/ZnS quantum dots. *Chem Commun (Camb),* **25**: 3144-3146

Schwartz EF, Capes EM, Diego-Garcia E, Zamudio FZ, Fuentes O, Possani LD, Valdivia HH (2009) Characterization of hadrucalcin, a peptide from Hadrurus gertschi scorpion venom with pharmacological activity on ryanodine receptors. *Br J Pharmacol* **157**: 392-403

Shahbazzadeh D, Srairi-Abid N, Feng W, Ram N, Borchani L, Ronjat M, Akbari A, Pessah IN, De Waard M, El Ayeb M (2007) Hemicalcin, a new toxin from the Iranian scorpion *Hemiscorpius lepturus* which is active on ryanodine-sensitive Ca2+ channels. *Biochem J* **404**: 89-96

Silver J, Ou W (2005) Photoactivation of quantum dot fluorescence following endocytosis. *Nano Lett* **5**: 1445-1449

Sukhanova A, Devy J, Venteo L, Kaplan H, Artemyev M, Oleinikov V, Klinov D, Pluot M, Cohen JH, Nabiev I (2004) Biocompatible fluorescent nanocrystals for immunolabeling of membrane proteins and cells. *Anal Biochem* **324**: 60-67

Szappanos H, Smida-Rezgui S, Cseri J, Simut C, Sabatier JM, De Waard M, Kovacs L, Csernoch L, Ronjat M (2005) Differential effects of maurocalcine on Ca^{2+} release events and depolarization-induced Ca2+ release in rat skeletal muscle. *J Physiol* **565**: 843-853

Voura EB, Jaiswal JK, Mattoussi H, Simon SM (2004) Tracking metastatic tumor cell extravasation with quantum dot nanocrystals and fluorescence emission-scanning microscopy. *Nat Med* **10**: 993-998

Wadia JS, Dowdy SF (2002) Protein transduction technology. *Curr Opin Biotechnol* **13**: 52-56

Zamudio FZ, Gurrola GB, Arevalo C, Sreekumar R, Walker JW, Valdivia HH, Possani LD (1997) Primary structure and synthesis of Imperatoxin A (IpTx(a)), a peptide activator of Ca^{2+} release channels/ryanodine receptors. *FEBS Lett* **405**: 385-389

Zhu S, Darbon H, Dyason K, Verdonck F, Tytgat J (2003) Evolutionary origin of inhibitor cystine knot peptides. *Faseb J* **17**: 1765-1767

b. Conclusion

Les CPP ont devant eux un brillant avenir en tant que vecteur de molécules d'intérêt. Ils ont déjà démontré leur potentiel pour l'administration *in vitro* et *in vivo* de différents cargos et les récents succès, en phase I et II d'essais cliniques sont encourageants pour une future utilisation des CPP pour les thérapies (Heitz, Morris et al. 2009).

2. Article 1

D-Maurocalcine, a Pharmacologically Inert Efficient Cell-penetrating Peptide Analogue

Cathy Poillot, Kaouthar Dridi, Hicham Bichraoui, Julien Pêcher, Sebastien Alphonse, Badreddine Douzi, Michel Ronjat, Hervé Darbon, Michel De Waard

The Journal Of Biological Chemistry Vol. 285, No.44, pp.34168-34180, October 29, 2010

a. Introduction

La maurocalcine (MCa) est un peptide issu d'une toxine de scorpion Tunisien, *Scorpio maurus palmatus*. Ce peptide de 33 acides aminés est structuré selon un motif « inhibitor cystine knot, avec trois ponts disulfures selon le modèle suivant Cys^{3}-Cys^{17}, Cys^{10}-Cys^{21} et Cys^{16}-Cys^{32}. La MCa possède une cible moléculaire naturelle, le récepteur à la ryanodine (RyR), un canal calcique qui est localisé à l'intérieur des cellules, à la membrane du réticulum endoplasmique. En étudiant comment cette toxine pouvait atteindre sa cible, il est apparu qu'elle possédait des propriétés de pénétration cellulaire. La MCa possède des qualités uniques comparée aux autres peptides de pénétration cellulaire (CPP pour Cell Penetrating Peptide) : i) une bonne stabilité, ii) une pénétration à des concentrations faibles, iii) une toxicité faible et iv) un mode d'entrée dans les cellules passant pour une bonne part par la translocation. Cependant, la MCa a un point faible en tant que vecteur de pénétration cellulaire : son activité pharmacologique. En effet, il est gênant de provoquer un relarguage de calcium intracytoplasmique lors de l'administration d'un composé attaché à la MCa dans les cellules. Pour pallier ce problème, plusieurs stratégies ont été expérimentées, toutes basées sur l'hypothèse que les conditions structurales nécessaires à l'action pharmacologique de la MCa soit plus stringente que celles requises à la pénétration cellulaire.

Premièrement, des mutations dans la séquence de la MCa ont été réalisées dans le but d'altérer les propriétés pharmacologiques de la MCa sans affecter la pénétration cellulaire. Grâce à cette stratégie, de nouveaux analogues de la MCa ont été synthétisés avec une perte partielle ou complète des effets pharmacologiques (Mabrouk, Ram et al. 2007). Cependant, aucun de ces analogues n'avaient conservés intégralement les facultés de pénétration de la MCa.

La deuxième approche a consisté en la synthèse d'un analogue de MCa, ou tous les résidus cystéines étaient remplacés par des résidus acide 2 aminobutyrique (Ram, Weiss et al. 2008). Le peptide obtenu n'avait plus de ponts disulfures de part la perte des résidus cystéine et a perdu ses propriétés pharmacologiques. Cet analogue a préservé les propriétés de pénétration cellulaire de la MCa, mais pas intactes, en effet, il est moins performant que la MCa

structurée. De plus, la perte des structures secondaires et l'absence de ponts disulfures faisaient perdre à la MCa ses avantages sur les autres CPP.

La troisième stratégie développée dans cet article a été de réaliser une synthèse de la MCa totalement constituée d'acides aminés de conformation D. La structure secondaire, les propriétés pharmacologiques ainsi que la capacité de pénétration cellulaire ont été testées, ainsi que la résistance enzymatique et la toxicité de ce nouvel analogue.

THE JOURNAL OF BIOLOGICAL CHEMISTRY VOL. 285, NO. 44, pp. 34168–34180, October 29, 2010

D-Maurocalcine, a Pharmacologically Inert Efficient Cell-penetrating Peptide Analogue*

Received for publication, January 16, 2010, and in revised form, June 3, 2010 Published, JBC Papers in Press, July 7, 2010, DOI 10.1074/jbc.M110.104919

Cathy Poillot[‡1], Kaouthar Dridi[§1], Hicham Bichraoui[‡2], Julien Pêcher[¶], Sebastien Alphonse[§], Badreddine Douzi[§], Michel Ronjat[‡2], Hervé Darbon[§], and Michel De Waard[‡¶3]

From the [‡]Grenoble Institute of Neuroscience, INSERM U836, Site Santé de la Tronche, Bâtiment Edmond J. Safra, Chemin Fortuné Ferrini, BP170, 38042 Grenoble Cedex 9, France, [§]Architecture et Function des Macromolécules Biologiques-CNRS, UMR 6098, Case 932, 163 Avenue de Luminy, F-13288 Marseille Cedex 9, France, and [¶]Smartox Biotechnologies, Floralis, Biopolis, 5 Avenue du Grand Sablon, 38700 La Tronche, France

Maurocalcine has been the first demonstrated animal toxin acting as a cell-penetrating peptide. Although it possesses competitive advantages, its use as a cell-penetrating peptide (CPP) requires that analogues be developed that lack its characteristic pharmacological activity on ryanodine-sensitive calcium channels without affecting its cell-penetrating and vector efficiencies. Here, we present the synthesis, three-dimensional ^{1}H NMR structure, and activity of D-maurocalcine. We demonstrate that it possesses all of the desired features for an excellent CPP: preserved structure, lack of pharmacological action, conserved vector properties, and absence of cell toxicity. This is the first report of a folded/oxidized animal toxin in its D-diastereomer conformation for use as a CPP. The protease resistance of this new peptide analogue, combined with its efficient cell penetration at concentrations devoid of cell toxicity, suggests that D-maurocalcine should be an excellent vector for *in vivo* applications.

Over the last 15 years, several peptides have been described as possessing the property of accumulating inside cells. These peptides have collectively been denominated cell-penetrating peptides (CPP)[4] (1). The common characteristic of these peptides is that they are unusually enriched in positively charged amino acids (2). The HIV-1 TAT peptide, penetratin, and the chimeric transportan are well known and frequently used CPP (3, 4). Reports on the use of CPP as vectors for the cell delivery of non-permeable membrane compounds are now on an exponential rise. As a consequence, many novel applications have been developed that are based on the cell delivery of drugs, peptides, proteins, antibodies, oligonucleotides, peptide nucleic acids, siRNA, cDNA, imaging agents, or nanoparticles (5–7). The mechanism(s) by which CPP enter cells remains largely debated, but the consensual view is that two non-concurrent pathways coexist: direct membrane translocation and one of many forms of endocytosis (8). This discussion is not only semantic because the intracellular distribution and fate of CPP differs with its mode of entry. If direct translocation is used, the peptide accumulates in the cytoplasm and reaches the nucleus, whereas, if endocytosis is the main pathway of cell entry, peptides end up in late endosomes. Translocation is the favored pathway for the cell delivery of cargoes by CPP because most drugs are active when delivered in the cytoplasm or in the nucleus, but not in late endosomes (4, 9).

While searching for pharmacological agents regulating the activity of ryanodine receptors (RyR), our group came across a cationic toxin of 33-mer, maurocalcine (L-MCa), which was originally isolated and purified from a Tunisian scorpion, *Scorpio maurus palmatus* (10). RyR are intracellular calcium channels that are inserted into the membrane of endoplasmic reticulum and that control Ca^{2+} release from intracellular stores. Several lines of evidence suggested that L-MCa represents the first member of a novel class of CPP. First, it was demonstrated that an extracellular application of L-MCa triggers an almost immediate Ca^{2+} release from internal stores in myotubes, suggesting rapid access of L-MCa to its binding site (11). Second, it was discovered that the binding site of this toxin is located on the cytoplasmic side of RyR (12). Kinetic and RyR topological considerations therefore suggest that cell entry of L-MCa more likely relies on membrane translocation to achieve rapid cytoplasmic accumulation than on endocytosis. Third, L-MCa acts as an efficient vector for the delivery of proteins, peptides, nanoparticles, and drugs inside cells. At the structural level, the peptide folds along an inhibitor cystine knot motif with three disulfide bridges connected according to the pattern Cys^3–Cys^{17}, Cys^{10}–Cys^{21}, and Cys^{16}–Cys^{32}. Landmark properties of CPP are also found in L-MCa because (i) 12 of the 33 residues of L-MCa are positively charged, (ii) many of the charged residues are critical for cell penetration, and (iii) L-MCa interacts with critical membrane components required for cell penetration, such as proteoglycans and negatively charged lipids (13, 14). Altogether, these considerations made L-MCa the first example of a folded and oxidized peptide toxin acting as CPP. Compared

* This work was supported by grants from Technology pour la Santé (Program TIMOMA2 of the Commissariat à l'Energie Atomique) and from Agence Nationale de la Recherche PNANO (Programs SYNERGIE and NanoFret).

The atomic coordinates and structure factors (code 2KQL) have been deposited in the Protein Data Bank, Research Collaboratory for Structural Bioinformatics, Rutgers University, New Brunswick, NJ (http://www.rcsb.org/).

[1] Both authors contributed equally to this work.

[2] Supported by a grant of the Association Française contre les Myopathies.

[3] To whom correspondence should be addressed: Grenoble Institute of Neuroscience, INSERM U836, BP170, 38042 Grenoble, France. Tel.: 33-4-56-52-05-63; Fax: 33-4-56-52-06-37; E-mail: michel.dewaard@ujf-grenoble.fr.

[4] The abbreviations used are: CPP, cell-penetrating peptide(s); FAM, 5(6)-carboxyfluorescein; MCa, maurocalcine; nOe, nuclear Overhauser effect(s); r.m.s., root mean square; SR, sarcoplasmic reticulum; RyR, ryanodine receptor; Fmoc, *N*-α-fluorenylmethyloxycarbonyl; MTT, 3-(4,5-dimethylthiazol-2-yl)-2,5-diphenyltetrazolium bromide; MOPS, 4-morpholinepropanesulfonic acid; NOESY, Nuclear Overhauser effect spectroscopy; TOCSY, total correlation spectroscopy.

with other CPP, it possesses some competitive features, such as greater stability, cell penetration at lower concentrations, very low toxicity, and membrane translocation as the expected mode of cell penetration. Besides it is one of the few CPP whose cell penetration can be studied independently of cargo attachment because it possesses a direct physiological readout under the form of Ca^{2+} release from internal stores. Two negative aspects related to the use of L-MCa instead of other CPP are (i) longer length of the peptide and (ii) pharmacological activity associated with cell penetration. Peptide length has little economical impact now because the cost of peptide production has sharply decreased. In contrast, pharmacological activity may represent a burden if one wants to use L-MCa as a vector for its application *in vivo*. To circumvent this problem, several strategies have been developed based on the assumption that the structural requirements for binding onto RyR were more stringent than those for cell penetration. First, single point mutagenesis of L-MCa was employed in order to alter peptide pharmacology without affecting cell penetration. Using this strategy, new L-MCa analogues have been defined with reduced or complete loss of pharmacological effects (13). Nevertheless, none of the analogues totally preserved the cell penetration efficiency of wild-type L-MCa. Second, an L-MCa analogue was produced in which all cysteine residues were substituted with isosteric 2-aminobutyric acid residues (15). The resulting peptide was unfolded due to the importance of disulfide bridges for folding/oxidation and lacked pharmacological properties. Interestingly, this analogue preserved correct cell penetration efficacy, albeit lower than L-MCa. In addition, lack of secondary structures and absence of disulfide bridges resulted in the loss of the competitive advantage of MCa over other CPP. Herein, we pursued another strategy with the aim to produce a cell-penetrating competent MCa analogue, similar in properties to L-MCa but without any pharmacological activity. We describe the chemical synthesis, successful folding, and oxidation of D-MCa; provide the three-dimensional structure of the resulting analogue; and demonstrate that it has cell penetration properties similar to those of L-MCa. In addition, D-MCa loses the protease sensitivity of L-MCa and is a non-toxic vector for cells. This is the first description of a folded/oxidized CPP build with D-amino acids designed on the basis of an animal toxin sequence.

EXPERIMENTAL PROCEDURES

Products—*N*-α-Fmoc-L-amino acid, *N*-α-Fmoc-D-amino acid, Wang-Tentagel resin, and reagents used for peptide synthesis were obtained from Iris Biotech. Solvents were analytical grade products from Acros Organics. Enzymes (trypsin, endoproteinase, and Asp-N) were obtained from Roche Applied Science.

Solid-phase Synthesis—The chemical synthesis of L-MCa was performed as previously described (10). D-MCa was chemically synthesized by the solid-phase method (16) using an automated peptide synthesizer (CEM® Liberty). The peptide chain was assembled stepwise on 0.24 mEq of Fmoc-D-Arg-Pbf-Wang-Tentagel resin using 0.24 mmol of Fmoc-D-amino acid derivatives. The side chain protecting groups were as follows: trityl for Cys and Asn; *tert*-butyl for Ser, Thr, Glu, and Asp; Pbf for Arg; and *tert*-butylcarbonyl for Lys. Reagents were at the following concentrations: Fmoc-amino acids (0.2 M Fmoc-amino acids-OH in dimethylformamide), activator (0.5 M (1H-benzotriazole-1-yl)-1,1,3,3-tetramethyluronium hexafluorophosphate in dimethylformamide), activator base (2 M *N*,*N*-diisopropylethylamine in *N*-methylpyrrolidone) and deprotection agent (5% piperazine, 0.1 M 1-hydroxybenzotriazole in dimethylformamide), as advised by PepDriver (CEM®). After peptide chain assembly, the resin was treated for 4 h at room temperature with a mixture of trifluoroacetic acid/water/triisopropylsilan/DTT (92.5:2.5:2.5:2.5). The peptide mixture was then filtered, and the filtrate was precipitated by adding cold *t*-butylmethyl ether. The crude peptide was pelleted by centrifugation (10,000 × *g*, 15 min), and the supernatant was discarded. The reduced peptide was dissolved in 200 mM Tris-HCl buffer, pH 8.3, at a final concentration of 1 mM and stirred for 72 h at room temperature under air for oxidation and folding. Oxidized D-MCa was purified by high performance liquid chromatography (HPLC) using a Vydac C18 column (218TP1010, 25 × 10 cm). Elution of D-MCa was performed with a 10–60% acetonitrile linear gradient containing 0.1% trifluoroacetic acid. The purified fraction was analyzed by analytical reversed phase HPLC (Vydac C18 column 218TP104, 25 × 4.6 cm). The pure fraction was lyophilized and quantified. 25 mg of D-MCa was purified, representing a theoretical yield of 25%. D-MCa was characterized by MALDI-TOF mass spectrometry.

D-MCa Labeling by 5(6)-carboxyfluorescein (FAM)—The carboxyl function of FAM (0.25 mmol; Novabiochem) was activated in 1 ml of solution of 1 M *N*,*N*′-diisopropylcarbodiimide (Sigma), 1 M 1-hydroxybenzotriazole in *N*-methylpyrrolidone for 30 min. This solution was then added to 100 mg (0.012 mmol) of resin (D-MCa protected on Wang-Tentagel resin). The reaction mixture was stirred for 2.5 h in the dark and then centrifuged. The resin was washed with *N*-methylpyrrolidone five times, followed by three washes with methanol. The final resin was dried and subjected for 4 h at room temperature to peptide cleavage with a mixture of trifluoroacetic acid/water/triisopropylsilan/DTT (92.5:2.5:2.5:2.5). Next, crude FAM-D-MCa was oxidized as described for D-MCa.

Proteolytic Digestion of L-MCa and D-MCa—The stability of D-MCa to proteolytic digestion was investigated under the same conditions used to determine the disulfide bridge of L-MCa toxin. D-MCa (400 μg) was dissolved in 50 mM sodium phosphate buffer and endoproteinase Asp-N (enzyme/substrate, 1:200 (w/w), 37 °C, 36 h) or trypsin (enzyme/substrate, 1:32 (w/w), 37 °C, 36 h). The digestion was terminated by acidification with 10% aqueous trifluoroacetic acid (TFA). The product was analyzed directly by reversed phase HPLC with a linear gradient of 1–60% acetonitrile into water containing 0.1% trifluoroacetic acid.

Circular Dichroism—The folding states of L- and D-MCa were checked by far-UV CD. The CD spectra were recorded on a Jasco 810 dichrograph using 1-mm-thick quartz cells in 300 μl of water. CD measurements were performed at 298 K, using a wavelength ranging from 260 to 190 nm. Peptide concentrations were 0.1 mM for these measurements. D-MCa thermal stability was assessed using CD by following changes in the spectrum with increasing temperature at a fixed wavelength

(200 nm). Measurements were performed in the temperature range of 20–100 °C with data pitch of 10 °C step and temperature rise of 5 °C/min.

NMR Experiments—Purified D-MCa was solubilized in 500 μl of a mixture of H_2O and D_2O (9:1, v/v) at a final concentration of 1.9 mM. Amide proton exchange rates were determined after freeze-drying of the sample and solubilization in 100% D_2O. All ^1H NMR spectra were recorded on a Bruker DRX500 Avance III spectrometer equipped with a QX1 probe with *z* axis gradients. The temperature was set to 300 K, and the spectra were recorded with 2048 complex points in the directly acquired dimension and 400 points in the indirectly detected dimension (4,096 × 512 points for the DQF-COSY). Solvent suppression was achieved using excitations sculpting with gradients (17). Two-dimensional spectra were acquired using the states-time-proportional phase increment method (18) to achieve F1 quadrature detection (19). NOESY spectra were acquired using a mixing time of 100 ms. TOCSY was performed with a spin locking field strength of 8 kHz for 80 ms. The individual amide proton exchange rates were determined by recording series of six NOESY spectra (10-h duration for each experiment) at 300 K using the D_2O sample. Amide proton exchange still giving rise to nuclear Overhauser effect (nOe) correlations after 60 h of exchange were considered as slowly exchanging and therefore engaged in a hydrogen bond, the partner of which was identified on the sight of preliminary calculated structures. All spectra were processed with NMRPipe (20).

Spectrum Analysis and Experimental Restraints—The identification of amino acid spin systems and the sequential assignment were done using the standard strategy described by Wüthrich (21), applied with NMRview 5.2 graphic software (22). The comparative analysis of COSY and TOCSY spectra recorded in water gave the spin system signatures of the peptide. The spin systems were then sequentially connected using NOESY spectra. The integration of nOe data were performed by measuring peak volumes. On the basis of known distances in regular secondary structures, these volumes were translated into upper limit distances with CYANA 2.1 (23). Remaining nOe were assigned using the CANDID/NOEASSIGN automatic procedure of CYANA 2.1. Chemical shifts have been deposited in the BMRB Data Bank with accession number 16605. The calculation, after modification of libraries to integrate D-amino acid configuration, consisted of seven cycles of iterative automated nOe assignment and structure calculation of 250 conformers in each cycle. At the end of each CYANA run, unambiguously assigned peaks were converted in distance restraints and used as inputs for the next calculation steps. To keep the similar assignment condition, the same nOe calibration parameter, calculated by CYANA during the first run of nOe assignment, was used in all other runs of calculation. The final structure calculations with CYANA were started from 600 conformers, and a simulated annealing with 20,000 time steps per conformer was done using the CYANA torsion angle dynamics algorithm (24, 25). The 100 best solutions were refined using a short restrained molecular dynamics simulation in explicit solvent (26, 27) in the program XPLOR-NIH (28). At the end of the refinement, the 20 lowest energy solutions were selected to form the final ensemble. The quality of the structure was analyzed with the PROCHECK-NMR (29) and WHATIF (30) programs. Superposition of the structures was performed using the McLachlan algorithm as implemented in the program ProFit (A. C. R. Martin; available on the World Wide Web). All structure representations were made with the program PyMOL (DeLano Scientific, Palo Alto, CA). The atomic coordinates and experimentally derived restraints have been deposited in the Protein Data Bank with accession number 2KQL.

Preparation of Heavy SR Vesicles—Heavy SR vesicles were prepared following the method of Kim *et al.* (31). Protein concentration was measured by the Biuret method.

[^{3}H]Ryanodine Binding Assay—Heavy SR vesicles (1 mg/ml) were incubated at 37 °C for 2 h in an assay buffer composed of 10 nM [^{3}H]ryanodine, 150 mM KCl, 2 mM EGTA, 2 mM $CaCl_2$ (pCa = 5), and 20 mM MOPS, pH 7.4. L-MCa or D-MCa was added prior to the addition of heavy SR vesicles. [^{3}H]ryanodine bound to heavy SR vesicles was measured by filtration through Whatman GF/B glass filters followed by three washes with 5 ml of ice-cold washing buffer composed of 150 mM NaCl, 20 mM HEPES, pH 7.4. [^{3}H]Ryanodine retained on the filters was measured by liquid scintillation. Nonspecific binding was measured in the presence of 80 μM unlabeled ryanodine. The data are presented as mean ± S.E. Each experiment was performed in triplicate.

Ca^{2+} Release Measurements—Ca^{2+} release from heavy SR vesicles was measured using the Ca^{2+}-sensitive dye antipyrylazo III. The absorbance was monitored at 710 nm by a diode array spectrophotometer (MOS-200 optical system, Biologic, Claix, France). Heavy SR vesicles (50 μg) were actively loaded with Ca^{2+} at 37 °C in 2 ml of a buffer containing 100 mM KCl, 7.5 mM sodium pyrophosphate, 20 mM MOPS, pH 7.0, supplemented with 250 μM antipyrylazo III, 1 mM ATP/$MgCl_2$, 5 mM phosphocreatine, and 12 μg/ml creatine phosphokinase (25). Ca^{2+} loading was started by sequential additions of 50 and 20 μM $CaCl_2$. In these loading conditions, no calcium-induced calcium release interfered with the observations. At the end of each experiment, Ca^{2+} remaining in the vesicles was determined by the addition of 4 μM Ca^{2+} ionophore A23187 (Sigma), and the absorbance signal was calibrated by two consecutive additions of 20 μM $CaCl_2$.

Cell Culture—A Chinese hamster ovary (CHO) cell line (from ATCC) was maintained at 37 °C in 5% CO_2 in F-12K nutrient medium (Invitrogen) supplemented with 10% (v/v) heat-inactivated fetal bovine serum (Invitrogen) and 10,000 units/ml streptomycin and penicillin (Invitrogen).

3-(4,5-Dimethylthiazol-2-yl)-2,5-diphenyltetrazolium bromide (MTT) Assay—Cells were seeded into 96-well microplates at a density of ~8 × 10^4 cells/well. After 2 days of culture, the cells were incubated for 24 h at 37 °C with L-MCa or D-MCa at a concentration of 10 μM. Control wells containing cell culture medium alone or with cells, both without peptide addition, were included in each experiment. 0.1% saponin was used as a toxic agent for comparison. The cells were then incubated with MTT for 30 min. Conversion of MTT into purple-colored MTT formazan by the living cells indicates the extent of cell viability. The crystals were dissolved with DMSO, and the opti-

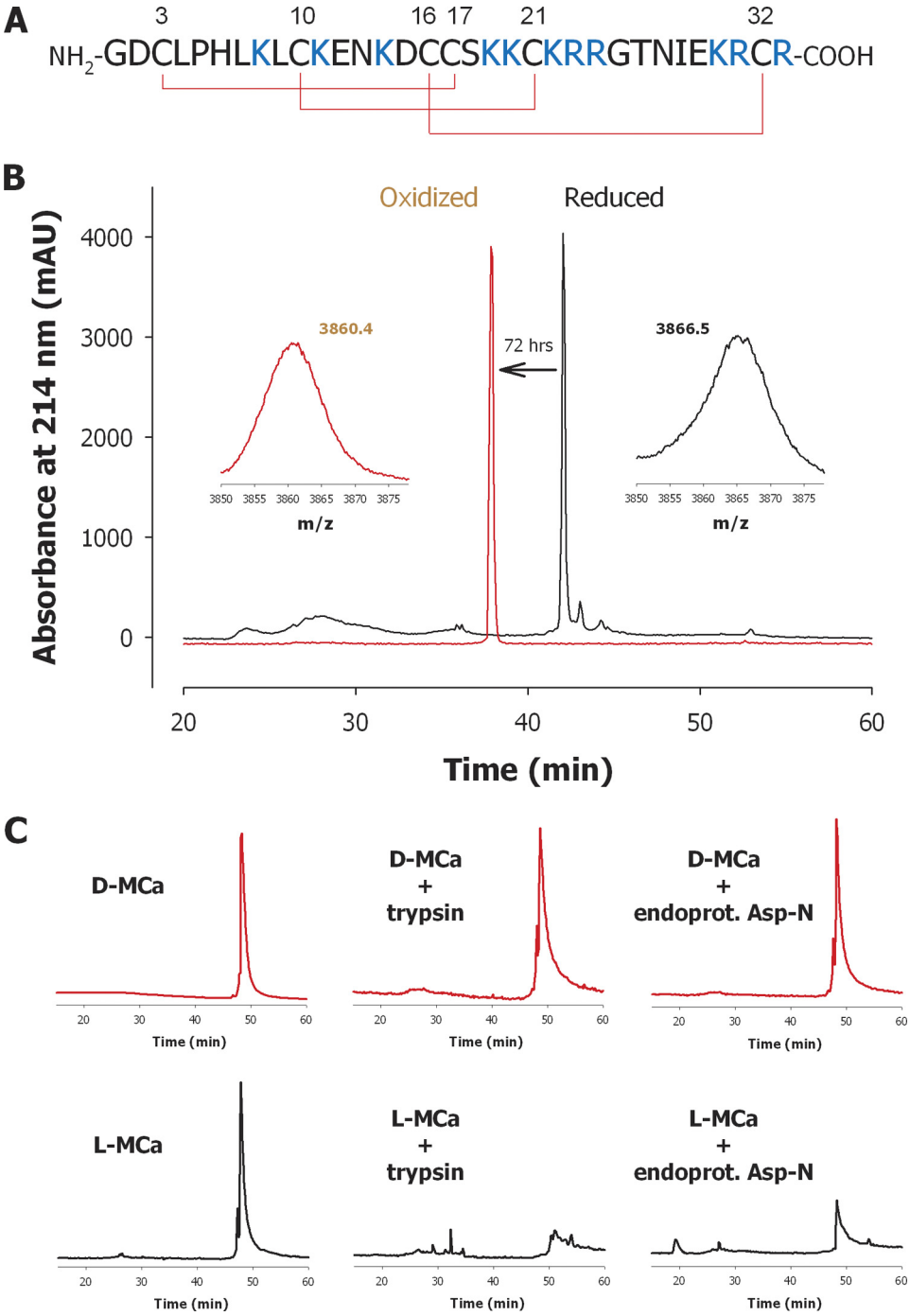

FIGURE 1. **Chemical synthesis and enzymatic resistance of D-MCa.** *A*, amino acid sequence of D-MCa in single-letter amino acid code. The positions of half-cystine residues are *highlighted*. The disulfide bridge organization of D-MCa, as expected from the connectivity of L-MCa, is illustrated by *red lines*. *B*, analytical C_{18} reversed phase HPLC profile of D-MCa at different stages of its chemical synthesis (*black line*, crude reduced peptide after final TFA treatment; *red line*, purified D-MCa 72 h after folding and oxidation as witnessed by the shift in elution time). *Insets*, mass spectra of reduced (*black line*, *right*) and oxidized (*red line*, *left*) D-MCa. *C*, analytical C_{18} reversed phase HPLC profiles illustrating the resistance of D-MCa to proteolysis by 36 h trypsin or endoproteinase Asp-N treatments (*upper panels*). In identical experimental conditions, these enzymes efficiently degrade L-MCa (*lower panels*).

cal density was measured at 540 nm using a microplate reader (Biotek ELx-800, Mandel Scientific Inc.) for quantification of cell viability. All assays were run in triplicates.

Confocal Microscopy—For analysis of the subcellular localization of FAM-L-MCa or FAM-D-MCa in living cells, cells were incubated with the fluorescent peptides for 2 h and then washed with phosphate-buffered saline (PBS) alone. The plasma membrane was stained with 5 μg/ml rhodamine-conjugated concanavalin A (Molecular Probes) for 5 min. Cells were washed once more. Live cells were then immediately analyzed by confocal laser-scanning microscopy using a Leica TCS-SPE operating system. Rhodamine (580 nm) and FAM (517 nm) were sequentially excited, and emission fluorescence was collected in *z*-confocal planes of 10–15-nm steps. In some experiments, FAM-D-MCa incubation with CHO cells coincided with a 20-min incubation with 50 nM LysoTracker red DND-99 before confocal acquisition.

FACS—FAM-L-MCa or FAM-D-MCa was incubated for 2 h with CHO cells to allow cell penetration. The cells were then washed twice with PBS to remove excess extracellular peptide. Next, the cells were treated with 1 mg/ml trypsin (Invitrogen) for 10 min at 37 °C to detach cells from the surface and centrifuged at 500 × *g* before suspension in PBS. For experiments concerning endocytosis inhibitors, CHO cells were initially washed with F12K and preincubated for 30 min at 37 °C with different inhibitors of endocytosis: (i) 1 mM amiloride, (ii) 5 μM cytochalasin D, (iii) 5 mM nocodazole, or (iv) 5 mM methyl-β-cyclodextrin (all from Sigma). The cells were then incubated for 2 h at 37 °C with 1 μM FAM-D-MCa. For all of these experimental conditions, flow cytometry analyses were performed with live cells using a Becton Dickinson FACS LSR II flow cytometer (BD Biosciences). Data were obtained and analyzed using FCS express software (De Novo). Live cells were gated by forward/side scattering from a total of 50,000 events.

Statistical Analyses—All data are given as mean ± S.D. for *n* number of observations, and statistical significance (*p*) was calculated using Student's *t* test.

RESULTS

Chemical Synthesis of D-MCa and Enzymatic Stability—The amino acid sequence and the expected disulfide bridge organi-

zation of D-MCa are illustrated in Fig. 1*A*. Solid-phase chemical synthesis of D-MCa was achieved stepwise on 0.1 mmol of Fmoc-D-Arg-(2,2,4,6,7-pentamethyldihydrobenzofuran-5-sulfonyl)-Wang-Tentagel resin by means of an Fmoc strategy. The amount of target peptide linked to the resin was 0.085 mmol, indicating an 85% yield of peptide assembly. Indeed, a relative homogeneity of crude D-MCa was obtained after TFA treatment as witnessed by analytical C_{18} reversed phase HPLC (Fig. 1*B*). Crude D-MCa was then folded/oxidized for 72 h in alkaline conditions, and the main peptide was purified to >99% homogeneity by semipreparative C18 reversed phase HPLC. The purity of D-MCa is illustrated by analytical C_{18} reversed phase HPLC, and the folding/oxidation process is witnessed by the shift in elution time (Fig. 1*B*). MS analyses (MALDI-TOF technique) of crude and folded/oxidized D-MCa provide experimental molecular masses $(M + H)^+$ of 3866.5 and 3860.4 Da, respectively. The shift in experimental molecular mass of 6.1 Da upon folding/oxidation is in agreement with the engagement of all six cysteine residues in the formation of three disulfide bridges. The yield of D-MCa synthesis, following peptide assembly, TFA treatment, oxidative folding, and purification was 25%. The enzymatic susceptibility of D-MCa was determined by *in vitro* incubation of D-MCa with either trypsin or endoproteinase Asp-N (Fig. 1*C*). As shown by analytical C_{18} reversed phase HPLC, D-MCa was totally resistant to the action of these enzymes, whereas L-MCa was significantly degraded. This is a significant advantage of D-MCa over L-MCa if *in vivo* applications are pursued with these CPP.

CD Analysis and Thermal Stability of D-MCa—The CD spectrum of D-MCa was determined to assess its secondary structure and compared with the CD spectrum of L-MCa (Fig. 2*A*). Measurements were performed at wavelengths ranging from 260 to 190 nm. The far-UV spectrum of D-MCa shows essentially π-π^* transitions of the amide chromophore of the peptide backbone and a large positive contribution between 200 and 210 nm, indicating the presence of β-strand structures, which is coherent with the structure of L-MCa (32). Interestingly, the CD spectrum of D-MCa is a mirror image of the one recorded for L-MCa, revealing the persistence of the conformation and the presence of α-carbons in D-configuration. The presence of disulfide bridges in D-MCa should represent a competitive advantage over other CPP in terms of peptide stability. To assess this point, the CD spectral of D-MCa were recorded at several different temperatures (20, 40, 60, 80, and 100 °C). All CD spectra coincided well, indicating that the structure of D-MCa was remarkably stable with increasing temperatures (Fig. 2*B*). A thermal denaturation/renaturation cycle has been performed on D-MCa from 20 to 100 °C by following the ellipticity value at 200 nm. This value remains constant within the temperature range, demonstrating that D-MCa structure is resistant to thermal denaturation (Fig. 2*C*).

Determination of the Three-dimensional Solution Structure of D-MCa—NMR resonance assignment and structure calculation were performed for D-MCa. The spin systems were identified on the basis of both COSY and TOCSY spectra. Once the assignment procedure was carried out, almost all protons were identified, and their resonance frequencies were determined (Table 1). The three-dimensional structure was determined by using 390 nOe-based distance restraints (including 158 intraresidue restraints, 116 sequential restraints, 36 medium range restraints, and 80 long range restraints). The distribution of these nOe-based distance restraints along the sequence is shown in Fig. 3*A*. In addition, 12 hydrogen bond restraints derived from hydrogen-deuterium exchange data have been included as well as nine distance restraints derived from the three disulfide bridges (Cys^3–Cys^{17}, Cys^{10}–Cys^{21}, and Cys^{16}–Cys^{32}) as previously determined for L-MCa (32). Altogether, the final experimental set corresponds to 11.81 constraints/residue on the average. The final step of calculation, including the whole set of restraints (see Table 2), led to 900 solutions, from which the 100 best were energy-minimized in explicit solvent. The 20 best solutions (no residual violation greater than 0.1 Å) were kept for analysis (Fig. 3*B*). The root mean square (r.m.s.) deviation calculated on the ensemble, excluding C- and N-terminal residues, is 1.1 ± 0.2 Å for backbone atoms and 2.32 ± 0.24 Å if all non-hydrogen atoms are included (Fig. 3*A* and Table 2). If only the ordered regions (amino acids 8–10, 20–23, and 30–32) are considered, these r.m.s. deviation values drop to 0.43 ± 0.08 and 1.37 ± 0.19 Å, respectively. These values indicate a lower resolution for the unordered regions (Fig. 3*B*). This is confirmed by the individual r.m.s. deviation values and by the scarcity of constraints in these regions (Fig. 3*A*). The correlation with the experimental data shows no nOe-derived distance violation greater than 0.1, and the Ramachandran plot, after modification of the library to include D-amino acid configurations, shows (in PROCHECK software nomenclature) 95.5% of the residues in the allowed regions and 0.5% in the disallowed regions.

The three-dimensional conformation of D-MCa (Protein Data Bank accession code 2KQL) consists of a compact disulfide-bonded core, from which several loops and the N terminus emerge. The main element of regular secondary structure is a double-stranded anti-parallel β-sheet comprising residues 20–23 and 30–32. A third peripheral extended strand composed by residues 8–10 is almost perpendicular to the double-stranded anti-parallel β-sheet (Fig. 3*C*). MCa is the first scorpion toxin known to adopt an ICK motif, whereas this fold has been observed for several other animal toxins from spider and shell venoms (33). To compare the native structure with the D-configuration herein described, we recalculated the L-configuration by using the previously published NMR data set (32) with the same protocol as for the D-configuration (Fig. 3*C*). This newly calculated structure of L-MCa is pretty close to the previously published one (r.m.s. deviation: 0.51 Å on the ordered regions) (32). To objectively compare the L- and D-MCa three-dimensional structures, we modified the Protein Data Bank file of D-MCa in order to draw the peptide in the L-configuration. The superimposition of both structures is shown in Fig. 4. The r.m.s. deviation values between both structures are 1.18 Å for backbone atoms (this value drops to 0.44 Å on ordered structures) and 2.07 Å for all non-hydrogen atoms. Therefore, the molecule, synthesized in D-configuration for α-carbons adopts a fold that is a pure mirror image of the L-configuration (Fig. 3*C*). This inversion is also seen on the organization of the molecular surface, leading to (i) the conservation of the basic patch and of the overall electrostatic anisotropy (the resulting

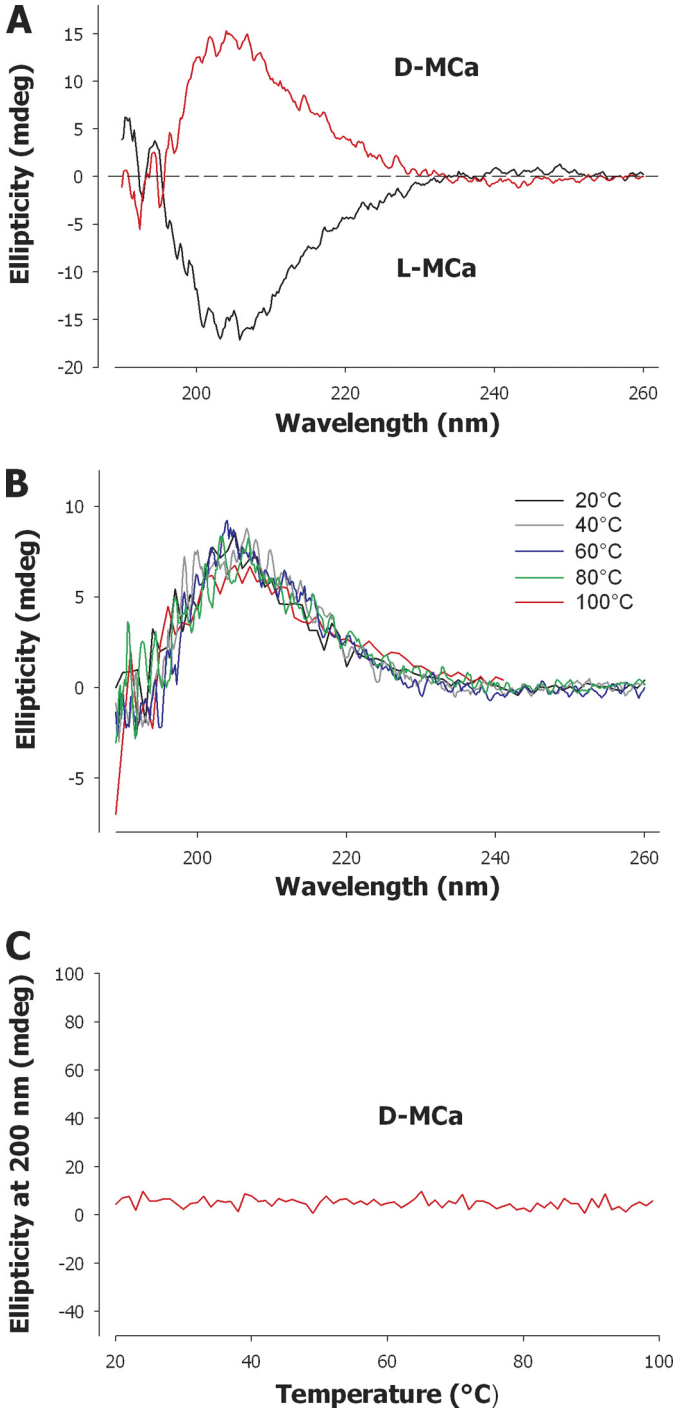

FIGURE 2. **Determination of the secondary structure of D-MCa by circular dichroism and thermal stability.** *A*, CD spectra of D-MCa *versus* L-MCa. *B*, CD spectra of D-MCa measured at various temperatures (from 20 up to 100 °C). *C*, ellipticity of D-MCa at 200 nm measured as a function of temperature.

TABLE 1
Resonance assignment of D-MCa
Chemical shifts are given in ppm.

Residue	HN	HC^{α}	HC^{β}	Other
	ppm	*ppm*	*ppm*	*ppm*
Gly^{1}		3.78, NO[a]		
Asp^{2}	8.69	4.74	2.72, 2.82	
Cys^{3}	8.17	4.65	2.82, 3.09	
Leu^{4}	9.11	4.72	2.1, NO	HC^{γ}: 1.78; $HC^{\delta1}$: 0.86; $HC^{\delta2}$: 1.24
Pro^{5}		4.48	2.12, 2.26	HC^{γ}: 1.72, 2.06; $HC^{\delta1}$: 3.53; $HC^{\delta2}$: 3.94
His^{6}	8.01	4.07	2.98, 3.13	2H: 7.3; 4H: 8.62
Leu^{7}	9.27	3.45	1.48, 1.86	HC^{γ}: 0.23; $HC^{\delta1}$: 0.52; $HC^{\delta2}$: 0.62, NO
Lys^{8}	7.36	4.21	1.71, 1.8	$HC^{\gamma1}$: 1.34; $HC^{\gamma2}$: 1.45; HC^{δ}: 1.62, NO; $HC^{\epsilon1}$: 2.83; $HC^{\epsilon2}$: 2.94; HN^{ζ}: NO
Leu^{9}	8.15	4.5	1.36, 1.51	HC^{γ}: 1.59; $HC^{\delta1}$: 0.75; $HC^{\delta2}$: 0.84, NO
Cys^{10}	7.88	4.81	2.95, 3.02	
Lys^{11}	8.6	4.31	1.53, 1.76	HC^{γ}: 1.25, NO; HC^{δ}: 2.89; HC^{ϵ}: NO; HN^{ζ}: NO
Glu^{12}	7.74	4.58	1.75	HC^{γ}: 2.21
Asn^{13}	8.96	3.87	2.72	NH_2: 6.76, 7.64
Lys^{14}	8.36	3.93	1.72, 1.83	HC^{γ}: 1.21, NO; HC^{δ}: 1.21, NO; HC^{ϵ}: 2.83, NO; HN^{ζ}: NO
Asp^{15}	7.67	4.31	2.89	
Cys^{16}	7.68	4.88	2.5, 3.39	
Cys^{17}	9.98	4.4	2.75, 3.11	
Ser^{18}	9.22	4.1	3.76, 3.98	
Lys^{19}	7.52	4.06	1.84, 2	$HC^{\gamma1}$: 1.17; $HC^{\gamma2}$: 1.28; $HC^{\delta1}$: 1.46; $HC^{\delta2}$:1.71; HC^{ϵ}: 2.91; HN^{ζ}: NO
Lys^{20}	7.3	4.31	1.58	$HC^{\gamma1}$: 1.11; $HC^{\gamma2}$: 1.27; HC^{δ}: 1.42, NO; HC^{ϵ}: 2.85, NO; HN^{ζ}: NO
Cys^{21}	8.88	4.84	2.6, 2.85	
Lys^{22}	8.24	4.85	1.51, 1.87	HC^{γ}: 1.25; HC^{δ}: 1.61; HC^{ϵ}: 2.88, NO; HN^{ζ}: NO
Arg^{23}	9	4.52	1.49, 1.63	HC^{γ}: 1.38, NO; HC^{δ}: 3.07, NO; HN^{ϵ}: 6.74
Arg^{24}	8.79	4.38	1.63, 1.67	HC^{γ}: 1.44, NO; HC^{δ}: 3.04, NO; HN^{ϵ}: 7.13
Gly^{25}	8.65	3.74		
Thr^{26}	8.42	4.06	4.3	HC^{γ}: 1.09
Asn^{27}	7.9	4.56	2.89	NH_2: 6.88, 7.59
Ile^{28}	8.24	3.87	1.87	$HC^{\gamma1}$: 1.18; $HC^{\gamma2}$: 1.26; $HC^{\gamma3}$: 0.87; HC^{δ}: 0.76
Glu^{29}	8.11	4.08	1.73, 1.85	HC^{γ}: 2.3
Lys^{30}	8.39	3.92	1.74	HC^{γ}: 0.96, NO; HC^{δ}: 1.47, NO; HC^{ϵ}: 2.77, NO; HN^{ζ}: NO
Arg^{31}	7.59	5.14	1.04, 1.12	HC^{γ}: 1.23; $HC^{\delta1}$: 2.76; $HC^{\delta2}$: 3.01; HN^{ϵ}: 7.2
Cys^{32}	8.52	5.17	2.86, 3.26	
Arg^{33}	9.05	4.33	1.75, 2	$HC^{\gamma1}$: 1.55; $HC^{\gamma2}$: 1.62; $HC^{\delta1}$: 2.84; $HC^{\delta2}$: 2.98; HN^{ϵ}: 6.63

[a] NO, resonance that cannot be observed.

dipole moment is conserved both in direction and strength) and (ii) the geometry inversion of the toxin surface involved in interaction with RyR (not shown). The conservation of the basic patch implies that membrane translocation properties should be well conserved, whereas geometry inversion of toxin surface should affect the ability of D-MCa to recognize RyR.

D-MCa Is a Pharmacologically Inert Analogue of L-MCa—D-Isomer ligands are supposed to lose their ability to recognize their pharmacological targets. L-MCa is known to bind onto a discrete binding site of RyR (12), thereby triggering an increase in channel opening probability and the occurrence of a long lasting subconductance state (34). Also, channel opening by L-MCa can indirectly be monitored by the conversion of a low affinity binding site for ryanodine to a high affinity one (11) and by Ca^{2+} release from purified sarcoplasmic reticulum (SR) vesicles (35). We therefore investigated the effects of D-MCa on these two paradigms (Fig. 5). As shown, L-MCa potently increases [^{3}H]ryanodine binding on heavy SR vesicles known to contain RyR. Maximal binding stimulation is 6.2-fold and occurs with an EC_{50} of 17.8 nM. In contrast to L-MCa, D-MCa had no effect on [^{3}H]ryanodine binding even for concentrations

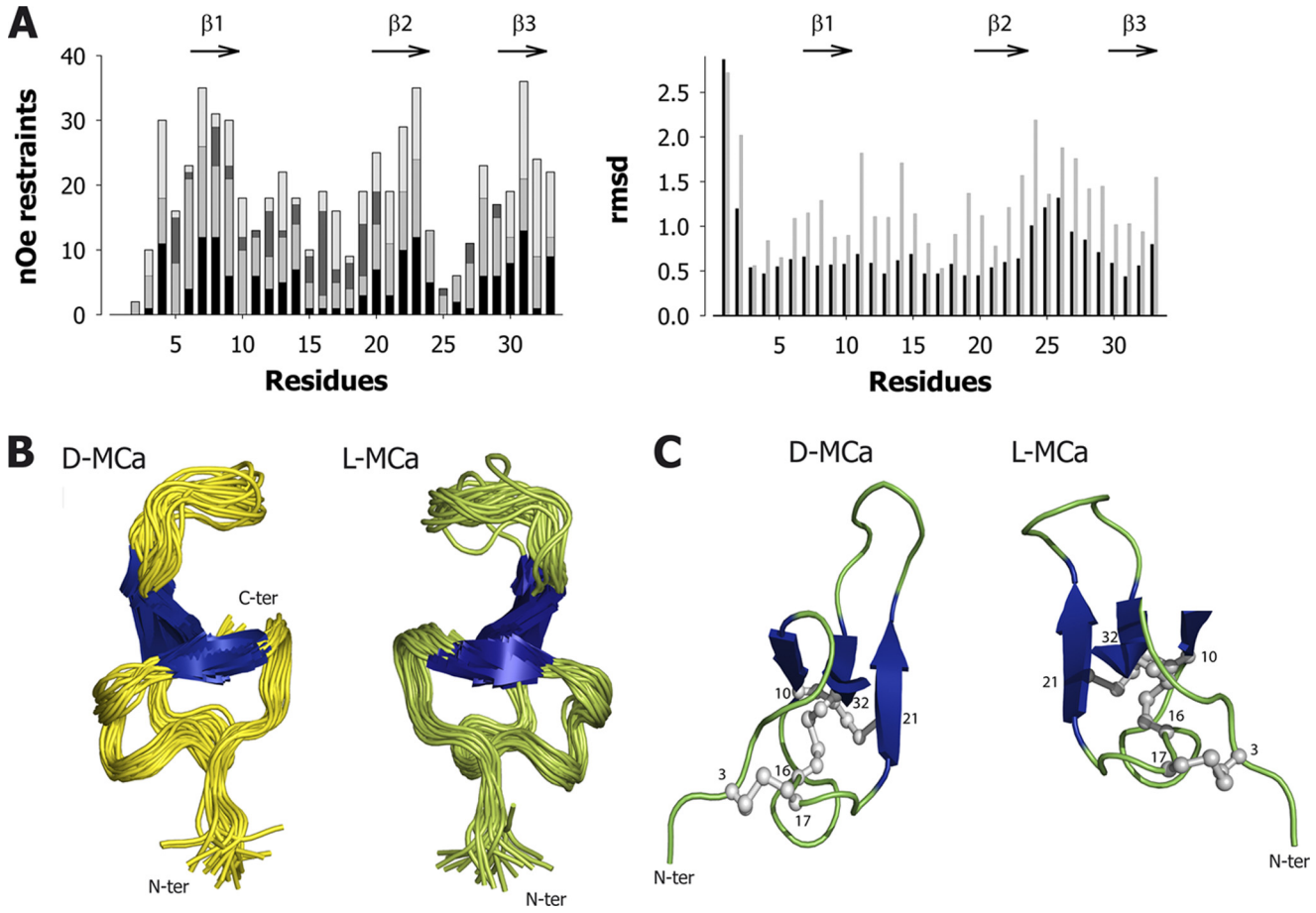

FIGURE 3. **^{1}H NMR three-dimensional structure of D-MCa in solution.** *A*, *left*, plot of the number of intraresidue (*black*), sequential (*medium gray*), medium (*dark gray*), and long range (*light gray*) nOe. The restraints were classified by Wüthrich's method. *Right*, local value of r.m.s. deviation (in Å) calculated on backbone atoms in *black* and in *gray* on all heavy atoms except hydrogen. The *arrows* denote β strands. *B*, 20 best D-MCa and L-MCa structures (only backbone atoms are displayed) superimposed for best fit. β strands are depicted in *blue*. *N-ter* and *C-ter*, N- and C-terminal extremity, respectively. *C*, *ribbon drawing* of the averaged D-MCa structure, compared with the L-MCa structure. The β strands, Cα backbone traces, and disulfide bridges are shown in *blue*, *green*, and *gray*, respectively. The disulfide bridges are shown in *ball-and-stick representations*. The six half-cystine residues are *numbered* according to their positions in the MCa amino acid sequence.

up to 1 μM (Fig. 5*A*). We have repeatedly illustrated that L-MCa triggers Ca^{2+} release from purified heavy SR vesicles (11, 35, 36). Under similar experimental conditions, heavy SR vesicles, initially loaded with Ca^{2+}, did not respond to an extravesicular application of 1 μM D-MCa. In contrast, when this application was followed by an application of a much lower concentration of L-MCa (60 nM), a massive Ca^{2+} release was observed (Fig. 5*B*). Altogether, these data argue that D-MCa, although a mirror structure of L-MCa, is totally pharmacologically inert with regard to RyR channel activation.

Labeling of D-MCa by FAM and Cell Penetration Properties—To investigate the cell penetration properties of D-MCa, it was first covalently coupled to FAM using a peptide bond at the N terminus of the peptide (Fig. 6*A*). FAM is represented here by two isomers that may differ slightly in hydrophobicity during HPLC purification. After synthesis, FAM-D-MCa was purified by reversed phase C18 HPLC. As shown, the purified folded/oxidized FAM-D-MCa differs significantly from D-MCa in elution time, suggesting that the resulting cargo-vector chimera was more hydrophobic than the vector itself (Fig. 6*B*). MS analysis of pure folded/oxidized FAM-D-MCa provides an experimental molecular mass $(M + H)^+$ of 4215.8 Da, confirming the correct assembly of the cargo-vector chimera molecule (Fig. 6*B*, *inset*). Next, we investigated whether FAM-D-MCa could penetrate into live CHO cells. 1 μM FAM-D-MCa was incubated for 2 h with live CHO cells, labeled for plasma membrane with concanavalin A-rhodamine, and examined immediately by confocal microscopy. As shown, FAM-D-MCa was present in all cells, but the distribution was variable from cell to cell (Fig. 6*C*). This distribution was fully comparable with the distribution observed for FAM-L-MCa, synthesized according to the same principles as FAM-D-MCa (synthesis not described here). These data indicate that D-MCa preserves the cell penetration properties of L-MCa. Confocal images further suggest that the labeling of D-MCa-FAM is intracellular rather than membranous. To reinforce this observation, we analyzed how much of the D-MCa-FAM colocalized with the plasma membrane staining (Fig. 6*D*). As shown, a very small fraction of the D-MCa-FAM was colocalized with concanavalin A-rhodamin staining (6.2% of total FAM-colored pixels).

In many cells, D-MCa-FAM penetration results in a mixed distribution (cytoplasm in addition to a punctuate distribution). These coincident distributions have been interpreted as evidence that two mechanisms of cell penetration of FAM-D-

TABLE 2
Structural statistics of the 20 best D-MCa structures

Parameters	Values
Restraint information[a]	
nOe-derived distance restraints	390
Intraresidual (i, i)	158
Sequential (i, $i+1$)	116
Medium range ($2 < \|i-j\| < 4$)	36
Long range ($\|i-j\| > 5$)	80
Hydrogen bonds	12
Pairwise cartesian r.m.s. deviation (Å)	
Backbone atoms[b] (C, Cα, N)	0.41 ± 0.09
All heavy atoms[b]	1.33 ± 0.22
Average r.m.s. *Z*-score deviation from current reliable structures[c]	
Bond lengths (Å)	0.76 ± 0.05
Bond angles (degrees)	0.83 ± 0.05
Average r.m.s. deviation from experimental restraints	
Distance restraints (Å)	$9.5 \times 10^{-3} \pm 0.3 \times 10^{-3}$
Energies (kcal/M)	
Total	−176.074
nOe	2.06
Ramachandran quality paramaters (%)	
Favored regions	73.8
Allowed regions	21.90
Additionally allowed regions	3.80
Disallowed regions	0.5

[a] No nOe restraint was violated by more than 0.1 Å.
[b] Residues involved in secondary structure elements: 8–10, 20–23, and 30–32.
[c] Values based on Whatif analysis.

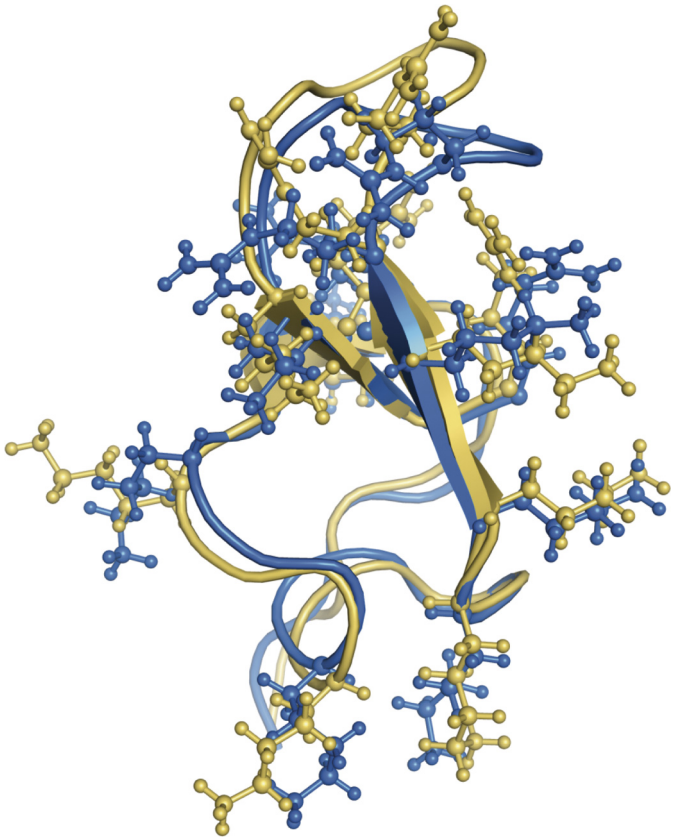

FIGURE 4. **Superimposition of L-MCa (in *blue*) with D-MCa drawn in the L-configuration (*yellow*).** To achieve this inversion, the Protein Data Bank file of D-MCa was modified. Lateral chains of seven Lys and four Arg residues are also shown.

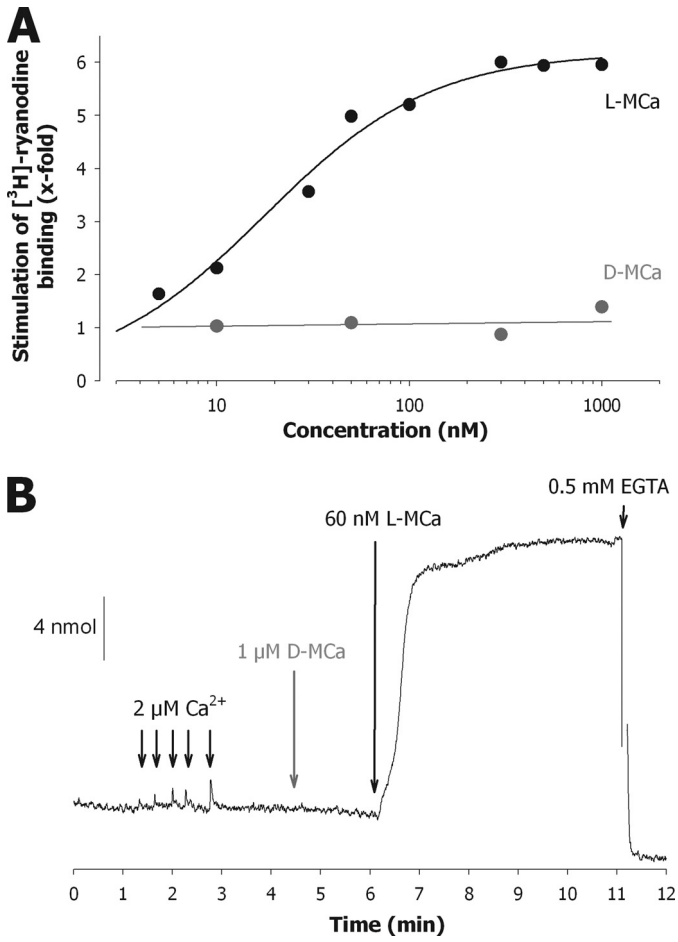

FIGURE 5. **D-MCa lacks pharmacological activity.** *A*, [^{3}H]ryanodine binding on heavy SR vesicles was measured in the presence of various concentrations of L-MCa (*black filled symbols*) or D-MCa (*red filled symbols*). [^{3}H]ryanodine binding was measured at *p*Ca 5 in the presence of 10 nM [^{3}H]ryanodine for 2.5 h at 37 °C. Nonspecific binding was constant at all MCa concentrations and in all cases represented less than 8% of total binding. Data for L-MCa were fitted with a sigmoid function, $y = y_0 + (a/(1 + x^b/c^b))$, where $y_0 = 0.06$ at MCa = 0 nM, $a = 6.2$ is the maximal binding stimulation factor over basal value, $b = -1$ is the slope coefficient, and $c = 17.8$ nM is the EC_{50} for L-MCa effect. D-MCa is without effect on [^{3}H]ryanodine binding. *B*, effect of D-MCa and L-MCa on Ca^{2+} release from heavy SR vesicles. Heavy SR vesicles were actively loaded with Ca^{2+} by five sequential additions of 2 µM Ca^{2+} in the monitoring chamber. The addition of 1 µM D-MCa has no effect on Ca^{2+} release, whereas a subsequent application of 60 nM L-MCa produces a massive sustained Ca^{2+} release. Application of 0.5 mM EGTA chelates the released Ca^{2+} and lowers the absorbance.

MCa coexist, translocation for cytoplasm distribution and a form of endocytosis for endosomal punctuate distribution, as evidenced in earlier studies (14, 15, 37). The use of either one of these two entry pathways is possibly under the influence of the nature and size of the cargo. Therefore, we reinvestigated the nature of FAM-D-MCa cell entry by using various inhibitors of the endocytosis route (Fig. 7). LysoTracker red stains endosomal structures. As shown, 73.5% of endosomal structures were also positive for FAM-D-MCa (Fig. 7, *A* and *B*). In addition, a significant fraction of FAM-D-MCa staining (55.4%) was endosome-negative, suggesting the coexistence of two types of cell distributions (more than half not related to endosomes and less than half endosomal). These ratios between both distributions differ from the one observed using fluorescent streptavidine as cargo. With streptavidine, we have shown that the macropinocytosis inhibitor, amiloride, blocks 80% of cell entry (14). Here, we quantified by fluorescence-activated cell sorting (FACS) the effects of nocodazole (microtubule formation inhibitor),

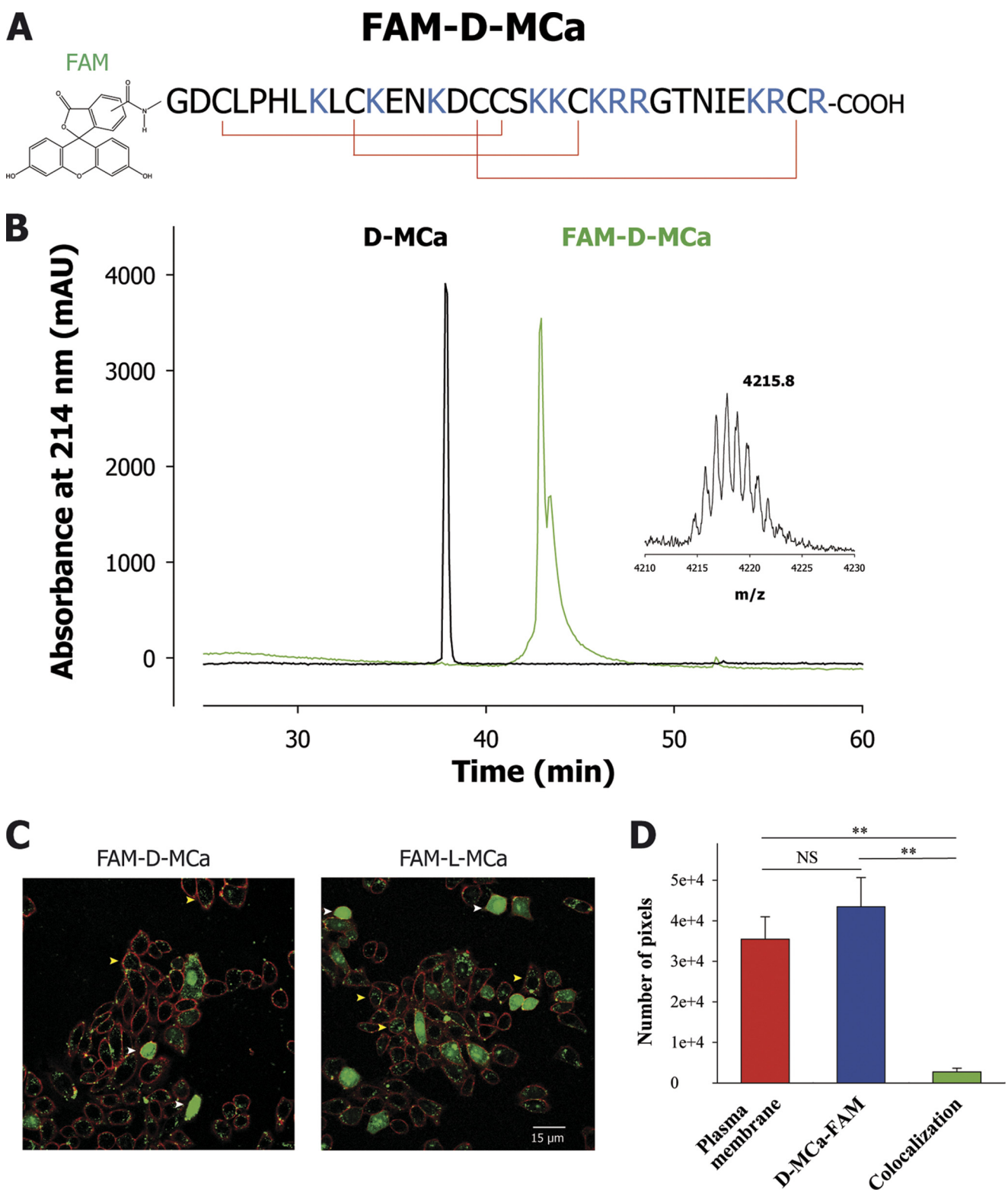

FIGURE 6. **D-MCa is comparable with L-MCa for cell penetration.** *A*, primary structure of FAM-D-MCa. 5(6)-carboxyfluorescein was coupled to D-MCa by a peptidic bond at the N terminus of the peptide. *B*, analytical C_{18} reversed phase HPLC profile of folded/oxidized D-MCa (*black line*) and of folded/oxidized FAM-D-MCa (*green line*). The rightward shift of the elution time for FAM-D-MCa is due to the hydrophobicity of FAM. The peak comes out as a doublet because of the presence of two isomers of FAM. *C*, confocal microscopy images comparing cell penetration of FAM-D-MCa with that of FAM-L-MCa (*green labeling*). Plasma membranes are labeled with concanavalin A-rhodamine (in *red*). *White arrows* denote diffuse cytoplasmic and nuclear distribution of FAM-D-MCa and FAM-L-MCa, whereas *yellow arrows* illustrate a predominant punctuate distribution of the peptides. CHO cells were incubated for 2 h with a 10 μM peptide concentration. *D*, average number of *colored pixels* per image for plasma membrane and FAM-D-MCa staining. The average number of *bicolored pixels* is also provided. $n = 3$ experiments, pixel quantification on 20 visual fields (×40 objective), average labeled pixels for 10 visual fields on one representative experiment. *NS*, nonsignificant; **, $p \leq 0.01$.

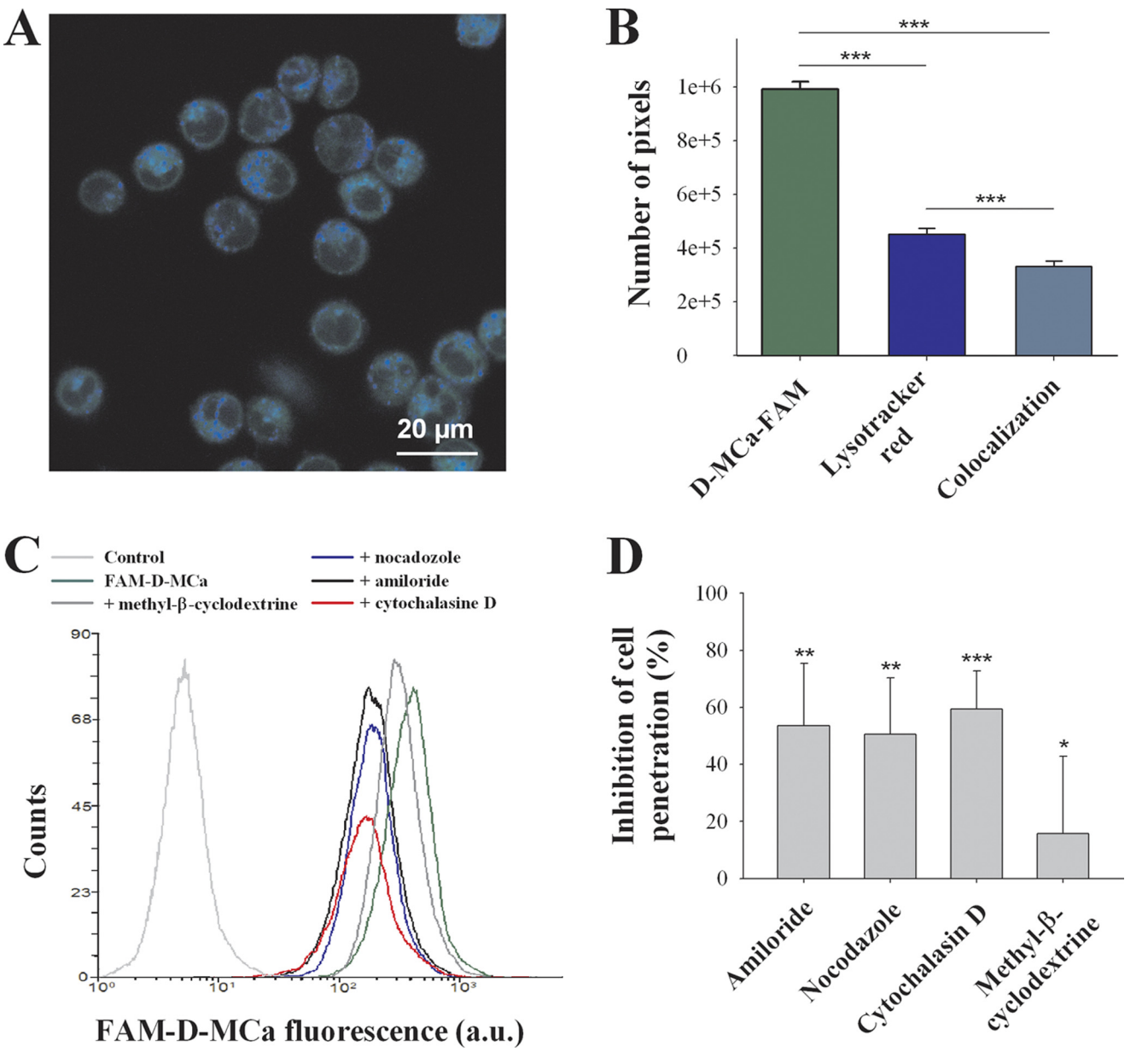

FIGURE 7. **Mode of cell penetration of FAM-D-MCa.** *A*, confocal microscopy image of CHO cells showing the intracellular distribution of FAM-D-MCa (in *green*) and LysoTracker red DND-99 (in *blue*, *pseudocolor*). Experimental conditions were as follows. Cells were incubated 2 h with 1 μM FAM-D-MCa and 20 min with 50 nM LysoTracker red DND-99 before confocal acquisition. *B*, average number of *colored pixels* per image for LysoTracker red DND-99 and FAM-D-MCa staining. The average number of *bicolored pixels* is also provided. $n = 3$ experiments, pixel quantification on 14 visual fields (×40 objective), average labeled pixels for 10 visual fields on one representative experiment. **, $p \leq 0.001$. *C*, representative example of FACS histograms for FAM-D-MCa cell penetration in the absence of any drug or in the presence of 1 mM amiloride, 5 μM cytochalasin D, 5 mM nocodazole, or 5 mM methyl-β-cyclodextrin. All of these drugs were also preincubated for 30 min with CHO cells before the addition of 1 μM FAM-D-MCa. *D*, average inhibition of FAM-D-MCa cell penetration by endocytosis-inhibiting drugs as calculated from FACS experiments. $n = 3$ experiments; *, $p \leq 0.05$; **, $p \leq 0.01$; ***, $p \leq 0.001$.

cytochalasin D (F-actin elongation inhibitor), methyl-β-cyclodextrin (lipid raft-dependent endocytosis inhibitor by cholesterol depletion), and amiloride (macropinocytosis inhibitor) on the cell penetration of FAM-D-MCa. As expected if endocytosis is involved in cell penetration of FAM-D-MCa, disturbing the microtubule or actin filament system with nocodazole or cytochalasin D induces a 50.5 ± 19.8 or 59.3 ± 13.4% inhibition of cell entry (Fig. 7, *C* and *D*). Amiloride inhibited cell entry of FAM-D-MCa by 53.4 ± 22%, which is less than when streptavidine is used as cargo. Interestingly, methyl-β-cyclodextrin, which inhibits lipid raft-dependent endocytosis, also inhibits mildly the cell penetration of FAM-D-MCa (by 15.8 ± 27%), which was not observed for streptavidine as cargo (14). This result indicates that macropinocytosis remains the major mode of FAM-D-MCa cell penetration by endocytosis. These data also show that the nature of cargo influences to what extent endocytosis is used over cell translocation for cell penetration. In particular, with a small cargo, such as FAM, a significant fraction of the peptide is susceptible to enter through membrane translocation even if endocytosis is a major route of cell entry.

D-MCa Is a Non-toxic Cell-penetrating Peptide of Similar Efficacy as L-MCa—Using FACS, we also compared the dose-response curve of the cell entry of FAM-D-MCa with that of FAM-L-MCa. CHO cells were incubated with various concen-

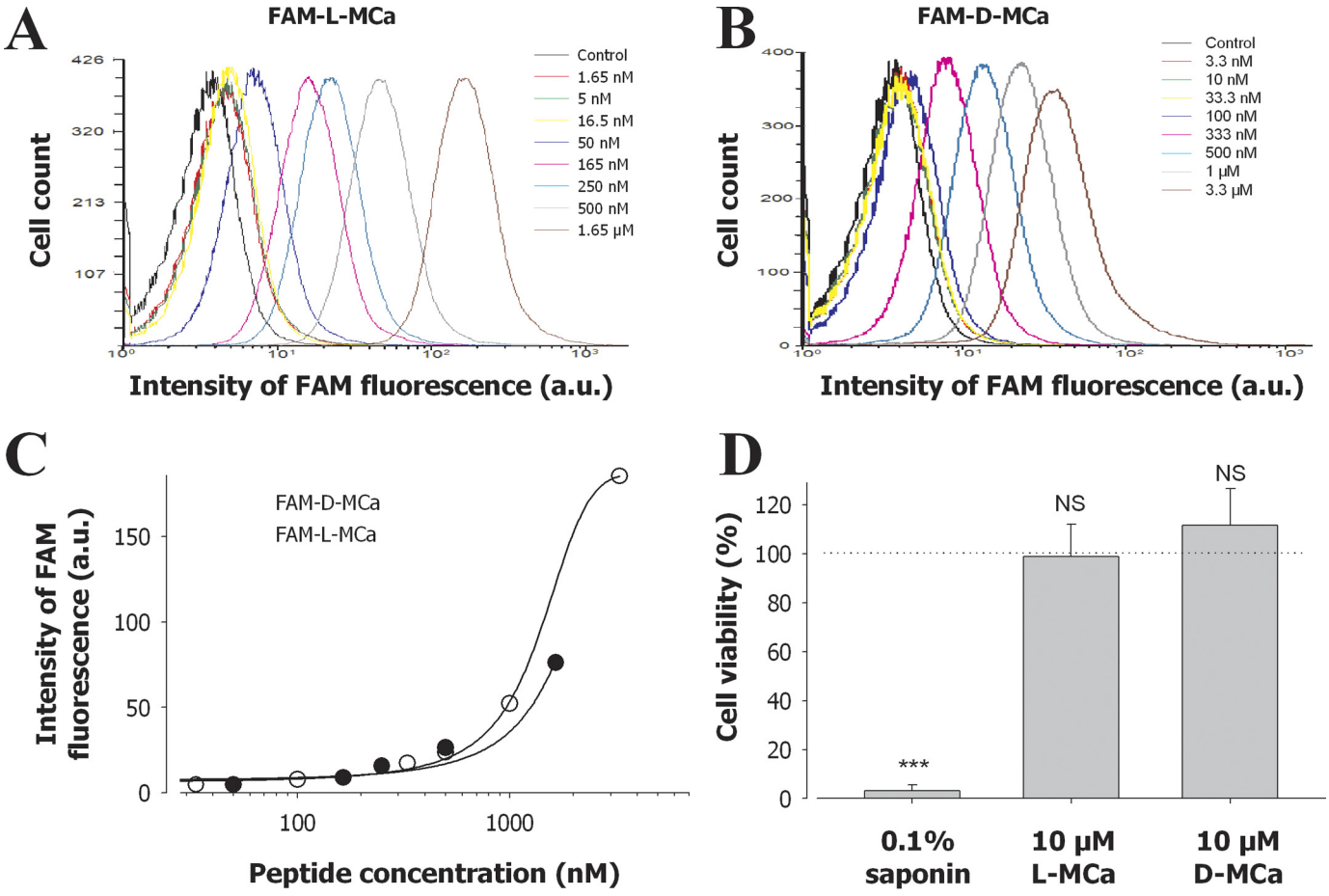

FIGURE 8. **Dose-dependent cell penetration of FAM-D-MCa and FAM-L-MCa and lack of cell toxicity.** *A*, FACS histograms for each FAM-D-MCa concentration. Cell penetration time was 2 h, and cells were gated immediately after cell detachment by trypsin treatment. 50,000 events were gated by FACS for each concentration. *B*, FACS histograms for FAM-L-MCa performed in similar conditions as for FAM-D-MCa. *C*, mean cell fluorescence as a function of FAM-D-MCa (*open symbols*) or FAM-L-MCa (*filled symbols*) concentration. Data were fitted with a sigmoid function $y = a/(1 + \exp(-(x/x_0)/b))$, where $a = 187$ (FAM-D-MCa) or 175 (FAM-L-MCa) maximal arbitrary fluorescence units; $x_0 = 1384$ nM (FAM-D-MCa) or 1783 nM (FAM-L-MCa), the concentration of half-maximal cell penetration; and $b = 417$ (FAM-D-MCa) or 576 (FAM-L-MCa). *D*, cell viability as assessed by the MTT test. 0.1% saponin, 10 μM L-MCa, or 10 μM D-MCa was incubated for 24 h with CHO cells in culture. $n = 3$ experiments, triplicates; *NS*, nonsignificant; ***, $p \leq 0.001$.

trations of FAM-D-MCa for 2 h, and cells were treated with trypsin for plastic support detachment and immediately evaluated for fluorescence intensity by FACS. As shown, the cell penetration of FAM-D-MCa is dose-dependent, with a positive signal starting at 100 nM and signals still increasing at a concentration of 3.3 μM (Fig. 8*A*). The dose-dependent cell penetration of FAM-L-MCa was identical to that of FAM-D-MCa at all concentrations tested (Fig. 8*B*). The average fluorescence of each CPP-cargo complex was plotted as a function of concentration (Fig. 8*C*). As shown, FAM-D-MCa penetrates with the same dose dependence as FAM-L-MCa. Concentrations required for half-maximal cell penetration were 1.38 and 1.78 μM for FAM-D-MCa and FAM-L-MCa, respectively. Finally, a good CPP is also one that presents no cell toxicity. Both D-MCa and L-MCa were evaluated for their toxic effects by incubation with CHO cells for 24 h. As shown, both peptides had no toxic effects at concentrations of 10 μM, contrary to 0.1% saponin (Fig. 8*D*).

DISCUSSION

MCa is one additional member of the exponentially growing list of reported CPP. It is, however, one of the rare CPP that is fully natural and that presents such a well defined three-dimensional structure. However, because of its intrinsic pharmacological properties, it requires the design of new analogues that take advantage of its peculiar cell penetrating efficacy without the drawback of its activity. One design strategy, based on the replacement of cysteine residues by 2-aminobutyric acid residues and the consequent loss of secondary structure, led to the successful production of a pharmacologically inert but potent cell-penetrating MCa analogue. This strategy, however, eliminated some of the MCa features that distinguish it from other classical CPP. In particular, this analogue is no longer folded, and it loses some of its cell penetrating efficacy. The present strategy, consisting of successfully producing D-MCa, was aimed to circumvent both of these drawbacks. In addition, the use of D-amino acids renders the peptide resistant to protease action, making it a particularly useful vector for *in vivo* applications. Although several natural toxin/peptides are known to contain D-amino acids, such as several conopeptides (38–40), none have a primary structure based on the sole use of D-amino acids. The presence of such amino acids in the sequence has been linked to toxin activity. In r11a, a 46-amino acid I_1-conotoxin (41), has a phenylalanine at position 44, which undergoes epimerization from an L-Phe to a D-Phe, a transition linked to a

dramatic gain in pharmacological activity (39). Similarly, isomerization of L-Phe to D-Phe also enhanced biological activity of conomap-Vt, a linear peptide from *Conus vitulinus* (40). The complete chemical synthesis of a toxin with only D-amino acids has been seldom reported. In one pioneering work, Di Luccio *et al.* (42) reported the chemical synthesis of D-maurotoxin, a four-disulfide-bridged toxin active on potassium channels. Interestingly, the kinetic features of the *in vitro* oxidation/folding of D-maurotoxin are indistinguishable from those of L-maurotoxin. In contrast, the effects of PDI (which catalyzes breakage and reformation of disulfide bridges) and PPIase (which controls isomerization between the cis and trans configurations of prolyl imidic peptide bonds) on *in vitro* oxidation/folding of maurotoxin were stereo-selective. In another example, the 35-amino acid residue sea anemone ShK toxin that blocks potassium channels was also synthesized with amino acids that have a D-configuration at α-carbon (43). This peptide also folded as a mirror image of L-ShK. Curiously, pharmacological experiments and docking simulation analyses indicate that D-ShK has the ability to recognize and block $K_v1.3$ channels, albeit with a reduced affinity. This may occur because of the 4-fold symmetry of $K_v1.3$ channels and because of the compact set of interactions taking place (Lys^{22} filling in the ion selectivity filter and Arg^{24} and Arg^{29} interacting with His^{404} of the channel). In another example of a violation of the traditional lock-and-key model of ligand-target interaction, it was found that the D-enantiomer of GsMTx4, a peptide of the venom of tarantula *Grammostola spatulata*, remained active on stretch-activated cation channels (44). This effect is proposed to occur through local bilayer thinning without requiring a physical contact with the channel. In the case of MCa, we found that producing this CPP with D-amino acids also does not interfere with its folding and with the correct formation of disulfide bridges. The disulfide bridge pattern could not be assessed as usual (*i.e.* by limited trypsin digestion of the folded/oxidized peptide followed by MS analyses). In contrast, we confirmed the correct folding and disulfide bridge organization through ^1H NMR. This approach demonstrated that D-MCa is a mirror structure of L-MCa still displaying a significant basic face. D-MCa is a diastereomer rather than an enantiomer because only C_α are in the D-configuration. It is only for Thr^{26} and Ile^{28} that the side chain configurations differ from the exact mirror images. However, the different stereochemistry of the Thr and Ile side chains in D-MCa relative to the backbone did not cause any significant perturbations in the structure. Importantly enough, we observed that D-MCa was completely pharmacologically inert, indicating that the lock-and-key concept for the interaction of L-MCa with RyR is well preserved. Also, despite the affinity of MCa for negatively charged lipids of the plasma membrane (13), this finding also argues for a direct protein interaction of L-MCa with RyR in agreement with the cytoplasmic localization of the MCa binding site identified on RyR (12). Amazingly enough, D-MCa would therefore be the first example of a diastereomer toxin inactive on its pharmacological target. We also found that D-MCa keeps its ability to penetrate into cells, making this toxin the first known example of a folded/oxidized D-CPP. Because D-MCa appears to penetrate as well as L-MCa but also presents cytoplasmic localization, a sign of membrane translocation, these data indicate that MCa/lipid interactions are conformation-insensitive. This was expected already from the finding that unfolded MCa, in which cysteine residues were replaced by 2-aminobutyric acid residues, also penetrated efficiently in cells and also targeted associated cargoes to the cytoplasm (15). Besides cytoplasmic localization, both FAM-L-MCa and FAM-D-MCa also enter through endocytosis and end up in endosomal structures, albeit to a lesser extent than with streptavidine as cargo instead of FAM. These findings argue also that endocytosis remains a major contributor of the cell entry of MCa. We conclude that D-MCa is a competitive pharmacologically inert CPP that has the added advantage of being protease-resistant. It should also not be recognized by the immune system because it is probably resistant to proteolytic processing by T cells for presentation on major histocompatibility complexes. The maintained cell penetrating efficacy of this peptide should make it an ideal vector for *in vivo* applications.

Acknowledgments—We thank Cédric Bernard for help in solving the D-MCa structure and Eric Denarier for image analysis. Mass spectrometry analyses were performed by the Centre d'Investigation Clinique of Grenoble under the direction of Dr. Michel Sève.

REFERENCES

1. Lindgren, M., Hällbrink, M., Prochiantz, A., and Langel, U. (2000) *Trends Pharmacol. Sci.* **21,** 99–103
2. Zorko, M., and Langel, U. (2005) *Adv. Drug Deliv. Rev.* **57,** 529–545
3. Pooga, M., Hällbrink, M., Zorko, M., and Langel, U. (1998) *FASEB J.* **12,** 67–77
4. Derossi, D., Chassaing, G., and Prochiantz, A. (1998) *Trends Cell Biol.* **8,** 84–87
5. Mäe, M., and Langel, U. (2006) *Curr. Opin. Pharmacol.* **6,** 509–514
6. Pooga, M., Soomets, U., Hällbrink, M., Valkna, A., Saar, K., Rezaei, K., Kahl, U., Hao, J. X., Xu, X. J., Wiesenfeld-Hallin, Z., Hökfelt, T., Bartfai, T., and Langel, U. (1998) *Nat. Biotechnol.* **16,** 857–861
7. Rhee, M., and Davis, P. (2006) *J. Biol. Chem.* **281,** 1233–1240
8. Patel, L. N., Zaro, J. L., and Shen, W. C. (2007) *Pharm. Res.* **24,** 1977–1992
9. Oehlke, J., Scheller, A., Wiesner, B., Krause, E., Beyermann, M., Klauschenz, E., Melzig, M., and Bienert, M. (1998) *Biochim. Biophys. Acta.* **1414,** 127–139
10. Fajloun, Z., Kharrat, R., Chen, L., Lecomte, C., Di Luccio, E., Bichet, D., El Ayeb, M., Rochat, H., Allen, P. D., Pessah, I. N., De Waard, M., and Sabatier, J. M. (2000) *FEBS Lett.* **469,** 179–185
11. Estève, E., Smida-Rezgui, S., Sarkozi, S., Szegedi, C., Regaya, I., Chen, L., Altafaj, X., Rochat, H., Allen, P., Pessah, I. N., Marty, I., Sabatier, J. M., Jona, I., De Waard, M., and Ronjat, M. (2003) *J. Biol. Chem.* **278,** 37822–37831
12. Altafaj, X., Cheng, W., Estève, E., Urbani, J., Grunwald, D., Sabatier, J. M., Coronado, R., De Waard, M., and Ronjat, M. (2005) *J. Biol. Chem.* **280,** 4013–4016
13. Mabrouk, K., Ram, N., Boisseau, S., Strappazzon, F., Rehaim, A., Sadoul, R., Darbon, H., Ronjat, M., and De Waard, M. (2007) *Biochim. Biophys. Acta* **1768,** 2528–2540
14. Ram, N., Aroui, S., Jaumain, E., Bichraoui, H., Mabrouk, K., Ronjat, M., Lortat-Jacob, H., and De Waard, M. (2008) *J. Biol. Chem.* **283,** 24274–24284
15. Ram, N., Weiss, N., Texier-Nogues, I., Aroui, S., Andreotti, N., Pirollet, F., Ronjat, M., Sabatier, J. M., Darbon, H., Jacquemond, V., and De Waard, M. (2008) *J. Biol. Chem.* **283,** 27048–27056
16. Merrifield, R. B. (1969) *Adv Enzymol. Relat. Areas Mol. Biol.* **32,** 221–296
17. Hwang, T. L., and Shaka, J. (1995) *Magn. Reson. Ser. A* **112,** 275–279
18. Marion, D., Ikuto, M., Tschudin, R., and Bax, A. (1989) *J. Mag. Res.* **85,** 393–399

19. Marion, D., and Wüthrich, K. (1983) *Biochem. Biophys. Res. Commun.* **113,** 967–974
20. Delaglio, F., Grzesiek, S., Vuister, G. W., Zhu, G., Pfeifer, J., and Bax, A. (1995) *J. Biomol. NMR* **6,** 277–293
21. Wüthrich, K. (1986) *NMR of Proteins and Nucleic Acids*, pp. 1–93, John Wiley & Sons, Inc., New York
22. Johnson, B. A., and Blevins, R. A. (1994) *J. Biomol. NMR* **4,** 603–614
23. Herrmann, T., Güntert, P., and Wüthrich, K. (2002) *J. Mol. Biol.* **319,** 209–227
24. Güntert, P., Mumenthaler, C., and Wüthrich, K. (1997) *J. Mol. Biol.* **273,** 283–298
25. Vranken, W. F., Boucher, W., Stevens, T. J., Fogh, R. H., Pajon, A., Llinas, M., Ulrich, E. L., Markley, J. L., Ionides, J., and Laue, E. D. (2005) *Proteins* **59,** 687–696
26. Linge, J. P., Williams, M. A., Spronk, C. A., Bonvin, A. M., and Nilges, M. (2003) *Proteins* **50,** 496–506
27. Nabuurs, S. B., Nederveen, A. J., Vranken, W., Doreleijers, J. F., Bonvin, A. M., Vuister, G. W., Vriend, G., and Spronk, C. A. (2004) *Proteins* **55,** 483–486
28. Schwieters, C. D., Kuszewski, J. J., Tjandra, N., and Clore, G. M. (2003) *J. Magn. Reson.* **160,** 65–73
29. Laskowski, R. A., Rullmannn, J. A., MacArthur, M. W., Kaptein, R., and Thornton, J. M. (1996) *J. Biomol. NMR* **8,** 477–486
30. Vriend, G. (1990) *J. Mol. Graph* **8,** 52–56
31. Kim, D. H., Ohnishi, S. T., and Ikemoto, N. (1983) *J. Biol. Chem.* **258,** 9662–9668
32. Mosbah, A., Kharrat, R., Fajloun, Z., Renisio, J. G., Blanc, E., Sabatier, J. M., El Ayeb, M., and Darbon, H. (2000) *Proteins* **40,** 436–442
33. Pallaghy, P. K., Nielsen, K. J., Craik, D. J., and Norton, R. S. (1994) *Protein Sci.* **3,** 1833–1839
34. Lukács, B., Sztretye, M., Almássy, J., Sárközi, S., Dienes, B., Mabrouk, K., Simut, C., Szabó, L., Szentesi, P., De Waard, M., Ronjat, M., Jóna, I., and Csernoch, L. (2008) *Biophys. J.* **95,** 3497–3509
35. Chen, L., Estève, E., Sabatier, J. M., Ronjat, M., De Waard, M., Allen, P. D., and Pessah, I. N. (2003) *J. Biol. Chem.* **278,** 16095–16106
36. Estève, E., Mabrouk, K., Dupuis, A., Smida-Rezgui, S., Altafaj, X., Grunwald, D., Platel, J. C., Andreotti, N., Marty, I., Sabatier, J. M., Ronjat, M., and De Waard, M. (2005) *J. Biol. Chem.* **280,** 12833–12839
37. Boisseau, S., Mabrouk, K., Ram, N., Garmy, N., Collin, V., Tadmouri, A., Mikati, M., Sabatier, J. M., Ronjat, M., Fantini, J., and De Waard, M. (2006) *Biochim. Biophys. Acta* **1758,** 308–319
38. Huang, F., and Du, W. (2009) *Toxicon* **54,** 153–160
39. Buczek, O., Yoshikami, D., Bulaj, G., Jimenez, E. C., and Olivera, B. M. (2005) *J. Biol. Chem.* **280,** 4247–4253
40. Dutertre, S., Lumsden, N. G., Alewood, P. F., and Lewis, R. J. (2006) *FEBS Lett.* **580,** 3860–3866
41. Buczek, O., Jimenez, E. C., Yoshikami, D., Imperial, J. S., Watkins, M., Morrison, A., and Olivera, B. M. (2008) *Toxicon* **51,** 218–229
42. di Luccio, E., Azulay, D. O., Regaya, I., Fajloun, Z., Sandoz, G., Mansuelle, P., Kharrat, R., Fathallah, M., Carrega, L., Estève, E., Rochat, H., De Waard, M., and Sabatier, J. M. (2001) *Biochem. J.* **358,** 681–692
43. Beeton, C., Smith, B. J., Sabo, J. K., Crossley, G., Nugent, D., Khaytin, I., Chi, V., Chandy, K. G., Pennington, M. W., and Norton, R. S. (2008) *J. Biol. Chem.* **283,** 988–997
44. Suchyna, T. M., Tape, S. E., Koeppe, R. E., 2nd, Andersen, O. S., Sachs, F., and Gottlieb, P. A. (2004) *Nature* **430,** 235–240

b. Conclusion

Le nouvel analogue de la MCa, la D-MCa a répondu à toutes les attentes espérées. La D-MCa a conservé ses trois ponts disulfures selon le même schéma que la L-MCa et est l'image miroir parfaite de la L-MCa. Les acides aminés basiques sont toujours regroupés sur la même face de la molécule, ce qui implique que les propriétés de pénétration cellulaire ne devraient pas être altérées, cependant, du fait de son inversion géométrique, le RyR ne reconnait pas ce nouvel analogue.

L'incubation *in vitro* de la D-MCa avec de la trypsine ou de l'endoprotéinase Asp-N, suivie d'une analyse par chromatographie liquide a permis de constater que la D-MCa était totalement résistante à ces enzymes, alors que la L-MCa était significativement dégradée. Ce résultat prouve que la D-MCa possède un sérieux avantage sur la L-MCa pour des éventuelles applications *in vivo*.

L'ouverture du canal par la L-MCa peut être mesurée par le relâchement de calcium dans des vésicules de réticulum sarcoplasmique et par la conversion d'un faible site d'affinité pour la ryanodine à un fort site d'affinité (Esteve, Smida-Rezgui et al. 2003). Les effets de la D-MCa ont été testés sur ces deux modèles. Alors que la L-MCa augmente l'affinité de la [^{3}H]-ryanodine, la D-MCa n'a aucun effet sur ce paramètre. De la même manière, une application de 1 µM de D-MCa sur des vésicules de réticulums sarcoplasmique préalablement chargés en calcium, n'a provoqué aucun relarguage de calcium, alors qu'une mise en contact avec 60 nM de L-MCa a induit un flux massif. Ces résultats confirment donc totalement la perte d'activité pharmacologique de la D-MCa.

Les L-MCa et D-MCa ont été couplées à un fluorochrome pour juger des facultés de pénétration cellulaire, la carboxy fluorescéine (FAM). Deux techniques ont été utilisées, la microscopie confocale pour apprécier la localisation des deux formes de MCa, et une analyse par cytométrie en flux pour comparer les facultés de la L-MCa et de la D-MCa à pénétrer dans les cellules. L'analyse confocale a permis de confirmer que la D-MCa n'avait pas perdu les propriétés de pénétration cellulaire de la L-MCa et est distribuée dans les cellules de façon similaire à la L-MCa. Une mesure de co-localisation a permis de constater qu'une petite fraction de la D-MCa était co-localisée avec la concanavaline A Rhodamine marquant la membrane plasmique. La D-MCa semble rentrer par deux voies distinctes (distribution diffuse

et ponctiforme), ce qui a été confirmé avec l'utilisation de différents inhibiteurs d'endocytose et de marqueurs de vésicules endosomales. L'analyse par cytométrie en flux nous donne la preuve que la D-MCa, n'a pas diminué en efficacité de pénétration cellulaire par rapport à la L-MCa.

Nous sommes donc parvenu à synthétiser un analogue de l a MCa qui ne conservait que ses qualités, la D-MCa. Cet analogue a conservé la faculté de la MCa à agir comme CPP, mais à perdu ses propriétés pharmacologiques. De plus ce nouvel analogue est résistant aux enzymes, contrairement à la MCa, et de plus n'est pas cytotoxique.

3. Article 2

Mini cell penetrating peptides derived from the scorpion toxin maurocalcine

Cathy Poillot, Hicham Bichraoui, Michel De Waard

Article en cours de soumission

a. Introduction

Comme nous l'avons vu dans l'article précédent, la maurocalcine (MCa) possède des qualités en tant que peptide de pénétration cellulaire (CPP pour Cell Penetrating Peptide) que les autres membres de cette famille ne possèdent pas tous. En effet, la MCa est structurée selon un motif « inhibitor Cystine Knot » avec trois ponts disulfures connectés selon le modèle suivant, Cys^1-Cys^4, Cys^2-Cys^5 et Cys^3-Cys^6 (Mosbah, Kharrat et al. 2000). Cependant, du fait de sa taille (33 acides aminés) et de la présence de trois ponts disulfures, la synthèse de la MCa est relativement complexe par rapport aux autres CPP et nécessiterait des simplifications. De plus, l'utilisation de peptides structurés avec des ponts disulfures, malgré l'avantage en terme de stabilité *in vivo*, rend les couplages chimiques avec les cargos difficiles. En effet, il est complexe d'ajouter lors de la synthèse un résidu cystéine surnuméraire à la séquence, sans interférer avec le processus correct de repliement et de formation des ponts disulfures.

Une stratégie à été testée en ce sens et a consisté en la synthèse d'un analogue de la MCa ou les résidus cystéines ont été remplacés par des groupements acides 2-aminobutyrique (Ram, Weiss et al. 2008). Ce nouvel analogue, nommé C-MCa_{UF1-33} (C- car un résidu cystéine à été ajouté, UF pour unfolded et 1-33 pour sa longueur) a toujours une séquence de 33 acides aminés, mais du fait de la perte des thiols sur des résidus cystéines, il est linéaire. Bien que ce peptide pénètre dans les cellules, il est moins efficace que la MCa structurée, ce qui suggère que des améliorations peuvent être faites à cet analogue.

Nous avons donc voulu mettre au point de nouveaux analogues de la MCa, plus efficaces que le précédent avec les trois critères suivants. Premièrement, ces analogues doivent avoir une séquence plus courte que la MCa, deuxièmement, ces peptides doivent être construits de façon à délimiter le domaine de la MCa responsable de la pénétration cellulaire et enfin, ces analogues doivent posséder un résidu cystéine supplémentaire afin de pouvoir coupler un cargo.

SMALL EFFICIENT CELL PENETRATING PEPTIDES DERIVED FROM THE SCORPION TOXIN MAUROCALCINE

From Cathy Poillot[1,2], Hicham Bichraoui[1,2], Michel Ronjat[1,2] & Michel De Waard[1,2,3]

[1]Inserm U836, Grenoble Neuroscience Institute, Site santé Tronche, Chemin Fortuné Ferrini, BP170, 38042 Grenoble Cedex 9, France ; [2]Université Joseph Fourier, Grenoble, France ; [3]Smartox Biotechnologies, Floralis, Biopolis, 5 Avenue du Grand Sablon, 38700 La Tronche, France.

Running head: Small Cell Penetrating Maurocalcine Peptides

Address correspondence to: Dr. Michel De Waard, GIN, Inserm U836, BP170, Grenoble Cedex 09, France. Phone: +(33) 4 56 52 05 63 - Fax: +(33) 4 56 52 06 37 - E-mail: michel.dewaard@ujf-grenoble.fr

Maurocalcine is the first demonstrated example of an animal toxin peptide with efficient cell penetration properties. While it is a highly competitive cell penetrating peptide (CPP), its relatively large size of 33 amino acids and the presence of three internal disulfide bridges may hamper its development for *in vitro* and *in vivo* applications. Here, we demonstrate that several efficient CPP can be derived from maurocalcine by replacing Cys residues by isosteric 2-aminobutyric acid residues and sequence truncation down to peptides of up to 9 residues in length. A surprising finding is that all the truncated maurocalcine analogues possessed cell penetrating properties indicating that the maurocalcine is a highly specialized CPP. Careful examination of the cell penetrating properties of the truncated analogues indicates that several maurocalcine-derived peptides should be of great interest for cell delivery applications where peptide size matters.

Maurocalcine (MCa) is a 33-mer peptide that was initially isolated from the venom of a Tunisian chactid scorpion, *Scorpio maurus palmatus* (1). The toxin belongs to a family of peptide that folds according to an Inhibitor Cystine Knot (ICK motif), and thus contains three disulfide bridges with a Cys^1-Cys^4, Cys^2-Cys^5 and Cys^3-Cys^6 connecting pattern (2). The solution structure, as defined by ^{1}H-NMR, illustrates that MCa contains three β-strands (strand 1 from amino acid residues 9 to 11, strand 2 from 20 to 23, and strand 3 from 30 to 33). One distinctiveness of MCa is the fact that it is greatly enriched in basic amino acid residues. Out of the 33 amino acids that compose MCa, twelve of them are basic, most of them represented by Lys residues. Interestingly, the β-strands of MCa encompass most of the basic domains (see Fig. 1*A*). MCa turned to be of interest to our research group for several reasons. First, it is an exquisite pharmacological activator of the ryanodine receptor type 1 (RyR1) from skeletal muscle since it promotes high Po gating modes and long-lasting subconductance states of the ion channel (3,4). On myotubes, application of MCa rapidly induces Ca^{2+} release from the sarcoplasmic reticulum (SR) (5), a result further confirmed by positive effect of MCa on the release of Ca^{2+} from purified SR vesicles (3,5). The interaction of MCa with RyR1 has been witnessed by increased [^{3}H]-ryanodine binding onto purified RyR1 (3,5). The binding site for MCa on RyR1 has also been mapped and shown to correspond to domain(s) that have a predicted localization within the cytoplasm (6). Second, MCa has a unique sequence homology with the II-III loop of the L-type calcium channel $Ca_V1.1$ subunit over a domain that is slightly larger than the second β-strand of MCa (see Fig. 1*A*) (5). This loop is heavily involved in excitation-contraction coupling through direct molecular interactions with RyR1 (6,7). This homology turns out to be of tremendous help for understanding how L-type channels are involved in excitation-contraction coupling (4,7,8). Third, and this is the scope of this manuscript, MCa has been shown to act as a cell penetrating peptide (CPP) (9). This discovery stemmed from earlier criticisms that MCa may not be an activator of RyR1 because peptide toxins were not known to cross the

plasma membrane, which would be required here to bind to RyR1. Studies that were undertaken to demonstrate the ability of MCa to reach its target showed that i) MCa triggers Ca^{2+} release from the sarcoplasmic reticulum a few seconds after its application in the extracellular medium (5), and ii) intracellular accumulation of fluorescent-streptavidine occurs if it incubated first with biotinylated MCa (9). Since these pioneering studies, MCa or analogues thereof proved powerful vectors for the cell entry of proteins, peptides (10), nanoparticles, or drugs such as doxorubicine (11-14). Although the mode of cell penetration of MCa may vary according to cargo nature, cell type or chemical linkage employed, the data gathered so far suggest that the peptide may enter cells according to two priming steps onto the plasma membrane: first an interaction with proteoglycans with an affinity in the micromolar range, followed by a second interaction with negatively charged lipids which occurs with greater affinity (15,16). The mode of cell entry of MCa is not altered by the absence of proteoglycans, but simply reduced quantitatively, suggesting that proteoglycans do not orient the mode of cell penetration. Two modes seem to concur to MCa cell entry, as far as observed, one related to macropinocytosis and another to membrane translocation. The balance between both modes of entry was found correlated to cargo nature and the type of MCa analogue used. It is of great interest to pursue the study of MCa as CPP in spite of the wealth of new CPP sequences that are discovered yearly. Among the competitive advantage of MCa over other CPP sequences are the facts that it has almost no associated toxicity *in vitro* and *in vivo*, penetrates into cells at very low concentrations, and is extremely stable *in vivo* upon intravenous injection (over 24 hrs - manuscript in preparation).

While MCa appears as an elaborate and efficient CPP, its pharmacological properties represent a serious hindrance while envisioning *in vitro* and *in vivo* applications. In addition, because of its length (33 amino acid residues) and the presence of three disulfide bridges, MCa is a relatively difficult to synthesize CPP, comparatively to other CPP, and would benefit from a downsizing approach. Several strategies have been successfully employed in the past to overcome one or both of these issues. The first strategy was based on single point mutations of MCa sequence. This strategy preserved the disulfide bridges and the 3D structure of the analogues. Overall, mutations affected more seriously the pharmacology of MCa than the cell penetration properties (17). Many of the amino acids involved in RyR1 binding and pharmacology were located within the cluster of basic amino acids that presented sequence homology with the L-type $Ca_v1.1$ channel. Some of these residues, but not all, were also important for cell penetration properties. Hence, several analogues could be defined that kept close to intact cell penetration properties while entirely losing their pharmacological action (MCa R24A for instance). Some other analogues were actually better than MCa itself for cell penetration suggesting that pairs of mutations, aiming at disrupting pharmacology and improving penetration, may be used in the future to define still better CPP analogues of MCa. The second strategy, that has yield success, is based on the chemical synthesis of D-MCa, an analogue entirely based on the use of D-amino acids. This peptide is a mirror image of the natural L-MCa but, like other D-CPP, preserves its cell penetration properties, while losing entirely its ability to interact with RyR1 (18). This method has several advantages. It no longer is sensitive to proteases which may be an additional advantage for *in vivo* experiments where the half-life of the circulating peptide matters. It is also possible to improve this analogue by introducing point mutations shown previously to improve cell penetration (18). In these two strategies, while being effective, one may argue that i) the peptides are still among the longest CPP known to date, implying increased costs of production, and ii) the yield of production of these peptides is hampered by the folding process. Also, the use of peptides with internal disulfide bridges, despite have advantageous features in term of stability *in vivo*, makes chemical coupling of these CPP to cargoes more complicated (difficulty to add extra Cys residues to the peptides for instance without interfering with the correct folding process). The third strategy that was used to circumvent one of this criticism was the chemical synthesis of an MCa analogue in which all internal Cys residues where replaced by isosteric 2-aminobutyric acid residues (10). The resulting peptide was still 33-mer long but one step in production was saved by avoiding the folding process. In addition, an extra-Cys residue could be added to the N-terminus of the peptide in order to favor simplified cargo grafting on this CPP analogue. This peptide, termed here C-MCa_{UF1-33} (C

for extra-Cys, UF for unfolded, and 1-33 for its length, Fig. 1*B*) has no longer any secondary structures, but efficiently penetrates into cells. Interestingly also, the peptide completely lacks pharmacological activity indicating that folding and secondary structures are essential for binding onto RyR1. While this peptide is an efficient CPP, it remains less potent than MCa in its folded version suggesting that further optimization should be brought to this analogue. Such optimization appears feasible on the basis of the fact that MCa fulfills three different functions (pharmacology, obligation to resemble the L-type channel, and cell penetration). We reasoned that since only cell penetration was the quality we searched for, the peptide could be further simplified and novel analogues be designed.

In this study, we undertook to identify new more potent MCa analogues with three criteria in mind. First, these analogues should be shorter than the folded version of MCa (MCa_F) or the unfolded version (MCa_{UF}). Second, these peptides should be designed in order to better delimitate the domains of MCa responsible for cell penetration. Third, we should be able to design analogues with extra free SH functions for cargo grafting. We present several new analogues that have highly potent cell penetration capabilities, while losing pharmacological activity, preserving lack of cell toxicity, and with facilitated cargo grafting. This new generation of MCa analogues is predicted to have bright futures for CPP applications *in vitro* and *in vivo*.

Experimental procedures

Reagents – N-α-Fmoc-L-aminoacid, Wang-Tentagel resin and reagents used for peptide syntheses were obtained from Iris Biotech. Solvents were analytical grade products from Acros Organics. Cy5 maleimide mono-reactive dye was purchased from GE Healthcare.

Solid-phase peptide syntheses - Chemical syntheses of MCa analogues were performed as previously described (18). Briefly, analogues of MCa were chemically synthesized by the solid-phase method (19) using an automated peptide synthesizer (CEM© Liberty). Peptide chains were assembled stepwise on 0.24 mEq of Fmoc-D-Arg-Pbf-Wang-Tentagel resin using 0.24 mmol of N-α-fluorenylmethyloxycarbonyl (Fmoc) L-amino-acid derivatives. The side-chain protecting groups were: Trityl for Cys and Asn, *tert*-butyl for Ser, Thr, Glu and Asp, Pbf for Arg and *tert*-butylcarbonyl for Lys. Reagents were at the following concentrations: Fmoc-amino-acids (0.2 M Fmoc-AA-OH in dimethylformamide (DMF)), activator (0.5 M 2-(1H-benzotriazole-1-yl)-1,1,3,3-tetramethyluronium hexafluorophosphate in DMF), activator base (2 M diisopropylethylamine in N-methyl-pyrrolidone (NMP)) and deprotecting agent (5% piperazine / 0.1 M 1-hydroxybenzotriazole in DMF), as advised by PepDriver (CEM©). After peptide chain assembly, resins were treated 4 hrs at room temperature with a mixture of trifluoroacetic acid/water/triisopropylsilan (TIS)/dithiothreitol (DTT) (92.5/2.5/2.5/2.5). The peptide mixtures were then filtered and the filtrates were precipitated by adding cold *t*-butylmethyl ether. The crude peptides were pelleted by centrifugation (10.000 × g, 15 min) and the supernatants were discarded. MCa analogues were purified by HPLC using a Vydac C18 column (218TP1010, 25×10 cm). Elutions of the peptides were performed with a 10-60% acetonitrile linear gradient containing 0.1% trifluoroacetic acid. The purified fractions were analyzed by analytical RP-HPLC (Vydac C18 column 218TP104, 25 × 4.6 cm). All analogues were characterized by MALDI-TOF mass spectrometry.

Labeling of peptide with Cy5 - Each peptide was labeled with Cy5 according to the manufacturer's protocol (GE Healthcare). Peptides were dissolved at 1 mg/ml in 0.1 M Na_2CO_3 buffer, pH 9.3. 300 µl of the solubilized peptides were added to Cy5-maleimide containing tubes. The mixtures were incubated during 2 hrs at room temperature and then purified by HPLC using an analytical Vydac C18 column. Elution of the Cy5-labeled peptides was performed with a 10-60% acetonitrile linear gradient containing 0.1% trifluoroacetic acid. The pure peak fractions were lyophilized and peptides quantified by UV spectrophotometer at 649 nm.

Cell culture - Chinese hamster ovary (CHO) cell line (from ATCC) were maintained at 37°C in 5% CO_2 in F-12K nutrient medium (InVitrogen) supplemented with 10% (v/v) heat-inactivated fetal bovine serum (InVitrogen) and 10,000 units/ml streptomycine and penicillin (InVitrogen).

MTT assay **-** Cells were seeded into 96-well micro plates at a density of approximately 8×10^4 cells/well. After 2 days of culture, the cells were incubated for 24 hrs at 37°C with MCa analogues at a concentration of 10 µM. Control wells containing cell culture medium alone or with cells,

both without peptide addition, were included in each experiment. 0.1% saponin was used as toxic agent for comparison. The cells were then incubated with 3-(4, 5-dimethylthiazol-2-yl)-2, 5-diphenyl-tetrazolium bromide (MTT) for 30 min. Conversion of MTT into purple colored MTT formazan by the living cells indicates the extent of cell viability. The crystals were dissolved with dimethyl sulfoxide (DMSO) and the optical density was measured at 540 nm using a microplate reader (Biotek ELx-800, Mandel Scientific Inc.) for quantification of cell viability. All assays were run in triplicates.

Confocal microscopy - For analysis of the subcellular localization of MCa-Cy5 analogues in living cells, cell cultures were incubated with the fluorescent peptides for 2 hrs, and then washed with phosphate-buffered saline (PBS) alone. The plasma membrane was stained with 5 µg/ml rhodamine-conjugated concanavalin A (Molecular Probes) for 5 min. Cells were washed once more. Live cells were then immediately analyzed by confocal laser scanning microscopy using a Leica TCS-SPE operating system. Rhodamine (580 nm) and Cy5 (670 nm) were sequentially excited and emission fluorescence were collected in z-confocal planes of 10–15 nm steps.

Fluorescence Activated Cell Sorting – CHO cells were incubated with various concentrations of Cy5-labeled peptides in F-12K culture medium without serum at 37°C for 2 hrs. The cells were then washed with PBS to remove excess extracellular peptide and treated with 1 mg/ml trypsin (Invitrogen) for 5 min at 37°C to detach cells from the surface, and centrifuged at 200 *g* before suspension in PBS. For experiments with the macropinocytosis inhibitor, amiloride, CHO cells were initially washed with F-12K and preincubated for 30 min at 37°C with 1 mM amiloride (Sigma). The cells were then incubated for 2 hrs at 37°C with 1 µM of the Cy5-MCa analogues. For all these experimental conditions, flow cytometry analyses were performed with live cells using a Becton Dickinson FACS LSR II flow cytometer (BD Biosciences). Data were obtained and analyzed using FCS express software (De Novo). Live cells were gated by forward/side scattering from a total of 10,000 events.

Preparation of heavy SR vesicles - Heavy SR vesicles were prepared following the method of Kim et al. (20). Protein concentration was measured by the Biuret method.

[^{3}H]-Ryanodine binding assay - Heavy SR vesicles (1 mg/ml) were incubated at 37°C for 2 hrs in an assay buffer composed of 10 nM [^{3}H]-ryanodine, 150 mM KCl, 2 mM EGTA, 2 mM $CaCl_2$ (*p*Ca = 5), and 20 mM MOPS, pH 7.4. Truncated MCa analogues were added prior to the addition of heavy SR vesicles. [^{3}H]-ryanodine bound to heavy SR vesicles was measured by filtration through Whatman GF/B glass filters followed by three washes with 5 ml of ice-cold washing buffer composed of 150 mM NaCl, 20 mM HEPES, pH 7.4. [^{3}H]-ryanodine retained on the filters was measured by liquid scintillation. Non-specific binding was measured in the presence of 80 µM unlabeled ryanodine. The data are presented as mean ± S.E. Each experiment was performed in triplicate.

Statistical analyses - All data are given as mean ± SD for n number of observations, and statistical significance (p) was calculated using Student's t test.

RESULTS

Non folded truncated maurocalcine peptides are efficient CPP

Figure 1A illustrates the primary structure of MCa with its secondary structures (β strands) and its pattern of disulfide bridges. This peptide will be termed MCa_F, for folded (F) MCa. An earlier report has demonstrated that replacing the six internal cysteine residues of MCa by Abu residues results in a pharmacologically-inert and unfolded (UF) CPP (MCa_{UF1-33}, Fig. 1*B*). This peptide loses its secondary structures (10). Since this project aims at identifying shorter CPP sequences based on MCa_{UF1-33} sequence by the delivery of Cy5 cargo, we first determined where at the N-terminus (C-MCa_{UF1-33}) or C-terminus (MCa_{UF1-33}-C) the cargo could be best grafted after addition of an extra cysteine residue (C) (Fig. 1*B*). As shown, both vector/cargo complexes Cy5-C-MCa_{UF1-33} and MCa_{UF1-33}-C-Cy5 penetrated efficiently within CHO cells, as estimated by confocal microscopy (Fig. 1*C*) or by FACS (Fig. 1*D*). At 3 µM, a slightly better cell penetration was observed with Cy5 localized at the C-terminus of MCa_{UF1-33}, but this difference was not significant. Since chemical syntheses of truncated MCa_{UF1-33} analogues was facilitated by adding the extra cysteine residue at the C-terminus of the sequence rather than at the N-terminus, we kept on working on the basis of MCa_{UF1-33}-C sequence. Nevertheless, these data

indicate for the first time that cargo grafting on the CPP MCa_{UF1-33} can be performed likewise at both extremities of the sequence.

Next, we designed a series of truncated MCa_{UF}-C peptides comprising either a C-terminal truncation (3 analogues: MCa_{UF1-20}-C, MCa_{UF1-15}-C and MCa_{UF1-9}-C), a N-terminal truncation (7 analogues: MCa_{UF8-33}-C, $MCa_{UF11-33}$-C, $MCa_{UF14-33}$-C, $MCa_{UF18-33}$-C, $MCa_{UF20-33}$-C, $MCa_{UF22-33}$-C and $MCa_{UF25-33}$-C), and Both N- and C-terminal truncations (2 analogues: MCa_{UF6-25}-C and $MCa_{UF14-25}$-C) (Fig. 2*A*). All of these analogues were then labeled with Cy5 to investigate their cell penetration properties. Every one of these peptides has been designed in such a way that the cargo would be removed from the peptide upon trypsin cleavage. This was useful for the FACS experiments in which the fluorescence associated to the cells is measured after trypsin treatment, thereby potentially removing the cargo from peptides that would eventually be associated to the outer part of the plasma membrane. The net positive charges of the peptides were drastically different, ranging from 0 (MCa_{UF1-15}-C and MCa_{UF1-9}-C) to +8 (MCa_{UF8-33}-C). However, many of the peptides contained a percentage of positively charged residues equal ($MCa_{UF-25-33}$-C) or superior to MCa_F or MCa_{UF1-33} (8 out of twelve analogues). Three analogues had a lower percentage of basic residues than MCa_F (all three C-terminal truncated analogues, MCa_{UF1-20}-C, MCa_{UF1-15}-C and MCa_{UF1-9}-C).

We first evaluated by FACS the fluorescence accumulation within CHO cells that occurred after 2 hrs incubation with 3 µM of positively charged MCa peptides (net charge ≥ +5; Fig. 2*B*). This first study revealed several unexpected findings. First, all of the charged peptides (8 tested) demonstrated CPP properties. These peptides had all the $K^{22}R^{23}R^{24}$ sequence in common, a cluster of basic amino acid residues shown to contribute to the dose-efficacy of cell penetration of MCa_F in an earlier study (17). Interestingly, removing the last 8 C-terminal amino acids of MCa had little impact on the cell penetration properties (if one compares $MCa_{UF14-25}$-C with $MCa_{UF14-33}$-C). Similarly, the removal of the amino acid region His^6-Asn^{13} did not drastically change cell penetration properties (MCa_{UF6-25}-C *versus* $MCa_{UF14-25}$-C). Second, all peptides appeared to behave better than the reference peptide MCa_{UF1-33}-C, suggesting that sequence truncation of MCa_{UF} may represent a potent strategy to define more efficient CPP. Less positively charged peptides were also tested for their ability to penetrate into CHO cells (Fig. 2*C*). No less surprisingly, all peptides showed CPP properties, including two peptides with no net positive charge (MCa_{UF1-9}-C and MCa_{UF1-15}-C). MCa_{UF1-9}-C appeared as a better CPP than MCa_{UF1-15}-C suggesting that the Abu^{10}-Asp^{15} region introduces no competitive advantage and confirming results shown in Fig. 2*B*. This may represent an inhibitory region because of the presence of Glu^{12} and and Asp^{15}, two negatively charged residues. The finding that mutation of Glu12 to Ala enhances cell penetration of both MCa_F (17) and MCa_{UF} (10) further supports this conclusion. $MCa_{UF25-33}$-C turned out to have also CPP properties, even though this sequence did not confer a competitive advantage to other MCa CPP analogues as shown in Fig. 2*B*. The overall message from this first study is that all truncated MCa_{UF} analogues can behave as CPP at the concentration tested. The findings suggest that MCa is a peptide fully specialized to achieve cell penetration including in domains that are not highly charged.

The intracellular distribution of all truncated MCa_{UF} analogues bear resemblance with that of the full length MCa_{UF}

While all truncated derivatives of MCa_{UF1-33} show cell penetration properties according to the FACS analyses, we examined whether there were differences in intracellular distribution among these peptides. This question was investigated by confocal microscopy after 2 hrs of peptide accumulation into CHO cells (Fig. 3). Interestingly, all peptides showed very resembling intracellular distributions, although the degree of accumulated cell fluorescence varied somewhat with peptide sequences. In confirmation of the FACS results, the peptide that appeared to penetrate the least was the full length unfolded MCa, MCa_{UF1-33}-C-Cy5 (Fig. 3*A*). The vast majority of the fluorescence appears in punctuate dots within the cells. In many cases, these dots appear at higher concentrations within one pole of the cell (see labeling of MCa_{UF8-33}-C-Cy5, $MCa_{UF11-33}$-C-Cy5, $MCa_{UF25-33}$-C-Cy5, and MCa_{UF1-9}-C-Cy5 for instance). On various occasions also, all of the peptides tend to present a sub-plasma membrane distribution, forming a rim of smaller circumference than the concanavalin A labeling itself. This sub-plasma membrane rim localization was more evident for CHO cells labeled with $MCa_{UF14-25}$-C-Cy5 as illustrated in Fig. 4*A*. Finally, more rarely, a direct plasma membrane labeling by the peptide-cargo complex

was observable (Fig. 4*B*). This type of labeling could be observed with N-terminal truncated vectors exclusively and was most evident for $MCa_{UF22-33}$-C-Cy5. The staining of the plasma membrane was always diffuse in contrast to intracellular staining which was mainly punctuated. Diffuse membrane labeling was also observed for $MCa_{UF25-33}$-C-Cy5 and $MCa_{UF20-33}$-C-Cy5, two peptides that differ from 2 to 3 amino acids of $MCa_{UF22-33}$-C-Cy5. It was difficult to evidence for the other vector/cargo complexes. We propose that this staining coincides with an alteration of the duration of peptide plasma membrane residency for these truncated MCa_{UF} analogues. The lower occurrence of this diffuse staining for the other truncated variants may reflect faster internalization by endocytosis and/or membrane translocation. Globally, these effects reflect cell entry and distribution tendencies that were hard to quantify and they should therefore be interpreted with caution.

In an attempt to better apprehend peptide behavior at the plasma membrane, we quantified the extent of Cy5 / rhodamine staining colocalization. Rhodamine-positive staining was also Cy5-positive for 63% to 86% of the pixels (best performing peptides were $MCa_{UF14-33}$-C-Cy5, $MCa_{UF18-33}$-C-Cy5, $MCa_{UF20-33}$-C-Cy5 and $MCa_{UF22-33}$-C-Cy5; data not shown). This finding indicates that the peptides invade large membrane areas and that membrane interaction is not limited to small specialized surface areas. In contrast, Cy5-positive pixels were rhodamine-positive to far more variable extents (Fig. 4*C*). For instance, 10.1 ± 2.6% of MCa_{UF1-33}-C-Cy5, the reference compound, was colocalized with the plasma membrane indicator. In spite of the fact that short plasma membrane staining times were used (few minutes), a fraction of the colocalization that is quantified also corresponds to intracellular staining following ongoing endocytosis. Nevertheless, this result indicates that this peptide does not remain stuck within the plasma membrane during its 2 hrs incubation with CHO cells. It indicates relatively fast cell penetration thus. Many of the other peptides however behaved differently from MCa_{UF1-33}-C-Cy5. Indeed, several peptides show surprisingly higher colocalization with rhodamine (21.3 ± 2.6% for $MCa_{UF11-33}$-C-Cy5 and 30.4 ± 1.4% for MCa_{UF1-20}-C-Cy5 for instance). These higher values of colocalization indicate that some peptides remain for longer periods of time or at higher concentration within the plasma membrane. Alternatively, these peptides may rely more heavily on endocytosis for cell penetration and are present within intracellular organelles to which subsequent endocytotic vesicles that contain rhodamine labeling will fuse. Peptides most concerned by these behaviors were $MCa_{UF11-33}$-C-Cy5 and $MCa_{UF14-33}$-C-Cy5, that contained two or one of the CPP inhibitory negative charges (Glu^{12} and Asp^{15}), and MCa_{UF1-9}-C-Cy5 and MCa_{UF1-20}-C-Cy5, that were poorly charged peptides.

Amiloride-sensitivity of the cell penetration of truncated MCa_{UF} analogues

In earlier studies, we have demonstrated that the cell entry of MCa_{UF1-33} was largely sensitive to amiloride, suggesting a predominant macropinocytosis mechanism for its cell penetration (16). However, it was likely that such a predominant reliance on macropinocytosis was also conferred by the cargo type transported (streptavidine in that report). We therefore conducted an in depth analysis of the amiloride-sensitivity of the various truncated MCa_{UF} peptides with Cy5 as cargo and quantified by FACS the degree of cell penetration inhibition. Fig. 5*A* illustrates the amiloride-sensitivity of four different truncated peptides. As shown, amiloride inhibits the cell penetration of MCa_{UF1-33}-C-Cy5 by 19.6% and of MCa_{UF1-15}-C-Cy5 by 39%. The finding that amiloride blocks to a far lesser extend the penetration of Cy5 compared to that of streptavidin (16) when MCa_{UF1-33} is the vector indicates the influence of the cargo nature on the mechanism of cell entry. Surprisingly, blocking macropinocytosis was found to enhance rather than inhibit the cell penetration of $MCa_{UF20-33}$-C-Cy5 and $MCa_{UF18-33}$-C-Cy5 (Fig. 5*A*). Preserving the plasma membrane from undergoing macropinocytosis may free surface areas for enhanced peptide translocation trough the membrane. The effect of amiloride was always associated with a sharpening of the fluorescence intensity distribution in the x axis (see for instance MCa_{UF1-15}-C-Cy5), reflecting reduced cell heterogeneity for the mechanisms underlying peptide penetration. The amiloride-sensitivity of cell penetration was further investigated for all truncated MCa_{UF} peptides and the results presented in Fig. 5*B*. Four peptides showed higher amiloride-sensitivity than MCa_{UF1-33}-C-Cy5 ($MCa_{UF11-33}$-C-Cy5, $MCa_{UF25-33}$-C-Cy5, MCa_{UF1-15}-C-Cy5 and $MCa_{UF14-25}$-C-Cy5). All other peptides showed reduced amiloride-sensitivities or a tendency for greater cell penetration under the

effect of amiloride. We conclude that the Cy5 cargo does not promote macropinocytosis as the main route of peptide entry, and that truncation of MCa_{UF} may lead to analogues that rely to a lesser extent on macropinocytosis for cell entry.

Comparative dose-dependent cell penetration of the MCa_{UF} analogues

While we compared the properties of cell penetration of truncated peptides at rather mild concentrations, we also aimed at comparing the dose-dependence of cell penetration of these peptides by FACS (Fig. 6). One example of such an analysis is shown for peptide MCa_{UF8-33}-C-Cy5 in Fig. 6*A*. 33 µM was the highest concentration that could be tested on CHO cells and obviously cell penetration did not show any sign of saturation for cell incubation times with this peptide of 2 hrs. The dose-dependent cell penetration were compared for all N-terminal truncated peptides (Fig. 6*B*), C-terminal truncated peptides (Fig. 6*C*), and double truncated analogues (Fig. 6*D*) with the same settings. These analyses confirm that MCa_{UF1-33}-C-Cy5 is the least-performing cell penetrating peptide. Most truncated peptides show detectable cell penetration at concentrations equal or above 1 µM. One remarkable exception to this rule was noticeable. MCa_{UF1-9}-C-Cy5 shows an unusual dose-dependent penetration with detectable cell penetration at 10 nM and only small progressive increases in fluorescence intensity with higher peptide concentrations (Fig. 6*C*). This peptide was therefore the best performing peptide for cell penetration at low concentrations. Finally, additional information that could be taken from these analyses is that the peptides differed significantly with regard to the maximal extent of cell penetration. Among the N-terminal truncated MCa_{UF} analogues, $MCa_{UF18-33}$-C-Cy5 performed drastically better than the other truncated peptides (Fig. 6*B*). The difference in cell penetration among $MCa_{UF11-33}$-C-Cy5 and $MCa_{UF18-33}$-C-Cy5 resides in the removal of KENKDAbuAbu sequence which we presume is inhibitory to some extent because of the presence of Glu^{12} and Asp^{15}. Among the C-terminal truncated peptides, MCa_{UF1-20}-C-Cy5 was performing as well as MCa_{UF8-33}-C-Cy5, and although not tested at higher concentrations, MCa_{UF1-9}-C-Cy5 would be expected to perform still better. Finally, for N- and C-terminal truncated analogues, the best peptide turns out to be $MCa_{UF14-25}$-C-Cy5 that yields the greatest fluorescence accumulation at 33 µM compared to all other truncated MCa_{UF} analogues.

Truncated MCa_{UF} peptides lack pharmacological effects and are predominantly non toxic

An earlier report has shown that MCa_{UF1-33} is unable to interact with MCa's target, the ryanodine receptor RyR1 (10). This is due to the loss of secondary structures owing to the lack of internal disulfide bridging. We did therefore expect that truncated analogues of MCa_{UF} should also be pharmacologically inert. This hypothesis was challenged by testing the ability of the Cy5-free peptides to stimulate [^{3}H]-ryanodine binding (Fig. 7*A*). As shown, contrary to MCa_F that contains secondary structures and disulfide bridges, none of the peptides we designed had an effect on [^{3}H]-ryanodine binding.

Finally, the peptides were challenged for their toxicity by incubating CHO cells with 1 or 10 µM peptide concentrations for an extended duration (24 hrs) that far exceeds the duration challenged for cell penetration (Fig. 7*B*). A 10 µM peptide concentration was generally slightly more toxic than 1 µM, except for $MCa_{UF14-25}$-C. At 1 µM, toxicity never exceeded 8% and significances of these effects were negligible. In contrast, toxicity could reach 20% at 10 µM peptide concentration and these effects had higher significance. Most peptides behaved equally well or better than MCa_{UF1-33}-C indicating that truncation did not enhance cell toxicity of the peptides.

Discussion

MCa_F is a rather large and complex CPP with its three disulfide bridges which makes its use in *in vitro* and *in vivo* applications more delicate because of production yield (peptide with correct disulfide bridging) and cargo coupling (thiol groups are for the moment difficult to use). It may also be argued that the size of the peptide introduces additional synthesis cost compared to other popular in use CPP such as Tat and penetratin. While size and folding most likely adds competitive advantage as well for *in vivo* applications because of peptide stability issues, it may be of interest to derive small CPP from MCa that could have a broader use than MCa itself. The study we conducted not only aimed at defining these smaller MCa-derived CPP sequences, but also provided interesting clues on how MCa may have evolve for cell penetration. The most surprising finding from this study was therefore that all of the analogues we defined could be considered as CPP, which suggests that MCa is a highly

specialized sequence for the purpose of cell penetration. While evidently none of the peptides could compete with MCa_F itself for cell penetration, it is nevertheless obvious that many of the truncated MCa_{UF} peptides are better CPP than MCa_{UF1-33} itself. These findings lead to two general conclusions. First, folding and disulfide bridging appears to be a prerequisite to properly optimize the CPP potential of all the MCa domains. It is highly likely that the secondary structures triggered by disulfide bridging play a key role in that respect. We therefore believe that we would be worthwhile to design additional MCa analogues presenting both truncations (like in the present study) and 1 to 2 disulfide bridges in order to regain some of the secondary structures that confer a competitive advantage to MCa_F for cell penetration. Second, the fact that all the truncated sequences are CPP that possess different properties and efficacies, suggests that this is further room for MCa cell penetrating optimization. In this study, our data indicate that the amino acid region Lys^{11}-Ser^{18} would be an ideal target for mutagenesis. Glu^{12} mutation has already been shown to improve cell penetration on various analogues (10,17). We now sense that Asp^{15} may also represent an excellent target for further optimization of MCa's properties. Double mutagenesis may be an option. However, it should be careful determined whether the disulfide bridging and folding ability of the native peptide is not affected by this procedure. Truncated MCa_{UF} peptides may also benefit from further mutagenesis of negatively charged residues, such as MCa_{UF1-20}. It is noteworthy that another well behaving truncated CPP, $MCa_{UF18-33}$, also contains a Glu residue at position 29 that could represent another target for mutagenesis and peptide optimization. This is also the case for MCa_{UF1-9} that contains an Asp residue at position 2.

Several other findings of this report merit some comments. First, we demonstrate that cargo coupling can occur at the N-terminus as well as the C-terminus of MCa enhancing the flexibility of cargo coupling to our vectors. Second, while it is obvious that most of our truncated MCa_{UF} analogues remain heavily basic, we also found out that poorly charged MCa peptides could behave as efficient CPP. This is the case for MCaUF1-9 which is one of our best performing CPP, especially when low concentration of use is a quality of importance. Third, small size CPP can be derived from MCa_{UF}, MCa_{UF1-9} and $MCa_{UF25-33}$ being our smallest peptides. While we did not test greater truncation, it is not impossible that still smaller CPP might be designed on the basis of MCa sequence. Fourth, the truncated MCa_{UF} analogues differ somewhat in their mode of cell penetration, some being more prone to enter cells by macropinocytosis than others. Various peptides were even insensitive to amiloride application suggesting that macropinocytosis did not contribute at all to their entry. We can't exclude at this stage that these peptides rely on other modes of endocytosis than macropinocytosis. This is suggested by the punctuate nature of intracellular Cy5 fluorescence distribution. How reliably a punctuate distribution reveals endocytosis is however not known, and one can't rule out also that this distribution is due to peptide aggregation with or without lipid components. When plasma membrane distribution could be observed, large diffuse staining was evident indicating that when peptides encountered the membrane no such aggregation occurred. In any case, many of the peptides had distribution that mostly differed from plasma membrane labeling (including these membranes that had undergone endocytosis) indicating that peptide intracellular distribution may not necessarily colocalize with the plasma membrane components. Refined studies will be required however to define how much of the peptides enter cells by direct membrane translocation *versus* endocytosis.

To conclude on this study, we identified several interesting lead CPP based on MCa_{UF} truncation strategy. This is the case for $MCa_{UF18-33}$ (macropinocytosis entry-independent), MCa_{UF1-9} (penetrates better at low concentration), and $MCa_{UF14-25}$ (yields the greatest cell entry of the dye). These peptides are easy to produce, yield good cell penetration, and we should be able to further improve their cell penetrating characteristics by mutagenesis or by reintroducing one disulfide bridge to restore some of the secondary structures. Faced to the diversity of cell penetration properties, it would also be of interest to investigate the cell-type specific affinity of these truncated peptides for future *in vivo* applications.

References

1. Fajloun, Z., Kharrat, R., Chen, L., Lecomte, C., Di Luccio, E., Bichet, D., El Ayeb, M., Rochat, H., Allen, P. D., Pessah, I. N., De Waard, M., and Sabatier, J. M. (2000) *FEBS Lett* **469**, 179-185
2. Mosbah, A., Kharrat, R., Fajloun, Z., Renisio, J. G., Blanc, E., Sabatier, J. M., El Ayeb, M., and Darbon, H. (2000) *Proteins* **40**, 436-442
3. Chen, L., Esteve, E., Sabatier, J. M., Ronjat, M., De Waard, M., Allen, P. D., and Pessah, I. N. (2003) *J Biol Chem* **278**, 16095-16106
4. Lukacs, B., Sztretye, M., Almassy, J., Sarkozi, S., Dienes, B., Mabrouk, K., Simut, C., Szabo, L., Szentesi, P., De Waard, M., Ronjat, M., Jona, I., and Csernoch, L. (2008) *Biophys J* **95**, 3497-3509
5. Esteve, E., Smida-Rezgui, S., Sarkozi, S., Szegedi, C., Regaya, I., Chen, L., Altafaj, X., Rochat, H., Allen, P., Pessah, I. N., Marty, I., Sabatier, J. M., Jona, I., De Waard, M., and Ronjat, M. (2003) *J Biol Chem* **278**, 37822-37831
6. Altafaj, X., Cheng, W., Esteve, E., Urbani, J., Grunwald, D., Sabatier, J. M., Coronado, R., De Waard, M., and Ronjat, M. (2005) *J Biol Chem* **280**, 4013-4016
7. Szappanos, H., Smida-Rezgui, S., Cseri, J., Simut, C., Sabatier, J. M., De Waard, M., Kovacs, L., Csernoch, L., and Ronjat, M. (2005) *J Physiol* **565**, 843-853
8. Pouvreau, S., Csernoch, L., Allard, B., Sabatier, J. M., De Waard, M., Ronjat, M., and Jacquemond, V. (2006) *Biophys J* **91**, 2206-2215
9. Esteve, E., Mabrouk, K., Dupuis, A., Smida-Rezgui, S., Altafaj, X., Grunwald, D., Platel, J. C., Andreotti, N., Marty, I., Sabatier, J. M., Ronjat, M., and De Waard, M. (2005) *J Biol Chem* **280**, 12833-12839
10. Ram, N., Weiss, N., Texier-Nogues, I., Aroui, S., Andreotti, N., Pirollet, F., Ronjat, M., Sabatier, J. M., Darbon, H., Jacquemond, V., and De Waard, M. (2008) *J Biol Chem*
11. Aroui, S., Brahim, S., De Waard, M., Breard, J., and Kenani, A. (2009) *Cancer Lett* **285**, 28-38
12. Aroui, S., Brahim, S., Hamelin, J., De Waard, M., Breard, J., and Kenani, A. (2009) *Apoptosis* **14**, 1352-1365
13. Aroui, S., Brahim, S., Waard, M. D., and Kenani, A. *Biochem Biophys Res Commun* **391**, 419-425
14. Aroui, S., Ram, N., Appaix, F., Ronjat, M., Kenani, A., Pirollet, F., and De Waard, M. (2009) *Pharm Res* **26**, 836-845
15. Boisseau, S., Mabrouk, K., Ram, N., Garmy, N., Collin, V., Tadmouri, A., Mikati, M., Sabatier, J. M., Ronjat, M., Fantini, J., and De Waard, M. (2006) *Biochim Biophys Acta* **1758**, 308-319
16. Ram, N., Aroui, S., Jaumain, E., Bichraoui, H., Mabrouk, K., Ronjat, M., Lortat-Jacob, H., and De Waard, M. (2008) *J Biol Chem* **283**, 24274-24284
17. Mabrouk, K., Ram, N., Boisseau, S., Strappazzon, F., Rehaim, A., Sadoul, R., Darbon, H., Ronjat, M., and De Waard, M. (2007) *Biochim Biophys Acta* **1768**, 2528-2540
18. Poillot, C., Dridi, K., Bichraoui, H., Pecher, J., Alphonse, S., Douzi, B., Ronjat, M., Darbon, H., and De Waard, M. *J Biol Chem* **285**, 34168-34180
19. Merrifield, R. B. (1969) *Adv Enzymol Relat Areas Mol Biol* **32**, 221-296
20. Kim, D. H., Ohnishi, S. T., and Ikemoto, N. (1983) *J Biol Chem* **258**, 9662-9668

FOOTNOTES

This work was supported by grants from Technology pour la Santé (Program TIMOMA2 of the Commissariat à l'Energie Atomique) and from Agence Nationale pour la Recherche PNANO (Programs SYNERGIE and NanoFret). Mass spectrometry analyses were performed by the Centre d'Investigation Clinique of Grenoble under the heading of Dr. Michel Sève.

The abbreviations used are: CD: Circular Dichroism; CPP: Cell Penetrating Peptide; DMF: dimethyformamide; FACS: Fluorescence-Activated Cell Sorting; HPLC: high-performance liquid chromatography; MCa: Maurocalcine; NMP: N-methyl-pyrrolidone; RS: Sarcoplasmic reticulum; RyR: Ryanodine Receptor; TFA: trifluoroacetic acid.

FIGURE LEGENDS

Fig. 1. Efficacy of cargo penetration as a function of grafting position on MCa_{UF1-33}. (A) Amino acid sequence of MCa_F in single letter code. The positions of half-cystine residues are highlighted in red. Cys residues are numbered and basic amino acids are highlighted in blue. Secondary structures (β strands) are indicated by arrows. The grey box is the sequence of homology of MCa with the dihydropyridine-sensitive $Ca_v1.1$ channel. (B) Amino acid sequences of unfolded MCa analogues in single letter code. Cys residues are replaced by isosteric 2-aminobutyric acid residues (Abu, in red) to form MCa_{UF1-33}. An additional N-terminal (C-MCa_{UF1-33}) or C-terminal (MCa_{UF1-33}-C) Cys residue was added in two novel analogues competent for cargo grafting (shown in grey). (C) Confocal microscopy images illustrating cell penetration of Cy5-C-MCa_{UF1-33} and MCa_{UF1-33}-C-Cy5 (green labeling). Plasma membranes are labeled with concanavalin-A-rhodamin (in red). CHO cells were incubated 2 hrs with 1 µM peptide concentration. (D) Comparison of cell penetration efficacy between Cy5-C-MCa_{UF1-33} and MCa_{UF1-33}-C-Cy5 as determined by FACS. CHO cells were incubated 2 hrs with 3 µM peptide, washed, and treated 5 min by 1 mg/ml trypsin before quantification of intracellular fluorescence.

Fig. 2. Primary structure of truncated MCa_{UF} analogues and comparison of cell penetration efficacies. (A) Primary structures of truncated MCa_{UF}-C analogues and determination of their net positive charge and percentage of basic amino acid residues within the sequence. A total of 12 truncated MCa_{UF}-C analogues were produced (three with truncations in C-terminus, seven in N-terminus, and two in both N- and C-termini). Positively charged residues are in blue (His residues were not counted), whereas Abu residues that replace Cys residues are in red. (B) Comparative cell penetration efficacy of all MCa_{UF}-C-Cy5 truncated analogues that possess a net positive charge ≥ +5. Code colors: red (net charge +8), blue (+7), pink (+6) and green (+5). The non-truncated MCa_{UF1-33}-C-Cy5 analogue is shown as reference (black line) for the efficacy of cell penetration of all analogues. Experimental conditions: CHO cell incubation with 1 µM of each analogue for 2 hrs and fluorescence quantification by FACS. (C) Same as (B) but for truncated MCa_{UF}-C-Cy5 analogues with positive net charge ≤ +2.

Fig. 3. All truncated MCa_{UF}-C-Cy5 vector/cargo complexes have resembling intracellular distributions. (A) Intracellular distribution of N-terminal truncated MCa_{UF} analogues. (B) Intracellular distribution of C-terminal truncated MCa_{UF} analogues. (C) Intracellular distribution of N- and C-terminal truncated MCa_{UF} analogues. CHO cells were incubated 2 hrs with 3 µM of MCa_{UF}-C-Cy5 vector/cargo complexes, before extensive washing, membrane labeling with rhodamine-conjugated concanavalin A, and live cell confocal microscopy imaging. Cy5 is in blue, and rhodamine in red. White arrows illustrate a tendency for a preferential apical localization of the Cy5 dye. Yellow arrows illustrate the tendency for a sub-plasma membrane labeling of the Cy5 dye.

Fig. 4. Membrane staining is diffuse whereas intracellular staining is punctuated. (A) Lower magnification image of CHO cells stained with 3 µM $MCa_{UF14-25}$-C-Cy5 that illustrates a predominant sub-plasma membrane rim-like distribution. (B) Diffuse membrane staining of CHO cells by $MCa_{UF22-33}$-C-Cy5. White arrows indicate domains of the plasma membrane where the diffuse staining of the peptide/cargo complex is the most evident. (C) Extent of colocalization of the Cy5-labeled peptides with the rhodamine-labeled plasma membrane. NS, non significant; * ≤ 0.1; ** ≤ 0.05; and *** ≤ 0.001.

Fig. 5. Amiloride sensitivity of truncated MCa_{UF} peptide cell entry. (A) Representative FACS analyses of the effect of 5 mM amiloride on MCa_{UF1-33}-C-Cy5 (upper left panel), MCa_{UF1-15}-C-Cy5 (upper right panel), $MCa_{UF20-33}$-C-Cy5 (lower left panel) and $MCa_{UF18-33}$-C-Cy5 (lower right panel) entries. Numbers in red represent average decrease or increase in peptide entry upon amiloride treatment. Cells were treated 2 hrs with 3 µM peptide concentration with or without 5 mM amiloride. (B) Average effect of amiloride on mean cell entry of the truncated peptides. Positive values reflect increase in cell entries, whereas negative values indicate reduction in cell penetration.

Fig. 6. Dose-dependent cell penetration of truncated MCaUF peptides. (A) Representative example of the dose-dependent cell penetration of MCa_{UF8-33}-C-Cy5 in CHO cells as analyzed by FACS. The peptide was incubated 2 hrs with the cells before analyses. There was no saturation of cell entry for a concentration up to 33 µM. (B) Dose-dependent cell penetration of N-terminal truncated MCa_{UF} peptides compared to MCa_{UF1-33}-C-Cy5 (open circle, dotted line). (C) Dose-dependent cell penetration of C-terminal truncated MCa_{UF} peptides. (D) Dose-dependent cell penetration of N- and C-terminal truncated MCa_{UF} peptides. Note the increase in scale for the penetration of these two peptides.

Fig. 7. Lack of pharmacology of the truncated peptides and reduced cell toxicity. (A) Effect of MCa_F, MCa_{UF1-33} and truncated MCa_{UF} peptides on [^{3}H]-ryanodine binding. Data were expressed as x-fold increase in binding induced by the peptides. (B) Effect of 1 and 10 µM MCa_{UF1-33} and truncated MCa_{UF} peptides on CHO cell viability. Peptides were incubated 24 hrs with the cells *in vitro*.

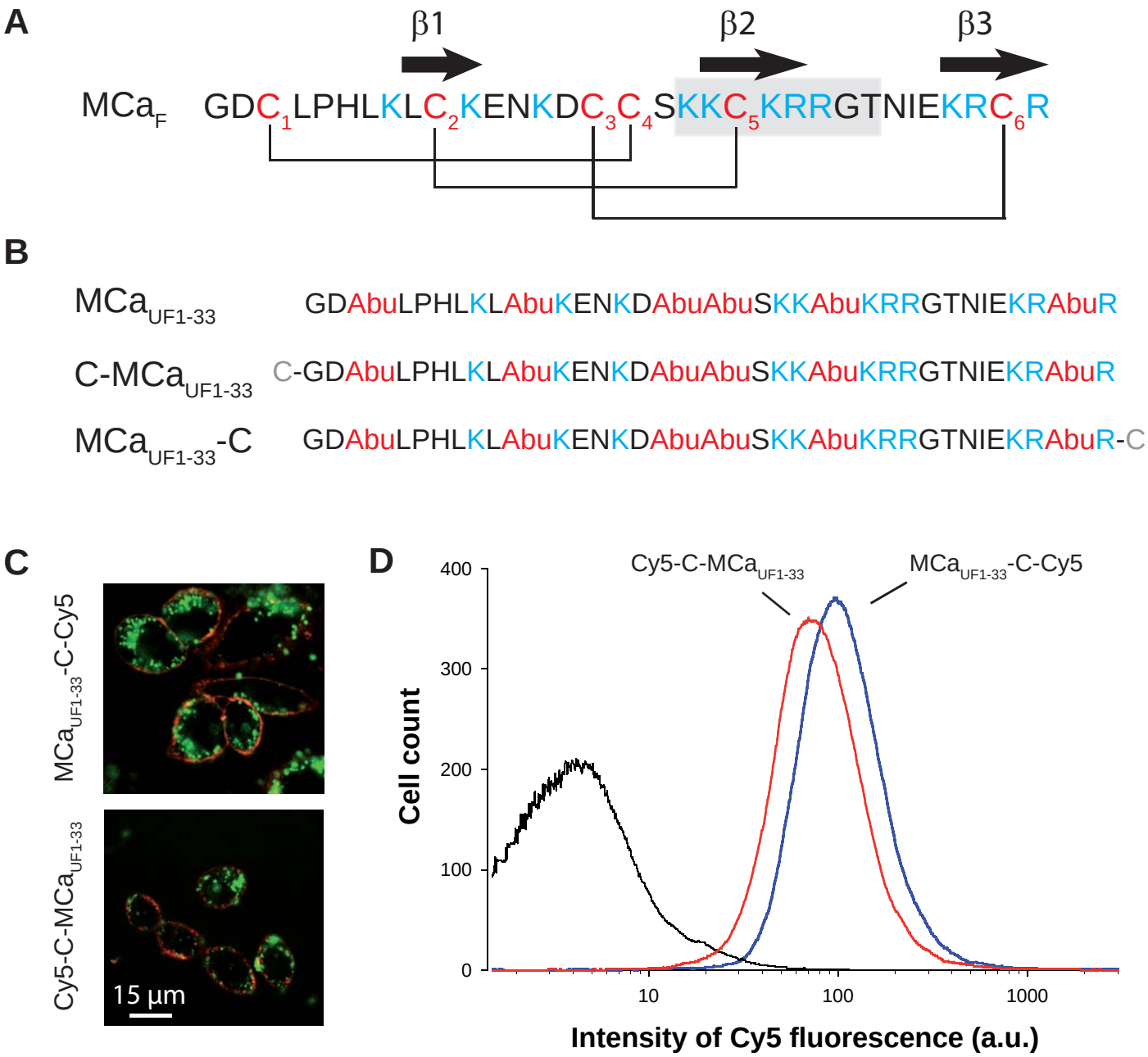
A
β1
β2
β3
MCa$_F$ GDC$_1$LPHLKLC$_2$KENKDC$_3$C$_4$SKKC$_5$KRRGTNIEKRC$_6$R
B
MCa$_{UF1-33}$ GDAbuLPHLKLAbuKENKDAbuAbuSKKAbuKRRGTNIEKRAbuR
C-MCa$_{UF1-33}$ C-GDAbuLPHLKLAbuKENKDAbuAbuSKKAbuKRRGTNIEKRAbuR
MCa$_{UF1-33}$-C GDAbuLPHLKLAbuKENKDAbuAbuSKKAbuKRRGTNIEKRAbuR-C
C
MCa$_{UF1-33}$-C-Cy5
Cy5-C-MCa$_{UF1-33}$
15 µm
D
Cy5-C-MCa$_{UF1-33}$
MCa$_{UF1-33}$-C-Cy5
Cell count
400
300
200
100
0
10
100
1000
Intensity of Cy5 fluorescence (a.u.)

Figure 1

A

		Net charge (NC)	%
MCa_{UF1-33}-C	GDAbuLPHLKLAbuKENKDAbuAbuSKKAbuKRRGTNIEKRAbuR-C	+7	33
MCa_{UF1-20}-C	GDAbuLPHLKLAbuKENKDAbuAbuSKK-C	+2	25
MCa_{UF1-15}-C	GDAbuLPHLKLAbuKENKD-C	0	20
MCa_{UF1-9}-C	GDAbuLPHLKL-C	0	11
MCa_{UF8-33}-C	KLAbuKENKDAbuAbuSKKAbuKRRGTNIEKRAbuR-C	+8	42
$MCa_{UF11-33}$-C	KENKDAbuAbuSKKAbuKRRGTNIEKRAbuR-C	+7	43
$MCa_{UF14-33}$-C	KDAbuAbuSKKAbuKRRGTNIEKRAbuR-C	+7	45
$MCa_{UF18-33}$-C	SKKAbuKRRGTNIEKRAbuR-C	+7	50
$MCa_{UF20-33}$-C	KAbuKRRGTNIEKRAbuR-C	+6	50
$MCa_{UF22-33}$-C	KRRGTNIEKRAbuR-C	+5	50
$MCa_{UF25-33}$-C	GTNIEKRAbuR-C	+2	33
MCa_{UF6-25}-C	HLKLAbuKENKDAbuAbuSKKAbuKRRG-C	+6	40
$MCa_{UF14-25}$-C	KDAbuAbuSKKAbuKRRG-C	+5	50

B

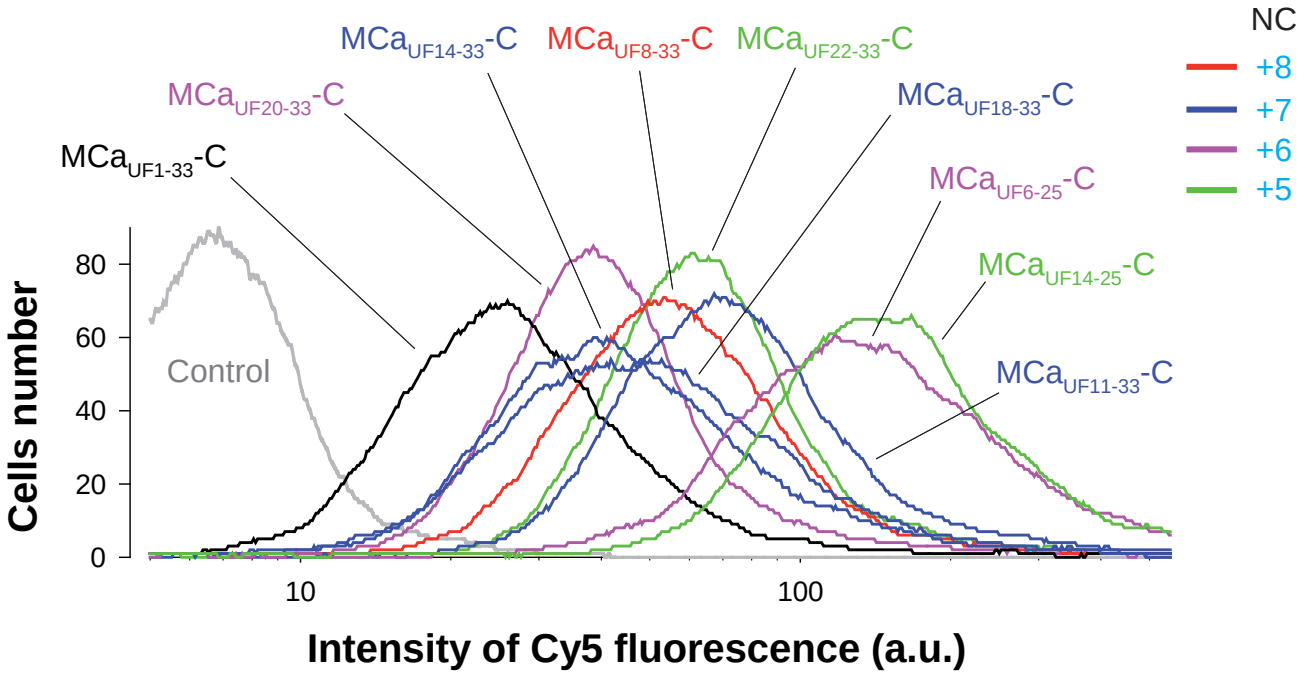

C

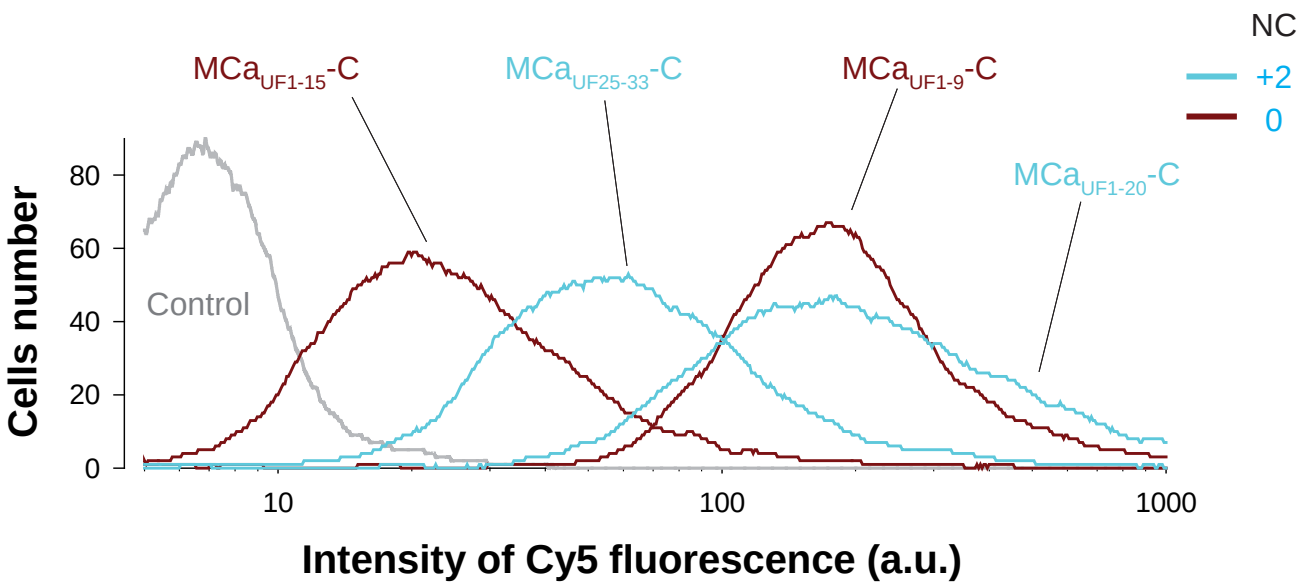

Figure 2

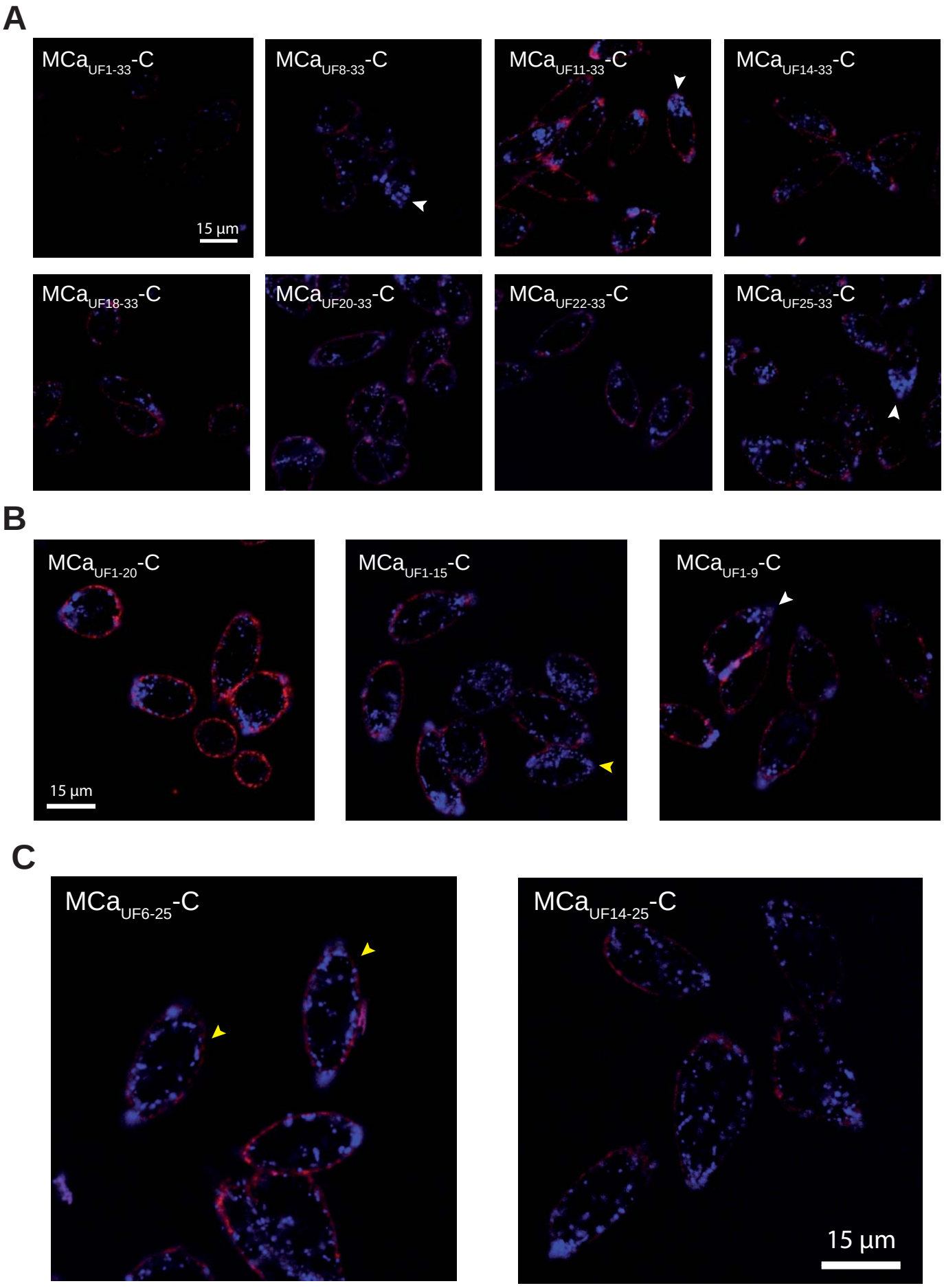
A
MCa$_{UF1-33}$-C
15 µm
MCa$_{UF8-33}$-C
MCa$_{UF11-33}$-C
MCa$_{UF14-33}$-C
MCa$_{UF18-33}$-C
MCa$_{UF20-33}$-C
MCa$_{UF22-33}$-C
MCa$_{UF25-33}$-C
B
MCa$_{UF1-20}$-C
15 µm
MCa$_{UF1-15}$-C
MCa$_{UF1-9}$-C
C
MCa$_{UF6-25}$-C
MCa$_{UF14-25}$-C
15 µm

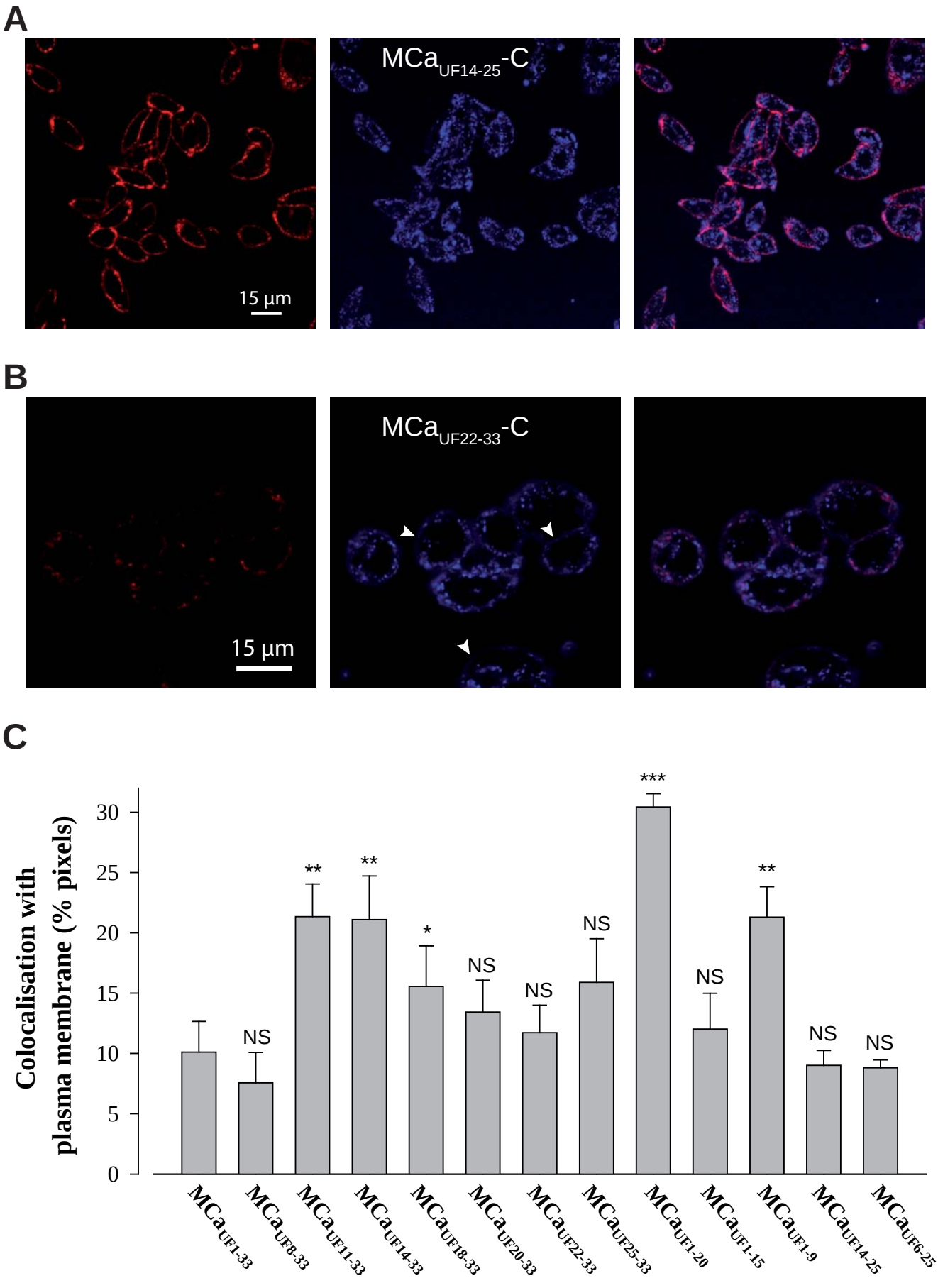
A
MCa$_{UF14-25}$-C
15 µm
B
MCa$_{UF22-33}$-C
15 µm
C
Colocalisation with plasma membrane (% pixels)
0
5
10
15
20
25
30
NS
**
**
*
NS
NS
NS
***
NS
**
NS
NS
MCa$_{UF1-33}$
MCa$_{UF8-33}$
MCa$_{UF11-33}$
MCa$_{UF14-33}$
MCa$_{UF18-33}$
MCa$_{UF20-33}$
MCa$_{UF22-33}$
MCa$_{UF25-33}$
MCa$_{UF1-20}$
MCa$_{UF1-15}$
MCa$_{UF1-9}$
MCa$_{UF14-25}$
MCa$_{UF6-25}$

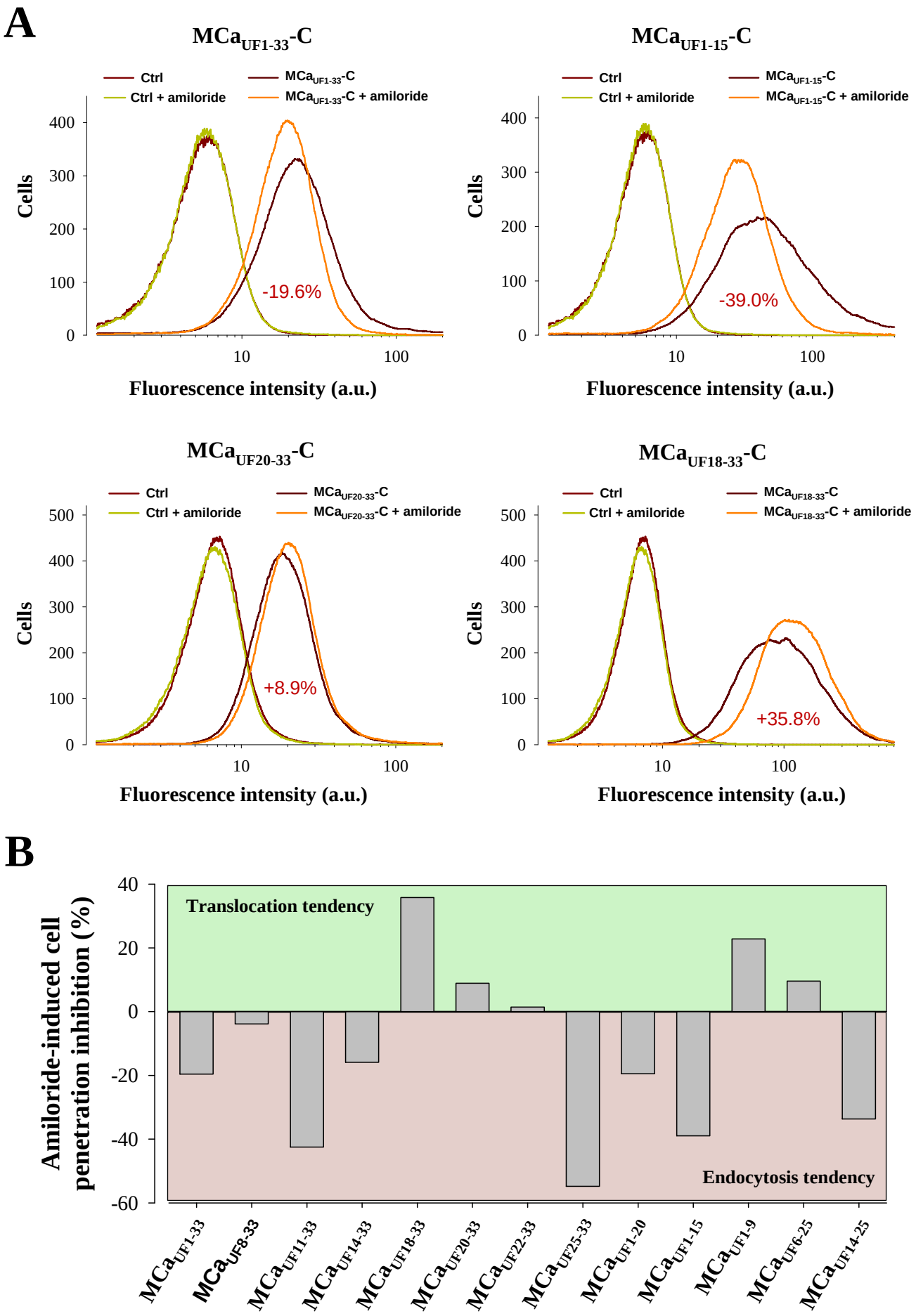
A
MCa$_{UF1-33}$-C
Ctrl
Ctrl + amiloride
MCa$_{UF1-33}$-C
MCa$_{UF1-33}$-C + amiloride
Cells
-19.6%
Fluorescence intensity (a.u.)
MCa$_{UF1-15}$-C
Ctrl
Ctrl + amiloride
MCa$_{UF1-15}$-C
MCa$_{UF1-15}$-C + amiloride
Cells
-39.0%
Fluorescence intensity (a.u.)
MCa$_{UF20-33}$-C
Ctrl
Ctrl + amiloride
MCa$_{UF20-33}$-C
MCa$_{UF20-33}$-C + amiloride
Cells
+8.9%
Fluorescence intensity (a.u.)
MCa$_{UF18-33}$-C
Ctrl
Ctrl + amiloride
MCa$_{UF18-33}$-C
MCa$_{UF18-33}$-C + amiloride
Cells
+35.8%
Fluorescence intensity (a.u.)
B
Amiloride-induced cell penetration inhibition (%)
Translocation tendency
Endocytosis tendency
MCa$_{UF1-33}$
MCa$_{UF8-33}$
MCa$_{UF11-33}$
MCa$_{UF14-33}$
MCa$_{UF18-33}$
MCa$_{UF20-33}$
MCa$_{UF22-33}$
MCa$_{UF25-33}$
MCa$_{UF1-20}$
MCa$_{UF1-15}$
MCa$_{UF1-9}$
MCa$_{UF6-25}$
MCa$_{UF14-25}$

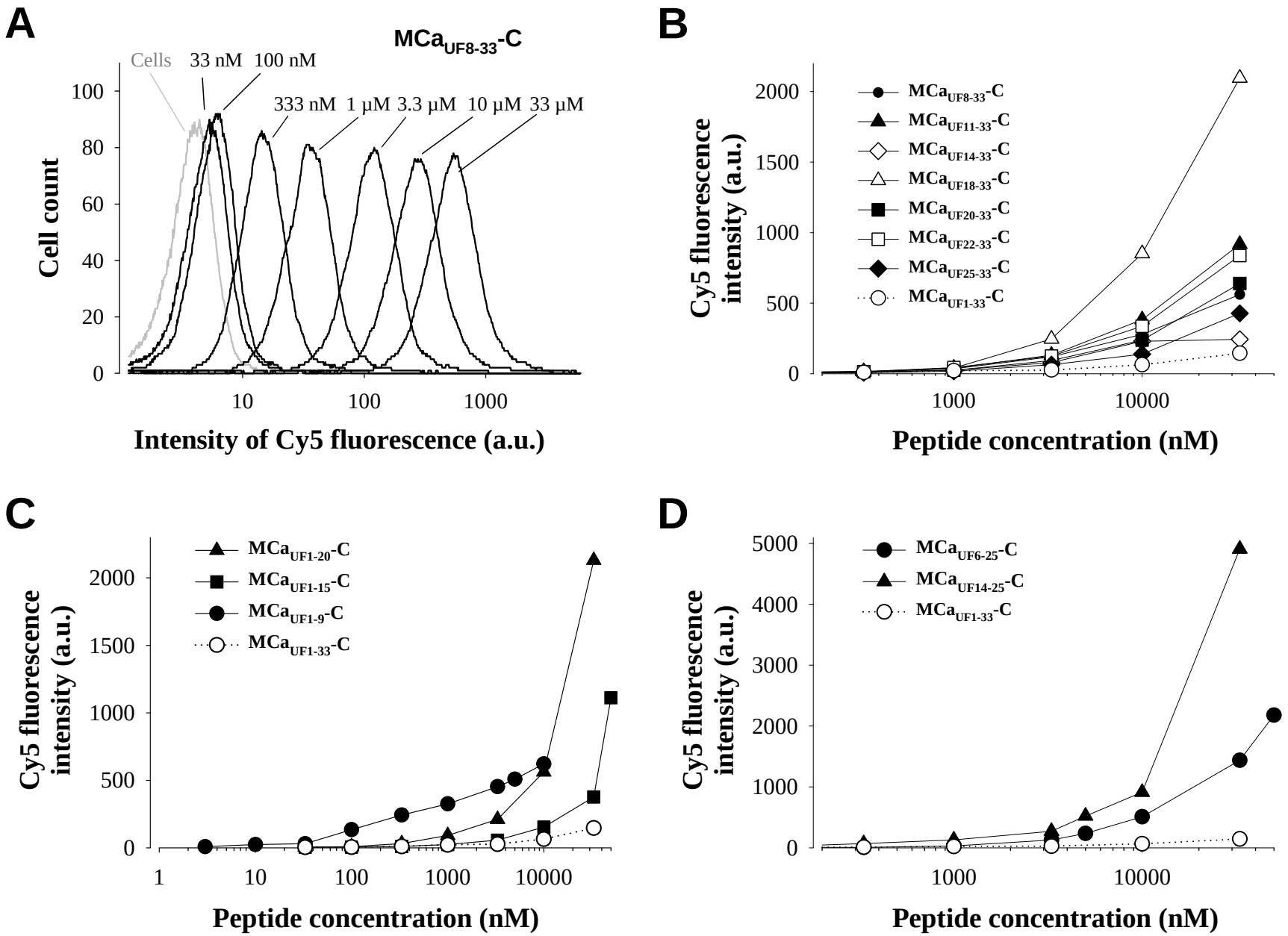
A
MCa$_{UF8-33}$-C
Cells
33 nM
100 nM
333 nM
1 µM
3.3 µM
10 µM
33 µM
Cell count
Intensity of Cy5 fluorescence (a.u.)
B
MCa$_{UF8-33}$-C
MCa$_{UF11-33}$-C
MCa$_{UF14-33}$-C
MCa$_{UF18-33}$-C
MCa$_{UF20-33}$-C
MCa$_{UF22-33}$-C
MCa$_{UF25-33}$-C
MCa$_{UF1-33}$-C
Cy5 fluorescence intensity (a.u.)
Peptide concentration (nM)
C
MCa$_{UF1-20}$-C
MCa$_{UF1-15}$-C
MCa$_{UF1-9}$-C
MCa$_{UF1-33}$-C
Cy5 fluorescence intensity (a.u.)
Peptide concentration (nM)
D
MCa$_{UF6-25}$-C
MCa$_{UF14-25}$-C
MCa$_{UF1-33}$-C
Cy5 fluorescence intensity (a.u.)
Peptide concentration (nM)

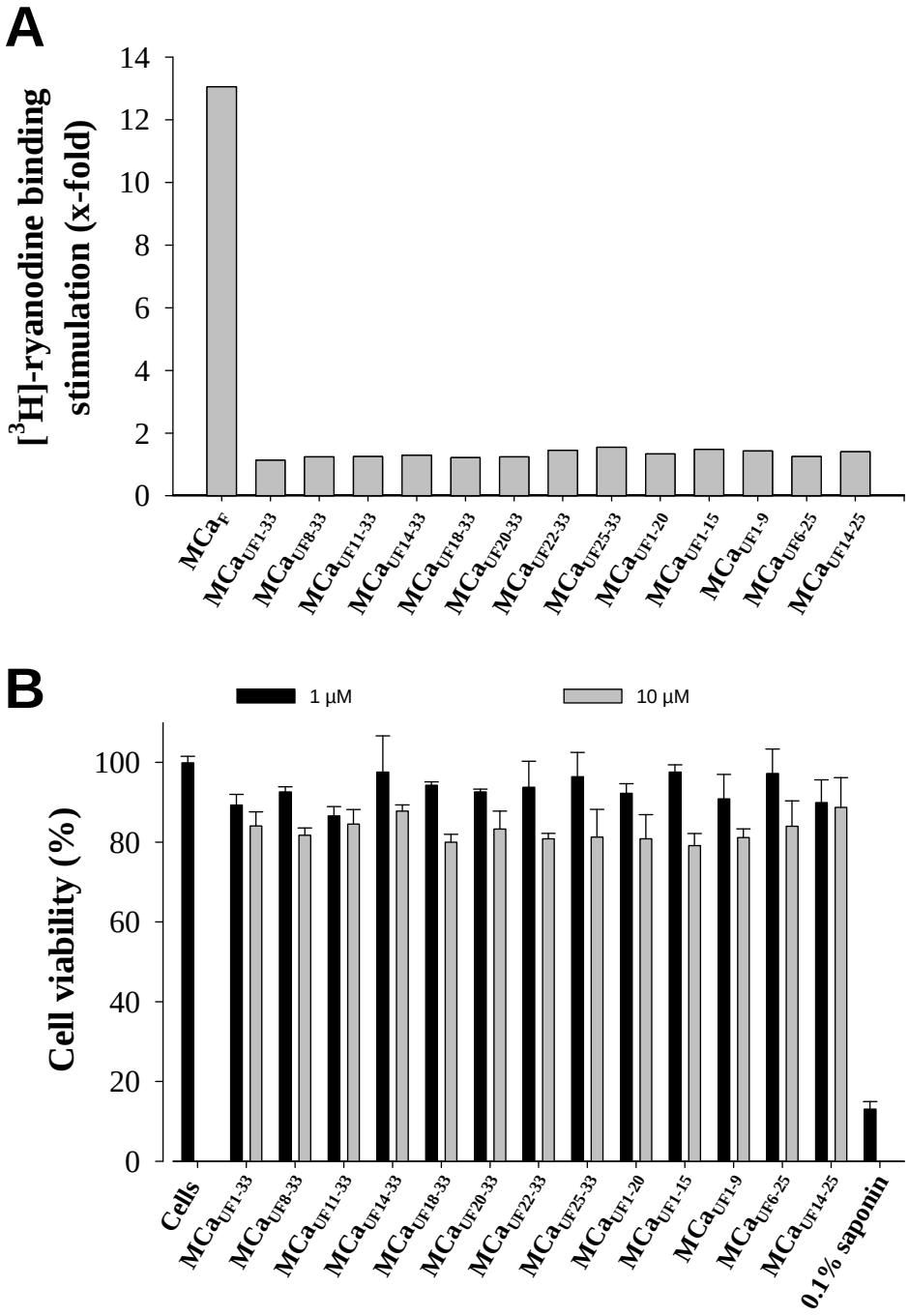
A
[3H]-ryanodine binding stimulation (x-fold)
0
2
4
6
8
10
12
14
MCaF
MCaUF1-33
MCaUF8-33
MCaUF11-33
MCaUF14-33
MCaUF18-33
MCaUF20-33
MCaUF22-33
MCaUF25-33
MCaUF1-20
MCaUF1-15
MCaUF1-9
MCaUF6-25
MCaUF14-25
B
1 µM
10 µM
Cell viability (%)
0
20
40
60
80
100
Cells
MCaUF1-33
MCaUF8-33
MCaUF11-33
MCaUF14-33
MCaUF18-33
MCaUF20-33
MCaUF22-33
MCaUF25-33
MCaUF1-20
MCaUF1-15
MCaUF1-9
MCaUF6-25
MCaUF14-25
0.1% saponin

b. Conclusion

C'est avec surprise que nous avons constaté que les treize analogues de la MCa synthétisés possédaient des propriétés de pénétration cellulaire. Ces analogues ont été synthétisés en délaitant des acides aminés en N-terminal (7 analogues : $MCaUF_{8-33}$-C, $MCaUF_{11-33}$-C, $MCaUF_{14-33}$-C, $MCaUF_{18-33}$-C, $MCaUF_{20-33}$-C, $MCaUF_{22-33}$-C et $MCaUF_{25-33}$-C), en C-terminal (3 analogues : $MCaUF_{1-20}$-C, $MCaUF_{1-15}$-C et $MCaUF_{1-9}$-C) ou les deux combinés (2 analogues : $MCaUF_{6-25}$-C et $MCaUF_{14-25}$-C). A part quelques analogues très prometteurs, les mini MCa bien que capables de pénétrer dans les cellules, sont néanmoins moins efficaces que la MCa. Cette constatation nous fait dire que la MCa est un peptide spécialisé dans la pénétration cellulaire, toutes les parties de sa séquence sont capables de transloquer dans les cellules. Fait important, tous les analogues testés ne présentent pas de toxicité majeure.

Il serait intéressant d'étudier l'affinité de la MCa, ainsi que de chaque analogue pour différents types cellulaire.

4. Article 3

Radiolabelling of Tyr-L-MCa by mono-iodination using the lactoperoxidase/H2O2 system

Mitra Ahmadi, Sandrine Martin, Marie-Dominique Desruet, Cathy Poillot, Laurent Riou, Julien Pecher, Michel De Waard, Daniel Fagret, Catherine Ghezzi

Article en cours de soumission

a. Introduction

Dans le but d'étudier la distribution *in vivo* de la MCa, ainsi que sa stabilité et son élimination une fois injecté chez l'animal, nous avons utilisé une technique de radio-marquage afin de suivre la MCa, le long de l'étude. La radio-iodination est une méthode de marquage commune pour l'étude des composés d'intérêt médicale.

Différentes techniques de marquage à l'iode existent. Après avoir utilisé une méthode à l'iodogene et une méthode à la chloramine-T qui nous ont donné des rendements très faibles, nous nous sommes tournés vers une méthode enzymatique, utilisant de la lactopéroxydase et de l'eau oxygénée. Afin de radio-iodiner la MCa, nous avons du synthétiser un analogue de la MCa contenant un résidu supplémentaire en N-terminal. L'atome d'iode vient se fixer en ortho de la fonction alcool de la tyrosine. Nous pouvons donc obtenir lors d'une iodination, un composé mono-iodé et un composé di-iodée du fait de l'accessibilité des deux positions en ortho de l'hydroxyle du résidu tyrosine. Afin d'obtenir un marquage à ^{125}I efficace, nous avons mis au point la méthode d'iodination en utilisant de l'^{127}I non radioactive, rendant ainsi possible un contrôle de la molécule obtenue par spectrométrie de masse. Une fois les bonnes conditions expérimentales obtenues, nous avons pu effectuer le marquage à l'^{125}I.

Radiolabeling of Tyr-L-MCa by mono-iodination using the lactoperoxidase/H_2O_2 system

Mitra Ahmadi[1,2*], Sandrine Martin[1,2], Marie-Dominique Desruet[1], Cathy Poillot[2,3], Laurent Riou[1,2], Julien Pecher[4], Michel De Waard[2,3], Daniel Fagret[1, 2] and Catherine Ghezzi[1,2]

[1]INSERM U1039, Radiopharmaceutiques Biocliniques, Université Joseph Fourier, Faculté de Médecine de Grenoble, 38700 La Tronche, Grenoble, France.

[2]Université de Grenoble 1, Grenoble, France

[3]INSERM U836, Grenoble Institute of Neuroscience, Bâtiment Edmond J. Safra, 38042 Grenoble, France.

[4]Smartox Biotechnologies, Bâtiment Biopolis, 5, avenue du Grand Sablon, 38700 La Tronche France.

* Send correspondance to Mitra Ahmadi: E-mail: mitra.ahmadih@yahoo.com - Phone: +33 (0)476 637 102 - Fax: +33 (0)476 637 142

ABSTRACT

Maurocalcine (MCa), a highly basic 33-mer peptide, is the first animal toxin acting as a cell-penetrating peptide. Radiolabeling of MCa would allow the determination of the biodistribution of this potent vector of therapeutic componds. Therefore, the aim of this study is to find the best conditions of mono-radioiodination of Tyr-L-MCa and to compare the influence of the ^{125}I labeling methodology on the radiochemical quality and stability of the radiolabeled peptide. An analogue of MCa containing a tyrosine residue was chemically synthesized by the solid-phase method in order to allow the iodination of the peptide. Three iodination methods (iodogen, chloramine-T or lactoperoxydase) were then evlauated. A High Performance Liquid Chromatography system (HPLC) equipped with a gamma detector and a MALDI-TOF were used to evaluate selected labeling methods and products. Radioiodination of MCa with current methods using Iodogene and Chloramine-T resulted in low radiochemical purity, whereas enzymatic labeling with lactoperoxidase in the presence of H_2O_2 led to a high yield of radiolabeling. We demonstrated that the best oxidant for radioiodination of Tyr-L-MCa is the enzymatic method. We showed that the iodine-lactoperoxydase-H_2O_2 system led to the formation of one or more iodinated-form depending on the reaction conditions as confirmed by MALDI-TOF analysis. We identified the best conditions for the mono-iodination of Tyr-L-MCa with high radiochemical purity and high stability without the need for a purification step.

INTRODUCTION

Maurocalcine (MCa) is a highly basic 33-mer peptide, isolated from the venom of the scorpion *Scorpio maurus palmatus*[1]. Twelve out of 33 residues of MCa are positively charged, because it contains only four negatively charged residues, the net global charge of the peptide is also positive. According to the ^{1}H NMR analysis, the peptide presents three disulfide bridges (Cys_3-Cys_{17}, Cys_{10}-Cys_{21} et Cys_{16}-Cys_{32}) and folds along an inhibitor cystine knot pattern. It contains three β-strands from amino acid residues 9-11 (strand 1), 20-23 (strand 2), and 30-33 (strand 3), respectively. The β-strands 2 and 3 form an antiparallel β-sheet. MCa efficiently binds to the ryanodine receptor in skeletal muscles and promotes channel opening and then calcium release from the sarcoplasmic reticulum. These observations suggested that MCa is able to cross the plasma membrane to reach its pharmacological target. We evidenced that a biotinylated derivative of MCa had the ability to trigger cell entry of fluorescent streptavidine[2]. It can be assure that MCa is a member of the exponentially growth family of cell penetrating peptide (CPP) because (i) MCa enters into cells, (ii) can be used for the cell entry of cargoes that would otherwise not enter cell. The precise determination of the biodistribution of MCa is of great importance considering its potential as a vector for the improved delivery of therapeutic compounds. Radiolabeling represents the most sensitive and quantitative method to follow whole-body distribution of a molecule of interest after in vivo administration. Radioiodination remains one of the most extensively used methods for labeling compounds of medical and biological interest either for *in vitro* radioligand investigations using ^{125}I[3] or for *in vivo* SPECT imaging using ^{123}I. Several direct and indirect iodination procedures have been previously described. The chloramine-T (CAT)[4,5], and Iodo-Gen® (1,3,4,6-tetrachloro-3a,6a-diphenylglycoluril)[6] methods are the most widely used direct labeling techniques for tyrosyl residues – containing compounds

whereas the enzymatic method using lactoperoxidase/H_2O_2 has been much less studied so far[7].

Radioiodination is based on the in situ oxidation of iodide to atomic iodine and its nucleophilic substitution into phenol rings in ortho position located in the hydroxyl group of tyrosyl residues of proteins. However, potential damage to target molecules is a matter of concern using the above-mentioned radiolabeling techniques. For example, a loss of immunological activity in proteins due to oxidation reagent action on disulphide bridges and sulfhydryl groups and the formation of a mixture of mono- and diiodotyrosine, often giving rise to macromolecular protein complexes, might be observed.

High radiochemical purity and stability of radioiodinated peptide are essential characteristics for a radiotracer to be used for *in vivo* administration. The objectives of the present study were to define the optimal radioiodination method and experimental conditions for the obtention of stable ^{125}I-labeled MCa with high radiochemical purity. The effects of different reaction parameters, such as duration, amount of iodide and oxidation reagent/iodide ratio on the production of mono- and di-iodinated peptide and iodination yield were investigated.

MATERIALS & METHODS

Materials

N-α-Fmoc-L-aminoacid, Wang-Tentagel resin and reagents used for peptide syntheses were obtained from Iris Biotech. Solvents were analytical grade products from Acros Organics. Acetonitrile was HPLC gradient grade from Fischer Scientific and trifluoroacetic acid (purum≥98%) from Fluka. IODO-GEN® pre-coated was purchased from Thermo Scientific, lactoperoxidase from bovine milk (80 U/mg) from Sigma (St Louis, MO), hydrogen peroxide

30% in water (w/w) from Carlo Erla and Na ^{125}I in dilution of (3700MBq/mL) from Perkin Elmer.

Solid-phase peptide syntheses

Chemical synthesis of Tyr-MCa was performed as previously described for other MCa analogues[8]. Briefly, Tyr-MCa was chemically synthesized by the SPPS method[9] using an automated peptide synthesizer (CEM© Liberty). Peptide chain was assembled stepwise on 0.24 mEq of Fmoc-L-Arg(Pbf)-Wang-Tentagel resin using 0.24 mmol of N-α-fluorenylmethyloxycarbonyl (Fmoc) L-amino-acid derivatives. The side-chain protecting groups were: Trityl for Cys and Asn, *tert*-butyl for Ser and Tyr, Thr, Glu and Asp, Pbf for Arg, and *tert*-butylcarbonyl for Lys. Reagents were at the following concentrations: 0.2 M Fmoc-amino-acids (Fmoc-AA-OH in dimethylformamide (DMF)), 0.5 M activator (2-(1H-benzotriazole-1-yl)-1,1,3,3-tetramethyluronium hexafluorophosphate in DMF), 2 M activator base (diisopropylethylamine in N-methyl-pyrrolidone (NMP)) and deprotecting agent (5% piperazine / 0.1 M 1-hydroxybenzotriazole in DMF), as advised by PepDriver (CEM©). After peptide chain assembly, the resin was treated 4 hrs at room temperature with a mixture of trifluoroacetic acid/water/triisopropylsilane (TIS)/1,4-dithiothreitol (DTT) (92.5/2.5/2.5/2.5). The peptide mixture was then filtered (to eliminate the resin) and the filtrate was precipitated by adding cold *t*-butylmethyl ether. The crude peptide was pelleted by centrifugation (10.000 × g, 15 min) and the supernatant was discarded. The reduced Tyr-MCA was submitted to oxidation for disulfide bridge formation in 0.1 M Tris/HCl buffer at pH 8.2 during 3 days at room temperature. Oxidized/folded Tyr-MCa was then purified by HPLC using a Vydac C18 column (218TP1010, 250×10 mm). Elution of the peptide was performed with a 10-60% acetonitrile linear gradient containing 0.1% trifluoroacetic acid over 40 min. The purity of the

purified fraction was analyzed by analytical RP-HPLC (Vydac C18 column 218TP104, 250 × 4.6 mm). Tyr-MCa was characterized by MALDI-TOF mass spectrometry.

Radiolabelling

Radioiodination of Tyr-L-MCa using Iodogen®. 5-50 µl of a solution of Iodogen® dissolved in dichloromethane (1mg/ml), were placed in 8 polypropylene tubes: tube 1-2 (5 µg, 11.5 nmoles), tubes 3-4 (25 µg, 57 nmoles), tubes 5-8 (50 µg, 115 nmoles). The organic solvent was then evaporated and the Iodogen® was left coated on the side of the tubes. 5-10 µl (18-37 MBq, 0.23-0.46 nmoles) of $Na^{125}I$ was added to the Iodogen® coated tubes containing 3 µL (10 µg, 2.5 nmol) of Tyr-L-MCa in saline, buffered by 50 µl of 50 mM phosphate buffer, pH 7.4, and the content of the tubes was mixed slowly. Different incubation times, from 10 min to 60 min, were tested and iodination reaction was then stopped by transferring the solution outside of the tube. The quality control of radiolabelled products was performed by RP-HPLC equipped by radiodetector (LabLogic) using a Vydac 218TP C18 column (10µm, 4.6*250mm). Tracer elution was achieved by applying a flow rate of 1mL/min by using the following eluents : eluent A was a mixture of H_2O–TFA 0.1% and eluent B contained acetonitrile 90%–TFA 0.1%. The gradient system started with 0% of B during 8.3 min, 0 -1 % B during 1.66 min, 1-10% B during 1.66min, 10- 60 % B during 33.2 min and 60-100% B during 1.66 min. The gradient remained at 100 % B for 8.3 min before switching back to 100% A during 8.3 min (total run time, 65 min).

Radioiodination of Tyr-L-MCa using chloramine-T. Chloramine-T (CAT) is commonly used in the radiolabelling, either as a solution or in an immobilized form (Iodobeads). In this study we have been chosen the method where CAT is immobilized on polymer beads (Iodobeads). Tyr-L-MCa was radio-iodinated using Chloramine-T method[4] with modifications. Briefly, 10 µl (37 MBq, 0.46 nmol) of $Na^{125}I$ was added to the reaction tube

and buffered by 50 µL of phosphate buffer (50 mM pH 7.4). 3 µL (10 µg, 2.5 nmol) ofTyr-L-MCa in saline following by an Iodobeads were added and then incubated for 5-15 min. To stop the labelling reaction, the coated beads was removed and quality control was performed by RP-HPLC as previously described.

Radioiodination of Tyr-L-MCa using lactoperoxydase. Condition I: 37 MBq (0.01 mL) of Na ^{125}I was added to 3 µL (10 µg, 2.5 nmoles) of Tyr-L-MCa in 50µL of phosphate buffer (50 mM, pH 7.4). The reaction was started by adding of 15 µL (0.25 mg/ml) lactoperoxidase and 10 µl H_2O_2 30% w/w (1: 10 000). After 2 minutes incubation at room temperature, a second amount of 10µl H_2O_2 30% w/w (1: 10000) was added and the reaction was allowed to proceed for 2 min. Condition II : the procedure is the same except the quantity of H_2O_2 (2*10µL, 1: 25 000). Condition III : 37 MBq (0.46 nmol) of Na ^{125}I was added to 3 µL (10 µg, 2.5 nmoles) of Tyr-L-MCa in 50µL of phosphate buffer (50mM, pH7.4). The reaction was allowed to proceed for 10 min at room temperature (RT) after addition of 7.5 µL (1.875µg, 0.25 mg/ml) lactoperoxidase and 20 µl H_2O_2 30% w/w (1: 50 000). Condition IV : the protocol is the same as condition 3 except in the amount of lactoperoxidase (4µg, 1 mg/ml) and H_2O_2 30% w/w (20 µL, 1: 50 000). A step of purification was conducted for the radiolabelled conditions 1-2, by use of an anion exchange cartridge (Waters-Oasis max). The column was activated with 1 ml of methanol and 1ml of normal saline. The radiolabelled Tyr-L-MCa was then eluted by 1ml of PBS while non-laballed $^{125}I^-$ was retained on column. For each condition, radioiodinated MCa was then analysed by RP-HPLC as previously described.

In vitro stability. All of the radioiodinated Tyr-L-MCa were incubated up to 24h at room temperature. HPLC analysis was then performed using the above mentioned conditions in order to determine the radiolabelling stability.

RESULTS

Chemical Synthesis of Tyr-MCa - The amino acid sequence and the expected disulfide bridge organization of Tyr-MCa are illustrated in Fig. 1*A*. Solid-phase chemical synthesis of Tyr-MCa was achieved stepwise on 0.24 mEq of Fmoc-L-Arg(Pbf)-Wang-Tentagel resin by means of an Fmoc strategy. The amount of targeted peptide linked to the resin was 0.1 mmol. The yield of peptide assembly was between 80-90%. A relative homogeneity of crude Tyr-MCa was obtained after TFA treatment as witnessed by analytical C_{18} reversed phase HPLC (Fig. 1*B*). Crude Tyr-MCa was then folded/oxidized for 72 hrs in alkaline conditions, and the main peptide was purified to >99% homogeneity by semi-preparative C_{18} reversed phase HPLC. The purity of Tyr-MCa is illustrated by analytical C_{18} reversed phase HPLC, and the folding/oxidation process is witnessed by the shift in elution time (Fig. 1*B*). MS analyses (MALDI-TOF technique) of crude and folded/oxidized Tyr-MCa provided experimental molecular masses $(M + H)^+$ of 4027.8 and 4021.8 Da, respectively. The shift in experimental molecular mass of 6 Da upon folding/oxidation is in agreement with the engagement of all six cysteine residues in the formation of three disulfide bridges.

Radioiodination of Tyr-L-MCa by Iodogen and Iodobeads methods

The main characteristics of radiolabeled Tyr-L-MCa that we wanted to optimize were the binding efficiency as determined by the effectiveness of the labelling of the radioisotope onto the Tyr-L-MCa and the stability of radiolabelling over time. Studies were performed in order to identify the parameters influencing these properties and to find the conditions for optimal radiolabelling conditions.

Radiolabeling efficiency in various conditions using Iodogen® and Chloramine T (Iodobeads) methods is shown in Fig. 2A. Each reaction mixture was analyzed by radio-HPLC without purification. We started the radiolabeling reactions with Iodogen method. Poor yields of the

radioiodination using this method were observed up to 60 min. A 10-fold increase in the oxidant agent concentration did not improve the radiochemical purity of labeling. On the other hand, a 2-fold decrease of specific activity, from 0.46 nmoles ^{125}I to 0.23 nmoles with the same Tyr-L-MCa quantity (2.5 nmoles) did not improve the final radiochemical purity. Two or more peaks on the HPLC profiles (between 25 to 37 minutes) of this group (Fig. 2B) showed several radioactive species correspond to mono-and di-iodinated Tyr-L-MCa and degradation products. The single peak of 4 min corresponds to free Iodine-125. Radiolabeling procedure was continued by CAT method using Iodobeads and no convincing results were obtained.

Radioiodination of Tyr-L-MCa by enzymatic method

Condition I: An enzymatic iodination of tyrosine using lactoperoxidase/H_2O_2 system was tested with condition I (as described in experimental section). A fairly good radiochemical purity (85%) was achieved from the first test. However, this radioiodinated Tyr-L-MCa was purified on an anionic resin to remove the 15% free ^{125}I. After purification, we have been observed 2 major peaks at 30 min and 34 min on the radio-HPLC profile (Fig 3A). The purified sample was analyzed 24h after radiolabeling and deiodination was observed. More than 80% of radioiodinated peptide was decomplexed and a major peak of free ^{125}I appeared (Fig 3B). To confirm the species formed during radiolabeling, an iodination with I-127 was used. Following iodination of Tyr-L-MCa with iodine-127 in the same condition than those used for labeling, the sample was analyzed by RP-HPLC. Three major peaks were observed on the RP-HPLC profile (Fig. 4A). Each fraction was collected and identified by MALDI-TOF. Mass analysis confirmed the presence of the non iodinated (Fig. 4B) and mono-iodinated (Fig. 4C) Tyr-L-MCa as well as that of a third peak (Fig. 4D) corresponding to di-iodinated Tyr-L-MCa as well as to other unidentifiable fractions.

Condition II: Reaction conditions such as concentration of lactoperoxydase and concentration and frequency of addition of hydrogen peroxide markedly affected the yield and quality of the radioiodinated protein. H_2O_2 concentration of reaction was therefore reduced from 200 µM to 80 µM. Reducing H_2O_2 concentration while keeping the same frequency of adding of H_2O_2 and same incubation time (2*2min) resulted in a 75% radiochemical purity immediately after reaction, which confirmed the need for purification. The purified ^{125}I- Tyr-L-MCa (95% of radiochemical purety) remained stable for 24h with radiochemical purity higher than 90%.

Condition III: It has been previously demonstrated that the longer the time of the incubation, the greater the risk of potential damage to the protein. Thus, it is best to keep the time of exposure of the protein to the radioactive iodide and oxidant reagent as short as possible, but commensurate with a good yield of radioactive product. In third condition, both H_2O_2 concentration of reaction and lactoperoxydase concentration were reduced from 80 to 40 µM and from 38.3 µg/ml to 20 µg/ml, respectively, whereas the incubation time was increased from 4 min (2 x 2 min) to 10 min (1 x 10 min). High radiochemical purity (>95%) was achieved. HPLC profile of this radiolabelled Tyr-L-MCa showed 5% free ^{125}I and 95% of a mixture of mono and di-iodinated Tyr-L-MCa. Each peak of ^{125}I-MCa was collected and analysed by MALDI-TOF. The presence of mono and di-iodinated MCa was confirmed (results not shown). HPLC analysis of radiolabeled peptide 24h after radiolabelling showed 40% radiochemical purity. The concentration of lactoperoxidase (20 µg/ml) was too low which resulted in time-dependent deiodination

Condition IV: In order to improve the third condition and to decrease the presence of di-iodinated Tyr-L-MCa H_2O_2 concentration of reaction was further decreased from 40 µM to 25 µM while keeping the lactoperoxidase concentration at 38.3 µg/ml and the frequency of adding of H_2O_2 at one time. Incubation time was increased to 20 minutes (Fig. 5A). Radiochemical purity higher than 95% was achieved without the need for a purification step.

HPLC profile at 24h after radiolabelling showed a high stability for radiolabelled Tyr-L-MCa. A single peak corresponding to mono-iodinated Tyr-L-MCa was observed (Fig. 5B).

DISCUSSION

MCa is the first example of a folded and oxidized peptide toxin acting as a cell penetrating peptide. The precise determination of the biodistribution of MCa is of great importance considering its potential as a vector for the improved delivery of therapeutic compounds. Radiolabeling represents the most sensitive and quantitative method to follow whole-body distribution of a molecule of interest after in vivo administration. The main findings of the present study indicated that stable ^{125}I-labeled MCa could be obtained with high radiochemical purity.

Tyr-MCa was synthesized for the first time for the present report. Chemical synthesis and folding/oxidation conditions were not affected by the extra tyrosine residue placed at the N-terminus. No particular change in folding condition was required, suggesting that alterations in the amino-terminal sequence of maurocalcine does not impact folding and oxidation of the peptide. The position of this extra tyrosine residue ensures that iodination occurs in a convenient way, without accessibility problems and also without modification of the native sequence. Hence, the probability that Tyr-MCa preserves the same activity than MCa is high.

In this study, the goal of any radiosynthesis methodology is to produce the radiotracer with a high radiochemical yield, high radiochemical purity and high specific activity [10, 11, 12] without the need for purification. Methods for direct radiolabeling of tyrosine residues in peptides with ^{125}I typically rely on basic approaches, which differ in the strength of the reaction process. The non-water soluble Iodogen is a mild oxidant and may be safe for maintaining the structure and function of a protein. This methodology can be used for a wide range proteins and peptides and theoretically allows iodine incorporation with minimum oxidation damage

while leading to relatively stable radiotracers[6]. The kinetics of iodogen-mediated labelling are slower than those observed with CAT, though maximum yields can be obtained as early as 30 min [13]. It should be noted that stronger oxidation typically involves the use of chloramine-T or freshly prepared Iodogen®. The method, using CAT as oxidant, is easy, rapid and maximum labelling yields can be obtained within a few minutes but CAT in solution is a rather potent oxidant and its use may cause disruption of disulfide bonds and loss of function of sensitive proteins. In the present study iodination coated beads were therefore used in order to avoid the damaging oxidative effects normally associated with chloramine-T in solution. Comparatively, gentle oxidation is achieved through enzymatic reactions. This method employs lactoperoxidase in the presence of a trace of hydrogen peroxide to oxidise ^{125}I and to produce the reactive species. Although, this technique should result in a lower probability of denaturation of susceptible proteins than observed using the CAT or Iodogen methods. It is more technically demanding and is subject to a more marked variation in optimum reaction conditions. For Tyr-L-MCa, the preferred method should involve a balance between yield and instability after oxidation. As a rule, as oxidative lability increases, more gentle methods are selected.

Covalent labelling of the peptide directly with ^{125}I involves oxidative generation of cationic iodine (I^+) and its spontaneous electrophilic addition to tyrosine residue. The main substitution is a monoiodotyrosyl residue, although di-iodotyrosyl residues may also be formed. The concentration of reagents should allow the tyrosine residue to be only mono ^{125}I-labelled and not di-^{125}I-labelled because (i) during iodination, incorporation of two iodines atoms on the same tyrosine residue or two different residues (for example histidine residue or another tyrosine residue) can be observed. We observed that the second labeled radioiodine, di-iodinated or bi-iodinated Tyr-L-MCa, degrades rapidly and makes instability while monoiodinated Tyr-L-MCa (condition IV) remained stable at least for 48h. (ii) Iodine is a

bulky atom that can disturb the tridimensional structure of the molecule or cause steric hindrance resulting in a decreased affinity of the targeting molecule for its specific binding sites. The problem is sometimes proportional to the number of radioisotopes added to the molecule [14]. Loot and al. [15] have showed that for iodine-labeled angiotensin analogs, only the mono-iodinated $Ang_{(1–7)}$ peptide can be used as a radioligand since di-iodinated species exhibit a 10-fold lower receptor binding activity with concomitant loss of AngII displacing potency. Another study confirmed that ligand–receptor interaction enhancement was found for radioiodinated urotensin II (UII) with its native or transfected UT receptor [16]. But the di-iodinated UII peptide, [di-iodo-Tyr^9]$UII_{(4–11)}$, behaved as a partial agonist [17].

Three method of iodination (iodogen, chloramine-T or lactoperoxydase) were evaluated in the present study in order to find the best radiosynthesis of Tyr-L-MCa with ^{125}I. The Iodogen and Iodobeads methods were initially evaluated. These strategies revealed unsatisfactory because they lead to a low radiochemical purity and also a mixture of radiolabelled species. On the opposite, the enzymatic method appeared best suited for MCa radiolabelling. Indeed, ^{125}I incorporation into the peptide was better than that observed using other methods from the first condition tested. However, a purification step was necessary and MALDI-TOF analysis indicated a mixture of undesired radioactive products. To optimize radiolabeling towards mono-iodination, the H_2O_2 concentration was modified (condition II), which resulted in a reduction of the radiochemical purity of 85% to 75%. In this second condition, the purification of a radiolabelled peptide is still mandatory, which is suboptimal because of the resulting imprecision regarding peptide concentration. Therefore, further modifications in the lactoperoxydase and H_2O_2 concentration, incubation time and frequency of addition of H_2O_2 were performed in Condition III. A minimum of 38.3 µg/ml of lactoperoxidase was needed to form a ^{125}I-tyrosyl stable bound. Finally, the best oxidant concentration for radioiodination of Tyr-L-MCa using the enzymatic method was determined in condition IV. We showed that the

minimum concentration necessary of lactoperoxidase and H_2O_2 must be determined in order to synthetize a monoiodinated peptide with high stability and radiochemical purity without the need for purification.

Conclusion

The iodination of Tyr-L-MCa was studied using a variety of iodination methods. Reversed phase (HPLC and MALDI-TOF were used to analyze and to identify the reaction products. The enzymatic method using lactoperoxidase-hydrogen peroxide system provided excellent results in terms of radiochemical purity of mono-iodinated Tyr-L-MCa, stability and reproducibility. The resulting mono-iodinated peptide will be valuable for the investigation of the *in vivo* kinetics of MCa.

REFERENCES

1. Mosbah, A., Kharrat, R., Fajloun, Z., Renisio, J.G., Blanc, E., Sabatier, J.M., El Ayeb, M., Darbon, H. (2000) A new fold in the scorpion toxin family, associated with an activity on a ryanodine-sensitive calcium channel. *Proteins. 40(3),* 436-42.

2. Estève, E., Mabrouk, K., Dupuis, A., Smida-Rezgui, S., Altafaj, X., Grunwald, D., Platel, J.C., Andreotti, N., Marty, I., Sabatier, J.M., Ronjat, M., De Waard M. (2005) Transduction of the scorpion toxin maurocalcine into cells. Evidence that the toxin crosses the plasma membrane. *J Biol Chem, 280(13),* 12833-12839.

3. Efimova, Y. M., Wierczinski, B., Haemers, S. and an Well, A. A. (2005) Changes in the secondary structure of proteins labeled with ^{125}I: CD spectroscopy and enzymatic activity studies. *Journal of Radioanalytical and Nuclear Chemistry, 264(N°1),* 91-96.

4. Hunter, W.M., Greenwood, F.C. (1962) Preparation of iodine-131 labelled human growth hormone of high specific activity. *Nature, 194*, 495–496.

5. Hussain,A. A., Jona, J. A., Yamada, A. and Dittert L. W. Chloramine-T in radiolabeling techniques. II. (1995) A nondestructive method for radiolabeling biomolecules by halogenation. *Analytical Biochemistry, 224,* 221-226.

6. Salacinski, P.R.P., McLean, C., Sykes, J.E.C., Clement-Jones, V.V., Lowry, P.J. (1981) Iodination of proteins, glycoproteins, and peptides using a solid-phase oxidizing agent, 1,3,4,6-tetrachloro-3α,6α-diphenyl glycoluril (Iodogen). *Anal. Biochem., 117(1),* 136–146.

7. Marchalonis, J.J. (1969) An Enzymic Method for the Trace lodination of Immunoglobulins and other Proteins. *Biochem. J., 113,* 299–305.

8. Poillot, C., Dridi, K., Bichraoui, H., Pêcher, J., Alphonse, S., Douzi, B., Ronjat, M., Darbon, H., De Waard, M. (2010) D-Maurocalcine, a pharmacologically inert efficient cell-penetrating peptide analogue. *J Biol Chem. 285 (44),* 34168-34180.

9. Merrifield RB. (1969) Solid-phase peptide synthesis. *Adv Enzymol Relat Areas Mol Biol., 32*, 221-296.

10. Coenen, H. H., Mertens, J., Maziere, B., Radioiodination Reactions for Pharmaceuticals - *Compendium for Effective Synthesis Strategies Dordrecht*, The Netherlands , Springer, 2006 1-4020-4560-3

11. Eersels, J.L.H., Travis, M.J., Herscheid, J.D.M (2005) Manufacturing I-123-labelled radiopharmaceuticals. Pitfalls and solutions. *J Labelled Compd Radiopharm, 48,* 241-257.

12. Hutchins, G.D., Miller, M.A., Soon, V.C., Receveur, T. (2008) Small animal PET imaging. *ILAR J, 49,* 54–65.

13. Tolmachev, V. and Stone-Elander, S. (2010) Radiolabelled proteins for positron emission tomography: Pros and cons of labelling methods. *Biochimica et Biophysica Acta, 1800(5),* 487-510

14. Fu, Y., Létourneau M., Chatenet, D., Dupuis, J. and Fournier, A. (2011) Characterization of iodinated adrenomedullin derivatives suitable for lung nuclear medicine. Nuclear Medicine and Biology , *article in press.*

15. Loot, A.E., Van Buiten, A., Roks, A.J., Henning, R.H. (2005) The suitability of iodinated Angiotensin-(1-7) peptides as pharmacological tools. *J Pharmacol Toxicol Methods, 51*, 51-55.

16. Leprince, J., Chatenet, D., Dubessy, C., Fournier, A., Pfeiffer, B., Scalbert, E., Renard, P., Pacaud, P., Oulyadi, H., Ségalas-Milazzo, I., Guilhaudis, L., Davoust, D., Tonon, M.C., Vaudry, H. Peptides. (2008) Structure-activity relationships of urotensin II and URP. *Peptides, 29 (5),* 658–673.

17. Batuwangala, M., Camarda, V., McDonald, J., Marzola, E., Lambert, D.G., Ng, L.L., Calo', G., Regoli, D., Trapella, C., Guerrini, R., Salvadori, S. (2009) Structure-activity relationship study on Tyr9 of urotensin-II(4-11): identification of a partial agonist of the UT receptor. Peptides, 30(6), 1130–1136.

FIGURE LEGENDS

Figure 1. Chemical synthesis of Tyr-MCa. (A) *A*mino acid sequence of Tyr-MCa in single-letter amino acid code. The positions of half-cystine residues are numbered and colored in red. The disulfide bridge organization of Tyr-MCa, as expected from the connectivity of MCa, is illustrated by red lines. (B) *A*nalytical C_{18} reversed phase HPLC profile of Tyr-MCa at different stages of its chemical synthesis (black line, crude reduced peptide; red line, purified Tyr-MCa 72 hrs after folding and oxidation as witnessed by the shift in elution time. *Insets*, mass spectra of reduced (black line, right) and oxidized (red line, left) Tyr-MCa. Note the mass reduction of 6 Da that correspond to the formation of three disulfide bridges.

Figure 2. Comparison of the effectiveness of the iodination ^{125}I on Tyr-L-MCa using current methods. (A) Chemical iodination using Iodogen (conditions 1-8) and Iodobeads (conditions 9-10). (B) A typical radiochromatogram obtained by radioiodination using Iodogen.

Figure 3. Enzymatic iodination in the presence of lactoperoxydase-H_2O_2 system, condition I as described in experimental section. Radiochromatogram immediately after radiolabelling and purification (A) and 24h after radiolabelling (B).

Figure 4. RP-HPLC and MS analysis for characterization of mono- and di-iodinated form. (A) RP-HPLC profile of ^{127}I-Tyr-L-MCa with non-iodinated, mono-iodinated and mixture of di-iodinated and degradation products, respectively. Mass spectrum of ^{127}I- Tyr-L-MCa : non-iodinated form (B), mono-iodinated form (C) and di-iodinated with presence of degradation products (D).

Figure 5. Effect of lactoperoxidase and/or H_2O_2 concentrations on the effectiveness of the iodination. (A) Radiochemical purity of L-Tyr-MCa before purification, after purification and after 24h of radiolabelling for 4 conditions of iodination depending on various concentrations of lactoperoxydase and H_2O_2, and also incubation time. (B) Radiochromatogram immediately after radiolabelling with the fourth condition, as described in experimental section.

FIGURE 1.

A

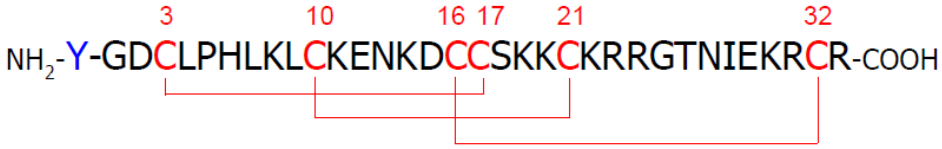
3
10
16 17
21
32
NH2-Y-GDCLPHLKLCKENKDCCSKKCKRRGTNIEKRCR-COOH

B

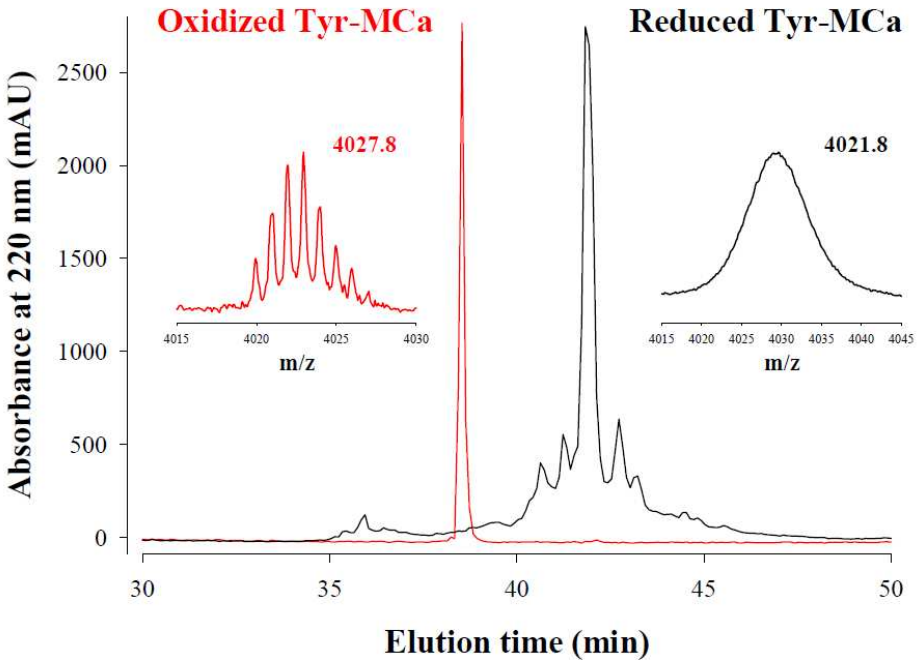
Oxidized Tyr-MCa
Reduced Tyr-MCa
4027.8
4021.8
m/z
m/z
Absorbance at 220 nm (mAU)
Elution time (min)

FIGURE 2.

A

	Oxydant	Tyr-L-MCa	I-125	Oxydant quantity	Incubation time	^{125}I-MCa (%)
1	Iodogen	10 µg (2.5 nmol)	37 MBq (0.46 nmole)	5 µg (11.5 nmol)	10 min	< 10%
2	Iodogen	10 µg (2.5 nmol)	37 MBq (0.46 nmole)	5 µg (11.5 nmol)	60 min	35%
3	Iodogen	10 µg (2.5 nmol)	37 MBq (0.46 nmole)	25 µg (57 nmol)	30 min	64%
4	Iodogen	10 µg (2.5 nmol)	37 MBq (0.46 nmole)	25 µg (57 nmol)	60 min	67%
5	Iodogen	10 µg (2.5 nmol)	37 MBq (0.46 nmole)	50 µg (115 nmol)	30 min	21%
6	Iodogen	10 µg (2.5 nmol)	37 MBq (0.46 nmole)	50 µg (115 nmol)	60 min	35%
7	Iodogen	10 µg (2.5 nmol)	18 MBq (0.23 nmole)	50 µg (115 nmol)	30 min	52%
8	Iodogen	10 µg (2.5 nmol)	18 MBq (0.23 nmole)	50 µg (115 nmol)	60 min	36%
9	Iodobeads	10 µg (2.5 nmol)	18 MBq (0.23 nmole)	1 iodobeads	5 min	33%
10	Iodobeads	10 µg (2.5 nmol)	18 MBq (0.23 nmole)	1 iodobeads	15 min	32%

B

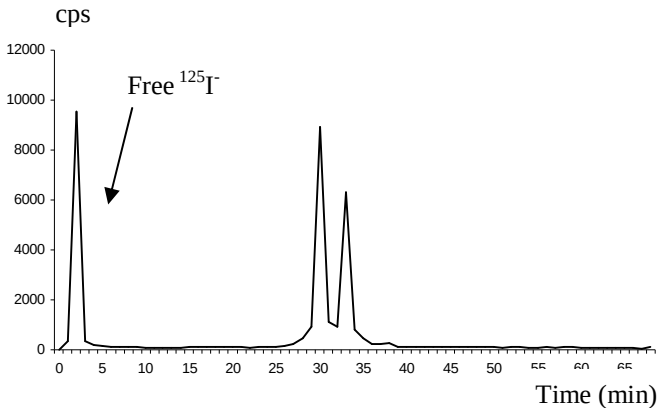

FIGURE 3.

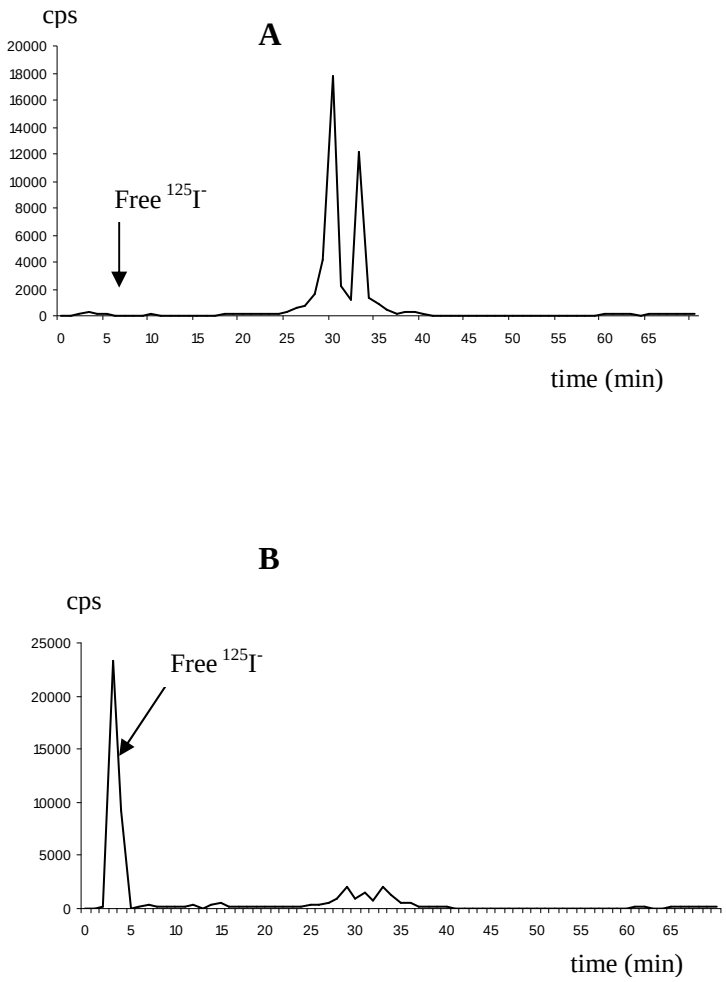
A
cps
20000
18000
16000
14000
12000
10000
8000
6000
4000
2000
0
Free $^{125}I^-$
0 5 10 15 20 25 30 35 40 45 50 55 60 65
time (min)
B
cps
25000
20000
15000
10000
5000
0
Free $^{125}I^-$
0 5 10 15 20 25 30 35 40 45 50 55 60 65
time (min)

FIGURE 4.

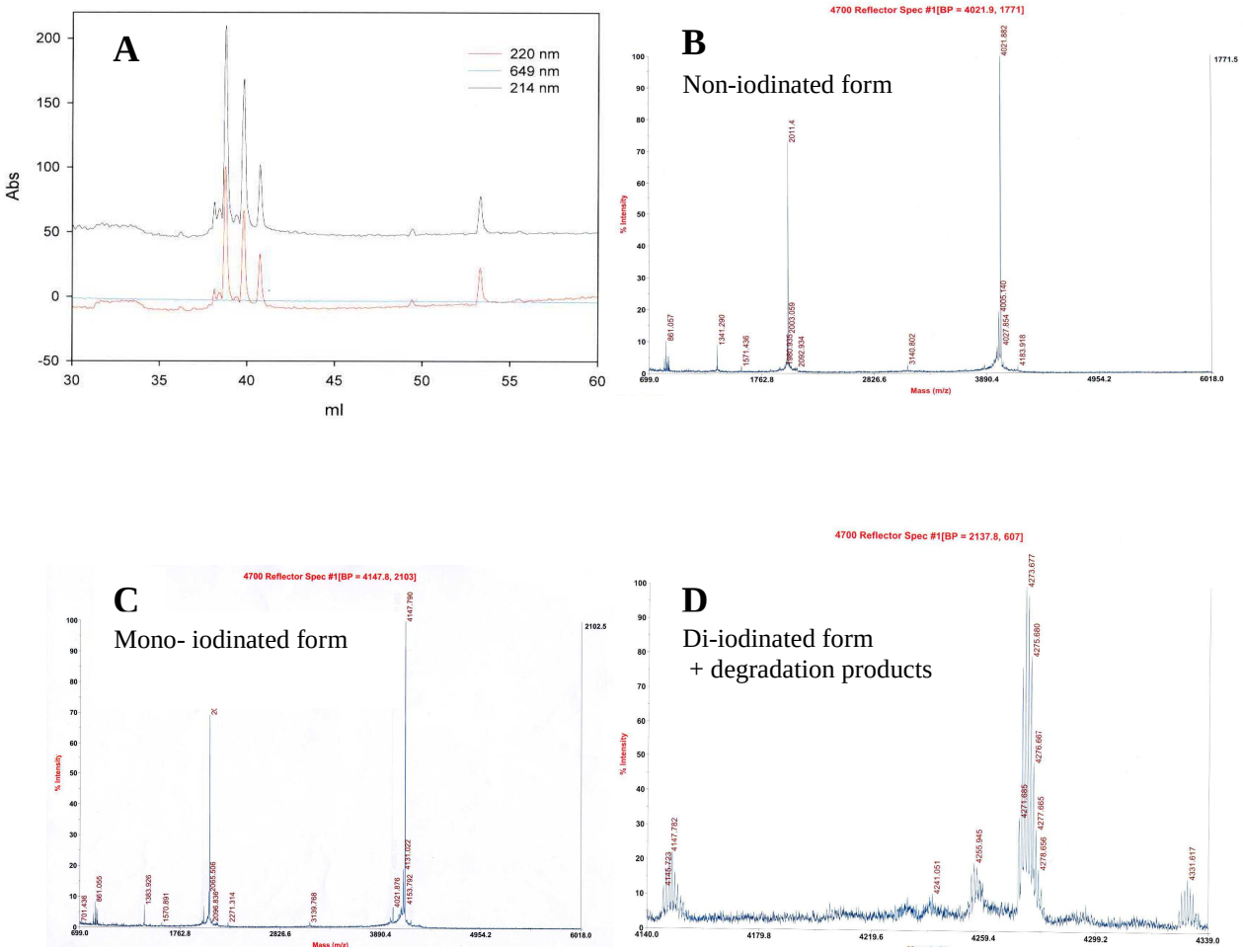
A
220 nm
649 nm
214 nm
Abs
ml
B
Non-iodinated form
4700 Reflector Spec #1[BP = 4021.9, 1771]
% Intensity
Mass (m/z)
C
Mono- iodinated form
4700 Reflector Spec #1[BP = 4147.8, 2103]
D
Di-iodinated form
+ degradation products
4700 Reflector Spec #1[BP = 2137.8, 607]

FIGURE 5.

A

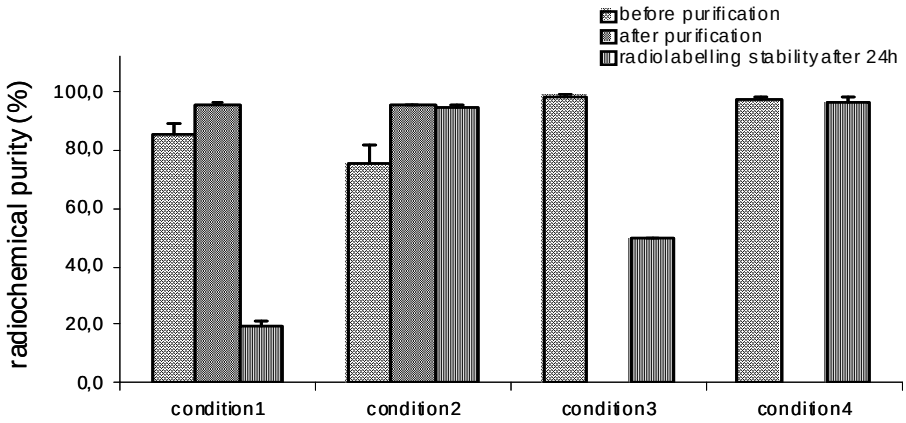

Lactoperoxydase (µg/ml)	38.3	38.3	20	38.3
H_2O_2 (µM)	200	80	40	25
Incubation time (min)	2*2	2*2	10	20

B

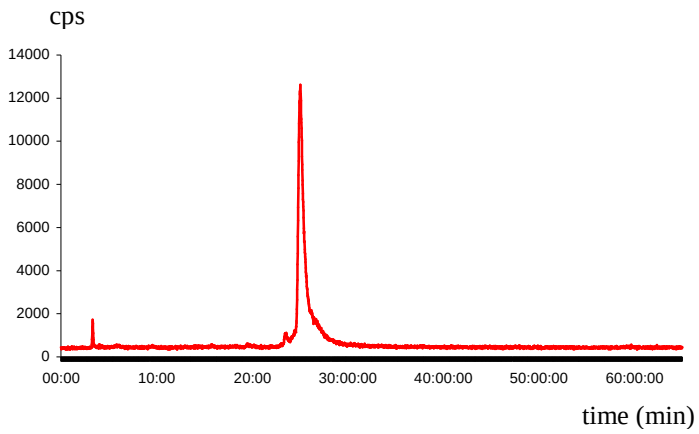

b. Conclusion

Différentes approches ont été testées afin d'obtenir un rendement de marquage le plus élevé et une stabilité radiochimique acceptable. La méthode la plus performante étant celle utilisant de la lactopéroxydase et de l'eau oxygénée. Nous avons ainsi pu obtenir un rendement de radio-marquage supérieur à 95%, ce qui nous a affranchi d'une étape supplémentaire de purification pour séparer le composé voulu de la Tyr-MCa non marquée ou du composé di-iodé. De plus, la méthode obtenue permet d'avoir un marquage stable dans le temps. Après 24 hrs, un pic unique est visible par chromatographie liquide, indiquant que la MCa ne s'est pas dégradée et qu'aucun atome d'iode ne s'est détaché de la Tyr-MCa. La tyrosine surnuméraire n'affecte pas le repliement de la MCa pour la formation de ses trois ponts disulfures et n'inhibe pas non plus les propriétés de pénétration cellulaire de la MCa comme l'ont montré des expériences de pénétration dans des cellules CHO (données non montrées dans l'article). Nous avons ainsi obtenu un dérivé de MCa avec lequel nous pourrons faire des études de biodistribution et de clairance, afin d'étudier le comportement de la MCa en *in vivo*. Enfin, cette méthode permettra d'effectuer des quantifications de la pénétration cellulaire, mais aussi des expériences de binding sur le récepteur à la ryanodine.

5. Article 4

In Vivo Biodistribution of Maurocalcine in CD-1 Mice

Cathy Poillot, Laurent Riou, Mitra Ahmadi, Sandrine Martin, Catherine Ghezzi, Michel De Waard

Article en cours de soumission

a. Introduction

Après avoir utilisé la MCa comme vecteur cellulaire pour différents composés, nous nous sommes intéressés à la biodistribution de la MCa ainsi qu'à sa clairance. Nous savons que la MCa n'est pas toxique, même à des concentrations très élevées, alors que la pénétration cellulaire s'effectue à des concentrations assez faibles, ceci nous indique que cet aspect ne sera pas limitant pour des futures applications thérapeutiques. Les informations sur les propriétés de la MCa *in vivo* obtenues lors de cette étude seront très utiles avant d'envisager des applications cliniques de ce vecteur prometteur. De plus, la MCa, grâce à la présence de trois ponts disulfures, possède une grande stabilité, une propriété souhaitable pour les applications *in vivo*. Nous avons pu faire le suivi de la MCa en ajoutant un résidu tyrosine à sa séquence, puis en la marquant à l'iode 125. Le peptide marqué ^{125}I-Tyr-MCa, peut ensuite être suivi dans le sang par analyse par chromatographie et dans les organes par imagerie nucléaire. Nous pouvons donc obtenir la durée de stabilité de la ^{125}I-Tyr-MCa dans le sang et la quantité de ^{125}I-Tyr-MCa dans les différents organes.

In Vitro Radiolabeling and In Vivo Biodistribution of Maurocalcine in CD-1 Mice

Cathy Poillot[1,2], Mitra Ahmadi[1,3], Laurent Riou[1,3], Sandrine Martin[1,3], Julien Pecher[4], Daniel Fagret[1,5], Catherine Ghezzi[1,3] & Michel De Waard[1,2,4,*]

[1]Université Joseph Fourier, Grenoble, France.

[2]INSERM U836, Grenoble Institute of Neuroscience, Bâtiment Edmond J. Safra, 38042 Grenoble, France.

[3]INSERM U877, Radiopharmaceutiques Biocliniques, Grenoble, France.

[4]Smartox Biotechnologies, Bâtiment Biopolis, 5, avenue du Grand Sablon, 38700 La Tronche France.

[5]INSERM 1039, Pôle Imagerie, Clinique Universitaire de Médecine Nucléaire, CHU de Grenoble, 38043 Grenoble, France.

* Send correspondance to MDW: E-mail: michel.dewaard@ujf-grenoble.fr - Phone: +33 0 4 56 52 05 63 - Fax: +33 4 56 52 06 37

Abstract

Maurocalcine is the first natural cell penetrating peptide to be discovered in animal venom. While maurocalcine is a potent vector for the cell penetration of structurally diverse therapeutic compounds, a property that it shares with other cell penetrating peptides, it has also several distinguishing features that should make it become a peptide of choice for clinical and biotechnological applications. Its binding site on its natural pharmacological target is of cytoplasmic location indicating that membrane translocation rather than endocytosis is its preferred route of cell entry. The peptide is amazingly non toxic, even at high concentrations, and cell penetration occurs at rather low concentration, suggesting that *in vivo* toxicity should not be an issue. Finally, the peptide is folded thanks to the presence of three disulfide bridges, conferring an unusual stability to the peptide, a property that we assume to be desirable for *in vivo* applications. In this study, we aimed at gaining new important information about the properties of maurocalcine *in vivo*; information that will be valuable before envisioning clinical applications of this vector. We demonstrate that i) it is possible to stably iodinate a Tyr-grafted analogue of maurocalcine, ii) the peptide is highly stable *in vitro* and *in vivo* following i.v. injection, and iii) the disulfide bridges confer a definitive competitive advantage for the *in vivo* stability of the peptide over a non folded Tyr-grafted maurocalcine. Further stability can be introduced in the peptide if it is produced with D-amino acids rather than L-amino acids. Finally, we evaluate the biodistribution of [^{125}I]-Tyr-maurocalcine following *in vivo* injection to CD-1 mice and define the route of elimination of the peptide.

Introduction

Maurocalcine (MCa) is a 33 amino acid peptide that was identified in 2000 by the Institut Pasteur of Tunis from the venom of the Tunisian scorpion *Scorpio maurus palmatus* (*1*). The peptide was bearing exquisite amino acid sequence resemblance with imperatoxin A, a toxin isolated from Pandinus

imperator, another scorpion species, and active on the ryanodine receptor type 1 (RyR1) (*2*). This observation had prompted us to investigate the interaction of MCa with RyR1 and, sure enough, the peptide was found active on the channel according to several technical approaches. Indeed, MCa was found to (i) increase Ca^{2+} efflux from the sarcoplasmic reticulum (*3*), (ii) increase the open probability and promote a long-lasting subconductance level of RyR1 channel activity (*4-6*), and (iii) stimulate [^{3}H]-ryanodine binding by virtue of its effect on channel activity (*3*). Owing to the fact that RyR1 is a calcium channel located within the membrane of the endoplasmic reticulum and that the binding site of MCa on RyR1 has been located within a domain predicted to be present in the cytoplasm (*7*), MCa was suspected to cross the plasma membrane and to easily reach the cytoplasm in order to implement its effect on RyR1. In agreement, external application of MCa rapidly triggers cytoplasmic Ca^{2+} elevation in myotubes even in the absence of external Ca^{2+}, demonstrating that the rise in Ca^{2+} concentration finds its origin from the mobilization of internal Ca^{2+} sources (*8*). Finally, the confounding evidence that the coupling of biotinylated derivative of MCa to streptavidin tagged with a fluorescent dye, leads to fluorescence accumulation in a variety of cell types, was the first demonstration that MCa could act as a peptide vector for the cell entrance of a cargo (*8*). Further attempts to understand how MCa may proceed to enter into cells and reach its pharmacological target lead to the identification of glycoaminoglycans and negatively charged phospholipids as membrane receptors of MCa (*9*). At the structural level, MCa folds according to an inhibitor cysteine knot motif and contains three well-defined β-strands (*1*). The secondary structures are constrained by three disulfide bridges with a pattern of connectivity forming the unusual knot. One particularity of MCa is that it is heavily charged owing to the presence of many basic amino acid residues (mainly lysine amino acids). This property, along with the fact that MCa has the ability to induce cell penetration of a variety of cargoes (*10-14*), led to the conclusion that MCa was the first identified toxin member of the large structurally-unrelated family of cell penetrating peptides (CPP). CPP are becoming increasingly popular to those that wish to utilize a vector for the cell entry of a cargo that would otherwise not enter cells. As such, MCa demonstrated

excellent vector properties for quantum dots, peptides, or drugs, and promising applications are envisioned in oncology (*10, 15-18*). While MCa is recognized as a competitive CPP, because of its low concentration efficacy and its ability to reach the cytoplasm, where most cargos should be addressed, many of our efforts focused on getting MCa analogues deprived of undesirable pharmacological effects but with high cell penetration properties. Luckily, this task of designing cell penetrating MCa analogues unable to bind RyR1 was considerably eased by the stringent structural requirements for RyR1 binding. This stringency was not found at all for cell penetration. Hence, all of the strategies tested so far provided cell penetrating competent analogues that lacked RyR1 binding: (i) point mutation of MCa (*19*), (ii) hindering disulfide bridged formation and hence secondary structure formation (*14*), and (iii) synthesis of the diastereoisomer of MCa, D-MCa (*13*).

While the design of good CPP derived from MCa has come to maturity, it now seems obvious that these vectors have great potential for the intracellular delivery of important therapeutic or diagnostic compounds *in vivo*. By essence, venomous toxins are delivered *in vivo* and are tailored to survive enough time within the blood stream of animal preys until the pharmacological potential of these molecules has been fully exploited. The presence of disulfide bridges appears to represent a strong asset for the *in vivo* stability of these molecules. To investigate the *in vivo* properties of MCa, we first synthesized a Tyr-tagged MCa for *in vitro* radio-iodination. We next studied the metabolic stability of the ^{125}I-labeled peptide in blood both *in vitro* and *in vivo*, and followed its body distribution. We finally investigated the routes of elimination of the peptide. This study will help delineating the type of *in vivo* application in which MCa can be used for intracellular delivery and the type organ that can be targeted. Our data demonstrate the wonderful stability of MCa *in vivo* and further highlight the advantages to use MCa for cell delivery purposes rather than other popular CPP.

Materials and Methods

Reagents

N-α-Fmoc-L-aminoacid, Wang-Tentagel resin and reagents used for peptide syntheses were obtained from Iris Biotech. Solvents were analytical grade products from Acros Organics.

Solid-phase peptide syntheses

Chemical synthesis of Tyr-MCa was performed as previously described for other MCa analogues (*13*). Briefly, Tyr-MCa was chemically synthesized by the SPPS method (*20*) using an automated peptide synthesizer (CEM© Liberty). Peptide chain was assembled stepwise on 0.24 mEq of Fmoc-L-Arg(Pbf)-Wang-Tentagel resin using 0.24 mmol of N-α-fluorenylmethyloxycarbonyl (Fmoc) L-amino-acid derivatives. The side-chain protecting groups were: Trityl for Cys and Asn, *tert*-butyl for Ser and Tyr, Thr, Glu and Asp, Pbf for Arg, and *tert*-butylcarbonyl for Lys. Reagents were at the following concentrations: 0.2 M Fmoc-amino-acids (Fmoc-AA-OH in dimethylformamide (DMF)), 0.5 M activator (2-(1H-benzotriazole-1-yl)-1,1,3,3-tetramethyluronium hexafluorophosphate in DMF), 2 M activator base (diisopropylethylamine in N-methyl-pyrrolidone (NMP)) and deprotecting agent (5% piperazine / 0.1 M 1-hydroxybenzotriazole in DMF), as advised by PepDriver (CEM©). After peptide chain assembly, the resin was treated 4 hrs at room temperature with a mixture of trifluoroacetic acid/water/triisopropylsilane (TIS)/1,4-dithiothreitol (DTT) (92.5/2.5/2.5/2.5). The peptide mixture was then filtered (to eliminate the resin) and the filtrate was precipitated by adding cold *t*-butylmethyl ether. The crude peptide was pelleted by centrifugation (10.000 × g, 15 min) and the supernatant was discarded. The reduced Tyr-MCA was submitted to oxidation for disulfide bridge formation in 0.1 M Tris/HCl buffer at pH 8.2 during 3 days at room temperature. Oxidized/folded Tyr-MCa was then purified by HPLC using a Vydac C18 column (218TP1010, 250×10 mm). Elution of the peptide was performed with a 10-60% acetonitrile linear gradient containing 0.1% trifluoroacetic acid over 40 min. The purity of the purified fraction was analyzed by analytical RP-HPLC (Vydac C18 column 218TP104, 250 × 4.6 mm). Tyr-MCa was characterized by MALDI-TOF mass spectrometry.

MCa radiolabeling and in vitro stability

[^{125}I]-Tyr-MCa was prepared using an oxidation reaction. Briefly, 148 MBq (4.0 mCi; 0.04 mL) of ^{125}I were added to 40 µg of Tyr-MCa in 200 µl of phosphate buffer (50 mM, pH 7.4). The reaction was allowed to proceed for 20 min at room temperature (RT) after addition of 15 µl (1 mg/ml) lactoperoxidase and 40 µl H_2O_2 (1:50,000). Radioiodinated Tyr-MCa was analysed by HPLC using a Vydac 218 TP C18 column, (10 µm, 4.6*250 mm). The solvent system consisted of H_2O–TFA 0.1% (solvent A) and acetonitrile 90%–TFA 0.1% (solvent B). Tracer elution was achieved by applying a gradient of 0% B during 8.3 min, 0-1% B during 1 min 40 sec, 1-10% B during 1 min 40 sec, 10-60% B during 33 min 12 sec, 60-100% B during 1 min 40 sec, 100% B during 8 min 18 sec and 100-0% B during 8 min 18 sec (total run time, 65 min) at a flow rate of 1 ml/min. The stability of the radio-labeling was determined by incubation of the complex at RT for 24 hrs, following which an HPLC analysis was performed as described above.

The *in vitro* stability of [^{125}I]-Tyr-MCa was evaluated in mouse blood. Twenty MBq of radio-labeled Tyr-MCa was incubated for 15, 30, 60, and 90 min in 0.5 ml of mouse blood at 37°C. At each time point, a 100 µl sample was centrifuged (2,000 g, 5 min) (pellet, fraction #1) and the plasma was filtered through a 10 K Omega™ membrane (Nanosep®;Pall Life Science, NY) at 7,000 g for 20 min (filter, fraction #2; filtered solution, fraction #3) followed by HPLC analyses using the above mentioned conditions. The blood samples were also used for the determination of the relative distribution of radioactivity in fractions #1, #2, and #3 corresponding to blood cells, plasma proteins, and protein-free plasma, respectively.

In Vivo Experimental Protocol

Eight standard CD-1 mice were obtained from Charles River Laboratories (France) and housed for 1 week prior to inclusion in the experimental protocol. Conscious animals were restrained for tracer injection in a tail vein.

In Vivo [^{125}I]-Tyr-MCa Stability – Two animals were dedicated to the evaluation of [^{125}I]-Tyr-MCa *in vivo* stability. The animals were injected with 55 MBq of tracer. At 15 and 30 min (n = 1 each)

following injection, the animals were anesthetized using pentobarbital (60 mg/kg, IP) and a thoracotomy was performed in order to withdraw a blood sample directly from the LV cavity through a transmural puncture. The blood sample was immediately centrifuged, the plasma was filtered, and the filtered solutions were analyzed by HPLC as described above. In addition, the distribution of radioactivity in fractions obtained as described above (see *METHODS – MCa radiolabeling and in vitro stability* paragraph) was also performed.

Biodistribution – [^{125}I]-Tyr-MCa (1.5 ± 0.0 MBq/g body weight; ~35 MBq total) was injected in the tail vein of 6 conscious and restrained animals (body weight, 23.7 ± 0.3 g). Three out of 6 animals were anesthetized immediately following tracer injection using isoflurane and imaged using a small animal nuclear imaging gamma-camera (nanoSPECT/CT, Bioscan, France). Tomographic *in vivo* images (24 projections, 20 sec / projection) were acquired at 15, 30, and 60 min post-tracer injection using a 15 – 75 keV energy window. A whole body CT acquisition was performed between the 30 and 60 min nuclear image acquisition. Gaseous anesthesia was maintained using isoflurane throughout the experimental imaging protocol.

Post Mortem Analysis

Sixty min following tracer injection, all 6 anesthetized animals were euthanized by cervical dislocation and samples from the heart, lung, liver, spleen, kidney, stomach, intestine, duodenum, pancreas, salivary glands, thyroid, skin, skeletal muscle, pancreas, thymus, brain, fat, brown fat, spinal cord, blood, and urine were obtained. Organs were quickly rinsed following excision and organ and blood activities of the tracers were assessed using a gamma-well counter (Cobra II, Packard Instruments, Courtaboeuf, France) with a 15–75 keV energy window for ^{125}I. All tissue counts were corrected for background.

Data Analysis

The results were expressed as mean ± SEM.

Biodistribution - Organ and blood activities by gamma-well counting were expressed as percent of the

injected dose per gram of wet weight (% ID/g).

Image Analyses - *In vivo* tomographic images were analysed using dedicated software (InVivoScope). Regions of interest (ROIs) were drawn on the thyroid, liver, kidney, skeletal muscle, stomach, salivary gland, brain, heart, myocardial left ventricle (for blood activity determination) and bladder. Tracer activities were expressed as % ID/cm^3.

Statistical Analysis - Statistical analysis was performed using Systat software. Mean values were compared using unpaired student *t*-test and Kruskall-Wallis non parametric test. A *P* value < 0.05 was considered significant.

RESULTS

Chemical synthesis, radiolabeling and *in vitro* stability of maurocalcine analogues

MCa amino acid sequence is devoid of internal Tyr residue for peptide iodination. To facilitate the labeling of MCa, we therefore chemically synthesized the 34 amino acid Tyr-MCa peptide which contains an additional Tyr residue at the N-terminus of the sequence (Figure 1A). The peptide folded well in spite of the extra Tyr residue and possessed the classical disulfide bridging patter, Cys^3-Cys^{17}, Cys^{10}-Cys^{21} and Cys^{16}-Cys^{32}. Next, the peptide was iodinated according to a procedure described earlier (Ahmadi *et al.*, in preparation). RP-HPLC analysis of [^{125}I]-Tyr-MCa immediately following radio-labeling is shown in Figure 1B. The results indicate that the conditions of iodination used yield a single major radioactive specie that elutes at 25 min with a radiochemical purity (RCP) > 95% . Mass spectrometry analyses using similar iodination conditions but with ^{127}I reveal that this single peak corresponds to the expected mass for a single iodination on the extra Tyr residue (data not shown). [^{125}I]-Tyr-MCa remained stable (RCP > 95%) at room temperature for at least 24 hrs following radio-labeling as demonstrated by RP-HPLC analysis (Figure 1B). For the subsequent experiments, [^{125}I]-Tyr-MCa was always used within 12 hrs following radio-labeling.

Blood stability of maurocalcine analogues

The *in vitro* distribution pattern of radioactivity after 15, 30, 60, and 90 min of [^{125}I]-Tyr-MCa incubation with whole mouse blood is indicated in Table 1 below. The results indicate that tracer distribution was quite stable over time. The radioactivity was mostly associated with plasma proteins (~60% of total). Blood cells and the protein-free plasma fraction presented similar amounts of radioactivity (~15-20% each). HPLC analyses of radioactive species in the protein-free plasma fraction of mouse blood samples after 15, 30, 60 and 90 min of incubation with the tracer followed by centrifugation and filtration is shown in Table 2. Three peaks were systematically detected. They correspond to free ^{125}I (retention time of 3 min), an iodinated metabolite (retention time of 19 min) and [^{125}I]-Tyr-MCa (retention time of 25 min). The iodinated metabolite represented a minor 2% of the total radioactivity at 15 min and increased to 7% at 90 min, whereas [^{125}I]-Tyr-MCa decreased from 75% at 15 min to 67% at 90 min. The amount of free ^{125}I was stable over time and represented ~20-25% of the protein-free plasma fraction of the tracer, i.e. ~4% of total blood activity assuming that free ^{125}I is present only in the protein-free plasma fraction.

***In Vivo* tracer stability**

The *in vivo* blood distribution pattern of radioactivity at 15 and 30 min following [^{125}I]-Tyr-MCa intravenous injection is indicated in Table 3 below. As observed *in vitro,* the radioactivity was mostly associated with plasma protein (~40-45%), although to a slightly lower level. The remaining activity was equally distributed between blood cells and the protein-free plasma fraction. Analysis of radioactive species in the protein-free plasma fraction of mouse blood at 15 and 30 min post-[^{125}I]-Tyr-MCa injection in mice indicated the presence of 2 peaks with retention times of 3 min and 24 min, which corresponded to free ^{125}I and [^{125}I]-Tyr-MCa, respectively (Figure 2). ^{125}I represented ~60% of the total protein-free plasma radioactivity, a value which did not increase over time. Considering that the protein-free plasma fraction of blood contained ~26% of the total blood activity (Table 3), one can therefore estimate that free ^{125}I represented ~16% of the total circulating activity following *in vivo*

injection of the tracer. Rather than indicating an increased deiodination of the tracer following *in vivo* injection, the apparently higher proportion of free ^{125}I following *in vivo* injection of [^{125}I]-Tyr-MCa (~16% of total blood activity) as compared with results from *in vitro* incubation of the tracer with mouse blood (~3% of total blood activity) was likely due to the fact that unbound [^{125}I]-Tyr-MCa was available for organ distribution following *in vivo* injection in mice whereas it was not the case following *in vitro* blood incubation of the tracer. These observations indicate that [^{125}I]-Tyr-MCa is probably accumulating in cells of various organs, which is expected for a cell penetrating peptide.

Biodistribution

The biodistribution of [^{125}I]-Tyr-MCa in CD-1 mice at 60 min following tracer injection is shown in Figure 3. The tracer was mainly eliminated through the kidneys as shown by the high renal and urinary activities. High activities were also observed in the stomach, salivary gland, and thyroid, which corresponded to ^{125}I uptake by these organs. [^{125}I]-Tyr-MCa did not cross the blood brain barrier as shown by the extremely low brain and cerebellum activities. Figure 3 also compares the biodistributions of [^{125}I]-Tyr-MCa with a pretreatment with the NaI symporter inhibitor, potassium perchlorate, to the condition without this pretreatment. This inhibitor prevents ^{125}I uptake into tissues. The biodistribution patterns were comparable between the two experiments. However, as expected, the presence of potassium perchlorate significantly inhibits ^{125}I uptake by the salivary glands and thyroid, which likely accounts for a significantly increased amount of blood circulating radioactivity.

***In vivo* imaging**

Presented in Figure 4 are representative images acquired in the same animal at 15 min (panel A), 30 min (panel B), and 60 min (panel C) following the intravenous injection of [^{125}I]-Tyr-MCa. The results from *in vivo* image quantification are presented in Figure 5. Non invasive 60-min image quantification accurately reflected post-mortem organ biodistribution. As shown on images and confirmed following image quantification, there was a progressive accumulation of ^{125}I in the thyroid, stomach, and salivary glands from 0 to 60 min post-injection. Renal elimination of the tracer began immediately following

injection and remained stable over time. Hepatic elimination of [^{125}I]-Tyr-MCa was lower than that occurring through the kidneys and was also stable over time.

Discussion

MCa lacks a tyrosine residue within its sequence which prevents its convenient labeling by ^{125}I. An extra-tyrosine has been added to the sequence at the N-terminus of MCa. It does not hamper the proper folding and oxidation of the peptide. Also, it did not prevent the peptide from binding onto its target receptor, RyR1 (data not shown); which was also observed for biotinylated MCa on which an extra lysine residue had been added at the N-terminus (*19*). N-terminal modifications also did not appear to affect cell penetration properties of MCa (*8*) suggesting that labeling at the N-terminus of MCa is a safe strategy to preserve the native properties of the peptide. In many respects, the ^{125}I labeling of a tyrosine residue placed at the N-terminus of peptide sequence appears preferable for preserving intact peptide properties than a labeling that would occur on an internal tyrosine residue, if this one had been present. It is therefore likely that the properties of *in vivo* biodistribution of [^{125}I]-Tyr-MCa, we report in this manuscript, properly describe what the biodistribution of MCa itself could be. The analyses we performed occurred at blood peptide concentrations in the range of 1 µM and are therefore also in good agreement with the effective concentrations required for cell penetration and pharmacological action. The labeling procedure we developed for this peptide produced a stable [125I]-Tyr-MCa molecule, at least within the 24 hrs post-labeling period.

This study led to several interesting conclusions. First, MCa is remarkably stable in blood according to the study we conducted. Apart from deiodination that leads to free ^{125}I, the peptide showed little or no degradation over a period of 90 min. This is in agreement with the expected stability of disulfide-bridged toxins *in vivo*. We hypothesize that, here also, the three disulfide bridges that connect the six internal cysteine residues of MCa confer a relatively high resistance to protease action to this

peptide. This finding further reinforces the competitiveness of MCa as a cell delivery vector. Second, this study brings in important conclusions on the fate of the peptide once injected in the blood stream. Both *in vitro* and *in vivo* data provide coherent conclusions. A fraction of the radioactivity (17 to 30% depending on the time scale) is associated to blood cells, which is a first indication that [^{125}I]-Tyr-MCa has the ability to enter these cell types. What kind of blood cell is preferentially targeted by [^{125}I]-Tyr-MCa will be an interesting question to investigate if applications need to be developed in which targeted blood cell delivery is required. Obviously, most of the radioactivity associates to plasma proteins, and a minor fraction (equivalent to the blood cell fraction) is associated to the protein-free plasma. Interestingly, there is a consistent difference in the proportion of radioactivity associated to plasma proteins and protein-free plasma between the *in vitro* and *in vivo* conditions. *In vivo*, there is approximately a reduction of a third in the amount of radioactivity associated to plasma proteins, as well as a 1.5 to 2-fold increase in radioactivity associated to the protein-free plasma. Both effects can be interpreted by the organ delivery of [^{125}I]-Tyr-MCa (that does not occur *in vitro*) and the proportional increase in free ^{125}I in the protein-free plasma (that does not reflect deiodination). Third, the data clearly demonstrate that [^{125}I]-Tyr-MCa does not reach neural tissues and that therefore the peptide is unlikely to cross the blood brain barrier. This observation will limit the number of application where vector delivery to the brain is required, except maybe in pathological conditions (brain cancers for instance) where disruption of the blood brain barrier is expected to occur. Important labeling is detected in the stomach, the spleen, the skin, lungs, intestine, duodenum, pancreas and liver. Non negligible labeling is observed in heart, skeletal muscle, thymus and brown fat. In some organs, such as salivary glands and thyroid, the accumulation of radioactivity was linked to a preferential accumulation of free ^{125}I. This could readily be suppressed by a treatment with potassium perchlorate.

Fourth, the strong kidney and urine accumulation of radioactivity implies that the kidneys are the main route of elimination of the peptide. Kidney labeling does not change much with time between 15 and 60 min suggesting that we face a rather rapid elimination immediately after IV injection of the peptide.

The only organs that showed increased levels of radioactivity with time were those that accumulated free ^{125}I suggesting that [^{125}I]-Tyr-MCa distribution *in vivo* had reached equilibrium rather fast after IV injection (within 15 min).

In summary, this study indicates that MCa is a stable peptide vector in vivo, that it targets peripheral organs mainly with interesting quantitative differences, that blood cells also appear to accumulate the peptide and that the main route of elimination occurs through the kidneys. This study will therefore delimitate the field of applications in which MCa can be used to deliver cargoes into cells *in vivo*.

References

1. Mosbah A, Kharrat R, Fajloun Z, et al. A new fold in the scorpion toxin family, associated with an activity on a ryanodine-sensitive calcium channel. *Proteins.* Aug 15 2000;40(3):436-442.

2. Zamudio FZ, Gurrola GB, Arevalo C, et al. Primary structure and synthesis of Imperatoxin A (IpTx(a)), a peptide activator of Ca2+ release channels/ryanodine receptors. *FEBS Lett.* Apr 1 1997;405(3):385-389.

3. Esteve E, Smida-Rezgui S, Sarkozi S, et al. Critical amino acid residues determine the binding affinity and the Ca2+ release efficacy of maurocalcine in skeletal muscle cells. *J Biol Chem.* Sep 26 2003;278(39):37822-37831.

4. Fajloun Z, Kharrat R, Chen L, et al. Chemical synthesis and characterization of maurocalcine, a scorpion toxin that activates Ca(2+) release channel/ryanodine receptors. *FEBS Lett.* Mar 10 2000;469(2-3):179-185.

5. Chen L, Esteve E, Sabatier JM, et al. Maurocalcine and peptide A stabilize distinct subconductance states of ryanodine receptor type 1, revealing a proportional gating mechanism. *J Biol Chem.* May 2 2003;278(18):16095-16106.

6. Lukacs B, Sztretye M, Almassy J, et al. Charged surface area of maurocalcine determines its interaction with the skeletal ryanodine receptor. *Biophys J.* Oct 2008;95(7):3497-3509.

7. Altafaj X, Cheng W, Esteve E, et al. Maurocalcine and domain A of the II-III loop of the dihydropyridine receptor Cav 1.1 subunit share common binding sites on the skeletal ryanodine receptor. *J Biol Chem.* Feb 11 2005;280(6):4013-4016.

8. Esteve E, Mabrouk K, Dupuis A, et al. Transduction of the scorpion toxin maurocalcine into cells. Evidence that the toxin crosses the plasma membrane. *J Biol Chem.* Apr 1 2005;280(13):12833-12839.

9. Ram N, Aroui S, Jaumain E, et al. Direct Peptide Interaction with Surface Glycosaminoglycans Contributes to the Cell Penetration of Maurocalcine. *J Biol Chem.* Aug 29 2008;283(35):24274-24284.

10. Aroui S, Ram N, Appaix F, et al. Maurocalcine as a Non Toxic Drug Carrier Overcomes Doxorubicin Resistance in the Cancer Cell Line MDA-MB 231. *Pharm Res.* Apr 2009;26(4):836-845.

11. Boisseau S, Mabrouk K, Ram N, et al. Cell penetration properties of maurocalcine, a natural venom peptide active on the intracellular ryanodine receptor. *Biochim Biophys Acta.* Mar 2006;1758(3):308-319.

12. Jayagopal A, Su YR, Blakemore JL, Linton MF, Fazio S, Haselton FR. Quantum dot mediated imaging of atherosclerosis. *Nanotechnology.* Apr 22 2009;20(16):165102.

13. Poillot C, Dridi K, Bichraoui H, et al. D-Maurocalcine, a pharmacologically inert efficient cell-penetrating peptide analogue. *J Biol Chem.* Oct 29;285(44):34168-34180.

14. Ram N, Weiss N, Texier-Nogues I, et al. Design of a disulfide-less, pharmacologically-inert and chemically-competent analog of maurocalcine for the efficient transport of impermeant compounds into cells. *J Biol Chem.* Jul 21 2008.

15. Aroui S, Brahim S, De Waard M, Breard J, Kenani A. Efficient induction of apoptosis by doxorubicin coupled to cell-penetrating peptides compared to unconjugated doxorubicin in the human breast cancer cell line MDA-MB 231. *Cancer Lett.* Nov 18 2009;285(1):28-38.

16. Aroui S, Brahim S, Hamelin J, De Waard M, Breard J, Kenani A. Conjugation of doxorubicin to cell penetrating peptides sensitizes human breast MDA-MB 231 cancer cells to endogenous TRAIL-induced apoptosis. *Apoptosis.* Nov 2009;14(11):1352-1365.

17. Aroui S, Brahim S, Waard MD, Kenani A. Cytotoxicity, intracellular distribution and uptake of doxorubicin and doxorubicin coupled to cell-penetrating peptides in different cell lines: a comparative study. *Biochem Biophys Res Commun.* Jan 1;391(1):419-425.

18. Aroui S, Mili D, Brahim S, De Waard M, Kenani A. Doxorubicin coupled to penetratin promotes apoptosis in CHO cells by a mechanism involving c-Jun NH2-terminal kinase. *Biochem Biophys Res Commun.* Jun 11;396(4):908-914.

19. Mabrouk K, Ram N, Boisseau S, et al. Critical amino acid residues of maurocalcine involved in pharmacology, lipid interaction and cell penetration. *Biochim Biophys Acta.* Oct 2007;1768(10):2528-2540.

Figure legends

Table 1. *In vitro* blood distribution pattern of radioactivity following [^{125}I]-Tyr-MCa incubation with whole mouse blood.

Table 2. *In vitro* stability analysis of [^{125}I]-Tyr-MCa after 15 to 90 min incubation with mouse blood. HPLC analysis was performed in the protein-free plasma fraction of mouse blood.

Table 3. *In vivo* blood distribution pattern of radioactivity following [^{125}I]-Tyr-MCa intravenous injection.

Figure 1. Radio-labeling of maurocalcine analogues and *in vitro* stability of the iodinated compounds. (A) HPLC chromatogram of [^{125}I]-Tyr-MCa immediately following radio-labelling. (B) HPLC chromatogram of [^{125}I]-Tyr-MCa at 24 hrs following radio-labelling.

Figure 2. *In vivo* stability of the iodinated MCa analogues. (A) HPLC chromatogram of [^{125}I]-Tyr-MCa at 15 min post-injection to mice. (B) HPLC chromatogram of [^{125}I]-Tyr-MCa at 30 min post-injection to mice. Analyses were conducted for the protein-free plasma fraction.

Figure 3. Biodistribution of [^{125}I]-Tyr-MCa in CD-1 mice 60 min post-injection and effect of the NaI symporter inhibitor potassium perchlorate. Biodistributions of [^{125}I]-Tyr-MCa were analyzed 60 min post-injection in CD-1 mice. Mean injected dose for control and potassium perchlorate pretreatment conditions were ~35 and ~17 MBq, respectively. SG, salivary gland; Cereb., cerebellum; Spinal C., Spinal Cord. *, $P \leq 0.05$.

Figure 4. 15-min *in vivo* tomographic whole-body imaging of [^{125}I]-Tyr-MCa biodistribution in CD-1 mice. (A) 15 min i.v. post-injection. (B) 30 min i.v. post-injection. (C) 60 min i.v. post-injection. From left to right, 3D rendering, sagittal, coronal, and transverse views of tracer activity.

Figure 5. Quantification of *in vivo* tomographic images of [^{125}I]-Tyr-MCa whole-body distribution at 15, 30, and 60 min post-injection. *, $P \leq 0.05$ *versus* 15 min condition.

A

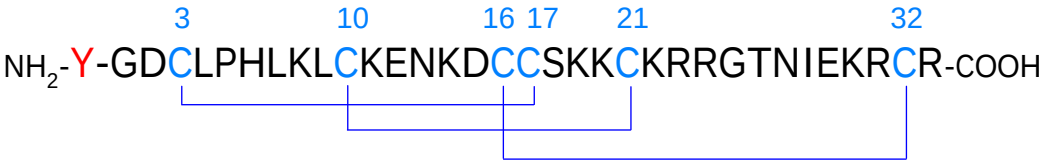
3
10
16 17
21
32
NH2-Y-GDCLPHLKLCKENKDCCSKKCKRRGTNIEKRCR-COOH

B

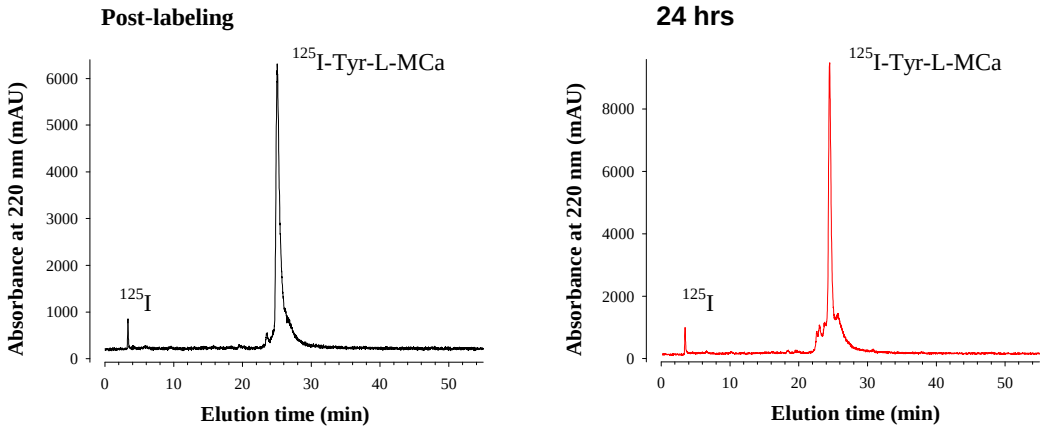
Post-labeling
125I-Tyr-L-MCa
125I
Absorbance at 220 nm (mAU)
Elution time (min)
24 hrs
125I-Tyr-L-MCa
125I
Absorbance at 220 nm (mAU)
Elution time (min)

In vivo plasma

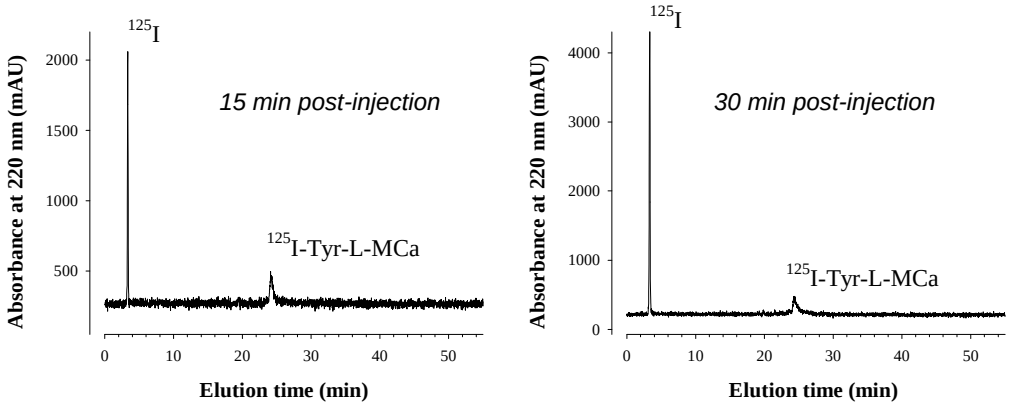

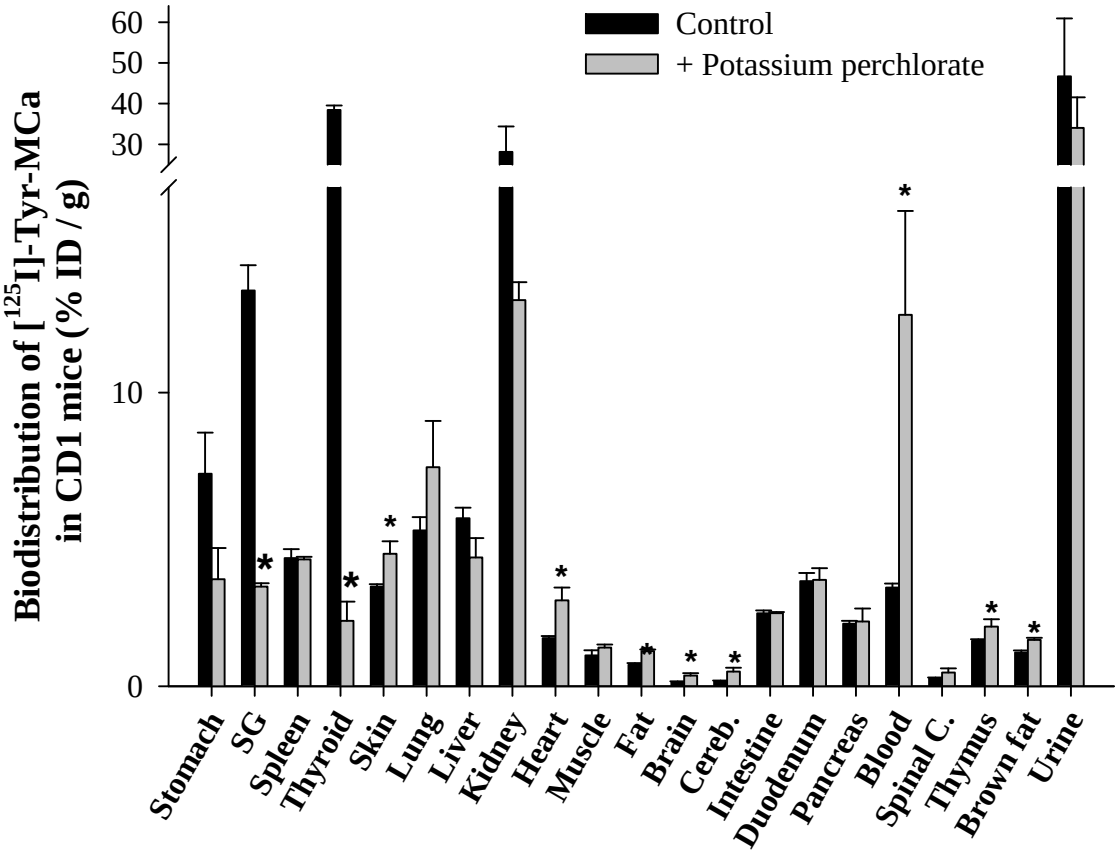
Biodistribution of [125I]-Tyr-MCa in CD1 mice (% ID / g)
Control
+ Potassium perchlorate
60
50
40
30
10
0
*
Stomach
SG
Spleen
Thyroid
Skin
Lung
Liver
Kidney
Heart
Muscle
Fat
Brain
Cereb.
Intestine
Duodenum
Pancreas
Blood
Spinal C.
Thymus
Brown fat
Urine

A

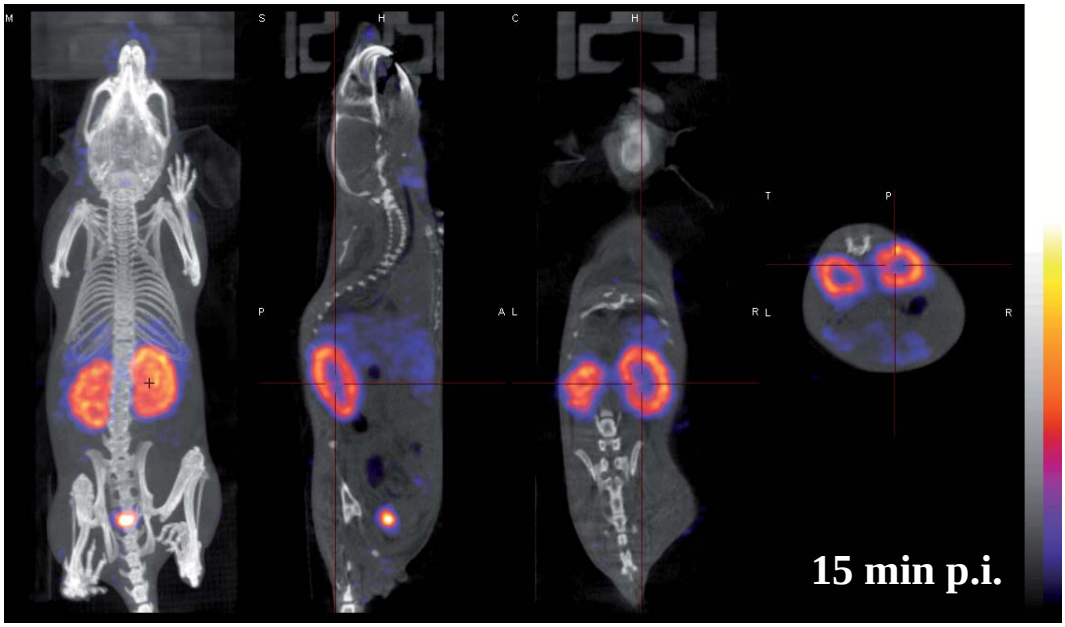

B

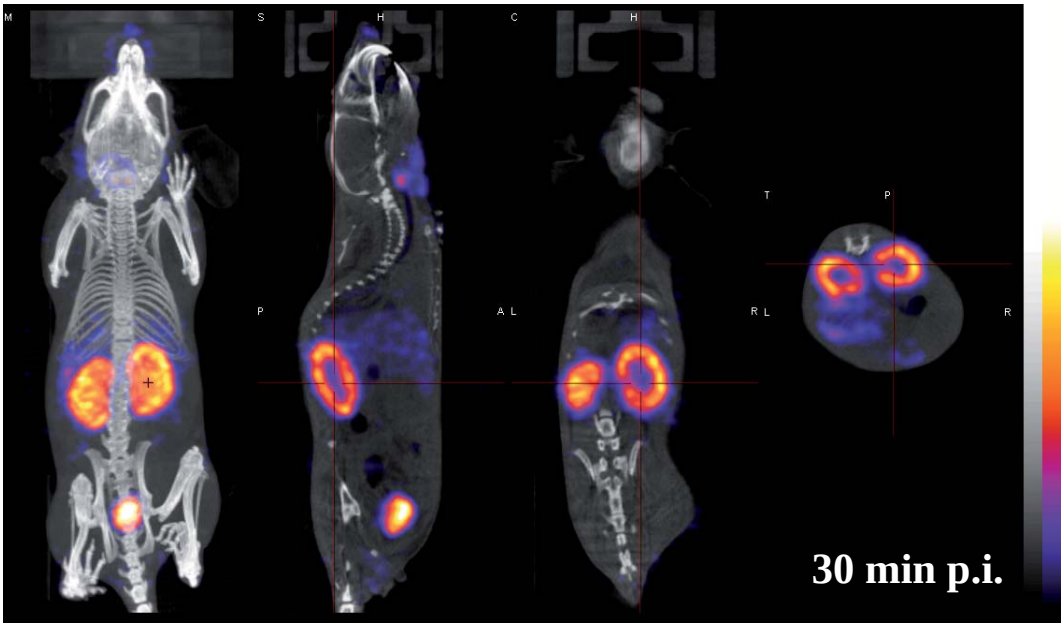

C

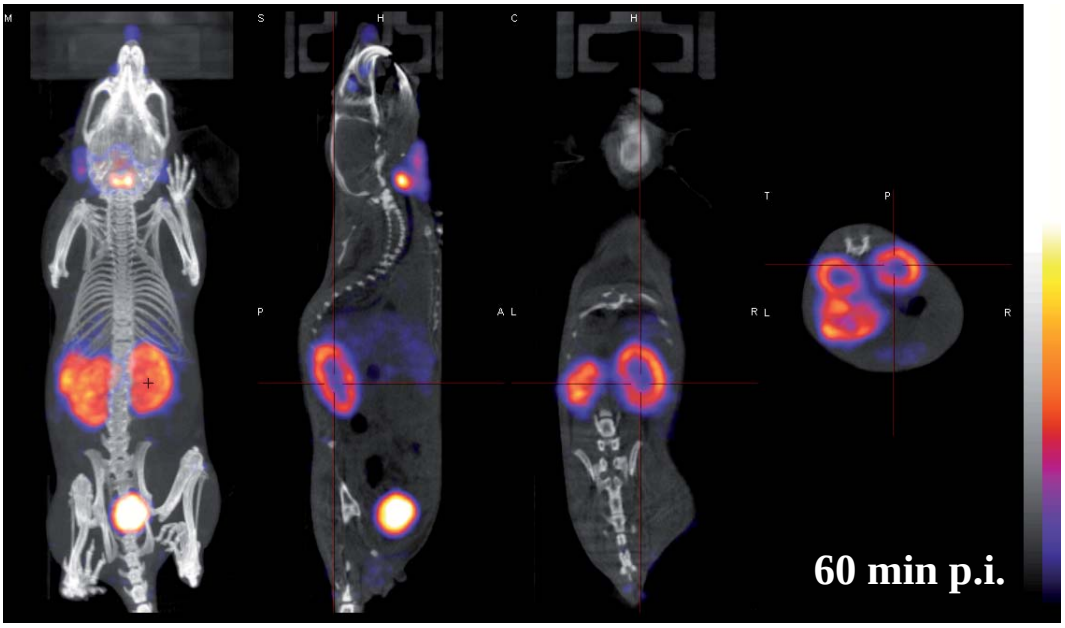

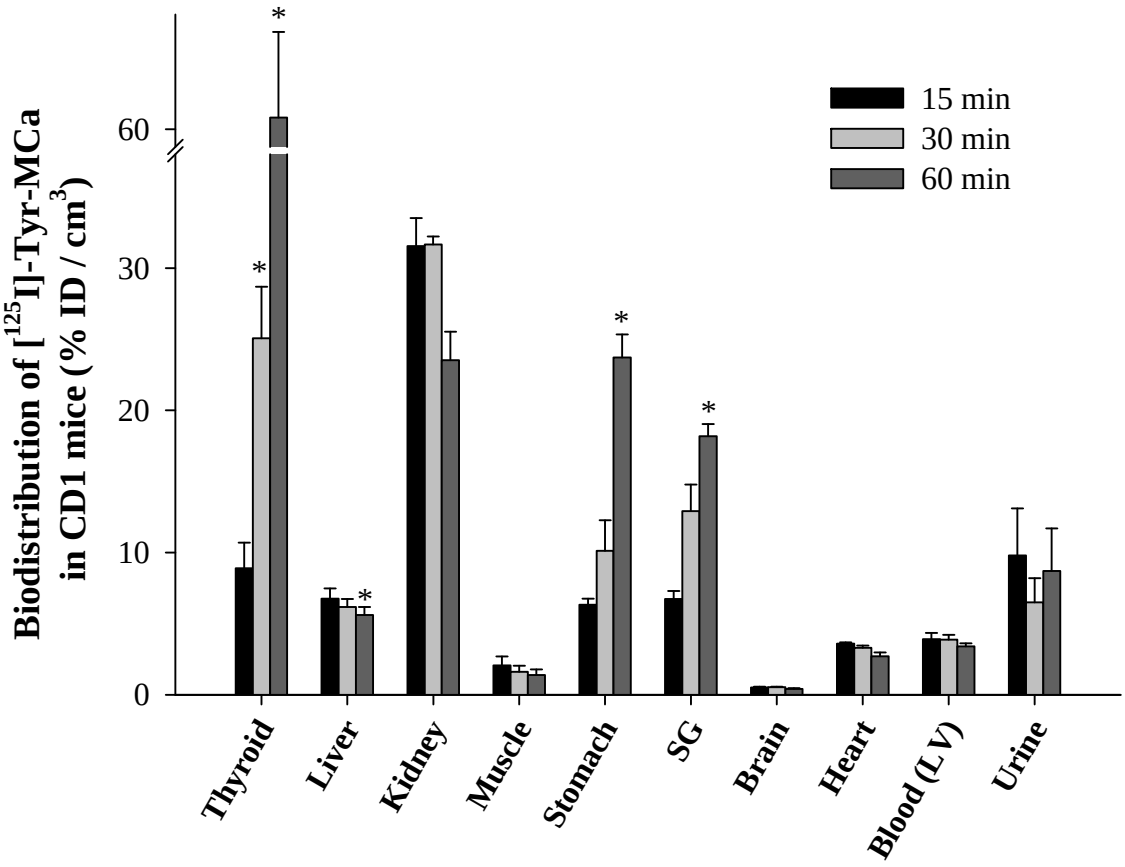
Biodistribution of [125I]-Tyr-MCa in CD1 mice (% ID / cm3)
15 min
30 min
60 min
0
10
20
30
60
*
Thyroid
Liver
Kidney
Muscle
Stomach
SG
Brain
Heart
Blood (LV)
Urine

Table 1. *In vitro* blood distribution pattern of radioactivity following [^{125}I]-Tyr-MCa incubation with whole mouse blood.

	Incubation time (min)			
	15	**30**	**60**	**90**
Blood cells	19%	23%	19%	17%
Plasma proteins	61%	59%	58%	67%
Protein-free plasma	17%	17%	14%	14%

Table 2. *In vitro* stability analysis of [^{125}I]-Tyr-MCa after 15 to 90 min incubation with mouse blood.

	Incubation time (min)			
	15	**30**	**60**	**90**
Free [^{125}I]	22%	20%	24%	24%
[^{125}I]-metabolite	2%	3%	5%	7%
[^{125}I]-Tyr-MCa	75%	75%	70%	67%

Table 3. *In vivo* blood distribution pattern of radioactivity following [^{125}I]-Tyr-MCa intravenous injection.

	Time post-injection (min)	
	15	**30**
Blood cells	24%	30%
Plasma proteins	47%	39%
Protein-free plasma	29%	26%

b. Conclusion

Lors de cette étude, nous avons pu extraire deux informations indispensables à propos de la MCa, sa stabilité *in vivo* ainsi que sa biodistribution. La ^{125}I-Tyr-MCa est stable *in vitro* dans le sang de souris à 75% après 30 min, puis à 67% après 90 min. *In vivo*, 39% de la ^{125}I-Tyr-MCa est présente après 30 min et 61% de la radioactivité est constituée d'iode libre. Le temps de rétention de la ^{125}I-Tyr-MCa sur la colonne après marquage et après injection dans la souris, nous montre que la Tyr-MCa n'est absolument pas dégradée à 30 min, la seule dégradation qui intervient est la radiolyse et en aucun cas l'intégrité de la séquence.

Deux techniques différentes ont été réalisées pour faire le calcul de la biodistribution. Dans un premier temps, l'animal a été sacrifié, les organes ont été prélevés puis analysés, la deuxième analyse à consister en l'imagerie *in vivo* sur corps entier, suivie d'une quantification *in vivo*.

La biodistribution 60 min post injection sur les organes montre que la ^{125}I-Tyr-MCa est stockée principalement dans la thyroïde, les reins et dans l'urine. A une dose plus faible, on la retrouve dans les glandes salivaires et l'estomac. ^{125}I-Tyr-MCa semble ne pas passer la barrière hémato-encéphalique, en effet, très peu de radioactivité est retrouvée dans le cerveau et dans le cervelet.

L'analyse *in vivo* sur corps entier donne des résultats similaires à l'analyse sur organes. La radioactivité est présente majoritairement dans la tyroïde, elle augmente de ± 2.5 fois entre 15 min et 30 min et + de 6 fois entre 15 min et 60 min. Dans les reins, la présence de ^{125}I-Tyr-MCa est constante de 15 min à 30 min puis baisse de ± un quart à 60 min. La présence dans l'estomac et les glandes salivaires est moindre que dans la tyroïde et les reins, et suit la même tendance que dans la tyroïde, elle augmente entre 15 min et 60 min.

La stabilité de la ^{125}I-Tyr-MCa est relativement bonne, mais il serait intéressant de refaire cette étude en utilisant la MCa sous sa conformation D, afin de vérifier si comme on le suppose, sa stabilité *in vivo* serait largement supérieure à la L-MCa.

6. Article 5

Cell permeable multimeric Ln (III) chelate functionalized quantum dots as multimodal imaging probes

Graeme J. Stasiuk, Sudarshan Tamang, Daniel Imbert, Cathy Poillot, Marco Giardiello, Céline Tisseyre, Emmanuel Barbier, Pascal H. Fries, Michel De Waard, Peter Reiss, Marinella Mazzanti

Article soumis à Imaging Agents

a. Introduction

L'article suivant est un exemple d'utilisation de la MCa pour l'administration *in vivo* d'une molécule d'intérêt. Nous nous somme intéressé à l'administration intracellulaire d'un agent de contraste au gadolinium pour l'imagerie par résonnance magnétique (IRM). En effet, les agents de contrastes sont obligatoires pour augmenter le contraste des images et obtenir un résultat exploitable lors d'acquisitions IRM. Les agents de contraste commerciaux n'ont pas une efficacité suffisante pour détecter des évènements à l'échelle moléculaire, ce qui est peut être dû au fait que ces agents de contraste sont extracellulaires. Une étude réalisée au laboratoire avait montré que la MCa lorsqu'elle était couplé à de la doxorubicine servait d'agent de rétention de cet agent antimorale dans les cellules (Aroui, Ram et al. 2009). Nous avons émit l'hypothèse que la MCa, si elle était couplée à des agents de contraste, pourrait avoir la même fonction de rétention des agents de contraste dans les cellules, ce qui permettrait de maintenir une concentration plus élevée en agents dans le tissu, ce qui représente un avantage si de plus la sensibilité IRM est accrue par des fonctionnalisations multiples d'agents de contrastes sur une plateforme nanoparticule.

L'actuel agent de contraste utilisé actuellement chez l'homme lors d'examen IRM est le dotarem®. Nous avons réalisé un couplage de manière covalente entre la MCa et des nanoparticules de cadmium/sélénium fonctionnalisées avec un agent de contraste au gadolinium (Gd) dans un ratio 5 :1 :200. Nous avons comparé la persistance du signal IRM entre le dotarem® et le complexe nanoparticule/agent de contraste au Gd/MCa.

Imaging Agents

DOI: 10.1002/anie.200((will be filled in by the editorial staff))

Cell Permeable Multimeric Ln (III) Chelate Functionalized Quantum Dots as Multimodal Imaging Probes

*Graeme J. Stasiuk, Sudarsan, Cathy Poillot, Tamang, Daniel Imbert, Marco Giardiello, Céline Tisseyre, Emanuel Barbier, Pascal H. Fries, Michel De Waard, Peter Reiss and Marinella Mazzanti**

Magnetic resonance imaging (MRI) is a powerful tool in medical diagnostic. MRI is a non invasive technique with impressive anatomic resolution and tissue penetration, but applications are limited by its low sensitivity and lack of cell specificity. MRI contrast agents (CAs), primarily gadolinium Gd^{III} complexes are used to enhance the image contrast. This enhancement is the result of the increase of the water proton relaxation rate $1/T_1$ induced by the neighbouring paramagnetic Gd^{III} ions. The efficiency of current commercial contrast agents, usually expressed in terms of their relaxivity r_1 ($s^{-1}\cdot mM^{-1}$), that is the increase of $1/T_1$ per mM of added Gd^{III} complexes, is too low for the detection of events at the molecular scale. Moreover, commercial CAs are limited to extracellular applications. A possible approach for increasing MRI sensitivity is the use of multimeric CAs in which a large number of small Gd^{III} chelates are bound to a nanosized carrier allowing for the accumulation of paramagnetic Gd^{III} ions at the site of interest.[1-4]

Another approach consists of combining MRI with a different high sensitivity imaging modality[5-7] such as fluorescence.[8-12] The accuracy of the analysis can be improved by a combined tissue study by optical microscopy and by MRI , which requires creating a multimodal reporter.[13] The majority of dual (MRI/optical) probes are MRI contrast agents coupled to organic dyes. More recently, dual-probes have been identified where the optical reporter is a transition metal, a Ln^{III} complex or a quantum dot.[10, 13-15] Quantum Dots (QDs) are highly luminescent, photostable semi-conductor nanoparticles of size-controlled emission. They are very attractive for use in diagnostic, molecular and cellular imaging due to their optical properties and their increased photostability as compared to organic dyes.[16-21] Luminescent lanthanide complexes, on the other hand, are characterized by large Stokes shifts and long-lived luminescence which render them very attractive for applications in cellular imaging.[22-28] Bimodal probes can be obtained simply by mixing luminescent Ln^{III} and Gd^{III} ions complexed by the same ligand due to chemical equivalence (leading to similar biodistribution) of lanthanide complexes.[15, 29, 30] We have previously shown that the pyridinecarboxylate based *bpatcn* (H_3bpatcn = 1-(carboxymethyl),4,7-bis[(6-carboxypyridin-2-yl)methyl]-1,4,7-triazacyclononane) ligand can be used to prepare both a Tb^{III} complex with high luminescence quantum yield and Gd^{III} complex with favourable relaxivity for MRI application.[31] Dual probes have been demonstrated to be highly valuable in the multimodal imaging[32] studies of animals allowing the combination of pre-operative and intra-operative visualization of tumors,[33] co-validation of CA distribution[34] and combined tracking of transplanted stem cells.[35] A challenge in the development of MRI CAs for investigating biochemical processes and cellular events is the efficient delivery of agents across cellular membranes. For instance, the monitoring of cell fate and migration *in vivo* will be essential to the development of cell-based therapies. While the development of MRI/optical imaging probes has significantly increased in the last few years, there are only few examples of high Gd^{III} payload dual-probes capable of penetrating cells.[8, 10, 36] QDs provide convenient scaffolds in the development of bimodal multimeric Gd-based CAs for molecular MRI.[10, 12, 13, 37] Notably, multiple ligands can be simultaneously attached to the QD surface to promote cell penetration and/or specific targeting. However, only one example of cell permeable Gd^{III} CAs based on CdSe/ZnS QDs[10] has been reported and there are no examples, to the best of our knowledge, of Gd^{III} CAs derived from non-toxic InP/ZnS QDs.

Here we report a new MRI/optical probe with high relaxivity of 900 $mM^{-1}s^{-1}$ at 35 MHz (0.81T), obtained by a direct procedure of covalent attachment of up to 80 Gd(bpatcn) complexes to fluorescent, non-toxic InP/ZnS QDs. The versatile synthetic strategy used herein allows the introduction of additional modalities on the QDs. In particular, the simultaneous grafting of the cell penetrating peptide maurocalcine and of up to 40 gadolinium chelates affords a cell permeable multimodal multimeric MRI CA. This multimodal agent reports cellular localization by fluorescence and provides bright MRI signal and increased tissue retention with respect to commercial contrast agents. We also demonstrate the covalent attachment of the chemically equivalent visible emitting Tb- and Eu(bptacn) complexes which provide a good analytical tool to monitor the grafting process and could be used in the development of different types of Ln-Gd-QD multimodal reporters including Ln based and QD based optical modalities.

The previously reported [Ln(bpatcn)] complexes[31] were functionalized for grafting on InP/ZnS QDs according to scheme 1 and scheme S1. Complex Ln.1 is an amine appended derivative of

[*] Dr. G. J. Stasiuk, Dr. M. Giardiello, Dr. D. Imbert, Dr. P. H. Fries, Dr. M. Mazzanti.
CEA, INAC, SCIB, Laboratoire de Reconnaissance Ionique et Chimie de Coordination, CEA-Grenoble, UJF, LCIB, UMR-E 3 CEA-UJF, 38054 Grenoble Cedex 9, France
Fax: (+33) 438-785-090
E-mail: marinella.mazzanti@cea.fr

S. Tamang, Dr. P. Reiss
CEA Grenoble INAC/SPrAM UMR 5819 CEA-CNRS-UJF, Laboratoire d'Electronique Moléculaire, Organique et Hybride

C. Poillot, C. Tisseyre, Dr E. Barbier, Dr M. De Waard.
Grenoble Institute of Neuroscience, Inserm U836, Site Santé de la Tronche, bâtiment Edmond J. Safra, Chemin Fortuné Ferrini, BP170, 38042 Grenoble Cedex 9, France

[**] This research was carried out in the frame of the EC COST Action D-38 "Metal-Based Systems for Molecular Imaging Applications" and the European Molecular Imaging Laboratories (EMIL) network. We acknowledge financial support from the French Research Agency (PNANO-07-NANO-044) and from CEA Technologies pour la Santé "TIMOMA2" and thank Lydia Plassais for help with synthetic chemistry.

Supporting information for this article is available on the WWW under http://www.angewandte.org or from the authors.

the [Ln(bpatcn)] complexes; Gd.1 has a r_1 of 4.12 mM^{-1} s^{-1} at 200 MHz (4.6T) which is comparable to the previously reported bpatcn analogues[16] and commercial CAs.[38, 39] Ligand L1 was prepared from 1,4,7-triazonane-1,4-di-bis(methylene)-dipicolinic acid and 6-aminohexanoic acid in 62% yield through a multi-step synthesis described in the supplementary data. The amine functionality brings versatility allowing for further modification. Notably, preliminary studies show that L1 can be directly conjugated through peptide chemistry coupling to different biomolecules such as peptides or oligonucleotides. In this work lipoic acid was successfully reacted with complex Ln.1 to afford the Ln.2 dithiol derivatives in 60% yield. The dithiol linker was chosen to ensure strong binding of the Ln chelates to the outer ZnS shell of the QDs.

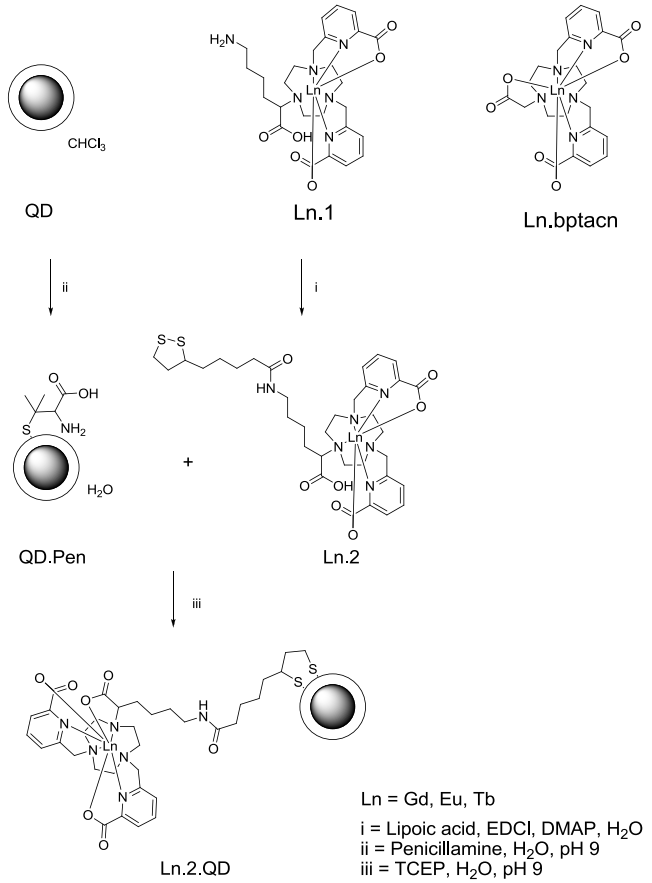

Scheme 1. Synthesis of Ln(III)-QDs.

InP/ZnS QDs are prepared in octadecene using phosphine as the phosphorus precursor and capped with a ZnS shell using standard methods.[40] Prior to the grafting of the water-soluble CA, a phase transfer reaction is performed using penicillamine at pH 9 in a 1:1 mixture of water and chloroform (reaction time 2 hours, transfer yield 60%).[41] The InP/ZnS QDs capped with penicillamine (QD.Pen) provide an efficient platform for grafting of lanthanide chelates and/or other bio-probes.

The dithiol functionalized lanthanide chelates are reacted overnight in a shaker with the QD.Pen in aqueous media at pH 9 and 20°C in the presence of the reducing agent tris(carboxyethyl)phosphine (TCEP) to cleave the disulfide bond. This process results in the grafting of 75 - 80 lanthanide chelates on a single InP/ZnS QD in a 40% yield. The hydrodynamic diameters measured using Dynamic Light Scattering, showed an increase from 6.9 nm for the QD.Pen to 8.6 - 9.2 nm for the lanthanide complex functionalized QDs. This increase of around 2 nm is consistent with the successful coverage of the QD surface by Gd chelates. The strongest indication of successful grafting is the NMRD profile shown in Figure 1. Both Gd.1 and Gd.2 show a classical profile for mono-aqua chelates. The Gd.2.QD system with its larger molecular weight, shows a very different profile, with an increase in r_1 from 3-35 MHz (0.07-0.81T) of 10 to 13 $mM^{-1}s^{-1}$. The NMRD profile provides unambiguous evidence of efficient grafting and shows that the optimum relaxivity for Gd.2.QD is at 30 MHz (0.7T) with r_1 = 13 $mM^{-1}s^{-1}$. This significant increase in r_1 with respect to the non-grafted chelate is consistent with a slower rotation of the grafted complex due to its larger size. Increasing the molecular weight of Gd complexes by macromolecule and protein binding is an effective way to increase the relaxivity of small Gd chelates in the magnetic field range of 30-100 MHz (0.7-2.3T).[39] Magnetic susceptibility measurements and UV visible spectroscopy showed the presence of 70-80 chelates grafted onto Gd.2.QD. As a result the relaxivity per quantum dot reaches 900 $mM^{-1}{\cdot}s^{-1}$ at 35 MHz (0.81T). As expected from the theory of relaxivity, the slow rotation is not favourable at higher fields (200 MHz) and the relaxivity decreases. However, the relaxivity per quantum dot is still around 200 $mM^{-1}{\cdot}s^{-1}$, thus providing a very bright contrast agent compared to smaller chelates and commercial agents (r_1 ~4 $mM^{-1}s^{-1}$) (Figure S1).

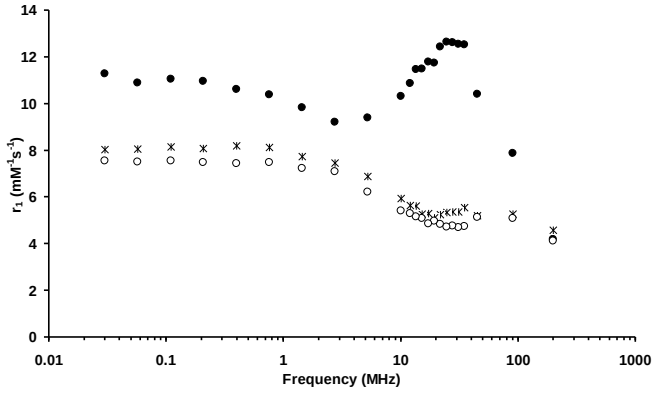

Figure 1. NMRD profile for Gd.1 (○), Gd.2 (ж) and Gd.2.QD (●). (pH 7.4, 298K)

In order to assess the full potential of Ln.2.QD systems as multimodal (optical/optical and optical/magnetic) probes we have investigated their photophysical properties. The water dispersible penicillamine-capped InP/ZnS QDs show a fluorescence quantum yield (QY) of 8.5% in water. A significant decrease in QY (QY in chloroform: 20%) after phase transfer *via* surface ligand exchange is generally observed in the literature.[21] The lack of difference in the emission spectra of QD.Pen and Gd.2.QD (Figure S2), suggests that grafting of the complex does not affect the luminescence of the QDs, resulting in a magnetic and optical dual mode imaging probe. The InP/ZnS photoluminescence peak is located at 620 nm, and the QY measured at 480 nm for Gd.2.QD in water (6.1 %) is comparable to the value of QD-pen (8.5%). Since the picolinate ligand can efficiently sensitize terbium and europium (Figure S3), the grafting of chelates containing these visible emitting lanthanide ions results in a dual mode optical probe with emission both from the QD (nanosecond time scale) and the Tb or Eu ions (millisecond time scale). Figure 2 shows the excitation and emission spectra of Tb.2.QD. The excitation spectrum of Tb.2.QD shows a large peak at 275 nm corresponding to the picolinate ligand absorption, while the excitation corresponding to the QDs extends over the range of 200-500 nm. Emission from one or the other of the two emitters or from both can be selectively turned on by a suitable choice of acquisition conditions. Notably, the excitation of Tb.2.QD at 275 nm with 0 ms delay, yields dual emission from the QDs and Tb ions at 620 nm and 546 nm. When a 0.05 ms delay is applied only the emission from the Tb^{III} ions is observed due to their longer luminescence lifetime with respect to the QDs. Conversely, when Tb.2.QD is excited at 320 nm with 0 ms delay, only emission from the QDs is observed. This provides a dual luminescent probe, which has two defined emission wavelengths on two different time scales, the millisecond and the

nanosecond scale. Similar results were obtained for Eu.2.QD (Figure S3).

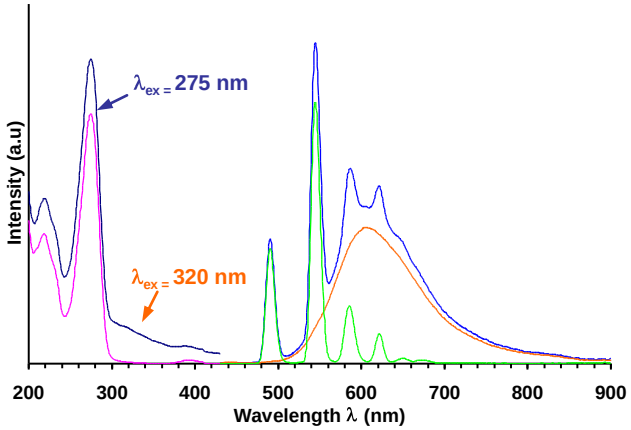

Figure 2 Luminescence of Tb.2.QD. (Left) Excitation spectra with λ_{em} = 546 nm (dark blue: 0 ms and pink: 0.05 ms delay, respectively); (Right) Emission spectra with λ_{ex} = 275 nm (blue: 0 ms and green: 0.05 ms delay, respectively) and 320 nm (orange: 0 ms delay).

The direct grafting of the Gd chelate on the QDs provides a bimodal architecture with high relaxivity and bright luminescence in water. The versatile synthetic method can be adapted to introduce on the QD one or several additional functionalities such as targeting and bioactive moieties or cell penetrating ligands. Cell penetration is crucial for the use of CAs in the monitoring of biological events such as enzyme activity or pH and temperature changes, or in the tracking of stems cells, but only few examples of cell penetrating CAs have been reported. The peptide maurocalcine (MCa) coupled to commercial QDs has shown a great potential for cell penetration serving to *in vivo* imaging of macrophages as indicator of atherosclerosis.[42] Therefore, we have used MCa as cell penetrating ligand for a further functionalization of our bimodal platform.

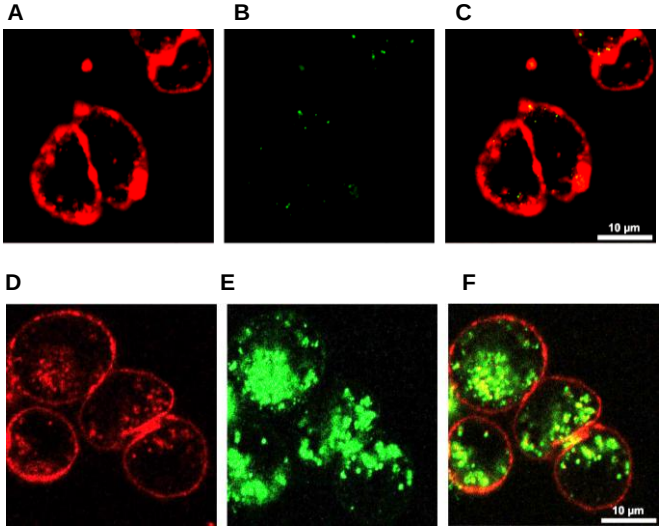

Figure 3. Confocal microscope images (false colours) of Chinese hamster ovarian cells (CHO) A) Stained with concanavalin A rhodamine (red); B) incubation with Gd.2.QD (green) for 2 hours followed by washing, C) merge of A and B. D) CHO cells as in A; E) incubation with Gd.2.QD.MCa for 2 hours followed by washing (green), F) merge of D and E.

We conjugated reproducibly both Gd.2 and the cell penetrating peptide maurocalcine (MCa) in its disulfide less version[43] through an additional N-terminal cysteine residue onto the penicillamine capped InP/ZnS QDs in a one step synthesis using a QD:Gd.2:TCEP:MCa ratio of 1:200:9000:5. TCEP was used at high concentration to cleave the disulfide bridge of Gd.2 and to prevent from the formation of undesired disulfide bridges. Magnetic susceptibility measurements[44] and UV visible spectroscopy showed the presence of 30 to 40 Gd chelates on the MCa QDs.

In order to probe the cell penetrating ability of this Gd.2.QD MCa dual probe, confocal microscopy images were recorded after incubation of the probe with Chinese Hamster Ovary (CHO) cells, (Figure 3). They clearly show that the MCa-conjugated Gd.2.QDs accumulate within CHO cells during the 2 hours incubation time, while no cell penetration is observed in the absence of MCa. Staining appeared as punctuate dots suggesting that these MCa-functionalized QD mostly entered the cells through endocytosis. Some diffuse staining was also evident suggesting that direct membrane translocation should not be excluded as one of the possible entry mechanisms. These data are coherent with earlier observations.[45] Importantly, similar experiments conducted with Gd.2.QD did not lead to intracellular accumulation of QD (Figure 3C), confirming that MCa was properly conjugated to Gd.2.QD and demonstrating that MCa is solely responsible for cell penetration of the complex.

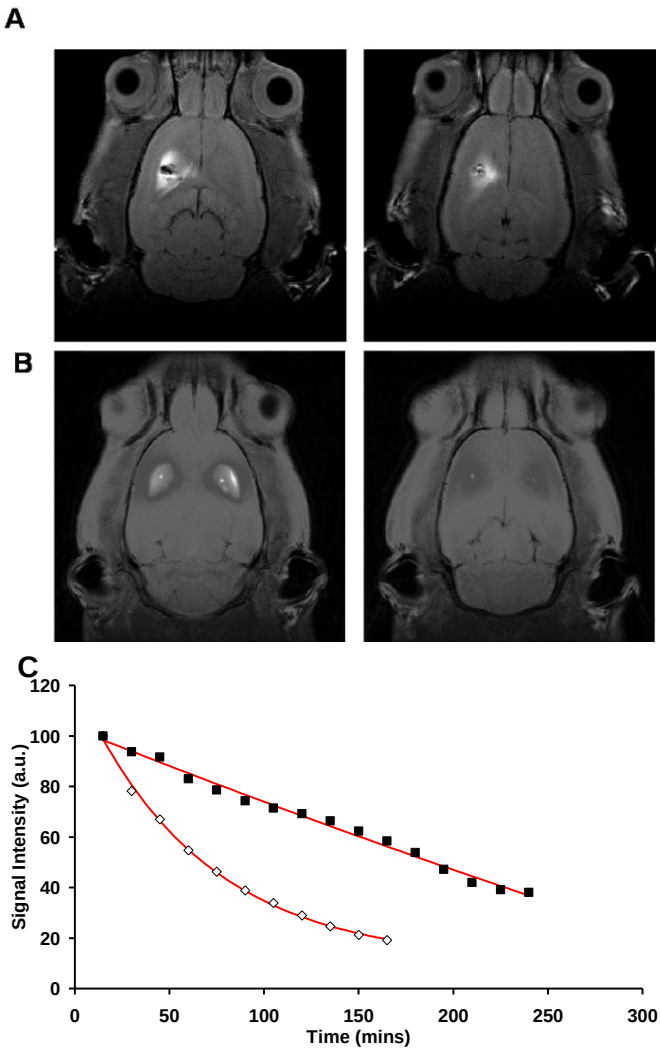

Figure 4. T1 weighted MRI images of rat brain at 7T (1 mM, 10 µl). A) Gd.2.QD.MCa at 15 minutes and 4 hours, B) Dotarem at 15 minutes and 4 hours. C) Signal intensity vs. time, Dotarem (◊) and Gd.2.QD.MCa (■).

The Gd.2Qd.MCa system provides a new high relaxivity bimodal probe which can penetrate cells. The cell permeability should lead to an increased retention of this contrast agent in brain tissue with respect to commercial CAs such as Dotarem ([Gd(DOTA)$^-$]. We therefore set out to compare whether Gd.2.QD.MCa provides a competitive advantage over Dotarem with regard to the retention time of the CA within the brain tissue.

To investigate this issue, 10 µl of 1 mM Dotarem or Gd.2.QD.MCa were injected directly into the striatum of 7 week-old rats (Figure 4). Both CAs led to a distinct signal within the injected striatum 15 min after injection. After 4 hours, the Dotarem signal almost disappeared, whereas distinct signal intensity was still measurable for Gd.2.QD.MCa (Figure 4A).

Data analysis of the signal intensity over time illustrates that Dotarem concentration decreases rapidly in the striatum, whereas the Gd.2.QD.MCa concentration decrease is significantly slower over the 4 hour period (Figure 4C). These data indicate a significant increase in tissue retention with respect to Dotarem. While MCa is probably contributing to some extent to the improved duration of the MRI signal at the injection point, it is also possible that the size of the agents is another important factor limiting the lateral tissue diffusion of the compound.

In conclusion we have synthesised a new bimodal MRI/optical probe through direct grafting of gadolinium chelates on fluorescent InP/ZnS QDs. The high payload of gadolinium (up to 80 chelates) results in a high relaxivity of the nanosized contrast agent (900 $mM^{-1}s^{-1}$ at 35 MHz (0.81T), 200 $mM^{-1}s^{-1}$ at 200 MHz (4.6T)) while the bright luminescence of the QD's is preserved. The versatile experimental strategy allows the simultaneous grafting of various probes to the QDs. Notably, the protocol could be easily extended to produce a trimodal probe, optical (Tb-chelate)/magnetic (Gd-chelate)/optical (QD), and will be the subject of future work. We have also shown, through the example of the cell penetrating peptide MCa, that additional targeting ligands can be co-grafted in a one-pot reaction. A new cell penetrating multimodal probe has been identified which shows bright luminescence, high relaxivity and excellent tissue retention properties allowing for longer MRI recording than with commercial CAS.

Received: ((will be filled in by the editorial staff))
Published online on ((will be filled in by the editorial staff))

Keywords: Gadolinium · Lanthanide complexes · Imaging agents · Quantum Dots · Fluorescence · Magnetic resonance imaging

[1] L. M. Manus, D. J. Mastarone, E. A. Waters, X. Q. Zhang, E. A. Schultz-Sikma, K. W. MacRenaris, D. Ho, T. J. Meade, *Nano Lett.*, **2010**, *10*, 484-489.
[2] A. Datta, J. M. Hooker, M. Botta, M. B. Francis, S. Aime, K. N. Raymond, *J. Am. Chem. Soc.* **2008**, *130*, 2546-2552.
[3] D. D. Castelli, E. Gianolio, S. G. Crich, E. Terreno, S. Aime, *Coord. Chem. Rev.* **2008**, *252*, 2424-2443.
[4] L. Moriggi, C. Cannizzo, E. Dumas, C. R. Mayer, A. Ulianov, L. Helm, *J. Am. Chem. Soc.* **2009**, *131*, 10828-10829.
[5] L. Frullano, C. Catana, T. Benner, A. D. Sherry, P. Caravan, *Angew. Chem.-Int. Edit.*,**2010**, *49*, 2382-2384.
[6] J. S. Choi, J. C. Park, H. Nah, S. Woo, J. Oh, K. M. Kim, G. J. Cheon, Y. Chang, J. Yoo, J. Cheon, *Angew. Chem.-Int. Edit.* **2008**, *47*, 6259-6262.
[7] M. Tsotsalas, M. Busby, E. Gianolio, S. Aime, L. De Cola, *Chem. Mat.* **2008**, *20*, 5888-5893.
[8] Y. Song, X. Y. Xu, K. W. MacRenaris, X. Q. Zhang, C. A. Mirkin, T. J. Meade, *Angew. Chem.-Int. Edit.* **2009**, *48*, 9143-9147.
[9] C. Q. Tu, X. C. Ma, P. Pantazis, S. M. Kauzlarich, A. Y. Louie, *J. Am. Chem. Soc.* **2010**, *132*, 2016-2023.
[10] W. J. M. Mulder, R. Koole, R. J. Brandwijk, G. Storm, P. T. K. Chin, G. J. Strijkers, C. D. Donega, K. Nicolay, A. W. Griffioen, *Nano Lett.* **2006**, *6*, 1-6.
[11] P. Howes, M. Green, A. Bowers, D. Parker, G. Varma, M. Kallumadil, M. Hughes, A. Warley, A. Brain, R. Botnar, *J. Am. Chem. Soc.* **2010**, *132*, 9833-9842.
[12] H. S. Yang, S. Santra, G. A. Walter, P. H. Holloway, *Adv. Mater.* **2006**, *18*, 2890-2894.
[13] L. E. Jennings, N. J. Long, *Chem. Commun.* **2009**, 3511-3524.
[14] T. Koullourou, L. S. Natrajan, H. Bhavsar, S. J. A. Pope, J. H. Feng, J. Narvainen, R. Shaw, E. Scales, R. Kauppinen, A. M. Kenwright, S. Faulkner, *J. Am. Chem. Soc.* **2008**, *130*, 2178-2179.
[15] S. G. Crich, L. Biancone, V. Cantaluppi, D. D. G. Esposito, S. Russo, G. Camussi, S. Aime, *Magn. Reson. Med.* **2004**, *51*, 938-944.
[16] X. Michalet, F. F. Pinaud, L. A. Bentolila, J. M. Tsay, S. Doose, J. J. Li, G. Sundaresan, A. M. Wu, S. S. Gambhir, S. Weiss, *Science* **2005**, *307*, 538-544.
[17] J. H. Lee, K. Lee, S. H. Moon, Y. Lee, T. G. Park, J. Cheon, *Angew. Chem.-Int. Edit.* **2009**, *48*, 4174-4179.
[18] D. Geissler, L. J. Charbonniere, R. F. Ziessel, N. G. Butlin, H. G. Lohmannsroben, N. Hildebrandt, *Angew. Chem.-Int. Edit.*, **2010**, *49*, 1396-1401.
[19] P. Reiss, M. Protière, L. Li, *Small* **2009**, *5*, 154-168.
[20] S. Hussain, N. Won, J. Nam, J. Bang, H. Chung, S. Kim, *ChemPhysChem* **2009**, *10*, 1466-1470.
[21] K. T. Yong, H. Ding, I. Roy, W. C. Law, E. J. Bergey, A. Maitra, P. N. Prasad, *Acs Nano* **2009**, *3*, 502-510.
[22] J. C. Frias, G. Bobba, M. J. Cann, C. J. Hutchison, D. Parker, *Org. Biomol. Chem.* **2003**, *1*, 905-907.
[23] E. J. New, A. Congreve, D. Parker, *Chem. Sci.* **2011**, *1*, 111-118.
[24] E. J. New, D. Parker, D. G. Smith, J. W. Walton, *Curr. Opin. Chem. Biol.* **2010**, *14*, 238-246.
[25] J. C. G. Bunzli, *Chem. Rev.* **2010**, *110*, 2729-2755.
[26] B. Song, C. D. B. Vandevyver, A. S. Chauvin, J. C. G. Bunzli, *Org. Biomol. Chem.* **2008**, *6*, 4125-4133.
[27] J. C. G. Bunzli, *Chemistry Letters* **2009**, *38*, 104-109.
[28] E. Deiters, B. Song, A. S. Chauvin, C. D. B. Vandevyver, F. Gumy, J. C. G. Bunzli, *Chem. Eur. J.* **2009**, *15*, 885-900.
[29] M. P. Lowe, D. Parker, O. Reany, S. Aime, M. Botta, G. Castellano, E. Gianolio, R. Pagliarin, *J. Am. Chem. Soc.* **2001**, *123*, 7601-7609.
[30] C. Picard, N. Geum, I. Nasso, B. Mestre, P. Tisnes, S. Laurent, R. N. Muller, L. Vander Elst, *Bioorganic & Medicinal Chemistry Letters* **2006**, *16*, 5309-5312.
[31] A. Nonat, C. Gateau, P. H. Fries, M. Mazzanti, *Chem. Eur. J.* **2006**, *12*, 7133-7150.
[32] L. Frullano, T. J. Meade, *J. Biol. Inorg. Chem.* **2007**, *12*, 939-949.
[33] M. F. Kircher, U. Mahmood, R. S. King, R. Weissleder, L. Josephson, *Cancer Res.* **2003**, *63*, 8122-8125.
[34] W. J. M. Mulder, G. J. Strijkers, J. W. Habets, E. J. W. Bleeker, D. W. J. van der Schaft, G. Storm, G. A. Koning, A. W. Griffioen, K. Nicolay, *Faseb J.* **2005**, *19*, 2008-2010.
[35] M. Modo, K. Mellodew, D. Cash, S. E. Fraser, T. J. Meade, J. Price, S. C. R. Williams, *Neuroimage* **2004**, *21*, 311-317.
[36] E. S. Olson, T. Jiang, T. A. Aguilera, Q. T. Nguyen, L. G. Ellies, M. Scadeng, R. Y. Tsien, *Proc. Nat. Acad. Sci. U.S.A.* **2010**, *107*, 4311-4316.
[37] L. Prinzen, R. Miserus, A. Dirksen, T. M. Hackeng, N. Deckers, N. J. Bitsch, R. T. A. Megens, K. Douma, J. W. Heemskerk, M. E. Kooi, P. M. Frederik, D. W. Slaaf, M. van Zandvoort, C. P. M. Reutelingsperger, *Nano Lett.* **2007**, *7*, 93-100.
[38] H. D. Powell, O. M. N. Ni Dhubhghaill, D. Pubanz, L. Helm, Y. S. Lebedev, W. Schlaepfer, A. E. Merbach, *J. Am. Chem. Soc.* **1996**, *118*, 9333-9346.
[39] A. E. Merbach, E. Toth, *The Chemistry of Contrast Agents in Medical Magnetic Resonance Imaging*, Wiley, Chichester, **2001**.
[40] L. Li, M. Protière, P. Reiss, *Chem. Mater.* **2008**, *20*, 2621-2623.
[41] S. Tamang, G. Beaune, C. Poillot, M. De Waard, I. Texier-Nogues, P. Reiss, *Proc. SPIE* **2011**, *7909*, 79091B.
[42] A. Jayagopal, Y. R. Su, J. L. Blakemore, M. F. Linton, S. Fazio, F. R. Haselton, *Nanotechnol.* **2009**, *20*, 165101-165113
[43] E. Esteve, K. Mabrouk, A. Dupuis, S. Smida-Rezgui, X. Altafaj, D. Grunwald, J. C. Platel, N. Andreotti, I. Marty, J. M. Sabatier, M. Ronjat, M. De Waard, *J. Biol. Chem.* **2005**, *280*, 12833-12839.
[44] D. M. Corsi, C. Platas-Iglesias, H. van Bekkum, J. A. Peters, *Magn. Reson. Chem.* **2001**, *39*, 723-726.
[45] N. Ram, N. Weiss, I. Texier-Nogues, S. Aroui, N. Andreotti, F. Pirollet, M. Ronjat, J. M. Sabatier, H. Darbon, V. Jacquemond, M. De Waard, *J. Biol. Chem.* **2008**, *283*, 27048-27056.
[46] N. Ram, I. Texier-Nogues, K. Pernet-Gallay, C. Poillot, M. Ronjat, A. Andrieux, C. Arnoult, J. Daou, M. De Waard, *IJBNN* **2011**, *2*, 13-32.

Imaging Agents

Graeme J. Stasiuk, Sudarsan Tamang, Daniel Imbert, Cathy Poillot, Marco Giardiello, Céline Tisseyre, Emanuel Barbier, Pascal H. Fries, Michel De Waard, Peter Reiss and Marinella Mazzanti* _____ **Page – Page**

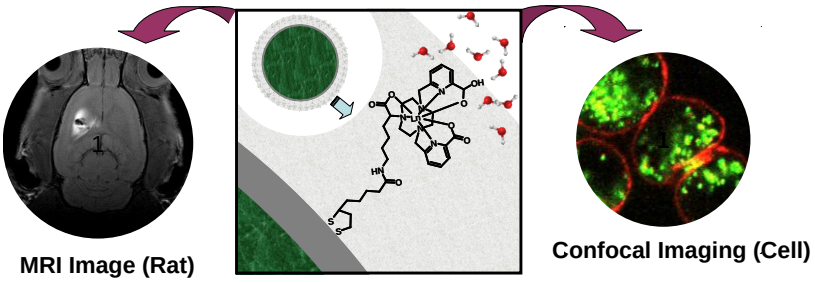

Cell Permeable Multimeric Ln (III) Chelate Functionalized Quantum Dots as Multimodal Imaging Probes

A new cell permeable bimodal MRI/optical probe with high gadolinium payload has been prepared trough direct grafting of Gd^{III} chelates and a cell penetrating peptide on non-toxic InP/ZnS QDs. This nanosized reporter shows high relaxivity, bright fluorescence and high tissue retention.

Cell Permeable Multimeric Ln (III) Chelate Functionalized Quantum Dots as Multimodal Imaging Probes

Graeme J. Stasiuk, Sudarsan Tamang, Daniel Imbert, Cathy Poillot, Marco Giardiello, Céline Tisseyre, Emmanuel L Barbier, Pascal H. Fries, Michel De Waard, Peter Reiss and Marinella Mazzanti*

Dr. G. J. Stasiuk, Dr. M. Giardiello, Dr. D. Imbert, Dr. P. H. Fries, Dr. M. Mazzanti.
CEA, INAC, SCIB, Laboratoire de Reconnaissance Ionique et Chimie de Coordination, CEA-Grenoble, UJF, LCIB, UMR-E 3 CEA-UJF, 38054 Grenoble Cedex 9, France
Fax: (+33) 438-785-090
E-mail: marinella.mazzanti@cea.fr

S. Tamang, Dr. P. Reiss
CEA Grenoble INAC/SPrAM UMR 5819 CEA-CNRS-UJF, Laboratoire d'Electronique Moléculaire, Organique et Hybride

C. Poillot, C. Tisseyre, Dr E. Barbier, Dr M. De Waard.
Grenoble Institute of Neuroscience, Inserm U836, Site Santé de la Tronche, bâtiment Edmond J. Safra, Chemin Fortuné Ferrini, BP170, 38042 Grenoble Cedex 9, France

General procedures. NMR spectra were recorded on Bruker DPX200 500 MHz spectrometers using standard Bruker software. Chemical shifts are reported in ppm with solvent as internal reference. ESMS were recorded on a Thermo Scientific (LXQ) spectrometer. Electronic absorption spectra were recorded on a Varian CARY 50 probe UV/vis spectrometer.

Materials. Solvents and starting materials were obtained from Aldrich, Fluka, Acros, and Alfa. They were used without further purification unless otherwise stated. Solvents were dried over the appropriate drying agents when required. Water and H_2O refer to high purity water with resistivity value of 18 MΩ·cm, obtained from the "Millipore/MilliQ" purification system. Lanthanide chloride salts were purchased from Aldrich. Dotarem was purchased from (Guerbet SA, Aulnay-s-bois, France).

The precise metal ion content was titrated by colorimetry in acetate buffer (pH = 4.5) using standardized H_2Na_2edta solution (Merck) and Xylenol orange indicator. 6,6'-((1,4,7-triazonane-1,4-diyl)bis(methylene))dipicolinate was prepared according to literature procedure.[1]

Ligand Synthesis

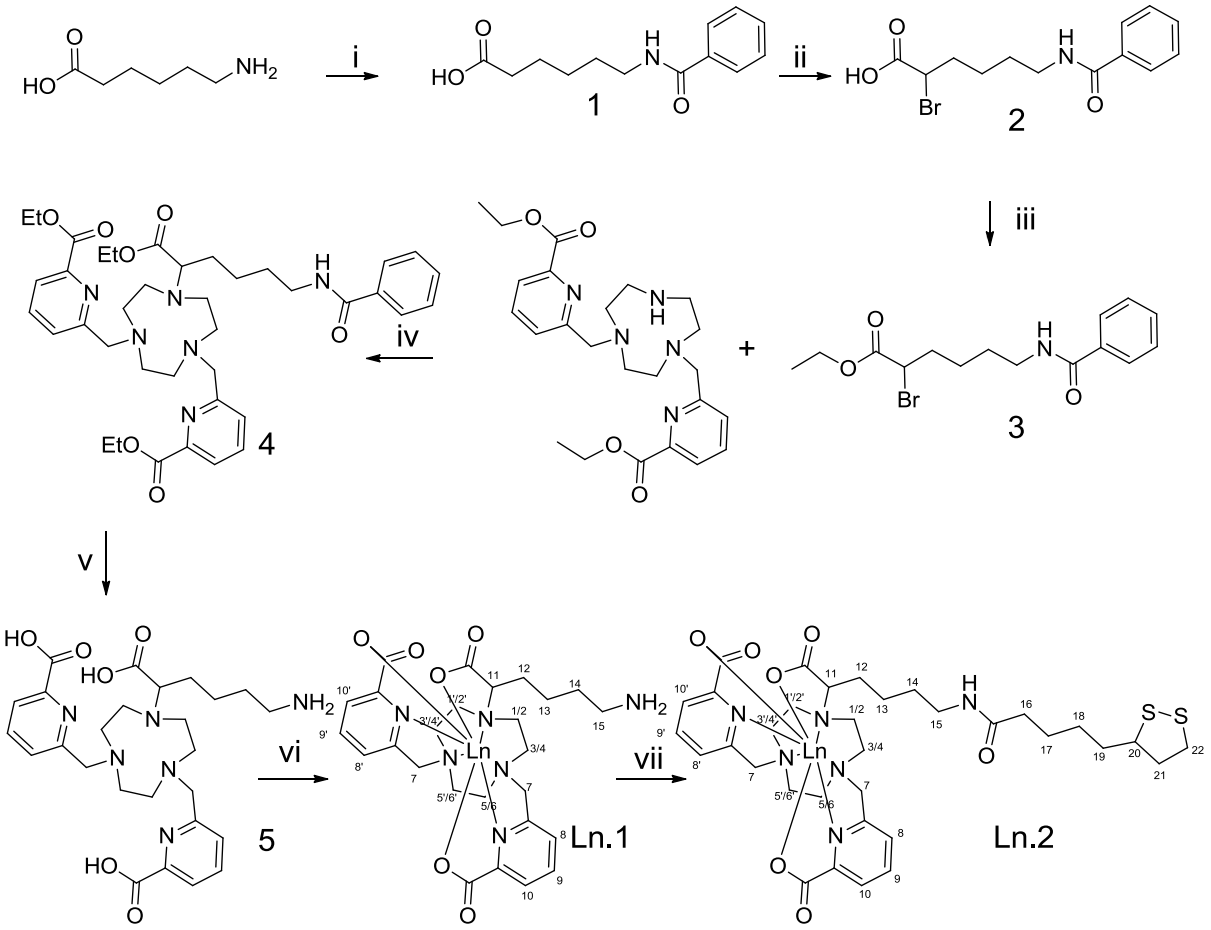

i) Benzoyl chloride, NaOH, H_2O. ii) Br_2, PBr_3, CCl_4. iii) EtOH, H_2SO_4. iv) K_2CO_3, KI, MeCN. v) HCl.
vi) $LnCl_3.6H_2O$, H_2O, pH 5.5. vii) DHLA, EDCI, DMAP, DMF/H_2O

Scheme S1. Synthesis of amino appended bptacn ligand

6-benzamidohexanoic acid(1)

A solution of NaOH (16.8 g, 0.419 moles) in water (17 mL) was added to a solution of 6-aminohexanoic acid (25.0 g, 0.191 moles) in of water (500 mL). The solution temperature was lowered to 10^{o}C and benzoyl chloride (29.5 g, 24.30 mL, 0.201 moles), was added dropwise. The desired product precipitated out of the solution as a white powder and was collected and washed 3 times with water followed by 3 times with petroleum ether and then dried under vacuum overnight. Yield = 30.45 g, 68 %. δ_H (MeOD; 200 MHz, 298 K) 7.78 (m,

2H, H_{ar}), 7.45 (m, 3H, H_{ar}), 3.42 (t, $^3J_{HH}$ = 6.9 Hz, 2H, NHCH_2), 2.24 (t, $^3J_{HH}$ = 7.6 Hz,2H, CH_2CO_2H), 1.66 (m, 4H, $CH_2CH_2CH_2CH_2CH_2$), 1.46 (m, 2H, $CH_2CH_2CH_2CH_2$); *m/z* (ESMS) $[M+H]^+$ 236.5

6-benzamido-2-bromohexanoic acid (2)

6-benzamidohexanoic acid (2.4 g, 0.010 moles) and phosphorous tribromide (3.03 g, 1.06 mL, 0.012 moles) were dissolved under argon in CCl_4 (20 mL), in a 250 mL three neck round bottom flask, equipped with a reflux condenser bearing a calcium chloride drying tube. Bromine (3.56 g, 1.15 mL, 0.022 moles), was added slowly in three portions to the reaction mixture over 30 minutes at 0°C. After this period the reaction was heated to reflux (85°C – 90°C) for 18 hours. After cooling, the reaction mixture was added to 10 mL of chloroform and then was poured carefully into approx 50 ml of methanol and then water. The solvents were evaporated to dryness and the crude mixture was dissolved again in 100 mL water. The solution was cooled to 0°C to afford a white precipitate which was collected and recrystallized from 20 mL of 5% water:ethanol solution at -85°C to yield the desired monohydrated carboxylic acid (2.15 g, yield 67%). δ_H (MeOD; 200 MHz, 298 K) 7.82 (m, 2H, H_{ar}), 7.52 (m, 3H, H_{ar}), 4.34 (t, $^3J_{HH}$ = 7.1 Hz, 1H, *CH*$BrCO_2H$), 3.43 (t, $^3J_{HH}$ = 6.0 Hz, 2H, NHCH_2), 2.07 (m, 2H, $CH_2CH_2CH_2CH_2$), 1.67 (m, 4H, $CH_2CH_2CH_2CH_2CH_2$); *m/z* (ESMS) $[M+H]^+$ = 314.5.

Ethyl 6-benzamido-2-bromohexanoate (3)

6-benzamido-2-bromohexanoic acid (1.35 g, 4.29 mmoles), was dissolved in ethanol (100 mL). H_2SO_4 (15 mL, 97%) was then added and the solution was heated to reflux for one hour. The solution was evaporated to dryness and the residue was extracted with 3 x 50 mL dichloromethane as a brown oil (.0.78 g, yield 77 %). δ_H ($CDCl_3$; 200 MHz, 298 K) 7.81 (m, 2H, H_{ar}), 7.51 (m, 3H, H_{ar}), 6.23 (broad s, 1H, NH) 4.25 (m, 3H, BrCH and CH_3CH_2O), 3.53 (q, J = 6.7 Hz, 2H, NHCH_2), 2.12 (bm, 2H, $CH_2CH_2CH_2CH_2$), 1.68 (bm, 4H, $CH_2CH_2CH_2CH_2CH_2$), 1.33 (t, J = 7.0 Hz 3H, CH_2CH_3); *m/z* (ESMS) $[M+H]^+$ 344.1.

Diethyl 6,6'-((7-(6-benzamido-1-ethoxy-1-oxohexan-2-yl)-1,4,7-triazonane-1,4-diyl)bis(methylene))dipicolinate (4)

Diethyl 6,6'-((1,4,7-triazonane-1,4-diyl)bis(methylene))dipicolinate (310 mg, 0.687 mmoles), was dissolved in dry acetonitrile (20 mL) in the presence of dry K_2CO_3 (107 mg, 0.776 mmoles) under argon. A solution of ethyl 6-benzamido-2-bromohexanoate (266 mg, 0.776 mmoles) in dry acetonitrile (10 mL) was then added to the solution under argon and the reaction mixture was heated to reflux for 48 hours. Upon cooling, the mixture was filtered over celite to remove K_2CO_3, the solvent was evaporated and the residue was purified *via* silica column chromatography using graduated dichloromethane:methanol as eluent (graduated from 0% to 10 % ethanol). Brown oil = 251 mg, yield 51%. δ_H (CDCN; 200 MHz, 298 K) 7.89 (br m, 8H), 7.43 (br m, 3H), 4.35 (q, $^3J_{HH}$ = 7.1 Hz, 4H,CH_3CH_2O), 4.06 (q, $^3J_{HH}$ = 7.2 Hz, 2H, CH_3CH_2O), 3.79 (s, 4H, NCH_2C), 3.36 (q, $^3J_{HH}$ = 6.1 Hz, 2H, CH_2CH_2NH), 3.24 (t, $^3J_{HH}$ = 6.4 Hz, 1H, $NCHCH_2$), 2.82 (bm, ring 12H), 1.61 (bm, 6H $CH_2CH_2CH_2$), 1.35 (t, 3JHH 7.1 Hz, 6H, CH_2CH_3), 1.16 (t, $^3J_{HH}$ = 7.1 Hz, 3H CH_2CH_3); *m/z* (ESMS) $[M+H]^+$ 717.6.

6,6'-((7-(5-amino-1-carboxypentyl)-1,4,7-triazonane-1,4-diyl)bis(methylene))dipicolinic acid (5)

Diethyl6,6'-((7-(6-benzamido-1-ethoxy-1-oxohexan-2-yl)-1,4,7-triazonane-1,4-diyl)bis(methylene))dipicolinate (200 mg, 0.279 mmoles) were dissolved in 6M HCl (30 mL) and the solution was heated at reflux for 24 hours. The solvents were removed and the residue was dissolved in water (20 ml). The pH was raised to 4.5 and the resulting aqueous solution was washed 3 times with 20 mL diethyl ether. δ_H (D_2O; 200 MHz, 298 K) 8.01 (t, $^3J_{HH}$ = 7.8 Hz 2H), 7.91 (d, $^3J_{HH}$ = 7.8, 2H), 7.62 (d, $^3J_{HH}$ = 7.9, 2H), 4.79 (s, 4H, N*CH*$_2$C), 3.73 (m, 13H, N*CH*CH_2 and *ring*), 2.84 (t, $^3J_{HH}$ = 7.1,Hz 2H, *CH*$_2$$NH_2$), 1.52 - 1.49 (broad m, 6H, *CH*$_2$*CH*$_2$*CH*$_2$); *m/z* (ESMS) $[M+H]^+$ 529.4, elemental analysis (%) calcd. for $C_{26}H_{41}Cl_5N_6O_6 \cdot 3H_2O$: C 40.82, H 6.19, N 10.99; found C 41.09, H 6.27, N 11.17.

Complex Synthesis

Ln 6,6'-((7-(5-amino-1-carboxypentyl)-1,4,7-triazonane-1,4-diyl)bis(methylene))dipicolinic acid (Ln.1)

6,6'-((7-(5-amino-1-carboxypentyl)-1,4,7-triazonane-1,4-diyl)bis(methylene))dipicolinic acid (0.076 mmoles) was dissolved in water (2mL) and the pH was adjusted to 5.5 with small aliquots of 1.0 M NaOH. $LnCl_3.6H_2O$ (0.076 mmoles) was dissolved in 1 ml of water at pH 5.5. The two solutions were combined and the pH re-adjusted to 5.5. The solution was then stirred for 30 minutes. The solvent was removed to give a hygroscopic white powder, this was purified on a Sephadex G25 resin (equilibrated with water) to remove inorganic salts. The resulting aliquots containing the complex were combined and the solvent removed, yielding the desired Ln.1 complexes as white hygroscopic solids in yield for Ln=Gd; 69% for Ln=Eu 79% and for Ln = Tb 75%.

Gd: *m/z* (ESMS) $[M+H]^+$ 684.3

Eu: *m/z* (ESMS) $[M+H]^+$ 679.31 H NMR (200 MHz, D2O, 278 K,): 25.7 (s, 1H; H1'/H2'), 14.89 (s, 1H; H7'), 9.15(s,1H; H8),8.89(s, 1H; H8'), 8.17 (s,1H; H9), 7.97 (s, 1H; H9'), 7.65 (s, 2H; H10/H10'), 5.44 (s, 1H; H7) , 3.72 (s, 1H; H11), 3.19 (s, 2H; H5'/H6'), 2.81 (s, 2H; H12), 2.41 (s, 2H; H7), 1.69 (s, 2H; H15), 1.36 (s, 2H; H13), 1.03 (s,1H; H7), 0.32 (s, 2H; H14), -0.86 (s, 1H; H3'/H4'), -1.16 (s, 1H; H5/H6), -2.35 (s, 1H; H3'/H4'), -4.18 (s, 1H; H7), -4.7 (s, 1H; H1/H2), -8.02 (s, 1H; H1'/H2'), -10.19 ppm (s, 1H; H5/H6), -13.48, (s, 1H; H3/H4) -15.05(s, 1H; H1/H2)

Tb:*m/z* (ESMS) $[M+H]^+$ 685.3

Ln 6,6'-((7-(13-12-dithiolanyl-5-pentaamido-1-carboxypentyl)-1,4,7-triazonane-1,4-diyl)bis(methylene))dipicolinic acid (Ln.2)

Ln. 6,6'-((7-(5-amino-1-carboxypentyl)-1,4,7-triazonane-1,4-diyl)bis(methylene))dipicolinic acid (0.073mmoles), thoctic acid (0.043 0.222 mmoles), EDCI (0.222 mmoles) and DMAP (0.222 mmoles) were dissolved in water:DMF (5 mL, 1:1). A precipitate formed, corresponding to the DMAP chloride salt. The solution was stirred for 18 hours and filtered. The volume was then concentrated to exactly 1 mL, the complex purified on a Sephadex G-25 size exclusion column, eluting with water. The aliquots containing the complex were combined as the desired Ln.2 complexes as a hygroscopic solids, in yield for Ln=Gd; 60% for Ln=Eu 59% and for Ln = Tb 61%.

Gd.2. *m/z* (ESMS) $[M+H]^+$ 874.3.

Eu.2: *m/z* (ESMS) $[M+H]^+$ 868.3. H NMR (200 MHz, D2O, 278 K,): 25.7 (s, 1H; H1'/H2'), 14.89 (s, 1H; H7'), 9.15(s,1H; H8),8.89(s, 1H; H8'), 8.17 (s,1H; H9), 7.97 (s, 1H; H9'), 7.65 (s, 2H; H10/H10'), 5.44 (s, 1H; H7) , 3.72 (s, 1H; H11), 3.19 (s, 2H; H5'/H6'), 2.94 (bm, 7H; H12, H17, H19, H20), 2.72 (bm, H16, H18), 2.41 (s, 2H; H7), 1.69 (s, 2H; H15), 1.36 (s, 2H; H13), 1.03 (s,1H; H7), 0.92 (bm, 4H, H21, H22), 0.32 (s, 2H; H14), -0.86 (s, 1H; H3'/H4'), -1.16 (s, 1H; H5/H6), -2.35 (s, 1H; H3'/H4'), -4.18 (s, 1H; H7), -4.7 (s, 1H; H1/H2), -8.02 (s, 1H; H1'/H2'), -10.19 ppm (s, 1H; H5/H6), -13.48, (s, 1H; H3/H4) -15.05(s, 1H; H1/H2)

Tb.2 *m/z* (ESMS) $[M+H]^+$ 875.3.

Quantum Dot Synthesis

The synthesis follows the protocol given in Ref. 2. Briefly, the indium precursor (1 eq. of indium myristate in 1-octadecene) was reacted under Ar atmosphere with *in situ* generated PH_3 gas at 250°C for 60 min to form the core InP QDs. For growth of the ZnS shell, 10 eq. of zinc stearate are added into the dispersion of the InP NCs and heated for 4 hrs to 280°C to form a Zn^{2+}-rich surface before injecting slowly 2.5 eq. of zinc ethylxanthate at 210°C during 30 min.

Synthesis of penicillamine–capped QDs (QD-pen)

Thorough purification of the initial QDs assuring the removal of excess hydrophobic ligands is crucial for the successful phase transfer. 5 mL of the QDs in organic solvent are mixed with anhydrous ethanol (1:3) and centrifuged at 10 000 rpm (rotations per minute) for 6 minutes. The clear solution of supernatant is discarded and the precipitate is re-dispersed in 15 mL of a 1:3 chloroform:ethanol mixture and centrifuged again. The precipitate is dispersed in a minimum amount of chloroform. The concentration is estimated from the first excitonic peak in the UV-Vis spectrum.[3]

A 0.2 M solution of penicillamine in degassed MilliQ water (1mL) with pH adjusted at 9 with 0.5 M TMAH (TetraMethylAmmonium Hydroxide), is mixed with a ~5 μM dispersion of the QDs in chloroform (1.5 mL). The resulting biphasic mixture is stirred vigorously at 1400 rpm for 2 hrs to afford a fine aqueous suspension of QD-pen which is separated from the organic layer (yield: 60%).

Synthesis of Gd.2.QD

Solutions of Gd.2 (0.25 mL, $2.1 \cdot 10^{-3}$ M) and TCEP (0.046 mL, 0.5 M) in degassed water were added to the suspension of QD-pen (0.5 mL, $5.2 \cdot 10^{-6}$ M) in degassed water and the pH of the resulting suspension was adjusted to 9 with 0.5 M TMAH. The mixture was shaken at 800

rpm overnight at 20°C. The resulting fine suspension was purified portionwise (200 µL) using PES 30K centrifuge filters at 1400 rpm for 60 seconds. The obtained nanoparticles were washed with 3 x 150 µl degassed H_2O/PBS to remove any ungrafted complex. The nanoparticle portions were combined and concentrated to 100 µl, giving a fine orange suspension (yield 40%).
This procedure was repeated several times. A gadolinium content in the range 70-80 complexes per QD was determined for independent syntheses by combined magnetic susceptibility measurements and UV-Vis spectroscopy.

Synthesis of Gd.2QD.MCa

Solutions of Gd.2 (0.25 mL, $2.1 \cdot 10^{-3}$ M), TCEP (0.046 mL, 0.5 M) and maurocalcine (MCa) (0.054mL, $2.5 \cdot 10^{-5}$ M) in degassed water were added to the suspension of QD-pen (0.5 mL, $5.2 \cdot 10^{-6}$ M) in degassed water and the pH of the resulting suspension was adjusted to 9. The mixture was shaken at 800 rpm overnight at 20°C. The resulting fine suspension was purified portionwise (200 µL) using modified PES 30K centrifuge filters at 1400 rpm for 60 seconds. The obtained nanoparticles were washed with 3 x 150 µl degassed H_2O/PBS to remove any ungrafted complex. The nanoparticle portions were combined and concentrated to 100 µl, giving a fine orange suspension.
This procedure was repeated several times. A gadolinium content in the range 30-40 complexes per QD was determined for independent synthesis by combined magnetic susceptibility measurements and UV-Vis spectroscopy,

The concentration of the samples before phase transfer and after grafting is estimated from the first excitonic peak in the UV-Vis spectra using the empirical correlations between the excitonic peak, size and molar extinction coefficient compiled in reference [3] The concentration of Gd(III) was checked by the chemical shift measurement of HOD induced by the magnetic susceptibility.[4]

Relaxivity measurements

The Gd.1 and Gd.2 samples were prepared *in situ* by mixing the appropriate amounts of ligand and $GdCl_3.6H_2O$ (99.99%; Aldrich) in H_2O followed by adjustment of the pH with NaOH aqueous solution (pH = 7.4). The pH of the Gd2.QD suspension were adjusted for relaxivity measurements at 7.4. The resulting suspension was placed in a 1.7 mm diameter capillary which was sealed. The absence of free gadolinium was checked in all samples by the xylenol orange test.[5] The NMRD profiles were measured at 298K in the range 0.1 and 35Mz, by using a Spinmaster FFC (fast field cycling) NMR relaxometer (Stelar, Italy). The $1/T_1$ measurement were performed on a Brucker Avance 200 spectrometer (200MHz). The 1/*T*1 measurements at 45 MHz (1.06 T) and 298K were performed on a BrukerMinispec “mqvar” ND2318. At higher magnetic fields relaxation measurements were performed on conventional high resolution NMR spectrometers.

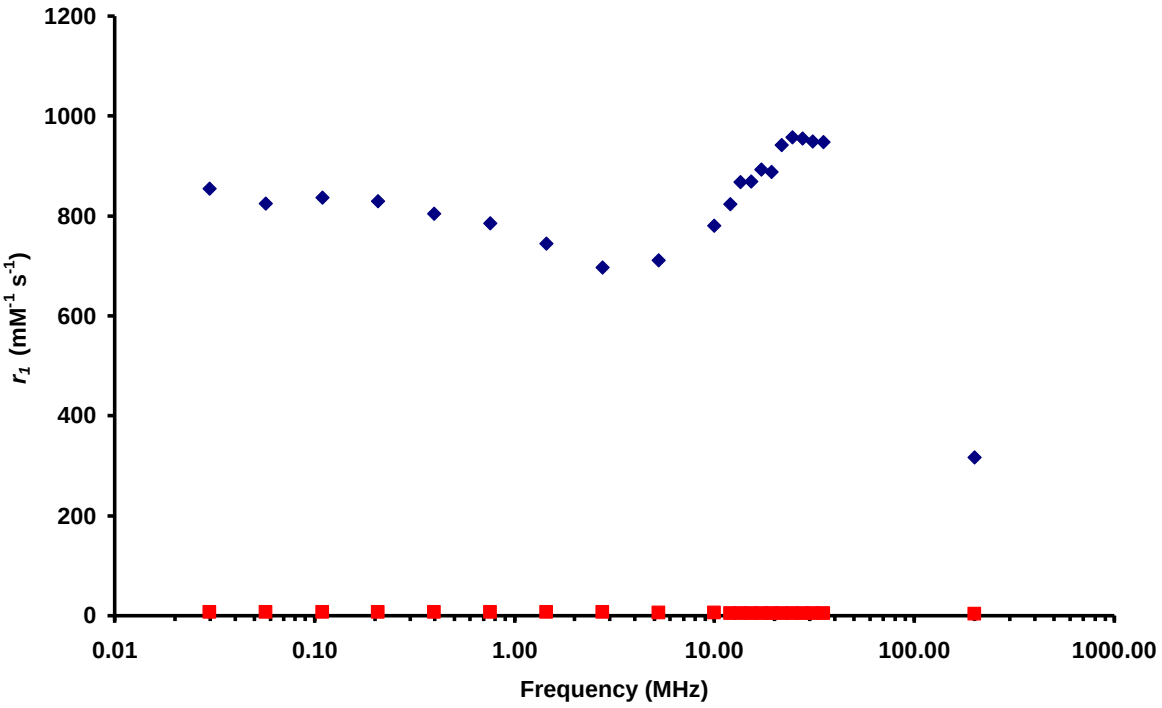

Figure S1: NMRD profile for Gd.2 (red squares) and Gd.2.QD (80 chelates) (Blue diamonds), relaxivity per object in H_2O at 298 K

Luminescence Spectroscopy

Luminescence data was recorded using a Perkin Elmer LS50B luminescence spectrometer (using FLWINLAB for Windows v2.2). Samples were held in a 10x10 nm or 10x2 nm quartz Hellma cuvette and cut-off filter (450 nm) was used to avoid second-order diffraction effects.

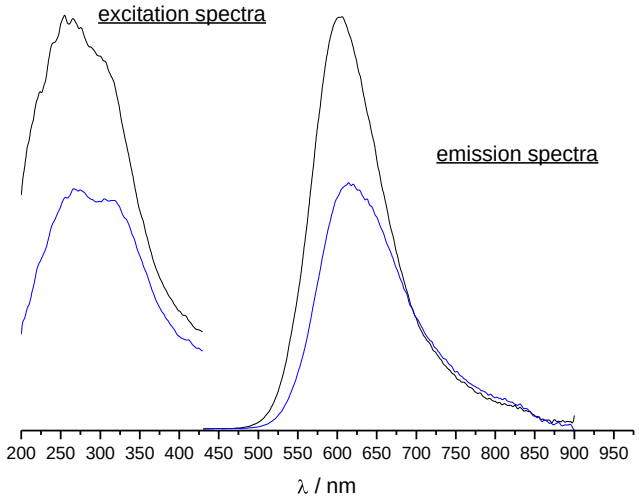

Figure S2: Excitation (λ_{em} = 620 nm) and emission (λ_{ex} = 320 nm spectra of QD-penicilamine (black) and QD.Gd (blue).

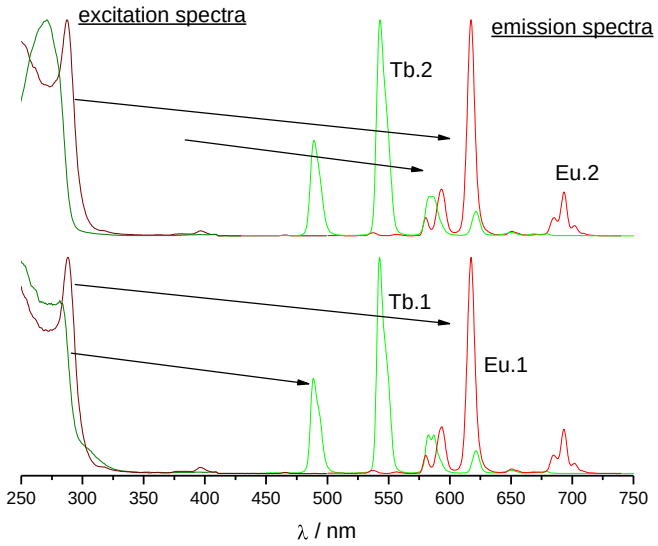

Figure S3: Excitation (λ_{em} = 546 or 612 nm) and emission (λ_{ex} = 275 nm spectra Eu.2, Tb.2 (top) Eu.1, Tb.1 (bottom)

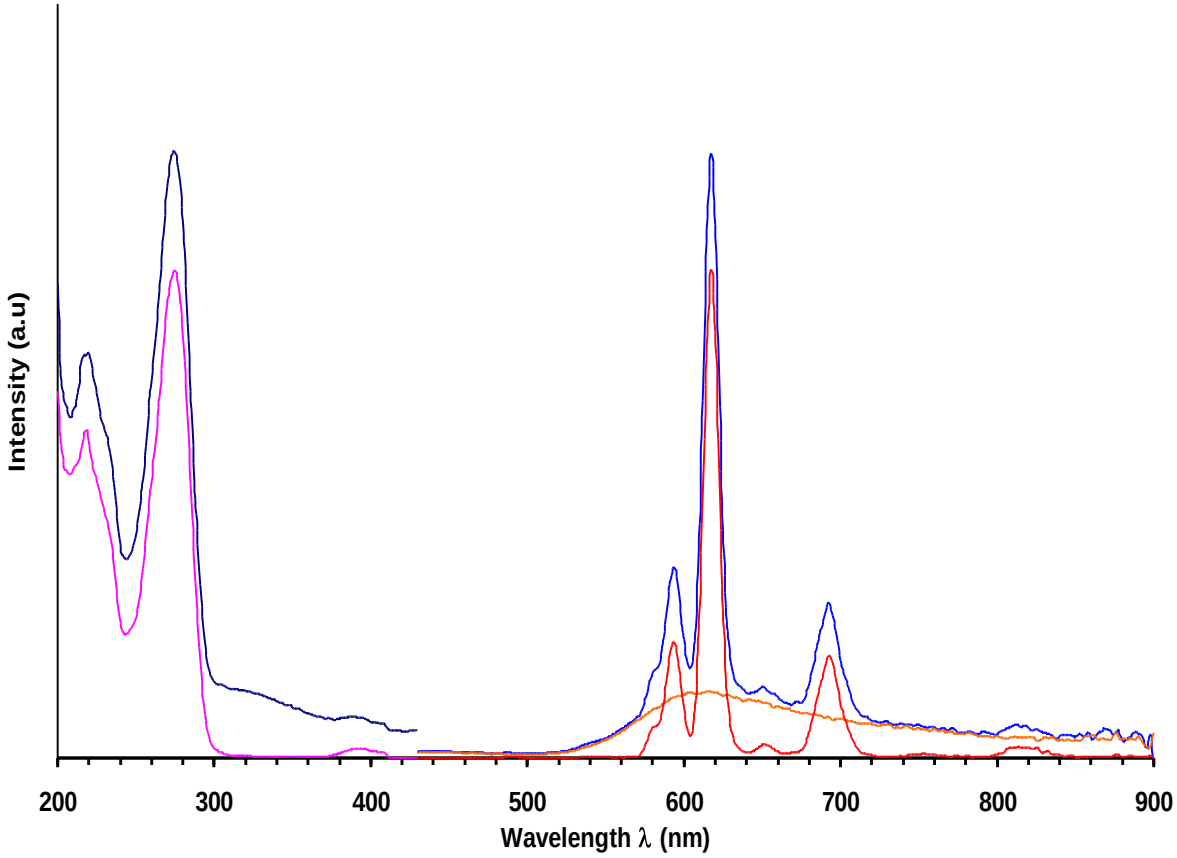

Figure S4. Luminescence spectra for Eu.2.QD, (Left) excitation spectra with λ_{em} = 617 nm (dark blue : 0 ms and pink : 0.05 ms delay, respectively); (Right) : emission spectra with λ_{ex} = 275 nm (blue : 0 ms delay and red 0.05 ms delay, respectively) and λ_{ex} = 320 nm (orange 0 ms delay)

Lifetime Measurements

Excited state lifetime measurements were made on a Perkin Elmer LS50B luminescence spectrometer (using FLWINLAB for Windows). Lifetimes were measured by direct excitation (275 nm) of the sample with a short 40 ms pulse of light (500 pulses per point) followed by monitoring the integrated intensity of light (617 nm for Eu and 546 nm for Tb) emitted during a fixed gate time of 0.1 ms, at a delay time later. Delay times were set at 0.1 ms intervals, covering 4 or more lifetimes. Excitation and emission slits were set to 5:5 nm bandpass respectively. The obtained decay curves were fitted to a simple mono exponential first-order decay curve using Microsoft Excel.

q-values were calculated using the following equations:[6]
$q = 1.2[kH2O - kD2O - 0.25]$ for Eu
$q = 5[kH2O - kD2O - 0.06]$ for Tb

Complex	***t*(H_2O)**	***t*(D_2O)**	***q***
Eu .1	1.5	0.52	1.2
Eu .2	1.51	0.53	1.2
Tb.1	1.34	1.95	1.1
Tb.2	1.35	2.26	1.2

Time gated Experiments

Time gated experiments were recorded using a Perkin Elmer LS50B luminescence spectrometer (using FLWINLAB for Windows), using a 0.05 ms delay to remove luminescence from the QD.

Luminescence and Quantum Yield measurements using a modular Fluorolog FL 3- 22 spectrometer from Horiba-Jobin Yvon-Spex

The excitation source was a 450W Xe arc lamp and all spectra were corrected for detection and optical spectral response (instrumental functions) of the spectrofluorimeter. It is equipped with a double grating excitation monochromator and a iHR320 imaging spectrometer coupled to a R928P Hamamatsu photomultiplier for visible measurement. The quantum yields were determined at room temperature through an absolute method[7] using a home-modified integrating sphere coupled to the modular Fluorolog FL 3-22 spectrofluorimeter. The values reported are the average of three independent determinations for each sample. The absolute quantum yield was calculated using the following expression:

$$\Phi = \frac{E_c}{L_a - L_c} = \frac{E_c}{L_a \cdot \alpha} \quad \text{and} \quad \alpha = \frac{L_a - L_c}{L_a}$$

Where *Ec* is the emission spectra in the emission range of the sample (ex: if the emission maximum is 620 nm, the range of this spectrum will be from 450 to 750 nm), *Lc* is the emission spectra of the excitation wavelength of the sample, *La* is the emission spectra of the excitation wavelength of the reference (quartz capillaries tube 4 mm in diameter filled with the solvent used).

DLS measurements

The hydrodynamic diameter of the water-soluble NCs dispersed in water was measured by dynamic light scattering (DLS), using a Malvern Zeta Sizer (NanoZS). The samples have been thoroughly purified with centrifugal filters from VWR (MWCO 30k) and dispersed in MilliQ water (18 m∧) prior to the measurements. Given the sensitivity of the instrument, multiple runs (> 3) were performed to avoid erroneous results. The spectra have been corrected by the instrument software for viscosity (0.882 mPa.s at 25°C), absorption (at 532nm), solvent (water) refractive index (1.33) and material (InP) refractive index (3.1). The data is collected in automatic mode and is expressed in number-%.

Quantum dot	**Size (nm)**
Quantum dot Penicilamine	6.9
Eu Grafted Quantum dot	9.2
Gd Grafted Quantum dot	8.6

TEM image of Gd.2.QD

TEM images of Gd.2.QD were taken with a JEOL 4000EX microscope operated at 400 kV. The samples were prepared by evaporating a drop of the colloidal solution on a copper grid supporting a thin carbon film. The circles drawn in the image show individual InP/ZnS Gd.2.QDs.

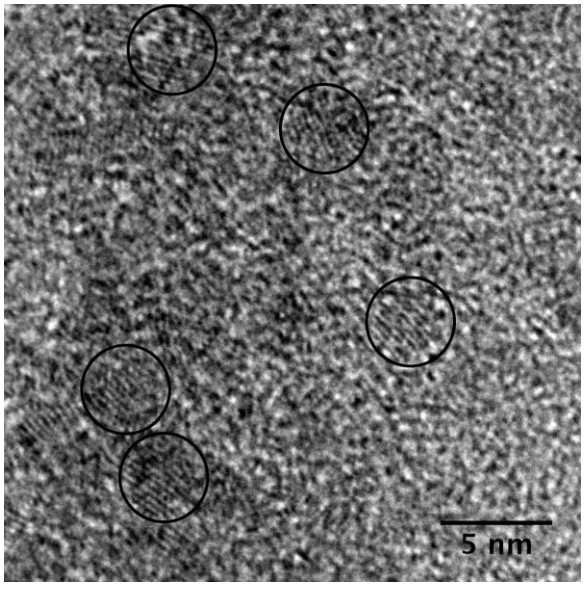

Biological tests

CHO cell culture - Chinese hamster ovary (CHO) cell line (from ATCC) were maintained at 37°C in 5% CO_2 in F-12K nutrient medium (InVitrogen) supplemented with 10% (v/v) heat-inactivated fetal bovine serum (InVitrogen) and 10,000 units/ml streptomycine and penicillin (InVitrogen).

Confocal microscopy - Live CHO cells were incubated for 2 hrs with 10 µM Gd.QD or Gd.QD-MCa in - F-12K cell culture medium without serum. Immediately after a two-time washing procedure with F-12K medium, the cell plasma membrane was stained with 5 µg/ml rhodamin-conjugated concanavalinA for 5 min and cells were then washed again with F-12K medium. Live cells were immediately analyzed by confocal laser scanning microscopy using a Zeiss LSM 710 (Gd.2.QD or Gd.2.QD.MCa) or a Zeiss AxioVert 200M. Rhodamine (580 nm) and QD (620 nm) were sequentially excited (at 488 nm for rhodamine and 561 nm for QD) and emission fluorescence were collected in z-confocal planes of 10-15 nm steps.

In vivo MRI studies

All animal experiments are conducted in agreement with the "Principles of Laboratory Animal Care" (NIH publication n°. 86-23, revised 1985). The guidelines of the French Ministry of Agriculture (87/848) and of the European Community (86/609/EEC) were also respected. The protocol was submitted for approval to the local Neuroscience institute committee to minimize animal suffering and abusive use of animal numbers. OFA 7 week-old rats were anesthetized by 5% isoflurane inhalation in a mixture air/O_2 30%, and maintained in anaesthesia in 2% isoflurane. Rats were then injected with 10 µl of 1 mM Dotarem or Gd.2.QD.MCa (Dotarem or Gd.2 concentration wise) in the striatum using a stereotaxic frame (coordinates: 0 mm frontal, 3.5 mm lateral, and 5.5 mm in depth) and at a rate of 2 µl/min. T1-weighted images (spin-echo, TR/TE=300/27 ms) of rat brain were acquired 15 min after intrastriatal injection and after placing the rats in a 7T magnet (Bruker BioSpec 70/20 USR AVIII; Preclinical MRI Facility of Grenoble). Sequences of 16 slices (slice thickness: 1 mm each) over a period of 15 min were taken. This sequence was repeated over a 4 hrs period, thus leading to the total acquisition of 16 sets of 16 slices. The temperature was maintained at 37.0°C throughout the experiments.

Data analyses of MRI images

Two types of MRI image analyses were performed. In each case, the most intense average T1 signal was selected from the set of 16 images at T=15 min, and kept for all other times. First, a region of interest (ROI) was drawn (10 pixels) close to the injection point (x mm of the injection point), and the average signal intensity calculated over the ROI minus the average intensity of the contra-lateral control area (zone with contrast agent). This type of analysis provides a hint of signal reduction with time. Second, the same type of analysis was conducted by drawing a similar sized ROI at a distance of Y mm away from the injection point, close to the outer limit of the detectable contrast agent signal. This second type of analysis provides some information about the lateral diffusion process of the contrast agent. Images and image analyses for Gd.2.QD.MCa were compared to Dotarem data.

References:

1) A. Nonat, C. Gateau, P. H. Fries and M. Mazzanti, *Chem. Eur. J*., **2006**, 12, 7133-7150.
2) L. Li, M. Protière, P. Reiss, *Chem. Mater*. **2008**, *20*, 2621-2623.
3) Reiss P.; Protière M.; Li L. *Small*, **2009**, *5*, 154–168.
4) D. M. Corsi, C. Platas-Iglesias,H. van Bekkum and J. A. Peters, *Magn Reson. Chem.*, **2001**, **3**9, 723–726
5) G. Brunisholz and M. Randin, *Helv. Chim. Acta*, **1959**, 42, 1927–1938
6) A. Beeby, I. M. Clarkson, R. S. Dickins, S. Faulkner, D. Parker, L. Royle, A. S. de Sousa, J. A. G. Williams and M. Woods, *J. Chem. Soc., Perkin Trans. 2*, **1999**, 493-503
7) deMello, J. C.; Wittmann, H. F.; Friend, R. H., *Adv. Mater*. **1997,** 9, 230-232.

b. Conclusion

Dans cette étude, la MCa a démontré son efficacité en tant que vecteur intracellulaire de composé d'intérêt. Après avoir constaté par microscopie confocale que le complexe nanoparticule/agent de contraste au Gd ne pouvait pas pénétrer seul dans les cellules, nous nous sommes assuré, toujours par la même technique que ce complexe additionné de MCa était bien délivré dans les cellules. Cette première étude in vitro nous a donné la preuve de l'efficacité de la MCa pour l'administration de nanoparticules fonctionnalisées avec des agents de contraste au gadolinium.

L'étude *in vivo* a consisté en l'injection intracérébrale de complexe nanoparticule/Gd/MCa versus une injection de la même quantité de dotarem®. Le résultat est sans conteste, alors que le contraste provoqué par le dotarem® décroit rapidement pour disparaitre entre 2h30 et 3h00, le contraste induit par le complexe nanoparticule/Gd/MCa persiste durant plus de 4h00. Ce premier résultat pourrait être une avancée dans de domaine de l'imagerie par résonnance médicale. Nous avons ici un composé dont la persistance dans le temps est supérieure à celle de l'agent utilisé en routine, ce qui laisserait une plage de manœuvre plus large pour réaliser ces actes d'imageries. Reste maintenant à déterminer la toxicité d'un tel complexe ainsi que ses voies d'élimination.

Conclusion générale, discussion et perspectives

IV. Conclusion générale, discussion et perspectives

Mon travail de thèse a consisté en l'étude de la MCa avec comme objectif premier de l'améliorer afin de ne conserver que les propriétés qui nous intéressaient. La recherche de nouveaux analogues de la MCa plus performants nous à permis de découvrir de nouveaux peptides de pénétration cellulaire, dérivés de la MCa, dont certains auront un avenir intéressant.

Afin d'étudier la biodistribution et la cinétique d'élimination de la MCa, nous avons choisi de radiomarquer la MCa avec de l'iode 125 comme cela a été fait avec la crotamine (Boni-Mitake, Costa et al. 2006). Afin de mettre au point la méthode de marquage et de vérifier que l'on obtenait bien la MCa mono iodée, nous nous sommes servi d'un autre isotope de l'iode, ^{127}I. Pour faire le marquage, nous avons rajouté une tyrosine en partie N-terminal de la séquence de la MCa. L'utilisation d'un atome d'iode non radioactif permet d'analyser le produit de synthèse par spectrométrie de masse. Cette méthode d'analyse permet de vérifier que le peptide n'a pas été dégradé lors du marquage à l'iode, et permet d'identifier les fractions mono-iodée de la di-iodée récoltés lors de la purification par chromatographie liquide. Nous avons réalisé un test de pénétration cellulaire *in vitro* afin de vérifier que l'ajout d'une tyrosine et d'un atome d'iode à la séquence de la MCa n'allait pas altérer sa capacité à transloquer dans les cellules. La courbe dose réponse obtenue après 2 hrs d'incubation dans des cellules CHO de 112 µCi de ^{125}I-Tyr-MCa, nous a permis de constater que l'iodination et l'ajout d'une tyrosine n'avait pas inhibé la pénétration cellulaire et que le peptide marqué rentrait dans les cellules à des concentrations supérieures à 33 nM. La cinétique d'internalisation montre une forte pénétration de ce peptide iodé dès 3 min.

L'analyse de la stabilité *in vitro* et *in vivo* a permis de récolter sur la MCa des données essentielles pour de potentielles utilisations en thérapeutique. La stabilité de la MCa radiomarquée est assez bonne, après 30 min d'incubation dans le sang de souris, elle est stable à 75%, alors que d'autres peptides incubés 15 min dans du plasma humain sont stables à 67% (Evangelou, Zikos et al. 2009). L'analyse de la biodistribution de la ^{125}I-Tyr-MCa nous a permis de savoir que la MCa ne passait pas la barrière hémato-encéphalique, vu qu'une très faible quantité de radioactivité a été retrouvée dans le cerveau et le cervelet. Nous apprenons

aussi que l'élimination se fait préférentiellement par voie rénale que par voie hépatique. Nous envisageons maintenant de réitérer cette étude avec la MCa linéaire ainsi qu'avec la MCa de conformation D. Il sera intéressant de savoir si les différents analogues seront localisés dans les tissus avec les mêmes proportions, et si leurs cinétiques d'élimination seront identiques. Nous nous attendons à ce que la D-MCa soit dégradée beaucoup plus lentement, et donc à ce qu'elle reste plus longtemps dans les organes et dans le sang.

La D-MCa est sans doute le plus prometteur de tous les analogues étudiés, malgré un coût de production plus élevé du fait des acides aminés de conformation D. En effet, la D-MCa a totalement perdu ses effets pharmacologiques, elle n'est plus reconnue par son récepteur, le RyR, du fait de son inversion de conformation et ne provoque donc plus de relâchement de calcium dans le cytoplasme, effet « indésirable » dont il était important de se défaire. En revanche, les capacités de la D-MCa à pénétrer dans les cellules sont intégralement préservées. Une mutation des acides aminés par leur isomères de conformation D a été réalisée sur des peptides Tat et polyarginine, ces analogues ont une pénétration cellulaire très supérieure à celle des formes L (Gammon, Villalobos et al. 2003). L'analyse par cytométrie en flux révèle que la D-MCa n'a pas subie de baisse d'internalisation cellulaire par rapport à la L-MCa et la microscopie confocale fait apparaitre que la distribution cellulaire est semblable pour les deux analogues. Cependant, le meilleur atout de la D-MCa sur les autres CPP est sa stabilité et sa résistance envers les enzymes et les protéases. Cette étude avait déjà été réalisée sur un CPP, et a montré des résultats similaires, alors que la L-SAP a une demi vie de 15 hrs, la D-SAP est totalement stable, sans augmentation de la toxicité et sans perte des propriétés de pénétration cellulaire (Pujals, Fernandez-Carneado et al. 2008). Cette caractéristique fait de la D-MCa un candidat approprié pour l'administration de drogues *in vivo*.

La stratégie développée dans l'article 2 nous a permis de découvrir treize nouveaux CPP. En effet, nous avons été particulièrement surpris de constater que tous les analogues synthétisés étaient capables de pénétrer dans les cellules. De plus, tous ces CPP sont plus efficaces que la séquence complète de la MCa linéaire (MCa_{UF1-33}-C), ce qui laisse penser que des réductions de séquence peuvent être une stratégie efficace pour l'amélioration des CPP. Ces analogues ont été obtenus en réduisant la séquence de la MCa_{UF1-33}-C à partir du C-terminal, à partir du

N-terminal, ou à partir du C- et du N-terminal conjointement. Bien qu'il soit difficile de comparer l'efficacité de ces peptides entre eux, deux analogues semblent sortir du lot, MCa_{UF6-25}-C et $MCa_{UF14-25}$-C. Ces deux peptides sont à la fois tronqués en C- et en N-terminal et possèdent 40% et 50% respectivement de charges positives. L'hypothèse que l'on pourrait tirer de cette constatation est que les acides aminés contenus dans le milieu de la séquence seraient les plus importants, cependant cette théorie a vite été rejeté du fait de la bonne internalisation du peptide MCa_{UF11-9}-C. Voila pourquoi, à l'heure actuelle il est très difficile de désigner le CPP le plus efficace parmi les 13 testés. Du fait de la supériorité supposée de MCa_{UF6-25}-C et $MCa_{UF14-25}$-C, nous avons synthétisé deux peptides supplémentaires tronqués en C- et en N-terminal, MCa_{F11-33}-C et MCa_{F8-33}-C mais dans lesquels nous avons rétablis respectivement, deux et quatre cystéines. MCa_{F11-33}-C est donc structuré par un pont disulfure et MCa_{F8-33}-C en possède deux entre les cystéines 3 et 14 et les cystéines 9 et 25. Nous avons construit ces deux analogues pour savoir si la structure secondaire du peptide pouvait avoir une conséquence sur sa capacité à pénétrer dans les cellules. Ces peptides possèdent l'avantage d'être simples à synthétiser du fait de leurs petites tailles et de leurs absences de structures, en revanche, ils n'ont pas une stabilité comparable à la L-MCa ou à la D-MCa. Comme nous l'avions supposé, les analogues linéaires de la MCa n'ont aucune activité sur le RyR, et ne provoquent donc pas de reflux intra cytoplasmique de calcium. Il en est de même pour les deux analogues structurés MCa_{F11-33}-C et MCa_{F8-33}-C, ces résultats seront présentés dans un article à venir.

Ces différentes stratégies nous ont permis de développer différents analogues CPP avec des caractéristiques différentes. En fonction de l'utilisation que nous aurons de la MCa, nous pourrons utiliser l'analogue le plus approprié. En effet, pour des études *in vitro* de l'internalisation de différents composés, qui nécessiteraient un couplage chimique, il serait plus avantageux d'utiliser les fragments linéaires de la MCa sur lesquels il est facile d'ajouter une cystéine. Si un couplage covalent avec le cargo n'est pas nécessaire, la MCa pourra être utilisée, en revanche, si nous voulons injecter des composés *in vivo*, nous aurons tout intérêt à utiliser la D-MCa pour sa supériorité sur la MCa et sur les analogues de MCa en termes de stabilité et de résistance aux enzymes et aux protéases. D'autres améliorations pourraient sans doute êtres apportées à la MCa, nous pourrions combiner les deux études, et synthétiser des

mini MCa composées en partie ou intégralement d'acides aminés de conformation D. Une autre approche pourrait être de faire des mutations ponctuelles sur la MCa, afin d'étudier l'impact sur la pénétration cellulaire. La mutation d'une asparagine par une ornithine a augmentée l'efficacité de pénétration cellulaire d'un CPP de 1.8 fois, la mutation d'un glutamate par une norleucine a aussi augmenté la pénétration cellulaire d'un autre CPP d'une valeur de 2.4 (Gammon, Villalobos et al. 2003). On pourrait aussi se demander si des mutations ponctuelles ne confèreraient pas à la MCa une sélectivité particulière pour différents types cellulaires.

En parallèle de cette quête de l'amélioration de la MCa, j'ai travaillé sur l'internalisation de nanoparticules et d'agents de contraste pour l'imagerie par résonnance magnétique. Le complexe nanoparticules/MCa linéaire (MCa_{UF}) s'est fait par échange de ligand entre la MCa_L et les fonctions pénicillamine présente autour du cœur de la nanoparticule. La MCa_L a permis une internalisation efficace de ces nanoparticules qui n'étaient pas capable de pénétrer seules dans les cellules. Ces résultats ont été obtenus par analyse par microscopie confocale de cellules CHO incubées pendant 2 hrs avec le complexe nanoparticule/MCa_L. Une fois ce résultat validé, nous avons voulu utiliser les nanoparticules comme plateformes sur lesquelles nous pourrions à la fois lier des molécules de MCa_L, et des autres composés à internaliser. Nous avons donc couplé sur les nanoparticules, de la MCa_L et un chélate de gadolinium, afin de faire de l'imagerie par résonnance magnétique nucléaire (RMN). Grâce à ces composés, nous avons pu valider le complexe par deux méthodes *in vitro*. La première reste la même que pour le complexe nanoparticules/MCa_L, il s'agit d'une étude par microscopie confocale. Dans la seconde, nous avons de la même façon incubé le complexe nanoparticule/MCa_L/chélate de gadolinium dans des cellules, puis après lavage et lyse de celles-ci, nous avons étudié le contenue cellulaire par RMN. Cette étude s'inscrit dans le cadre d'un projet que nous allons développer, dans lequel nous allons coupler de la D-MCa à un PNA ciblé contre les canaux T, comme complexe qui sera utilisé comme traitement contre la douleur. Nous injecterons ce complexe par voie intrathécale, c'est pourquoi nous allons utiliser la D-MCa. Nous avons démontré précédemment que la D-MCa était résistante *in vitro* à la trypsine et à l'endoprotéinase Asp-N, de plus, il est établi que les isomères D des acides aminés sont résistants au clivage enzymatique et subsistent plus longtemps dans la circulation (Wright,

Rothbard et al. 2003). Nous espérons en effet, que grâce à la stabilité de la D-MCa, le complexe D-MCa/PNA sera dégradé très lentement et qu'ainsi, une injection du complexe suffira à calmer la douleur durant plusieurs heures. Le chélate de gadolinium entre en jeu dans cette étude pour confirmer la présence du complexe D-MCa/PNA au cours du temps, ainsi que pour corréler l'absence ou la diminution de la douleur avec la présence du PNA sur son lieu d'action. Cette étude sera donc suivie de deux façons, des tests de douleur et de l'imagerie par RMN. Une étude similaire a déjà été réalisée avec de la D-Tat, un PNA et un agent de contraste (AC). L'internalisation du complexe D-Tat-PNA AC dans les cellules a pu être vérifiée par imagerie par RMN. Il s'avère dans ce cas, que malgré une internalisation efficace du complexe D-Tat-PNA AC dans les cellules, l'interaction entre le PNA et l'ARNm cible reste limité, ce qu'ils expliquent par une localisation du complexe et de l'ARNm cible dans des compartiments cellulaires différents (Mishra, Su et al. 2009). L'équipe de Jörn Engelmann met l'accent sur le fait que le greffage d'un PNA sur un complexe CPP-AC fait plus que doubler la taille du complexe. Il est donc important de prendre en comte la mobilité de ce gros composé *un vivo* (Mishra, Su et al. 2009).

Deux études à venir pourront donc mesurer la stabilité *in vivo* et la distribution de la D-MCa. La ^{125}I-Tyr-D-MCa sera injectée par voie intraveineuse et sera suivie par des prélèvements sanguins réguliers qui seront analysés par chromatographie liquide. Puis, dans le but d'étudier la biodistribution, les organes seront prélevés pour mesurer la radioactivité contenue et il sera aussi réalisé une mesure tomographique de la radioactivité *in vivo*. Le complexe D-MCa/PNA/AC sera injecté par voie intrathécale et sera suivi par imagerie par RMN jusqu'à la complète disparition du signal. Une injection par voie intraveineuse pourra aussi être réalisée, afin de faire des prélèvements régulier de sang, et des organes, qui pourront être étudiés par RMN. Les résultats des deux expériences pourront être comparés, nous auront alors une idée de l'impact du cargo sur la biodistribution et l'élimination de la D-MCa.

Nous nous sommes récemment interrogés sur une autre propriété potentielle de la MCa, aurait-elle des propriétés antibactérienne ? Les petits peptides cationiques (Hancock 1997; Hancock and Patrzykat 2002) sont abondants dans la nature et ont été décrits comme des antibiotiques naturels des peptides cationiques antimicrobiens (Garibotto, Garro et al.). Ces peptides font entre 12 et 50 acides aminés et possèdent une charge nette positive de +2 ou

plus, du à une grande proportion de résidus arginine et lysine, et approximativement 50% d'acides aminés hydrophobes (Hancock 1997). Ces peptides sont amphipathique et possèdent une structure en trois dimensions avec une face hydrophobe contenant les acides aminés non polaires et une face hydrophile composée des acides aminés polaires et chargés (Masman, Rodriguez et al. 2009). Avec ces 33 acides aminés, ses trois feuillets β, ses trois ponts disulfures et sa charge nette de +7, la MCa pourrait rentrer dans la catégorie des peptides antibactériens. Une étude sur la pénétratine, a montrée que ce peptide possédait des propriétés antifongiques (Masman, Rodriguez et al. 2009). Un analogue de la pénétratine avec une séquence aléatoire ainsi que six peptides tronqués et mutés ponctuellement de la pénétratine ont été testés. Alors que la pénétratine présente une activité antifongique sur *C. albicans* et *C. neoformans*, l'analogue de séquence aléatoire n'a quasiment aucune activité (Masman, Rodriguez et al. 2009), ce qui indique que la charge nette du peptide n'est pas la seule condition nécessaire pour des propriétés antifongiques. Tous les autres analogues de plus petites tailles ont présentés une activité antifongique réduite par rapport à la pénétratine (Masman, Rodriguez et al. 2009). Contrairement à cette étude, nous avons commencé à tester la MCa sur des bactéries et non pas sur des champignons. Seulement une expérience préliminaire à été réalisée à ce jour sur *E. Coli*, des streptocoques et des entérocoques. Les premiers résultats semblent montrer un effet de la MCa sur *E. Coli* et les streptocoques. L'expérience sur les entérocoques est à recommencer car les résultats obtenus étaient totalement abérrant. L'expérience sur *E. Coli* et les streptocoques est quand à elle à refaire pour confirmer la tendance.

Après l'étude des interactions entre les CPP et la membrane plasmique, ainsi que du mécanisme d'entrée dans la cellule du CPP seul ou comme vecteur de molécules, l'avancement naturel des recherches sur ce sujet nous pousse à regarder vers une transposition du savoir acquis sur les CPP. En effet, de nombreuses données ont été accumulées sur la large gamme des CPP lorsqu'ils étaient utilisés en tant que vecteur sur des modèles *in vitro* puis *in vivo*. A l'heure actuelle, il est question de l'utilisation des CPP en clinique et en administration thérapeutique. Différents paramètres doivent être pris en compte afin de sélectionner le CPP adéquate pour l'administration de drogues. Les CPP possèdent des modes d'entrée dans les cellules différents qui peuvent d'ailleurs êtres affectées par le cargo qui lui

sera attaché, ou par le linker qui servira à les lier entre eux. D'autres facteurs entrent en compte, comme l'efficacité de pénétration cellulaire, notamment en fonction du type cellulaire visé, ainsi que la cible intracellulaire ciblée et éventuellement, la sortie des endosomes (Johnson, Harrison et al. 2011). Selon la pharmacocinétique propre de la drogue à internaliser, la concentration du peptide à administrer devra être étudiée. L'étude de la voie d'administration, de la dose, ainsi que de la fréquence est essentielle pour obtenir l'effet désiré (Johnson, Harrison et al. 2011). Plusieurs voies d'administration des CPP ont été utilisées pour l'administration de drogues. Par exemple, des injections intra-vasculaires ont été utilisées efficacement lors d'études précliniques et cliniques (Inagaki, Chen et al. 2003; Bates, Bode et al. 2008; Liu, Gingrich et al. 2008). La société KAI Pharmaceuticals travaille sur les protéines kinases C, trois études cliniques sont menées par cette société, toutes trois sont basées sur l'étude de protéine kinase couplées à Tat. KAI-9803 qui est en phase 2 réduit chez les patients les dommages sur les muscles du cœur causés lors d'une attaque cardiaque. KAI-4169 est un agent pharmaceutique pour le traitement de l'hyperparathyroïdie secondaire, qui est une complication fréquente des maladies chroniques des reins. Ce composé en phase 1 a démontré lors de l'étude son activité par une réduction dose dépendante de l'hormone parathyroïde. L'entrée en phase 2 de ce composé est prévue pour 2011. KAI-4169 peut être formulée pour une administration intraveineuse pour le traitement de l'hyperparathyroïdie secondaire chez les patients en dialyse rénale en phase terminale pendant les séances régulières d'hémodialyses, ou bien sous forme de patch transdermique pour les patients chez lesquels l'hémodialyse n'est pas indiquée comme dans les cas d'hyperparathyroïdie primaire, ou pour les patients souffrants de maladie chronique des reins accompagnée d'une hyperparathyroïdie secondaire et d'une greffe de reins (informations récoltées sur le site internet de la société KAI Pharmaceuticals). La troisième étude clinique porte sur le composé KAI-1678 qui est en phase 2. KAI-1678 est un composé utilisé dans le traitement de la douleur (Johnson, Harrison et al. 2011).

Quelques points doivent être étudiés plus en détails dans le domaine des CPP afin de diminuer les limitations pour l'utilisation en thérapeutiques. Les interactions entre les CPP et les cellules cibles, les mécanismes d'entrées dans la cellule, la sortie des endosomes de même que la toxicité, ou la biodistribution sont des sujets capitaux et dont la connaissance est

obligatoire afin d'obtenir des transporteurs idéaux pour la vectorisation de molécules d'intérêt. Si on considère tous ces points importants, l'utilisation des CPP pourrait provoquer des avancées importantes dans différents domaines, comme les maladies cardiaques, la douleur, ou les cancers pour n'en citer que quelqu'uns.

Annexes

1. Annexe 1

In vitro and in vivo intracellular delivery of quantum dots by maurocalcine

Narendra Ram, Isabelle Texier-Nogues, Karine Pernet-Gallay, Cathy Poillot, Fabienne Pirollet, Michel Ronjat, Annie Andrieux, Christophe Arnoult, Jean, T. Daou, Michel De Waard

Article paru dans le journal Int. J. Biomedical Nanoscience and Nanotechnology, Vol 2, No. 1, 2011

In vitro and in vivo intracellular delivery of quantum dots by maurocalcine

Narendra Ram

Research group 3 'Calcium Channels, Functions and Pathologies',
Grenoble Institute of Neuroscience,
Université Joseph Fourier,
Site Santé, BP 170, 38042 Grenoble Cedex 09, France
E-mail: msnram@yahoo.com

Isabelle Texier-Nogues

CEA Grenoble/LETI-DTBS,
17 rue des Martyrs, 38054 Grenoble Cedex, France
E-mail: isabelle.texier-nogues@cea.fr

Karine Pernet-Gallay

Inserm U836,
Grenoble Institute of Neuroscience,
Université Joseph Fourier,
Site Santé Tronche, BP170, 38042 Grenoble, France
E-mail: karin.pernet-gallay@ujf-grenoble.fr

Cathy Poillot, Fabienne Pirollet and Michel Ronjat

Research group 3 'Calcium Channels, Functions and Pathologies',
Grenoble Institute of Neuroscience,
Université Joseph Fourier,
Site Santé, BP 170, 38042 Grenoble Cedex 09, France
E-mail: cathy.poillot@ujf-grenoble.fr
E-mail: fabienne.pirollet@ujf-grenoble.fr
E-mail: michel.ronjat@ujf-grenoble.fr

Annie Andrieux

Research group 1 'Physiopathologie du Cytosquelette',
Inserm U836,
Grenoble Institute of Neuroscience,
Université Joseph Fourier,
Site Santé Tronche, BP170, 38042 Grenoble, France
E-mail: annie.andrieux@ujf-grenoble.fr

Christophe Arnoult

Research group 3 'Calcium Channels, Functions and Pathologies',
Grenoble Institute of Neuroscience,
Université Joseph Fourier,
Site Santé, BP 170, 38042 Grenoble Cedex 09, France
E-mail: christophe.arnoult@ujf-grenoble.fr

T. Jean Daou

Equipe Matériaux à Porosité Contrôlée,
Institut de Science des Matériaux de Mulhouse (IS2M) LRC CNRS,
7228 – UHA ENSCMu, Mulhouse, France
E-mail: Jean.daou@uha.fr

Michel De Waard*

Research group 3 'Calcium Channels, Functions and Pathologies',
Grenoble Institute of Neuroscience,
Université Joseph Fourier,
Site Santé, BP 170, 38042 Grenoble Cedex 09, France
E-mail: michel.dewaard@ujf-grenoble.fr
*Corresponding author

Abstract: Maurocalcine is a new member of the increasing family of cell penetrating peptides. We report for the first time that this peptide is able to deliver quantum dots inside a variety of cells, both in vitro and in vivo. In vivo, maurocalcine produces intracellular delivery of the nanoparticles without affecting the relative distribution of quantum dots within organs. The data stress out that maurocalcine can be used for intracellular delivery of functionalised nanoparticles in vivo.

Keywords: quantum dot; nanoparticles; maurocalcine; cell penetrating peptide; endocytosis; cell delivery; in vivo imaging; streptavidin.

Reference to this paper should be made as follows: Ram, N., Texier-Nogues, I., Pernet-Gallay, K., Poillot, C., Pirollet, F., Ronjat, M., Andrieux, A., Arnoult, C., Daou, T.J. and De Waard, M. (2011) 'In vitro and in vivo intracellular delivery of quantum dots by maurocalcine', *Int. J. Biomedical Nanoscience and Nanotechnology*, Vol. 2, No. 1, pp.12–32.

Biographical notes: Narendra Ram has completed his PhD in 2008 under the guidance of Dr. Michel De Waard. His PhD program aimed at understanding the mechanisms and cell determinants of maurocalcine penetration. He also developed new analogues of maurocalcine devoid of pharmacological activity. Before his PhD, he was working in a private company in Bangalore, India.

Cathy Poillot is starting her PhD program at the University Joseph Fourier. She works in Team 3 of the Grenoble Neuroscience Institute under the guidance of Dr. Michel De Waard.

Fabienne Pirollet is an Inserm Researcher working at the Grenoble Neuroscience Institute under the scientific guidance of Dr. Michel De Waard. She has worked previously in close collaboration with Dr. Annie Andrieux and has strong expertise on tumour cell differentiating factors. In the institute, she has now a strong commitment in innovation and intellectual property rights.

Michel Ronjat is a CNRS Research Director at the Grenoble Neuroscience Institute. He completed his Doctoral studies at the Commissariat à l'Energie Atomique in Grenoble at the laboratory of Molecular and Cellular Biology. His current research is focused on the interaction of proteins that form the excitation-contraction coupling.

Christophe Arnoult is a CNRS Researcher at the Grenoble Neuroscience Institute. He has also completed a complete veterinarian education. His current research activity focuses on the understanding of sperm physiology and has broad knowledge of biophysical techniques.

Michel De Waard is a Group Leader at the Grenoble Neuroscience Institute. He is also an Inserm Research Director. He has worked mainly on voltage-gated calcium channels, but has also strong expertise on toxins. He identified maurocalcine as an interesting peptide for investigating ryanodine receptor pharmacology and discovered that it acts as a cell penetrating peptide. He got his PhD at Université Aix-Marseille II and performed a postdoctoral stay at the Howard Hughes Medical Institute of the Université of Iowa under the guidance of Pr. Kevin Campbell.

Isabelle Texier is a Project Leader at the Commissariat à l'Energie Atomique. She heads several projects on nanotechnology and is specialised in chemically functionalising nano-objects. She currently heads the transversal program 'Techno pour la Santé' of the CEA that coordinates the efforts of many different groups in order to improve intellectual property in this field.

Karine Pernet-Gallay has recently been recruited at Inserm and is responsible for the management of a service platform for transmission electron microscopy at the Grenoble Neuroscience Institute.

Annie Andrieux is a Research Director at the Commissariat à l'Energie Atomique and has since more than a year joined the Grenoble Neuroscience Institute to work as a Team Leader. She is specialised on microtubule-associated proteins, and most particularly on STOP.

T. Jean Daou is an Assistant Professor in the University of Haute Alsace, Mulhouse, France. His current research is focused on nanotechnology: synthesis, characterisation and chemical functionalisation of new nano-objects. He got his PhD at the University Louis Pasteur and performed a postdoctoral stay at the Commissariat à l'Energie Atomique under the guidance of Dr. Isabelle Texier.

1 Introduction

Semiconductor quantum dots, herein referred as Qdots, are new classes of fluorescent probes with a large surface to volume ratio, a property that is largely exploited to graft new functional entities at their surface. They possess excellent photo stability, that far

exceeds that of conventional organic fluorophores, and high emission quantum yield, which leads to increased fluorescence detection sensitivity. Qdots consist of a core of semi-conducting material, typically cadmium-telluride (CdTe) or cadmium-selenium (CdSe) for emission in the visible to the near infrared domain, for which tissue auto-fluorescence and absorption are reduced. This core is most of the time covered by a shell composed of zinc sulphide (ZnS), in order to improve the chemical stability and emission quantum yield of Qdot (Lim et al., 2003; Michalet et al., 2005). These nanocrystals, produced in organic solvents, are further surface-modified for their stabilisation in aqueous media and biological functionalisation. In particular, the coating of the nanoparticles by a polyethylene glycol polymer (PEGylation) has been shown to improve their colloidal stability (Lee et al., 2008) and their blood circulation time (Ballou et al., 2004) by reducing non-specific opsonin binding. In this study, commercial streptavidin-PEG_{2000}-Qdots (invitrogen) are used.

These properties enlarge their usefulness in various biological applications. They have namely been used for immunostaining of membrane proteins (Sukhanova et al., 2004) and staining of organelles like mitochondria or nuclei (Hoshino et al., 2004) in fixed cells, and for tracking single molecules in living cells by videomicroscopy (Dahan et al., 2003; Lidke et al., 2004; Mansson et al., 2004). *In vivo* imaging (Akerman et al., 2002; Choi et al., 2007; Dubertret et al., 2002; Gao et al., 2004; Michalet et al., 2005) applications have also been reported. Qdot coated with water-compatible organic materials have been developed for multiphoton fluorescence imaging *in vivo* (Larson et al., 2003). Peptides have been used to improve Qdot solubility in aqueous solution and kept bioactive for targeting cell surface proteins of interest (Pinaud et al., 2004). In spite of this wealth of applications, the uses of Qdot for intracellular applications *in vitro* or *in vivo* are still limited because of their inability to cross the plasma membrane. Several experimental strategies have been developed to physically deliver the Qdots, including direct microinjection, but this limits the number of cells that can be studied, or electroporation (Chen and Gerion, 2004; Derfus et al., 2004; Voura et al., 2004). in the formation of Qdot aggregates (Voura et al., 2004). None of these delivery systems seem therefore promising for *in vivo* applications because of their limited cell penetration efficiencies. Recently, a different strategy of Qdot delivery has been developed that uses cell penetrating peptides (CPP). Polyarginine (Silver and Ou, 2005) and TAT (Santra et al., 2005) have been used for the delivery of Qdot into living cells *in vitro* or across the blood brain barrier *in vivo*, respectively. This delivery system sounds very promising because CPP have found many applications for the cell delivery of a wealth of cargoes including peptides, proteins, siRNA, peptide nucleic acids, cDNA or drugs (Wadia and Dowdy, 2002). Here, we report on the use of a new CPP, maurocalcine (MCa), to deliver Qdots both *in vitro* and *in vivo*. Originally used for its pharmacological properties as a peptide/toxin active on an intracellular channel, MCa was shown to possess the ability to efficiently carry various cargo molecules inside cells (Boisseau et al., 2006; Mabrouk et al., 2007; Ram et al., 2008a, 2008b). MCa is a 33 amino acid residue peptide isolated from the venom of the scorpion toxin *scorpio maurus palmatus* that, as determined by ^{1}H-NMR, possesses three disulphide bridges and is folded along an inhibitor cystine knot motif (Mosbah et al., 2000). Folding occurs in such a manner that most of its basic residues are oriented towards one face of the molecule. The opposite face of the peptide is hydrophobic indicating the existence of a strong dipole moment capable to orient the molecule in an electrical field. The basic nature of the peptide is a feature shared by most

CPP. MCa interacts with various negatively charged components of the cell surface, including lipids (Mabrouk et al., 2007) and glycosaminoglycans (Ram et al., 2008a). This priming step is mandatory before the entry process itself of the peptide can occur. Initial studies have indicated the importance of macropinocytosis in the entry of MCa, at least when coupled to streptavidin (strep) (Ram et al., 2008a).

By using fluorescence activated cell sorting (FACS) and confocal microscopy, we show in the present study that strep-Qdot, bound to biotinylated maurocalcine (MCa_b), can efficiently be delivered in living Chinese hamster ovary (CHO) cells as well as primary neuronal cultures. The Qdots were found to be localised in endosomes in co-localisation studies by confocal microscopy and on ultrastructural images by transmission electron microscopy. Inhibition of cell entry by amiloride suggests that macropinocytosis is implicated in the entry pathway of strep-Qdot. Studying the *in vivo* distribution of the complex in mice indicates that the coupling of MCa_b to strep-Qdot does not alter Qdot organ distribution but allows cell penetration. These data indicate that, in this chemical configuration, MCa is a potent vector for the *in vivo* intracellular delivery of Qdots. These findings will undoubtedly enlarge the potential biological applications of MCa and Qdot for *in vivo* delivery of therapeutics.

2 Materials and methods

2.1 Reagents

Streptavidin-quantum dots emitting at 585 nm, 655 nm or 705 nm (strep-Qdot585, strep-Qdot655 or strep-Qdot705) were purchased from molecular probes (USA) and streptavidin-gold particles (strep-gold, 15 nm in diameter) from Aurion (Netherlands). On average, each Qdot and each gold particle contains nine and 20 strep molecules at its surface, respectively. MCa_b was stock from a previous synthesis (Mabrouk et al., 2007).

2.2 Cell culture

CHO cell line (American type culture collection, ATCC) was maintained at 37°C in 5% CO_2 in F-12K nutrient medium (invitrogen) supplemented with 10% (v/v) heat-inactivated fetal bovine serum (invitrogen) and 10,000 units/ml streptomycin and penicillin (invitrogen).

2.3 Primary culture of dorsal root ganglia (DRG) neurons

DRG neurons were isolated from 17 days old embryos of rat and initially treated with collagenase A at room temperature for 15 min. Cells were later digested with 0.25% trypsin-ethylenediaminetetraacetic acid (EDTA) for 10 min at 37°C, followed by mechanical dissociation. Dissociated cells were platted on poly-L-lysine-coated (10 µg/ml) plates and grown in Dulbecco modified eagle medium (DMEM) supplemented with 10% fetal bovine serum, 5 mg/ml glucose, 40 ng/ml gentamicin, 200 ng/ml nerve growth factor (NGF), and 10 µM arabinoside C before assayed for cell penetration of the complex.

2.4 Formation of MCa_b-streptavidin-quantum dots (MCa_b/strep-Qdot) or MCa_b/streptavidin-gold complex (MCa_b/strep-gold)

Soluble strep-Qdot or strep-gold were mixed with four molar equivalents of MCa_b (4 MCa_b / 1 Qdot) for 2 hrs at 37°C in the dark in phosphate-buffered saline (PBS) (in mM): NaCl 136, Na_2HPO_4 4.3, KH_2PO_4 1.47, KCl 2.6, $CaCl_2$ 1, $MgCl_2$ 0.5, pH 7.2. The fluorescence emission properties (wavelength and intensity) were not altered by the coupling of MCa_b to strep-Qdots (data not shown).

2.5 Injection of Qdots into mice, organ isolation and blood collection

For flow cytometry experiments, whole animal and organ imaging experiments, and tissue section imaging, 200 µl of Qdots (65 pmol, 325 nM in PBS 1X buffer) are injected intravenous via a catheter placed into the jugular vein of anesthetised OF1 mice (isofluorane/oxygen 3.5%, and 1.5% thereafter only for whole animal imaging). Three conditions were studied: control animals (non-injected), animals injected with strep-Qdot705 alone, and animals injected with strep-Qdot705 in complex with MCa_b. Whole mouse imaging was performed immediately after Qdot injection. For organ imaging, mice were sacrificed for 24 hrs after Qdot injection, and various organs are isolated for imaging. After imaging of the organs, the organs were preserved in 4% paraformaldehyde for tissue sectioning experiments. For blood collection, 200 µl of 1,000 UI heparin in PBS was injected into mice 2 hrs after injection with Qdots, then 100 µl of blood were collected. All animal experiments are conducted in agreement with the 'Principles of laboratory animal care'. The guidelines of the French Ministry of Agriculture (87/848) and of the European Community (86/609/EEC) were also respected.

2.6 Flow cytometry

Live CHO cells were incubated with MCa_b/strep-Qdot complexes in PBS. Concentration and duration of this incubation is specified in the Results section. In some experiments, the effect of 5 mM amiloride, a macropinocytosis inhibitor, was tested on cell penetration of Qdots. The cells were then washed twice with PBS to remove excess extracellular complexes. In addition, they were treated with 1 mg/ml trypsin (invitrogen) for 10 min at 37°C to remove remaining extracellular membrane-associated complexes. After trypsin incubation, the cell suspension was centrifuged at 500 g and resuspended in PBS. Flow cytometry analyses were performed with live cells using a Becton Dickinson FACSCalibur flow cytometer (BD biosciences). Data were obtained and analysed using CellQuest software (BD biosciences). Live cells were gated by forward/side scattering from a total of 10,000 events. In another set of experiments, similar flow cytometry analyses were performed with mouse blood cells. Briefly, 200 µl of collected blood samples were added to 2 ml PBS, centrifuged in 5 min at 300 g, the pellets resuspended and washed with PBS two more times. Finally, the pellets were resuspended in 200 µl PBS for flow cytometry analyses.

2.7 Tissue sectioning

Paraformaldehyde-treated isolated organs were embedded in OCT compound (VWR), and frozen with liquid nitrogen. 10- to 15-µm thick cryosections (Leica cryomicrotome) were collected on microscope slides and fixed with 4% paraformaldehyde for 10 min at room temperature. Slides were used for staining and confocal analysis.

2.8 Confocal microscopy

For analysis of the subcellular localisation of MCa_b/strep-Qdot complexes in CHO living cells, cells were incubated with the complexes in PBS for 2 hrs, and then washed with PBS. Immediately after washing, the plasma membrane was stained with 5 µg/ml FITC-conjugated concanavalin A (molecular probes) for 3 min. Cells were washed once more with PBS and immediately analysed by confocal laser scanning microscopy. In another set of experiments with living CHO cells, cells were incubated with 50 nM lysotracker red DND-99 in PBS for 20 min at 37°C to determine whether the MCa_b/strep-Qdot655 complex co-localises with endosomes after cell penetration. Cells were again washed with PBS and immediately visualised by confocal microscopy. For the analysis of DRG neurons, cells were fixed for 20 min with 4% formaldehyde after penetration of the MCa_b/strep-Qdot655 complex, and the cytoskeleton stained with tuj1 (1:500, Covance) before confocal microscopy analyses. Finally, for the analysis of tissue sections, the sections were incubated with 50 nM lysotracker red DND-99 in PBS for 20 min at 37°C, washed with PBS, and analysed by confocal microscopy. All analyses were performed using a Leica TCS-SP2 operating system. Alexa-488 (FITC) and tuj1 were excited at 488 nm, Qdot655 and Qdot705 at 645 nm, and Qdot585 and lysotracker red DND-99 at 545 nm, and emission fluorescence were collected in z-confocal planes.

2.9 Transmission electron microscopy

CHO cells were incubated with MCa_b/strep-Qdot585 or MCa_b/strep-gold in PBS for 2 hrs, and then washed with PBS. Plate-adherent cells were fixed with 2.5% glutaraldehyde in 0.1 M cacodylate buffer pH 7.4 during 2 hrs at room temperature. Cells were then washed with cacodylate buffer and post-fixed with 1% osmium tetroxyde in the same buffer for 1 hr at 4°C. After extensive washing with water, cells were then stained with 1% uranile acetate pH 4.0 during 1 hr at 4°C. Cells were then serially dehydrated using progressively more graded alcohol (30%-60%-90%-100%-100%-100%) and infiltrated with a mix of 1/1 epon/alcohol 100% during 1 hr before several baths of fresh epon (Flukka) lasting for 3 hrs. Finally, a capsule full of epon was deposited on the surface of the cells and the resin left to polymerise during 72 hrs at 60°C. The polymerised block was then detached from the culture plate and ultrathin sections of 70 nm of the cell monolayer were cut with an ultramicrotome (Leica). Sections were post-stained with 4% uranile acetate and lead citrate before being observed with an electron microscope at 80 kV (JEOL 1200EX).

2.10 Whole mouse and organ imaging system

A home-made set-up, adapted from the commercially available Aequoria™ system from Hamamatsu, is used. The excitation device is composed of 144 LEDs emitting at 633 nm (adapted from the LuxiFlux™ device available from Hamamatsu) and equipped with interference band pass filters (633BP10 nm from Schott) for a light illumination power of 2.4 $\mu W.mm^{-2}$. The filtered fluorescence signal (filter RG665 from Schott) is measured by a cooled CCD Camera (Orca-AG, Hamamatsu), placed at 160 mm from the imaging field. For mouse imaging, the integration time used is 100 ms, the gain of the camera is set at low and the binning is 1 × 1. For organ imaging, the integration time used is 200 ms (highly fluorescent organs: intestine, liver, kidneys) or 5 s (low fluorescent organs: brain, heart, testis, spleen, lungs, bladder). The Wasabi™ software (Hamamatsu) is used to drive the set-up and for image processing. Imaging was performed at each desired time point after Qdot injection into mouse as indicated in the Results section.

3 Results

3.1 Evidence that MCa promotes strep-Qdot cell entry

Figure 1(a) shows the primary structure of MCa, modified by an extra biotinylated lysine residue at its N-terminus. All concentrations provided in this study refer to Qdot concentration. The schematic representation of MCa_b/strep-Qdot is given in Figure 1(b). The presence of several strep molecules at the surface of Qdot (an average of seven according to the provider), combined with the ability of one strep molecule to bind up to four MCa_b entities, provides the possibility to greatly vary the MCa_b/Qdot ratio. For most experiments described herein, a 4/1/0.14 MCa_b/strep/Qdot ratio was used unless stated otherwise. A 2 hrs incubation of 100 nM strep-Qdot585 with CHO cells at 75% confluence leads to no cell entry at all as inspected by confocal microscopy (Figure 1c, top panel). In contrast, an important dot-shaped cytoplasmic labelling within CHO cells was observed when cells were incubated in the same conditions with MCa_b/strep-Qdot585 (Figure 1c, lower panel). MCa_b also produces cell entry of strep-Qdot655, a quantum dot of different emission wavelength, in living differentiated dorsal root ganglion neurons (2 hrs incubation, Figure 2a lower panel). Again, no cell entry of strep-Qdot655 is observed in the absence of MCa_b (Figure 2a upper panel). Since these primary cultures also contain glial cells, the neuronal specific tuj1 class III β-tubulin marker was used to discriminate between neurons and glial cells. Figure 2(b) indicates that both neurons and non neuronal cells have undergone cell penetration of MCa_b/strep-Qdot655.

Figure 1 MCa is a peptide vector for the cell entry of quantum dots

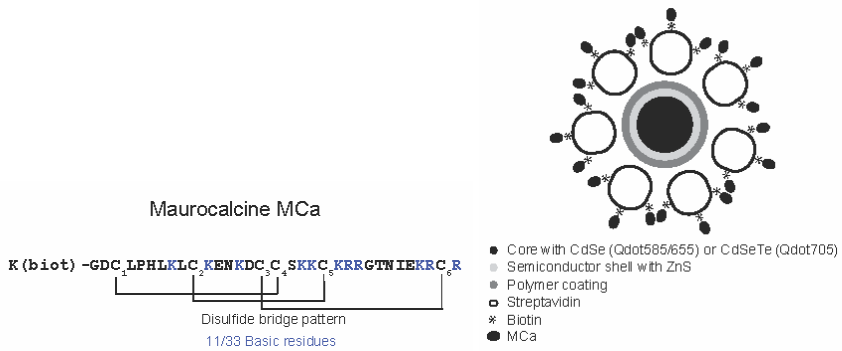

(a) (b)

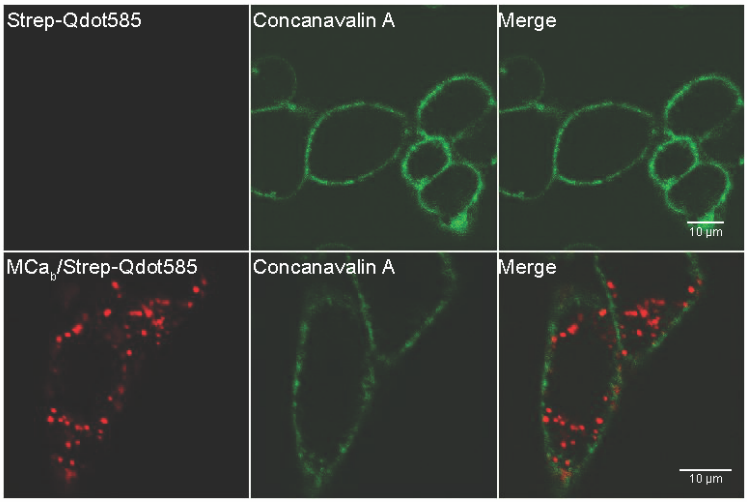

(c)

Notes: (a) Primary structure of biotinylated MCa with the Cys^3-Cys^{17}, Cys^{10}-Cys^{21} and Cys^{16}-Cys^{32} arrangement of its three disulfide bridges. The biotinylated lysine was positioned at the N-terminus of MCa.
(b) Schematic diagram depicting the structural organisation of MCa_b/strep-Qdot. The core can be composed of CdSe to form Qdot585 or Qdot655 or of CdTe to form Qdot705. Shell is composed of ZnS. The polymer coating is 2,000 Da molecular weight polyethyleneglycol (PEG_{2000}), to which an average of seven strep are immobilised. MCa_b/strep-Qdot are formed by the addition of a molar excess of MCa_b.
(c) MCa_b induces the cell penetration of strep-Qdot585 into living CHO cells. In the absence of MCa_b, no cell penetration is observed (top panels). When CHO cells were incubated for 2 hrs with 100 nM of MCa_b/strep-Qdot585, a punctuate cytoplasmic staining was observed (lower panels). Qdot fluorescence are indicated in left panels (red), plasma membrane staining with concanavalin A in middle panels (green), and merge pictures in right panels.

Figure 2 MCa_b also allows cell entry of Qdot655 into neurons

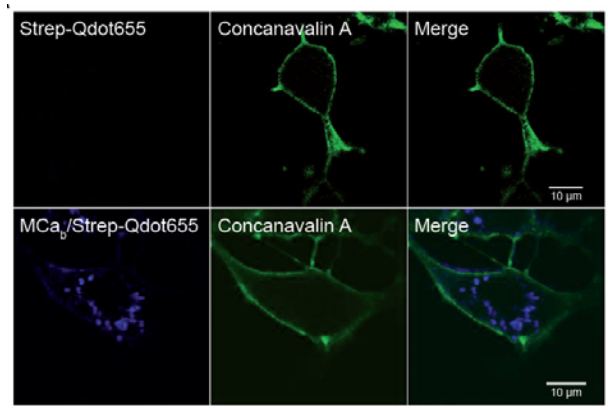

(a)

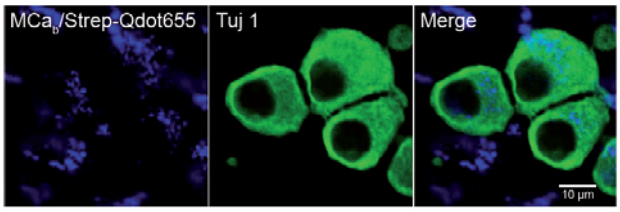

(b)

Notes: (a) Cell entry of 100 nM strep-Qdot655 (upper panel) or MCa_b/strep-Qdot655 (lower panel) into live cells from primary cultures of dorsal root ganglions after 2 hrs incubation. Qdot655 are in blue (left panels), and membrane staining with concanavalin A in green (middle panels). Right panels are merge pictures.
(b) Same as in (a) except that cells were fixed with 4% paraformaldehyde and stained with tuj1 (green marker for neuronal class III β-tubulin).

3.2 MCa_b/Qdots cell entry relies on macropinocytosis and the complex ends up into endosomes

MCa_b/strep-Qdot655 entry results in a punctuated cytoplasmic staining in CHO cells indicating that Qdots end up into endosomal structures. To challenge this hypothesis, CHO cells were labelled with lysotracker red DND-99, a marker of endosomal structures, and the staining compared to that of MCa_b/strep-Qdot655 (Figure 3a). As shown, there was an almost complete overlap between the two stainings in living cells indicating that one or several endocytic pathways should be responsible for cell entry of strep-Qdots.

To confirm that MCa_b/strep-Qdots really end up into the endocytic pathway, a set of electron microscopic studies were performed. CHO cells were incubated for 2 hrs with 100 nM of strep-Qdot585 or MCa_b/strep-Qdot585, washed, fixed, sliced and observed under transmission electron microscopy as detailed in the supplementary section. In CHO cells, endosomes had normal appearances and strep-Qdot585 presence was barely detectable (Figure 3b). The average surface of the endosomes were 0.111 ± 0.091 µm² ($n = 25$). Strep-Qdot585 presence at the extracellular face of CHO cells was undetectable indicating a total lack of affinity of strep-Qdot585 for the plasma membrane.

Figure 3 MCa_b/strep-Qdot585 and MCa_b/strep-gold particles enter CHO cells by macropinocytosis and end up into endosomes

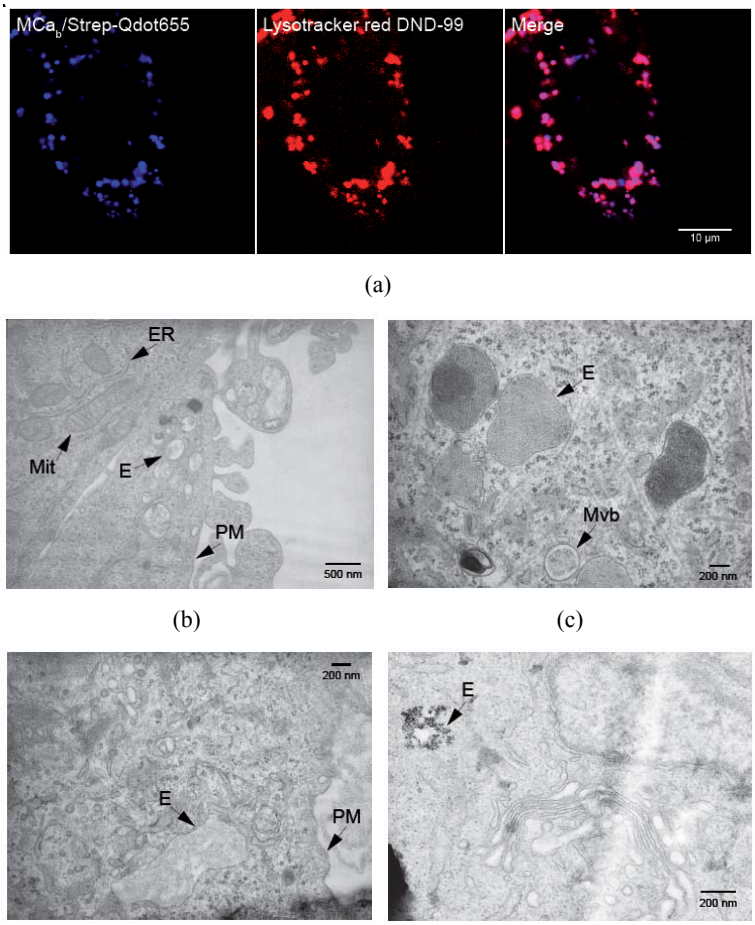

Notes: (a) Colocalisation of MCa_b/strep-Qdot585 with the endosomal marker Lysotracker red DND-99 in living CHO cells.
(b) Transmission electron microscopy images of CHO cells incubated with strep-Qdot585 alone.
(c,d) MCa_b/strep-Qdot585
(e) strep-gold particles
(f) MCa_b/strep-gold particles.
E: endosome; ER: endoplasmic reticulum; Mit: mitochondria;
Mvb: multivesicular body; PM: plasma membrane. In (c), (d) and (e), note that endosomes are densely filled with nanoparticles.
(g) Effect of 5 mM amiloride on the cell penetration of MCa_b/strep-Qdot585. Cells were preincubated with 5 mM amiloride for 45 min, and then coincubated with the complex for an additional 2 hrs. Cell fluorescence was analysed by flow cytometry. Control: cells that were incubated with strep-Qdot585 in the absence of MCa_b.

Figure 3 MCa_b/strep-Qdot585 and MCa_b/strep-gold particles enter CHO cells by macropinocytosis and end up into endosomes (continued)

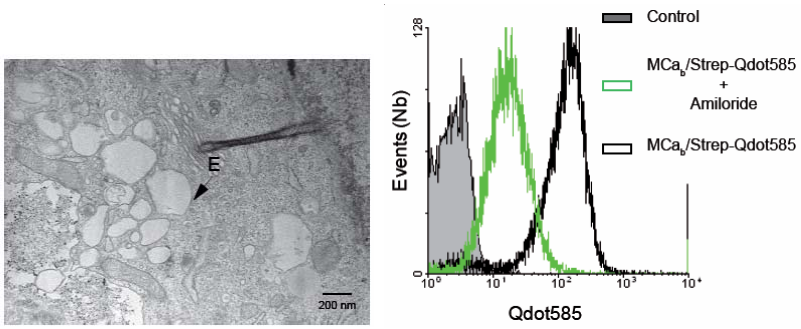

(f) (g)

Notes: (a) Colocalisation of MCa_b/strep-Qdot585 with the endosomal marker Lysotracker red DND-99 in living CHO cells.
(b) Transmission electron microscopy images of CHO cells incubated with strep-Qdot585 alone.
(c,d) MCa_b/strep-Qdot585
(e) strep-gold particles
(f) MCa_b/strep-gold particles.
E: endosome; ER: endoplasmic reticulum; Mit: mitochondria; Mvb: multivesicular body; PM: plasma membrane. In (c), (d) and (e), note that endosomes are densely filled with nanoparticles.
(g) Effect of 5 mM amiloride on the cell penetration of MCa_b/strep-Qdot585. Cells were preincubated with 5 mM amiloride for 45 min, and then coincubated with the complex for an additional 2 hrs. Cell fluorescence was analysed by flow cytometry. Control: cells that were incubated with strep-Qdot585 in the absence of MCa_b.

Normal endocytic structures devoid of strep-Qdot585 were also observed (average surface of 0.122 ± 0.093 µm², n = 25) in CHO cells incubated with MCa_b/strep-Qdot585. However, these cells also possessed larger vacuoles filled with Qdots (average surface of 0.386 ± 0.151 µm², n = 25) that were not observed in control cells (Figure 3c). These structures lack coat proteins and their morphological features are typical of macropinosomes. Interestingly, MCa_b/strep-Qdot585 presence was detected as well at the extracellular face of the plasma membrane of CHO cells (Figure 3d) owing to the affinity of MCa_b for plasma membrane components (Ram et al., 2008a). This finding was expected since cells were not treated with trypsin after incubation with MCa_b/strep-Qdot585. MCa_b/strep-Qdot585 were not detected in the cytoplasm, either because they were absent at that location or because individual MCa_b/strep-Qdot585 is poorly electron dense. Since Qdots are more difficult to visualise by transmission electron microscopy than gold particles, we chose to use strep-gold particles to confirm these findings. As shown, MCa_b/strep-gold particles were also found exclusively in endocytic structures and not in the cytoplasm (Figure 3e). Again, MCa_b is responsible for the penetration of strep-gold particles since CHO cells are devoid of particles in the absence of MCa_b (Figure 3f). Finally, we also investigated whether the massive presence

of MCa_b/strep-Qdot585 in endocytic structures is due to macropinocytosis. Figure 3(g) indicates that an addition of 5 mM amiloride during MCa_b/strep-Qdot585 incubation leads to 84% reduction in the average MCa_b/strep-Qdot585 internalisation, as assessed by flow cytometry (arbitrary mean fluorescence intensity of 104.3 and 16.4 for MCa_b/strep-Qdot585 treated CHO cells in the absence and presence of amiloride, respectively). We conclude that macropinocytosis is the major pathway of MCa_b/strep-Qdot585 entry into cells and that it leads to the formation of Qdot-enriched macropinosomes. The absence of macropinosomes in control cells (those not incubated with MCa_b) suggests that MCa_b/strep-Qdot585 binding at the surface of CHO cells triggers macropinocytosis. These findings are coherent with the observation that MCa_b/strep-Cy5 complexes also enter into CHO cell lines through macropinocytosis to end up into endosomes (Ram et al., 2008a). These results thus suggest that Qdot coupling to strep do not alter the cell penetration mechanism of this cargo when coupled to MCa_b.

Figure 4 Dose- and time-dependent cell penetration of MCa_b/strep-Qdots

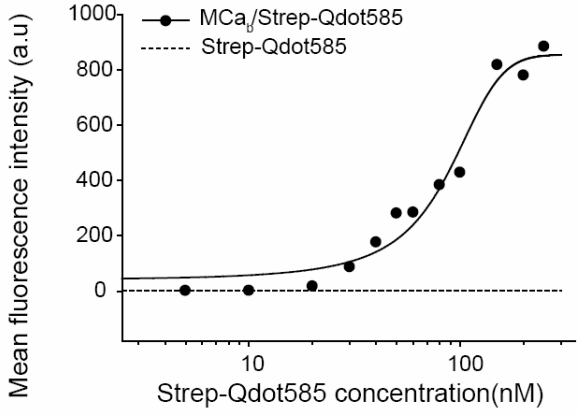

(a)

Notes: (a) Mean fluorescence level produced by MCa_b/strep-Qdot585 penetration into CHO cells as a function of strep-Qdot585 concentration. Mean fluorescence levels assessed by flow cytometry. Molar ratio of MCa_b versus Qdot585 is 4/1 and time of incubation with CHO cells is 2 hrs. Data were fitted with a sigmoid function $MF = MF_{max}/(1 + \exp(-(X - PC_{50})/b))$ where MF is the mean fluorescence, $MF_{max} = 854 \pm 45$, $PC_{50} = 87 \pm 7$ nM, and b the slope = 29 ± 5 nM. a.u. = arbitrary units.
(b) Mean fluorescence level produced by MCa_b/strep-Qdot585 penetration into CHO cells as a function of the molar ratio between MCa_b and Qdot585 (lower scale), or MCa_b and strep (top scale). Qdot585 concentration was 50 nM and CHO cells were incubated for 2 hrs with the complexes. Fit of the data as in (a) yield $MF_{max} = 479 \pm 171$, $MR_{50} = 20 \pm 17$ nM, and b the slope = 23 ± 9 nM.
(c) Time course of cell penetration of MCa_b/strep-Qdot585. Qdot concentration is 50 nM and MCa_b/Qdot ratio is 4/1. Data were fitted as in (a) and (b) and yield $MF_{max} = 222 \pm 11$, half-maximal penetration at 60 ± 2 min, and b the slope = 15 ± 3 min.

Figure 4 Dose- and time-dependent cell penetration of MCa_b/strep-Qdots (continued)

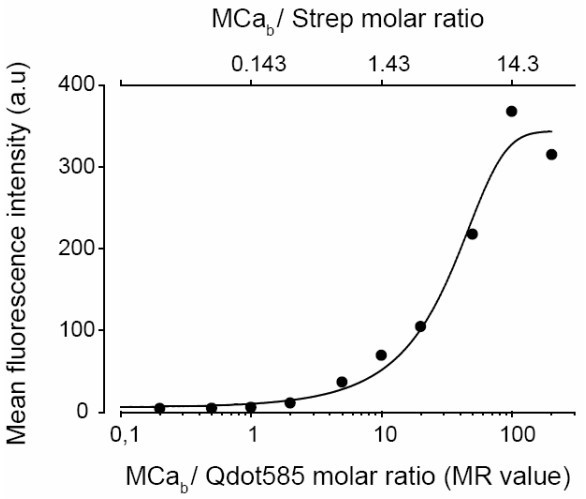

(b)

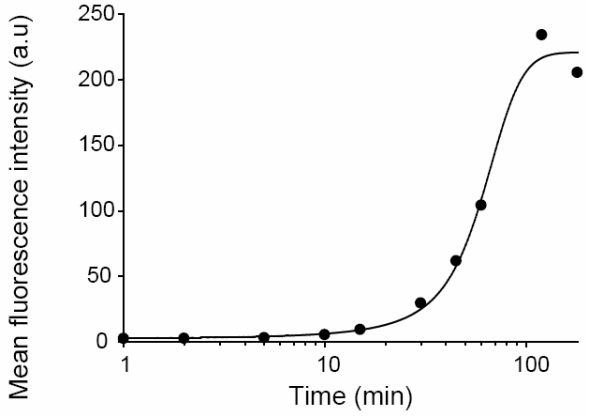

(c)

Notes: (a) Mean fluorescence level produced by MCa_b/strep-Qdot585 penetration into CHO cells as a function of strep-Qdot585 concentration. Mean fluorescence levels assessed by flow cytometry. Molar ratio of MCa_b versus Qdot585 is 4/1 and time of incubation with CHO cells is 2 hrs. Data were fitted with a sigmoid function $MF = MF_{max}/(1 + \exp(-(X - PC_{50})/b))$ where MF is the mean fluorescence, $MF_{max} = 854 \pm 45$, $PC_{50} = 87 \pm 7$ nM, and b the slope = 29 ± 5 nM. a.u. = arbitrary units.
(b) Mean fluorescence level produced by MCa_b/strep-Qdot585 penetration into CHO cells as a function of the molar ratio between MCa_b and Qdot585 (lower scale), or MCa_b and strep (top scale). Qdot585 concentration was 50 nM and CHO cells were incubated for 2 hrs with the complexes. Fit of the data as in (a) yield $MF_{max} = 479 \pm 171$, $MR_{50} = 20 \pm 17$ nM, and b the slope = 23 ± 9 nM.
(c) Time course of cell penetration of MCa_b/strep-Qdot585. Qdot concentration is 50 nM and MCa_b/Qdot ratio is 4/1. Data were fitted as in (a) and (b) and yield $MF_{max} = 222 \pm 11$, half-maximal penetration at 60 ± 2 min, and b the slope = 15 ± 3 min.

3.3 Concentration-dependence and kinetics of MCa_b/strep-Qdot cell entry

Previous studies have shown that MCa_b/strep-Cy5 cell entry occurs with a half-efficient penetration concentration (PC_{50}) of about 700 nM (Ram et al., 2008a) (with a 4/1 MCa_b/strep molar ratio). We thus checked how coupling Qdot585 with strep could influence the PC_{50} value of MCa_b for the penetration of Qdots (Figure 4a). CHO cells were incubated for two hours with variable concentrations of strep-Qdot585 (with a fixed MCa_b/Qdot585 of 4/1, equivalent to an estimated fixed MCa_b/strep ratio of 0.57/1), washed, treated with trypsin to remove surface bound Qdots, and analysed by flow cytometry. As shown, the measured PC_{50} value for strep-Qdot585 cell penetration was 87 ± 7 nM in these conditions. Saturation was observed for 200 nM MCa_b/strep-Qdot585 meaning that reasonably low concentrations of Qdots can be used in cell penetration studies. Next, the importance of the MCa_b/Qdot585 ratio was investigated (Figure 4b). Increasing concentrations of MCa_b were incubated (2 hrs) with a constant concentration of strep-Qdot585 (50 nM) in order to increase the MCa_b/strep-Qdot ratio of the complexes. The FACS data indicate a 50% molar ratio value (MR_{50}) of 20.4 ± 17.8. This value is close to the maximal theoretic value of 28 that can be reached when the average seven strep molecules of a single strep-Qdot585 are saturated by the binding of MCa_b molecules. For comparison the estimated MCa_b/strep ratios are also indicated in Figure 4(b). Finally, the kinetics of Qdot cell entry was investigated by incubating CHO cells for increasing time durations with 50 nM MCa_b/strep-Qdot585 (200 nM MCa_b complexed with 50 nM strep-Qdot585, MR value of 4). As shown, half-maximal cell entry of MCa_b/strep-Qdot585 occurred at 60 ± 3 min. This is three-fold slower than the entry of MCa_b/strep-Cy5 as assessed from an earlier study (Esteve et al., 2005).

3.4 Effect of MCa_b on the in vivo distribution of strep-Qdot705

Anesthetised OF1 mice were injected with strep-Qdot705 or MCa_b/strep-Qdot705 and the resulting fluorescence measured on the whole animal as described in the supplementary section. Control animals (before injection) displayed very little auto-fluorescence (Figure 5a). Immediately after injection, a general fluorescence was observed throughout the body in both conditions. A very rapid rise in fluorescence levels of strep-Qdot705 was observed within the liver after 15 min that lasted for 4 hrs, indicating a preferential accumulation in this tissue. A similar time course of accumulation in the liver was observed for MCa_b/strep-Qdot705, although the intensity of fluorescence observed in the liver was weaker suggesting that MCa_b kept strep-Qdot705 longer in circulation. After 2 to 4 hrs, the level of fluorescence within the liver decreases in both conditions, indicating body clearance and/or body redistribution of quantum dots into alternative organs. Whole animal imaging is however not discriminative enough to decide where and in what proportion the Qdots are distributed in the body. Therefore, the animals were sacrificed for 24 hrs after injection, the organs imaged and the fluorescence quantified. This time point was chosen to maximise the clearance of strep-Qdot705 from the body and see the effect of MCa_b on the cell penetration of strep-Qdot705 *in vivo*. As compared to control organs from non-injected animals, strep-Qdot705 and MCa_b/strep-Qdot705 distribute and

accumulate into intestine, liver, kidneys, brain, testis, heart, spleen and lungs (Figure 5b). Quantification of the fluorescence accumulated into the organs reveal only mild differences in brain, spleen and liver (Figure 5c), suggesting that MCa_b did not influence to major levels the distribution of strep-Qdot705 *in vivo*.

Figure 5 *In vivo* distribution of strep-Qdot705 and effect of MCa_b

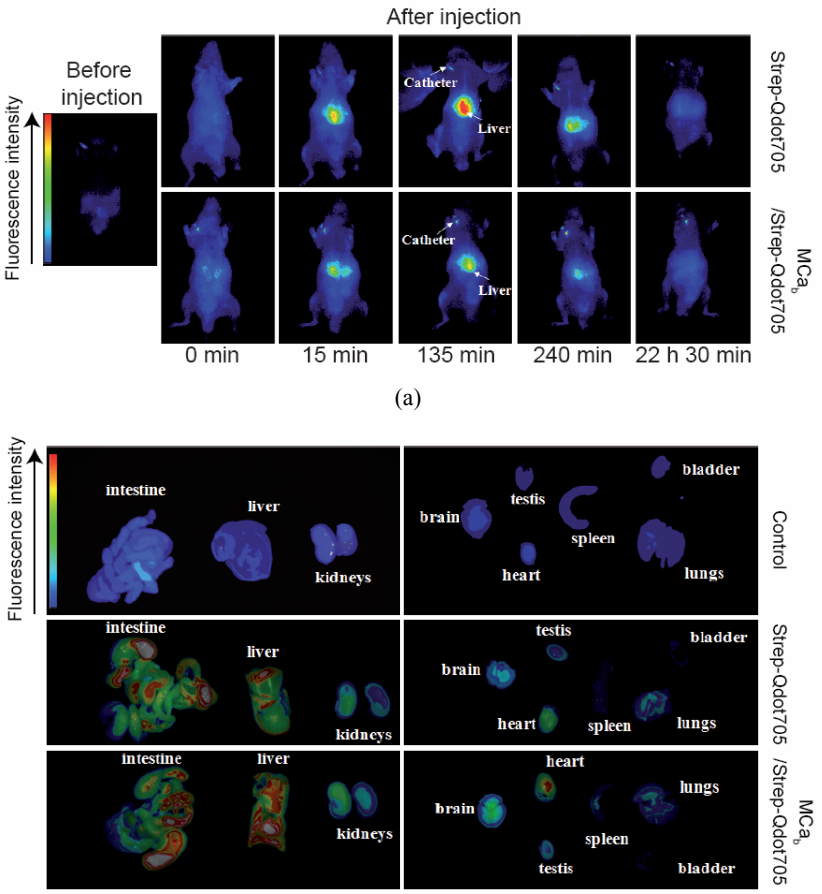

Notes: (a) Time course of the *in vivo* distribution of strep-Qdot705 (top panels) and MCa_b/strep-Qdot705 (lower panels) by whole animal imaging. Left middle panel shows the auto-fluorescence of a mouse before injection and the fluorescence intensity scale.
(b) Fluorescence levels of organs from control mouse (top panels), 24 hrs after injection of strep-Qdot705 (middle panels), or 24 hrs after injection of MCa_b/strep-Qdot705 (lower panels).
(c) Quantification of fluorescence intensity of isolated organs from control, strep-Qdot705 and MCa_b/strep-Qdot705 mice.

Figure 5 *In vivo* distribution of strep-Qdot705 and effect of MCa_b (continued)

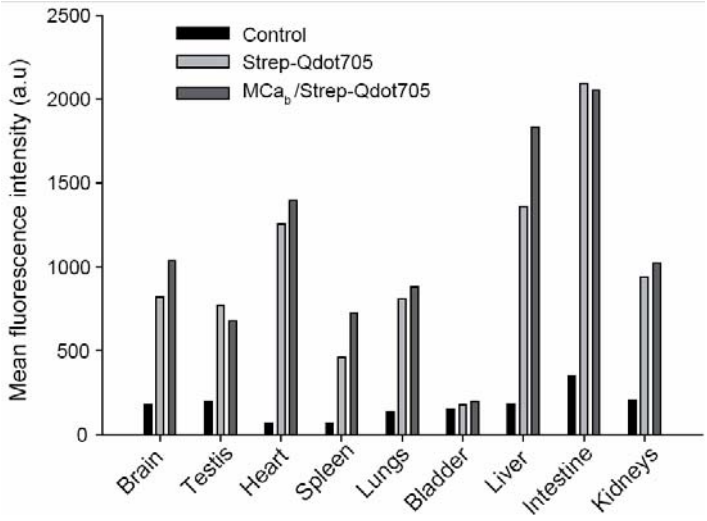

(c)

Notes: (a) Time course of the *in vivo* distribution of strep-Qdot705 (top panels) and MCa_b/strep-Qdot705 (lower panels) by whole animal imaging. Left middle panel shows the auto-fluorescence of a mouse before injection and the fluorescence intensity scale.
(b) Fluorescence levels of organs from control mouse (top panels), 24 hrs after injection of strep-Qdot705 (middle panels), or 24 hrs after injection of MCa_b/strep-Qdot705 (lower panels).
(c) Quantification of fluorescence intensity of isolated organs from control, strep-Qdot705 and MCa_b/strep-Qdot705 mice.

3.5 Coupling of MCa_b to strep-Qdot705 favours Qdot entry into cells in vivo

MCa_b is a cell penetrating peptide and has the capability to induce intracellular accumulation of Qdots *in vitro*. It was therefore of interest to determine whether this property of cell penetration of MCa_b could be preserved *in vivo*. Because MCa_b localises strep-Qdots into endosomes *in vitro*, we also used an endosomal marker to detect the intracellular presence of strep-Qdots *in vivo*. Spleen from injected mice (strep-Qdot705 or MCa_b/strep-Qdot705) were isolated after 24 hrs, sectioned and stained with the endosomal marker lysotracker red DND-99. As shown in Figure 6(a), clear co-localisation between MCa_b/strep-Qdot705 and lysotracker red DND-99 was observed indicating that accumulation of Qdots in this organ results in cell penetration when MCa_b is coupled to the Qdots. In contrast, no co-localisation was observed when strep-Qdots alone were injected in mice (Figure 6a). Also, fewer Qdots were observed in this later condition probably because of facilitated Qdot clearance in the absence of MCa_b. The first cells that MCa_b/strep-Qdot705 may encounter immediately after injection into the jugular vein are blood cells. Thus, we also examined whether blood cells could accumulate strep-Qdots in the presence of MCa_b (Figure 6b). As shown, by flow cytometry, the presence of MCa_b leads to an increased fluorescence of blood cells from an average value of 19.9 to 31.5 (arbitrary units). In contrast, no differences were observed between the mean fluorescence levels of control blood cells or blood cells

collected from mice injected with strep-Qdot705 alone. These data indicate that, besides spleen cells, MCa_b also favours cell penetration of strep-Qdots into blood cells.

Figure 6 Intracellular delivery of strep-Qdots *in vivo* by MCa_b

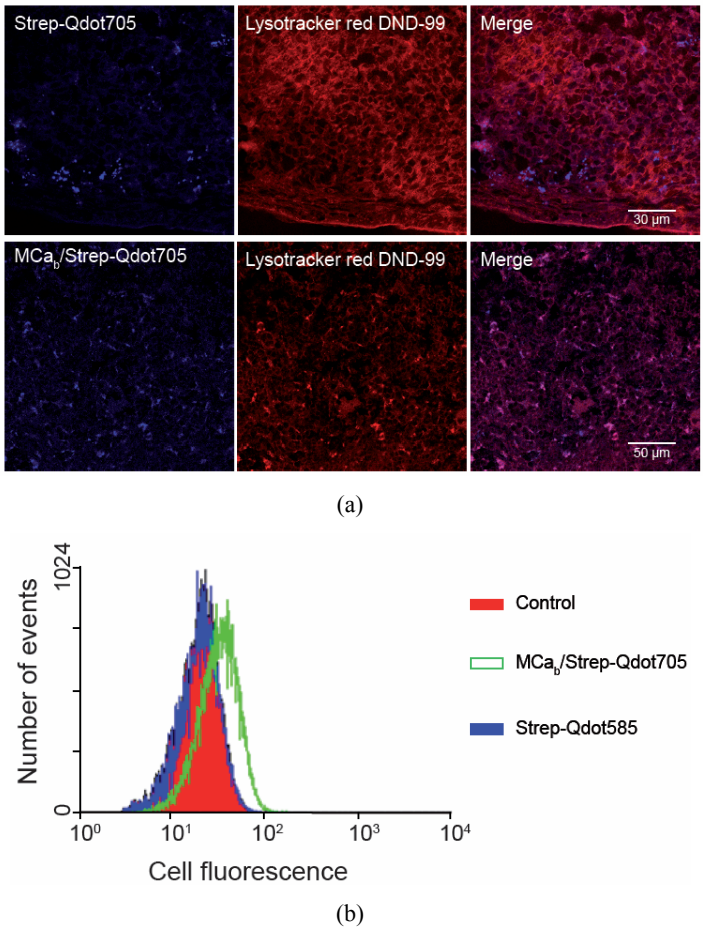

Notes: (a) Confocal microscopy images of spleen tissue sections showing the distribution of strep-Qdot705 (top panels) and MCa_b/strep-Qdot705 (lower panels).
(b) Flow cytometry analyses of blood cells collected 2 hrs after injection of strep-Qdot705 or MCa_b/strep-Qdot705 into mice.

4 Discussion

In summary, these data indicate that MCa_b is a good carrier for the cell penetration of Qdots *in vitro* and *in vivo*. It turns out to be an efficient vector since it is active at concentrations below the micromolar level. We confirm that, for Qdots also, the molar ratio between MCa_b and Qdots has a positive influence on the level of the cell penetration of these Qdots. In the chemical configuration used here, using strep as an attachment method, these Qdots concentrate massively into macropinosomes and are poorly or not

released into the cytoplasm. From *in vivo* distribution studies, MCa does not dramatically affect the organ distribution of Qdots making it a neutral cell penetrating vector for targeting purposes. Further studies are envisioned to determine whether Qdots coupled or not to MCa_b may cross the blood brain barrier. Qdots are interesting platforms for grafting biologically active molecules. It will also be of interest to determine whether in vivo intracellular delivery of MCa_b/strep-Qdots may be associated to biological activity. Further development will also be required to enhance the escape of endosomes for a delivery of Qdots into the cytoplasm.

Acknowledgements

We acknowledge financial support from a grant emergence to MDW of the Région Rhône-Alpes, TIMOMA2, a research program of the Commissariat à l'Energie Atomique, and from the PNANO program of the Agence Nationale de la Recherche. NR was supported by a fellowship of the emergence grant.

References

Akerman, M.E., Chan, W.C., Laakkonen, P., Bhatia, S.N. and Ruoslahti, E. (2002) 'Nanocrystal targeting in vivo', *Proceedings of National Academy Science USA*, Vol. 99, No. 20, pp.12617–12621.

Ballou, B., Lagerholm, B.C., Ernst, L.A., Bruchez, M.P. and Waggoner, A.S. (2004) 'Noninvasive imaging of quantum dots in mice', *Bioconjug Chem*, Vol. 15, No. 1, pp.79–86.

Boisseau, S., Mabrouk, K., Ram, N., Garmy, N., Collin, V., Tadmouri, A., et al. (2006) 'Cell penetration properties of maurocalcine, a natural venom peptide active on the intracellular ryanodine receptor', *Biochim Biophys Acta*, Vol. 1758, No. 3, pp.308–319.

Chen, F. and Gerion, D. (2004) 'Fluorescent CdSe/ZnS nanocrystal-peptide conjugates for long-term, nontoxic imaging and nuclear targeting in living cells', *Nano Lett*, Vol. 4, pp.1827–1832.

Choi, H.S., Liu, W., Misra, P., Tanaka, E., Zimmer, J.P., Itty Ipe, B., et al. (2007) 'Renal clearance of quantum dots', *Nat Biotechnol*, Vol. 25, No. 10, pp.1165–1170.

Dahan, M., Levi, S., Luccardini, C., Rostaing, P., Riveau, B. and Triller, A. (2003) 'Diffusion dynamics of glycine receptors revealed by single-quantum dot tracking', *Science*, Vol. 302, No. 5644, pp.442–445.

Derfus, A.M., Chen, W.C.W. and Bhatia, S.N. (2004) 'Intracellular delivery of quantum dots for live cell labeling and organelle tracking', *Adv Mater*, Vol. 16, pp.961–966.

Dubertret, B., Skourides, P., Norris, D.J., Noireaux, V., Brivanlou, A.H. and Libchaber, A. (2002) 'In vivo imaging of quantum dots encapsulated in phospholipid micelles', *Science*, Vol. 298, No. 5599, pp.1759–1762.

Esteve, E., Mabrouk, K., Dupuis, A., Smida-Rezgui, S., Altafaj, X., Grunwald, D., et al. (2005) 'Transduction of the scorpion toxin maurocalcine into cells. Evidence that the toxin crosses the plasma membrane', *J Biol Chem*, Vol. 280, No. 13, pp.12833–12839.

Gao, X., Cui, Y., Levenson, R.M., Chung, L.W. and Nie, S. (2004) 'In vivo cancer targeting and imaging with semiconductor quantum dots', *Nat Biotechnol*, Vol. 22, No. 8, pp.969–976.

Hoshino, A., Fujioka, K., Oku, T., Nakamura, S., Suga, M., Yamaguchi, Y., et al. (2004) 'Quantum dots targeted to the assigned organelle in living cells', *Microbiol Immunol*, Vol. 48, No. 12, pp.985–994.

Larson, D.R., Zipfel, W.R., Williams, R.M., Clark, S.W., Bruchez, M.P., Wise, F.W., et al. (2003) 'Water-soluble quantum dots for multiphoton fluorescence imaging in vivo', *Science*, Vol. 300, No. 5624, pp.1434–1436.

Lee, J., Kim, J., Park, E., Jo, S. and Song, R. (2008) 'PEG-ylated cationic CdSe/ZnS QDs as an efficient intracellular labeling agent', *Phys Chem Chem Phys*, Vol. 10, No. 13, pp.1739–1742.

Lidke, D.S., Nagy, P., Heintzmann, R., Arndt-Jovin, D.J., Post, J.N., Grecco, H.E., et al. (2004) 'Quantum dot ligands provide new insights into erbB/HER receptor-mediated signal transduction', *Nat Biotechnol*, Vol. 22, No. 2, pp.198–203.

Lim, Y.T., Kim, S., Nakayama, A., Stott, N.E., Bawendi, M.G. and Frangioni, J.V. (2003) 'Selection of quantum dot wavelengths for biomedical assays and imaging', *Mol Imaging*, Vol. 2, No. 1, pp.50–64.

Mabrouk, K., Ram, N., Boisseau, S., Strappazzon, F., Rehaim, A., Sadoul, R., et al. (2007) 'Critical amino acid residues of maurocalcine involved in pharmacology, lipid interaction and cell penetration', *Biochim Biophys Acta*, Vol. 1768, No. 10, pp.2528–2540.

Mansson, A., Sundberg, M., Balaz, M., Bunk, R., Nicholls, I.A., Omling, P., et al. (2004) 'In vitro sliding of actin filaments labelled with single quantum dots', *Biochem Biophys Res Commun*, Vol. 314, No. 2, pp.529–534.

Michalet, X., Pinaud, F.F., Bentolila, L.A., Tsay, J.M., Doose, S., Li, J.J., et al. (2005) 'Quantum dots for live cells, in vivo imaging, and diagnostics', *Science*, Vol. 307, No. 5709, pp.538–544.

Mosbah, A., Kharrat, R., Fajloun, Z., Renisio, J.G., Blanc, E., Sabatier, J.M., et al. (2000) 'A new fold in the scorpion toxin family, associated with an activity on a ryanodine-sensitive calcium channel', *Proteins*, Vol. 40, No. 3, pp.436–442.

Pinaud, F., King, D., Moore, H.P. and Weiss, S. (2004) 'Bioactivation and cell targeting of semiconductor CdSe/ZnS nanocrystals with phytochelatin-related peptides', *J Am Chem Soc*, Vol. 126, No. 19, pp.6115–6123.

Ram, N., Aroui, S., Jaumain, E., Bichraoui, H., Mabrouk, K., Ronjat, M., et al. (2008a) 'Direct peptide interaction with surface glycosaminoglycans contributes to the cell penetration of maurocalcine', *J Biol Chem*, Vol. 283, No. 35, pp.24274–24284.

Ram, N., Weiss, N., Texier-Nogues, I., Aroui, S., Andreotti, N., Pirollet, F., et al. (2008b) 'Design of a disulfide-less, pharmacologically-inert and chemically-competent analog of maurocalcine for the efficient transport of impermeant compounds into cells', *J Biol Chem*.

Santra, S., Yang, H., Stanley, J.T., Holloway, P.H., Moudgil, B.M., Walter, G. et al. (2005) 'Rapid and effective labeling of brain tissue using TAT-conjugated CdS:Mn/ZnS quantum dots', *Chem Commun (Camb)*, No. 25, pp.3144–3146.

Silver, J. and Ou, W. (2005) 'Photoactivation of quantum dot fluorescence following endocytosis', *Nano Lett*, Vol. 5, No. 7, pp.1445–1449.

Sukhanova, A., Devy, J., Venteo, L., Kaplan, H., Artemyev, M., Oleinikov, V., et al. (2004) 'Biocompatible fluorescent nanocrystals for immunolabeling of membrane proteins and cells', *Anal Biochem*, Vol. 324, No. 1, pp.60–67.

Voura, E.B., Jaiswal, J.K., Mattoussi, H. and Simon, S.M. (2004) 'Tracking metastatic tumor cell extravasation with quantum dot nanocrystals and fluorescence emission-scanning microscopy', *Nat Med*, Vol. 10, No. 9, pp.993–998.

Wadia, J.S. and Dowdy, S.F. (2002) 'Protein transduction technology', *Curr Opin Biotechnol*, Vol. 13, No. 1, pp.52–56.

Abbreviations

CdSe	cadmium-selenium
CdTe	cadmium-telluride
CHO	Chinese hamster ovary
CPP	cell penetrating peptide
DRG	dorsal root ganglia
FACS	fluorescence activated cell sorting
MCa	maurocalcine
MCa_b	biotinylated maurocalcine
NGF	nerve growth factor
PBS	phosphate-buffered saline
Qdot	quantum dot
strep	streptavidin.

2. Annexe 2

Compact and highly stable quantum dots through optimized aqueous phase transfer

Sudarsan Tamang, Grégory Beaune, Cathy Poillot, Michel De Waard, Isabelle Texier-Nogues, Peter Reiss

Proceeding of SPIE Vol. 7909 79091B-1

3. Annexe 3

Preferential effects of synchrotron microbeam radiation therapy on intracerebral 9L gliosarcoma vascular networks

A. Bouchet, B. Lemasson, G. Le Duc, C. Maisin, E. Bräuer-Krisch, E. A. Siegbahn, L. Renaud, E. Khalil, C. Rémy, C. Poillot, A. Bravin, J. A. Laissue, E. L. Barbier, R. Serduc

Int. J. Radiation Oncology Biol. Phys., Vol. 78, No. 5, pp 1503-12, 2010

Int. J. Radiation Oncology Biol. Phys., Vol. ■, No. ■, pp. 1–10, 2010

0360-3016/$–see front matter

ELSEVIER

doi:10.1016/j.ijrobp.2010.06.021

BIOLOGY CONTRIBUTION

PREFERENTIAL EFFECT OF SYNCHROTRON MICROBEAM RADIATION THERAPY ON INTRACEREBRAL 9L GLIOSARCOMA VASCULAR NETWORKS

Audrey Bouchet, M.S.,* Benjamin Lemasson, M.S.,[†‡§] Géraldine Le Duc, Ph.D.,* Cécile Maisin, M.S.,[†‡] Elke Bräuer-Krisch, M.S.,* Erik Albert Siegbahn, Ph.D.,[¶] Luc Renaud,[‖**] Enam Khalil, Ph.D.,[††] Chantal Rémy, Ph.D.,[†§] Cathy Poillot, M.S.,[†§] Alberto Bravin, Ph.D.,* Jean A. Laissue, M.D.,[‡‡] Emmanuel L. Barbier, Ph.D.,[†§] and Raphaël Serduc, Ph.D.*

*ESRF, Grenoble, France; [†]INSERM, U836, Grenoble, France; [‡]Université Joseph Fourier, Grenoble Institut des Neurosciences, Grenoble, France; [§]Onco*design* Biotechnology, Dijon, France; [¶]Department of Medical Physics, Karolinska Hospital, Stockholm, Sweden; [‖]Université de Toulouse; UPS, Toulouse, France; Centre de Recherche Cerveau et Cognition, France; **CNRS; CerCo, Toulouse, France; [††]Faculty of Pharmacy, University of Jordan, Amman, Jordan; and [‡‡]Institute of Pathology, University of Bern, Switzerland

Purpose: Synchrotron microbeam radiation therapy (MRT) relies on spatial fractionation of the incident photon beam into parallel micron-wide beams. Our aim was to analyze the effects of MRT on normal brain and 9L gliosarcoma tissues, particularly on blood vessels.

Methods and Materials: Responses to MRT (two arrays, one lateral, one anteroposterior (2 × 400 Gy), intersecting orthogonally in the tumor region) were studied during 6 weeks using MRI, immunohistochemistry, and vascular endothelial growth factor Western blot.

Results: MRT increased the median survival time of irradiated rats (×3.25), significantly increased blood vessel permeability, and inhibited tumor growth; a cytotoxic effect on 9L cells was detected 5 days after irradiation. Significant decreases in tumoral blood volume fraction and vessel diameter were measured from 8 days after irradiation, due to loss of endothelial cells in tumors as detected by immunochemistry. Edema was observed in the normal brain exposed to both crossfired arrays about 6 weeks after irradiation. This edema was associated with changes in blood vessel morphology and an overexpression of vascular endothelial growth factor. Conversely, vascular parameters and vessel morphology in brain regions exposed to one of the two arrays were not damaged, and there was no loss of vascular endothelia.

Conclusions: We show for the first time that preferential damage of MRT to tumor vessels versus preservation of radioresistant normal brain vessels contributes to the efficient palliation of 9L gliosarcomas in rats. Molecular pathways of repair mechanisms in normal and tumoral vascular networks after MRT may be essential for the improvement of such differential effects on the vasculature. © 2010 Elsevier Inc.

Synchrotron Microbeam radiation therapy, Intracerebral 9L gliosarcoma, tumor vasculature.

INTRODUCTION

Tumor vasculature is deemed to be a promising target for the treatment of solid cancerous lesions. Different therapeutic approaches, alone or combined, such as antiangiogenic therapy, chemo- , radio-, and immunotherapy are currently refined to interfere specifically with blood vessel growth in the tumor (1). This objective might also be achieved by a novel form of radiosurgery, known as microbeam radiation therapy (MRT) (2), which uses a particular irradiation geometry and X-rays generated in a synchrotron light source; the beam is spatially fractionated into an array of quasi-parallel planar microbeams that are a few tens microns wide and separated by a few hundred microns. This unique irradiation geometry allows high dose (hectogray) deposition efficient for the treatment of brain tumors in small animals while ensuring an unusually high normal tissue tolerance, even in developing larger animals (3, 4).

The preferential effect on malignant tissues has been mainly attributed to selective effects of microbeams on immature tumor vessels versus lack of microbeam effects on the differentiated normal vasculature (5), although other factors might be operative. Lesions induced by the microbeams in the normal capillary network can be rapidly repaired (6, 7), and normal arteries are also microbeam-resistant (8). Thus,

Reprint requests to: Raphaël Serduc, Ph.D., Monash Institute of Medical Research, 3168 Clayton, Victoria, Australia. Tel: (+61) 3-8540-4100; Fax: (+61) 3-8540-4200; E-mail: raph.serduc@gmail.com

Authors AB and BL contributed equally to this work.

Supplementary material appears online.

Conflict of interest: none.

Received Dec 12, 2009, and in revised form June 10, 2010. Accepted for publication June 15, 2010.

there is no decrease in vessel density or blood volume, no hemorrhage, and no ischemic necrosis after MRT in normal mammalian tissues. Conversely, no clear experimental proof of the effect of MRT on tumor vessels has been given in the literature. Our recent MRI study failed to reveal important damage to tumor vessels after MRT (9). Cross-fired MRT slowed the growth of the heterologously implanted 9L gliosarcoma (9LGS) and the development of its vasculature. We now characterize the biological effects of 50-μm-wide microbeams, efficient in terms of tumor control and normal tissue sparing (10), on normal rat brain and intracerebral 9LGS, particularly on growth and morphometric parameters of blood vessels from 2 to 45 days after irradiation and on the expression of the vascular endothelial growth factor (VEGF).

METHODS AND MATERIALS

All procedures related to animal care conformed to the Guidelines of the French Government with licenses 380325 and 380321. Rats were anesthetized with an intraperitoneal injection of xylazine/ketamine (64.5/5.4mg.kg^{-1} for irradiations) and 2.5% isoflurane (MRI follow-up) for maintenance.

Tumor inoculation

Transplantable 9LGS cells were implanted in fifty-nine 10-week-old Fisher rats weighing between 180 and 220 g. Implantation procedure followed the protocol described in Serduc *et al*. (10). Briefly, 10^4 9LGS cells suspended in a 1 μL Dulbecco's Modified Eagle Medium were injected into the right caudate nucleus (3.5 mm from the bregma) at a depth of 5.5 mm from the dura.

Magnetic resonance imaging and group sorting

We used a 4.7-T Bruker Avance console and volume/surface cross coil configuration. Seven days after 9LGS implantation, rats underwent anatomical MRI (T_2-weighted image) to sort them two groups with similar mean tumor size. Those 59 rats were divided into a control group ($n = 25$) and a group of 34 rats was irradiated by MRT 10 days after 9LGS implantation. Rats (n = 4–8) underwent MRI, and 4 were culled at

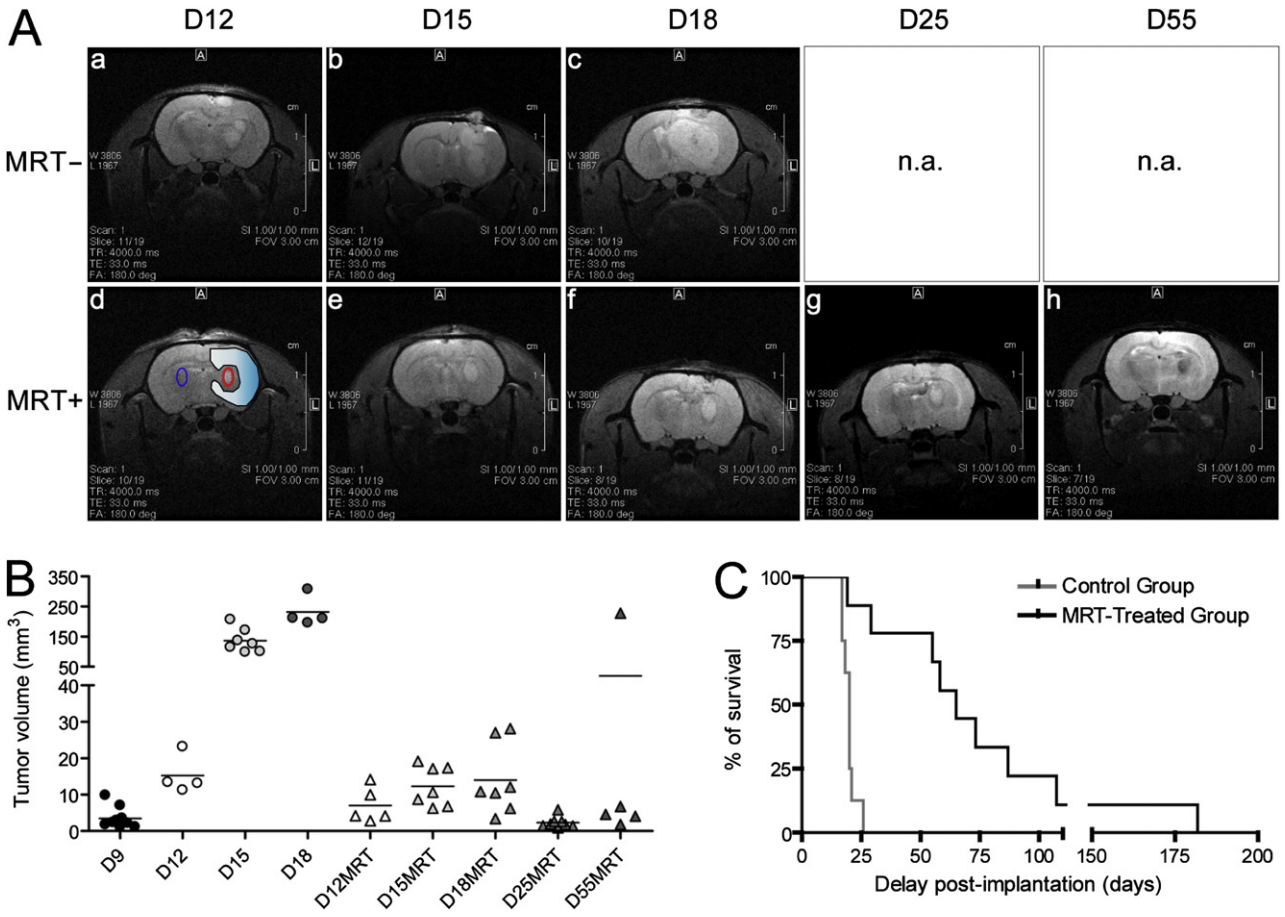

Fig. 1. MRI follow-up, survival curves, and lesion size evolution. T_2-weighted MR images of a nonirradiated (1A, a–c) and of an irradiated (MRT, microbeam radiation therapy) (1A, d–h) 9LGS bearing rat at different delays after implantation. (B) Individual values (plots) and means (lines) of tumor volumes measured on T_2-weighted images at different delays after tumor inoculation for the untreated and MRT-treated groups. Circle and triangle symbols represent the untreated and MRT-treated groups, respectively. (C) Kaplan-Meier curves showing the survival of 9LGS bearing rats. Untreated controls are represented in gray, and animals treated by MRT are plotted in black. The MRT treatment induced a significant increase in the median survival time of animals (D65 vs. D20, log-rank test, $p = 0.0003$).

each delay for biological studies. The survival curves were established using 9 rats of each group. The number of days elapsed after implantation (n) and treatment (m) is designated as D_nT_m.

Radiation source and irradiation geometry

Irradiations were performed on the ID17 biomedical beamline at the European Synchrotron Radiation Facility using X-rays emitted tangentially from relativistic electron bunches circulating in a storage ring. The wiggler produces a wide spectrum of photons that extends from 50 to over 350 keV (median energy, 90 keV). The quasi-laminar beam was shaped into an array (8 mm wide) of rectangular, microscopically thin and quasi-parallel microbeams using a multislit collimator (11). Rats in the treated group were irradiated ($D_{10}T_0$) after tumor inoculation using two 10-mm-high arrays of 40 vertical, planar microbeams (width 50 μm, 200 μm on-center spacing), one anteroposterior, the other lateral, both focused for orthogonal intersection (cross-firing) in the anterior part of the right hemisphere, where the 9LGS was located. Before reaching and after leaving the volume of intersection enclosing the tumor, each array alone covered a volume of the rat's head in which it was unidirectional. Animals were aligned into the beam using three live cameras, and the coordinates of the center of the microbeam arrays were 3.5 mm left from the mediolateral line, –6 mm in the dorsoventral direction from the skin surface and at the bregma point in the anterioposterior direction. The in-microbeam entrance dose was 400 Gy per array, and the mean dose rate ~16,000 Gy.s^{-1}.

Monte Carlo simulation and doses calculations

The doses were calculated by means of the Monte Carlo method normally used for MRT dose planning and quality assurance at the European Synchrotron Radiation Facility (ESRF) (12). Further details of our MRT dosimetry protocols are provided in Supplement 1.

Rat follow-up by MRI

Eight rats were imaged 1 day before (D_9T_{-1}) and animals from all groups at 2, 5, 8, 15, and 45 days after MRT treatment. For each group, four rats were followed up and imaged at every time point. Four rats per groups were also imaged at every delay after irradiation and culled for immunohistological studies and Western blot analysis.

Each MRI session (duration 1h 15 min), detailed in the Supplement 1, was organized as follows:

- Anatomical T_2-weighted images
- blood volume fraction (BVf) and vessel size index (VSI) measurements
- Vascular permeability of P846 (Gd-based contrast agent) measurements

MRI data analysis

BVf, VSI, and vessel permeability maps were computed pixel by pixel using an in-house program developed under Matlab (MathWorks, Natick, MA). BVf and VSI were calculated as described previously (13, 14). Null pixels were excluded in the mean calculation to give information only on perfused brain regions. Vessel permeability was estimated by subtracting the peak MR signal obtained after the injection of gadolinium-tetraazacyclododecane tetraacetic acid (Gd-DOTA) from the peak MR signal measured before injection and expressed as a percentage of contrast enhancement. Three regions of interest (ROIs) were manually delineated on the T_2-weighted image on which the tumor appeared the largest (see Fig. 1): (*1*) the whole tumor, (*2*) the ipsilateral (right) hemisphere without tumor, and (*3*) the contralateral hemisphere; these were reported on the other maps. Tumor and surrounding parts of the normal brain in the right hemisphere were exposed to the two intersecting

Table 1. Microbeam radiation therapy (MRT) effects on blood vessels located either in a 9LGS (''tumor'') or in normal brain tissue

Parameter	Location of Blood vessels	Irradiation	Observations
Blood vessel morphology	Normal brain	Uni	No changes; endothelial cells and vascular basal membranes are immunolabeled
		Cross	Long-term changes ($D_{55}T_{45}$) and increased tortuosity; narrow channels without endothelia; reduced RECA reactivity
	Tumor	Cross	Short-term changes ($D_{12}T_2$); gradual decrease of RECA reactivity; loss of tumor endothelia (denudation)
Blood volume fraction	Normal brain	Uni	No changes
		Cross	No changes
	Tumor	Cross	Significant decrease from $D_{18}T_8$
Vessel size index	Normal brain	Uni	No changes
		Cross	Significant increase at $D_{55}T_{45}$
	Tumor	Cross	Significant decrease from $D_{18}T_8$
Vessel permeability	Normal Brain	Uni	No changes
		Cross	No changes
	Tumor	Cross	Short-term increase at $D_{12}T_2$ and $D_{15}T_5$

Abbreviation: RECA = rat endothelial cell antigen.

Parts of left hemisphere were irradiated unidirectionally by the lateral array (Uni). Extratumoral anterior parts of the right hemisphere were irradiated by the intersecting lateral and anteroposterior arrays (Cross). The 9LGS tumor in the right anterior hemisphere was also cross-irradiated. The number of days (n) elapsed after implantation or irradiation is designated as DnTn, respectively.

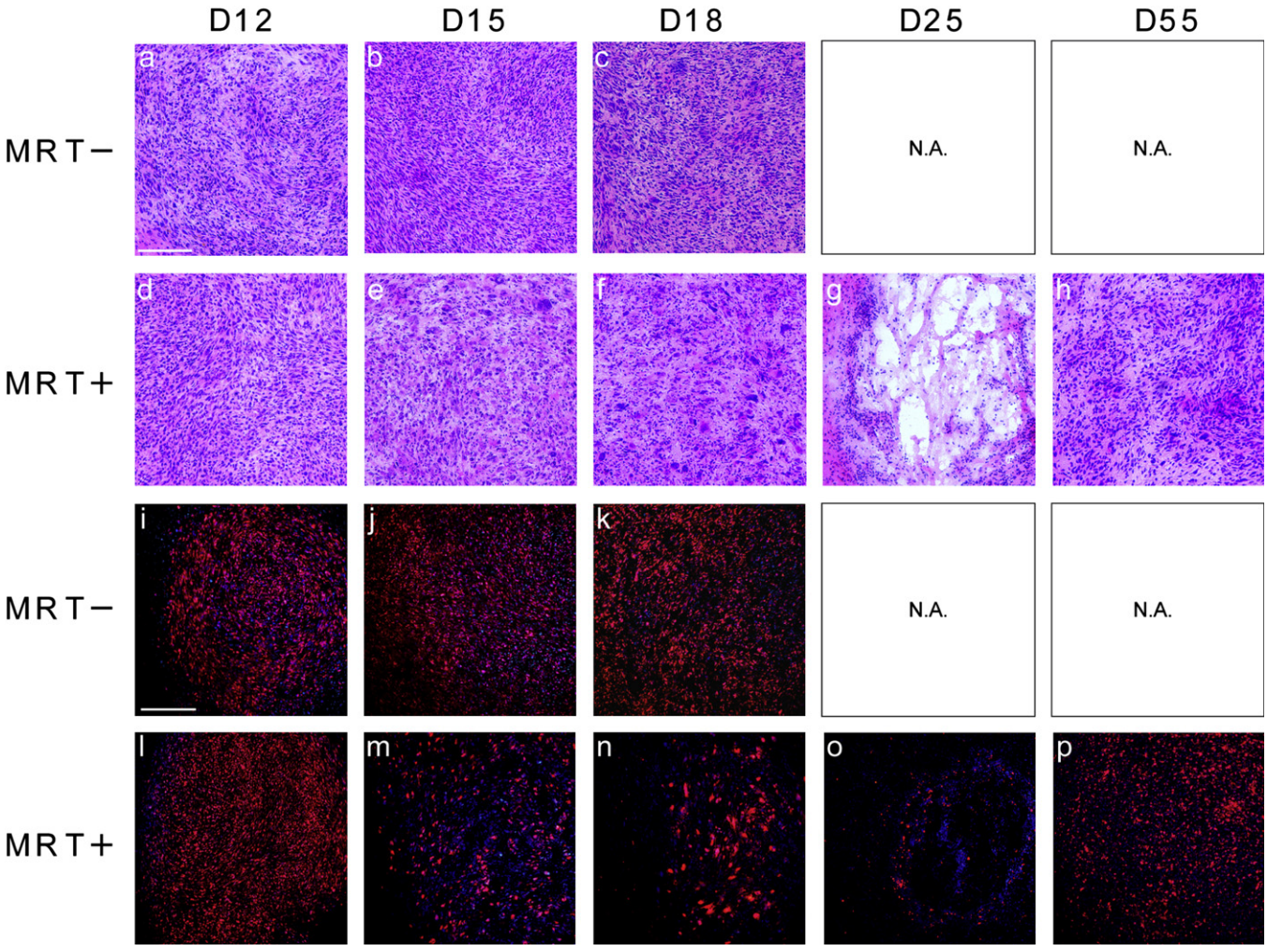

Fig. 2. Temporal immunohistological follow-up of untreated or irradiated tumors. MRT = microbeam radiation therapy. H&E (a–h) staining and Ki67 ([i–p], red; DAPI (4',6'-Diamidino-2'-phenylindole) counterstained nuclei, blue) immunolabeling observed in irradiated (MRT+) and nonirradiated tumors (MRT–) at different delays after implantation. Scale bars: 200 μm.

arrays, normal brain parts of the left hemisphere unidirectionally to the lateral array alone. Tumor volumes were determined by multiplying the pixel size by the number of ''tumoral pixels'' on all MR slices on which the tumor was visible. Two-way analysis of variance followed by Bonferroni *post hoc* tests were used for statistics. A Mann-Whitney test was used to compare 9LGS volumes. The statistical analyses were performed with the Prism program (GraphPad Software). Values were considered significantly different when $p < 0.05$.

Immunological- and histological analyses

Type-IV collagen (C_{IV}), a protein constituent of the vessel *basal lamina*, and RECA-1 (*rat endothelial cell antigen*), an antigen of endothelial cells, were labeled as previously described (7, 15). Cell proliferation activity was assessed by means of Ki67 labeling. Further details of our Immunohistology protocols and quantification are provided in Supplement 1.

Western blot analysis of vascular endothelial growth factor

The Western blot protocol of VEGF is described in Supplement 1 section.

RESULTS

The main results of this study are summarized in Table 1. Radiation doses were calculated in a rat head phantom using Monte Carlo simulations. The peak dose deposited at 1 cm depth in rat brain was 350/700 Gy, generating a valley dose of 12.5/25 Gy in the unidirectionally/bidirectionally irradiated brain regions, respectively.

Survival curves

Figure 1C shows the Kaplan-Meier representation of the survival of untreated and MRT-treated 9LGS bearing rats. MRT significantly increased the mean survival time (MST) of treated animals compared with the control group of

nonirradiated rats (65 days vs. 20, respectively, log-rank test: $p = 0.003$).

MRT effects on 9LGS growth

Figure 1A shows a T_2-weighted MRI follow-up of irradiated and nonirradiated 9LGS that grew exponentially and equally between D_9T_{-1} and $D_{18}T_8$ and reached comparable sizes at $D_{12}T_2$ (15.2 ± 5.3 mm^3 in nonirradiated vs. 7.0 ± 4.8 mm^3 in irradiated rats). Tumor volume measured on T_2-weighted MR images are reported in Fig. 1B. The effects of MRT were observed from $D_{15}T_5$: tumors were significantly smaller in MRT-treated rats compared with controls by a factor of about 17 at $D_{18}T_8$ (Fig. 13.9 ± 9.7 mm^2 [MRT] vs. 231.7 ± 51.3 mm^3 [untreated], $p < 0.001$). Later, between D_9T_{-1} and $D_{25}T_{15}$, no difference in tumor size was found. Thereafter, the evaluation of tumor volume using on T_2-weighted MR images became more problematic because two rats did not exhibit tumor anymore (the hyposignal as shown in Fig. 1Ah was taken into account for lesion size determination); two rats showed small tumors, and one rat had a recurrent tumor comparable to those measured in control rats at $D_{18}T_8$.

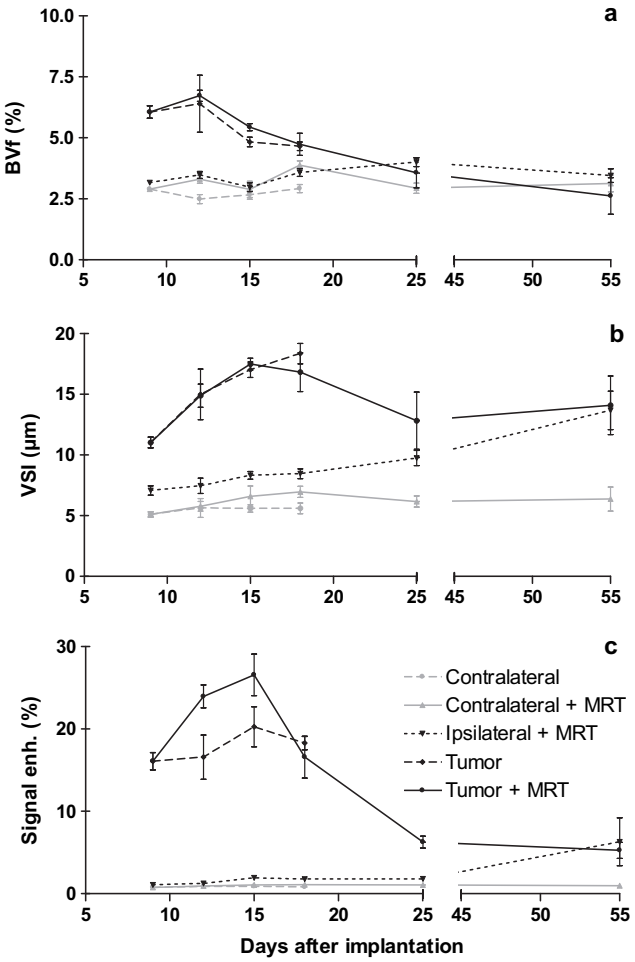

Fig. 3. MRI vessel parameter measurements. (a) Blood volume fraction (BVf), (b) vessel size index (VSI), and (c) vessel permeability values measured by MRI in the tumor in the contralateral and ipsilateral hemispheres at different times after tumor inoculation. MRT = microbeam radiation therapy.

MRT effects on 9LGS proliferative activity

The analyses Ki67 immunolabeling and hematoxylin and eosin (H&E) stained sections revealed that MRT-induced damages were detectable from $D_{15}T_5$ (Fig. 2): cell density decreased on H&E-stained brain sections in irradiated tumors; the proliferative activity (proportion of Ki67-positive cells) of the tumor was distinctly reduced. Giant tumoral cells were observed. At $D_{25}T_{15}$, the 9LGS tissue was strongly disorganized, exhibiting cellular polymorphism and large lacunae and/or necrotic regions in the core. Only a few dividing cells were found at the tumor periphery. For two thirds of the animals observed at $D_{55}T_{45}$ by immunohistology, it was not possible to delimit a tumor. Conversely, one third of the animals presented a tumor with numerous Ki67-positive cells that had invaded the whole ipsilateral hemisphere (Fig. 2). Normal tissue exhibited astrocyte and neuron loss in the microbeam paths starting 5 days after irradiation.

MRT effects on the evolution of normal and tumoral blood vessels of the brain

Blood volume fraction: cerebral BVf (Fig. 3) was significantly higher in the 9LGS than in the ipsi- and contralateral normal brain for all observation times. A decrease in tumoral blood volume fraction (TBVf) was detected between D_9T_{-1} and $D_{18}T_8$ in irradiated or nonirradiated tumors ($p < 0.001$), whereas the cerebral BVfs of the ipsi- and contralateral normal hemisphere did not change. Thereafter, in irradiated animals, TBVf decreased between $D_{18}T_8$ and $D_{25}T_{15}$ (<0.001).

Vessel size index: VSI values increased similarly in both irradiated and nonirradiated tumors until D18, when they were significantly higher in tumors than in normal tissues ($p < 0.001$). Thereafter, VSI values decreased in irradiated tumors between $D_{18}T_8$ and $D_{25}T_{15}$ (–23.8%, $p < 0.001$). In normal tissues surrounding the tumor within the volume targeted by the intersecting, crossfired arrays (ipsilateral + MRT), VSI increased between $D_{18}T_8$ and $D_{55}T_{45}$ (8.5–13.7μm, $p < 0.001$).

Contrast enhancement: Vessel permeability (indicated as contrast MR enhancement, Fig. 3) was significantly higher in 9LGS than in the normal ipsi- or contralateral hemisphere, and it was not modified in normal brain tissue after unidirectional or crossfired irradiations. Conversely, MRT led to an increase in tumor vessel permeability during the 5 days following the irradiation: the MR signal enhancement reached 26.6% at D15, whereas it was only 20.3% in nonirradiated tumors ($p < 0.001$). Then, the blood vessel permeability of irradiated tumors decreased by 74% between $D_{15}T_5$ and $D_{25}T_{15}$ ($p < 0.001$).

Blood vessels—immunohistological observations: Vascular networks were observed on brain sections labeled by C_{IV} (basal membrane) and RECA-1 (endothelial cells, Figs. 4 and 5). The coexpression ratio of these proteins in vessels is reported in on each image on Fig. 4. During the entire experiment, no damage was detected in the unidirectionally

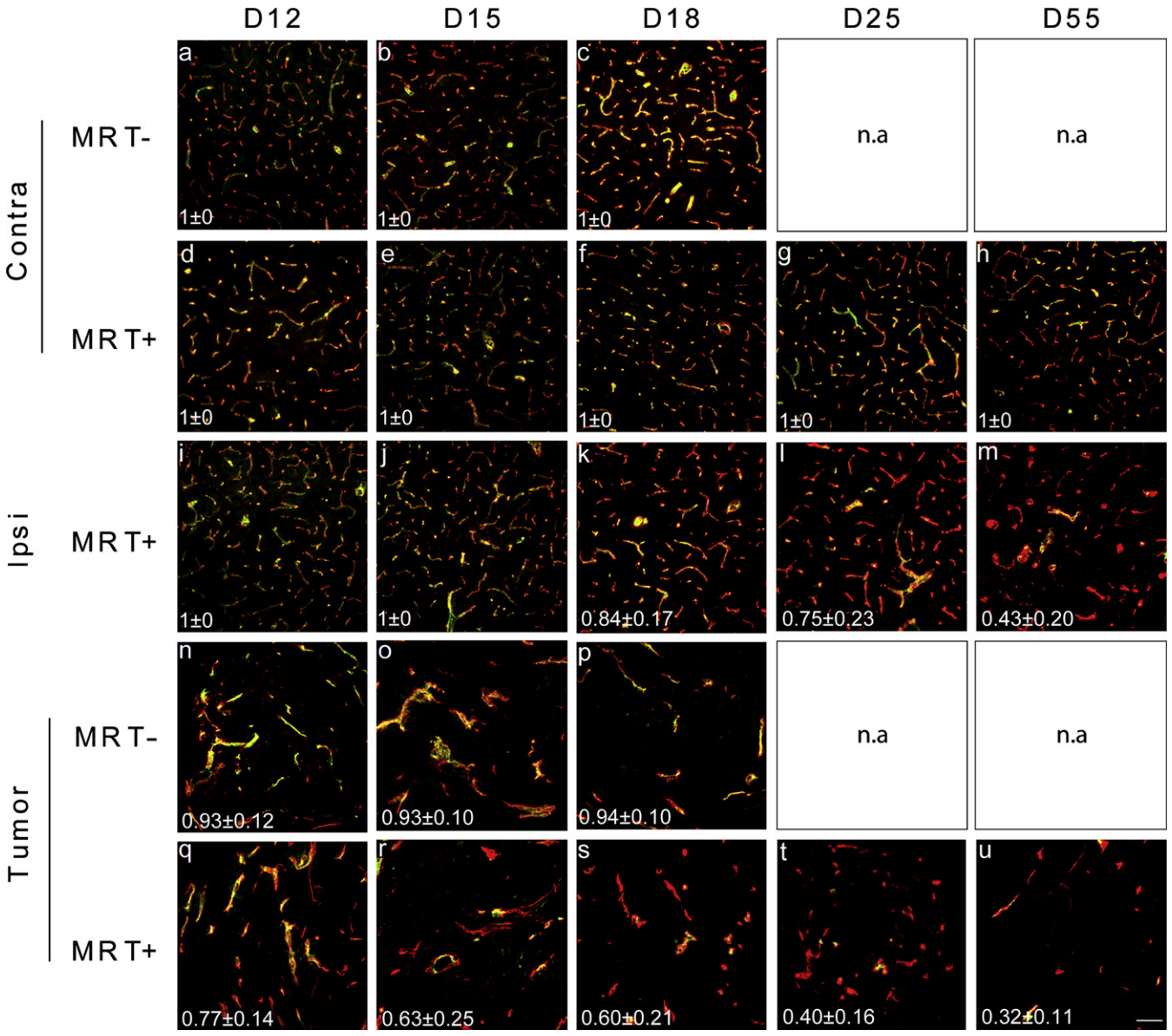

Fig. 4. Temporal immunohistological follow-up of unirradiated or irradiated normal and tumoral brain vessels. MRT = microbeam radiation therapy. Type IV collagen (red) and RECA-1 (green) immunolabeling observed in tumors in the contralateral (Contra) and ipsilateral (Ipsi) hemispheres of irradiated (MRT+) and control rats (MRT–) at different delays after implantation. Scale bar: 200 μm. Numbers on each image correspond to the level of coexpression of Type IV collagen and RECA estimated as described in the Supplement 1.

irradiated volume of the contralateral hemisphere (Fig. 4). All brain capillaries were double stained by C_{IV}/ RECA-1 antisera. Conversely, the morphology of blood vessels located in the normal brain tissue surrounding the tumor within the volume of intersecting arrays changed around $D_{55}T_{45}$: the normal vascular network showed an important disorganization and increased tortuosity. C_{IV} immunolabeling revealed the presence of narrow (diameter 1–2 μm) entities without endothelial cells, as shown by a quasi-complete lack of reactivity for RECA-1 labeling. Few capillaries of normal size lacked homogenous RECA-1 labeling.

Tumor vessel density was lower than that observed in normal brain tissue. Spatial vessel distribution was irregular and vessel diameters were distinctly larger compared with normal brain blood vessels. The number of blood vessels per surface area in nonirradiated as well as in irradiated tumors decreased with time after implantation. However, beginning at $D_{12}T_2$, RECA-1 labeling intensity gradually faded in 9LGS vessels in the beam-crossing volume. In tumors observed from $D_{18}T_8$ to $D_{55}T_{45}$, most of 9LGS vessels were not immunoreactive for RECA-1, as shown in Fig. 5 for a rat culled at $D_{18}T_8$.

MRT effects on VEGF expression

No VEGF expression was detected in contralateral (left) hemispheres of control rats during the whole experiment. Conversely, MRT induced an expression of VEGF increasing with time in normal brain tissues, *i.e.*, from $D_{12}T_2$ or $D_{15}T_5$, in

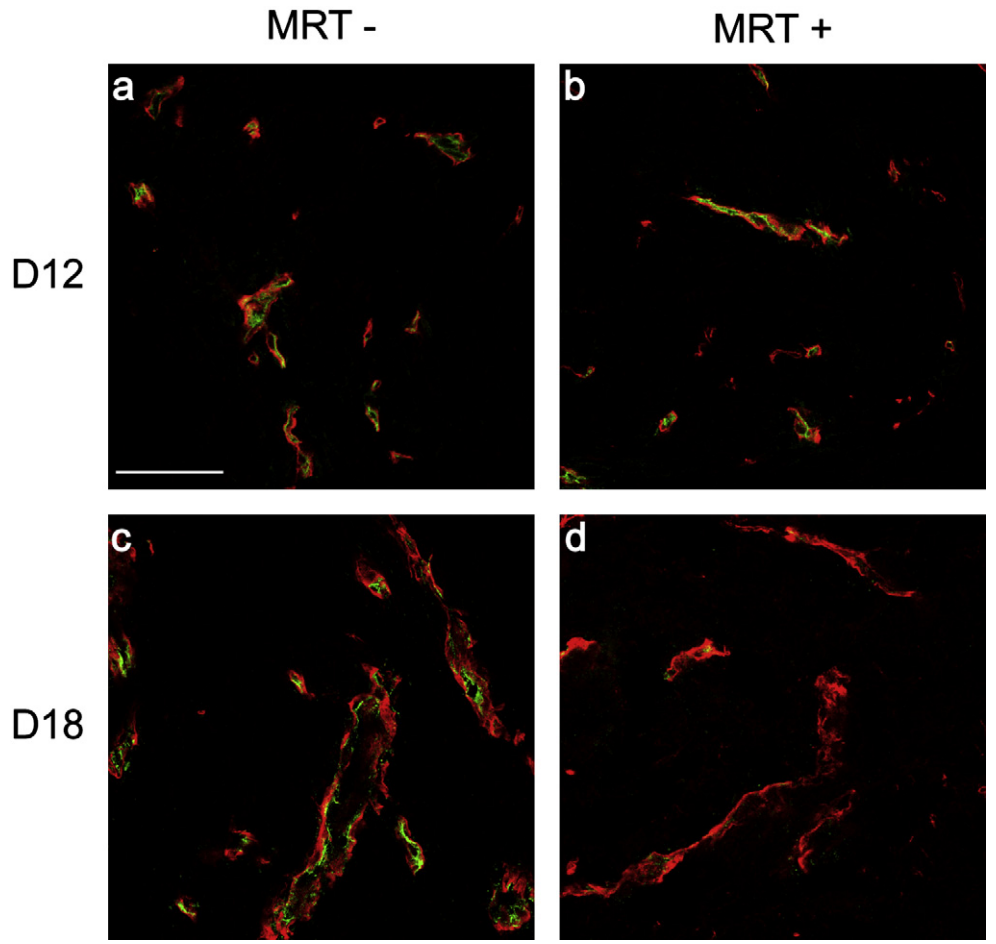

Fig. 5. Confocal images of unirradiated or irradiated 9LGS blood vessels. MRT = microbeam radiation therapy. Type IV collagen (red) and RECA-1 (green) immunolabeling observed in irradiated (MRT+) and untreated control tumors (MRT–) at D12 and 18 after implantation. Scale bar: 70 μm.

both hemispheres, whether irradiated by one or by both intersecting arrays (Fig. 6). At $D_{55}T_{45}$, the amount of VEGF detected in normal brain parts of the ipsilateral hemisphere situated in the beam-crossing region was >2.5-times higher (p <0.001) than the one measured in the left hemisphere irradiated unidirectionally by the lateral array (Contra + MRT).

In 9LGS, the relatively low expression of VEGF did not markedly change during their growth (Fig. 6). Conversely, the irradiation led to a progressive and significant increase in VEGF expression in tumors. Indeed, the ratio VEGF/GADPH (glyceraldehyde-3-phosphate dehydrogenase) changed from 0.4 to 1.1 between $D_{12}T_2$ and $D_{18}T_8$, whereas it fluctuated from 0.5 to 0.8 in untreated tumors during the same period (ns for untreated tumors, p <0.05 in irradiated tumors). At $D_{25}T_{15}$ and $D_{55}T_{45}$, the relative expression of VEGF increased significantly in irradiated tumors (p <0.001) to values 1.35 and 1.8 times higher than the one measured at $D_{18}T_8$.

DISCUSSION

The cross-fired irradiation increased significantly the MST of rats bearing intracerebral 9LGS compared with unirradiated controls (p = 0.0003). MRT inhibited tumor growth for a few weeks after treatment as shown by MRI. Histopathologically, MRT induced a decrease in tumor cell density and reduced the proliferative activity of the lesion. The salient findings in this study were (*1*) the preferential loss of endothelial cells in tumor vessels exposed to crossfired arrays, from 5 days after treatment and (*2*) the significant decrease in tumoral blood volume fraction during the second week after irradiation; conversely, the microvasculature and the perfusion in the normal brain volumes irradiated unidirectionally in the contralateral hemisphere remained undamaged. Normal blood vessels in peritumoral normal brain tissue were damaged by both intersecting arrays.

The hypothesis of a preferential effect of MRT on tumoral blood vessels rather than on normal vasculature is well established (5, 16). However, Serduc *et al.* (9) described a limited influence of the vascular component during 9LGS palliation in mice by MRT. A significant increase in tumor vessel permeability on $D_{12}T_2$ and $D_{15}T_5$ (+44% and +23%) preceded tumor necrosis in the present experiment. No change in blood–brain barrier breakdown permeability was detected in ipsilateral (exposed to both arrays) and contralateral (exposed to one array only) normal brain tissues. This transient tumor–blood barrier breakdown might be used to deliver intravenously injected

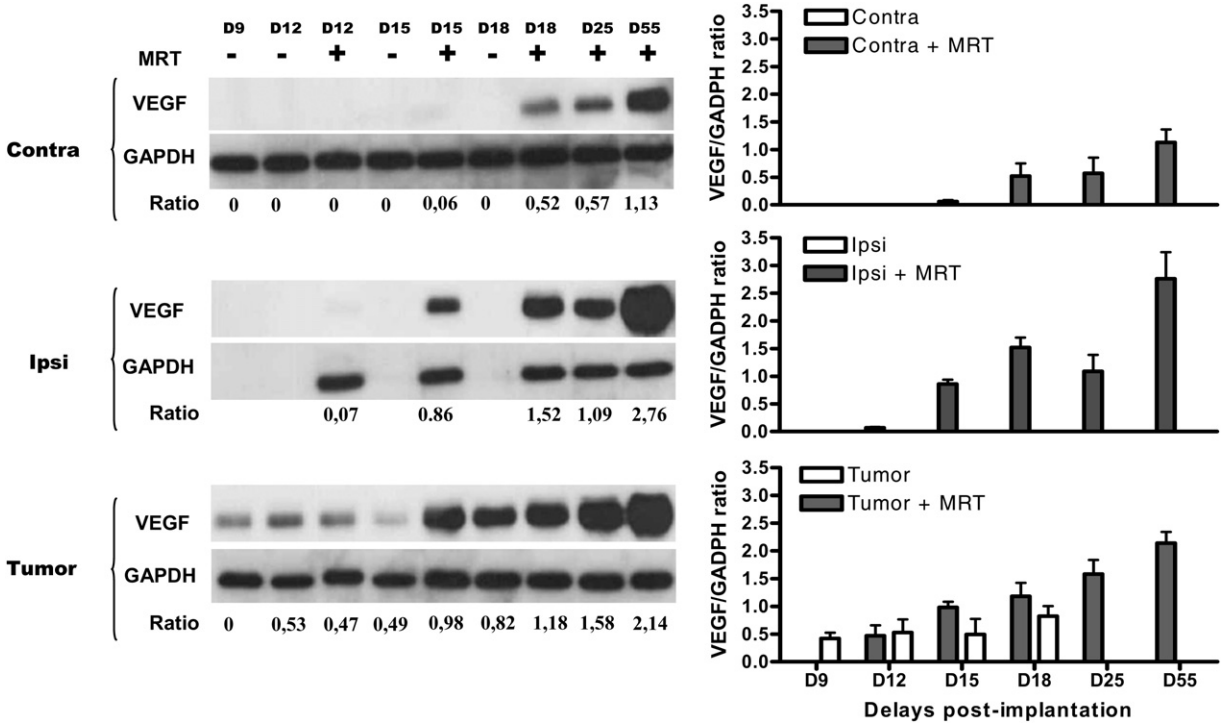

Fig. 6. Vascular endothelial growth factor (VEGF) expression evolution. Western blot for VEGF in the contralateral (Contra) and ipsilateral (Ipsi) hemispheres and tumors of irradiated (unidirectional [Contra] or cross-fired [Ipsi and tumor] irradiations [+]) and control rats (–) at different times after implantation. The VEGF/GADPH (gylceraldehyde-3-phosphate dehydrogenase) ratio is given under each blot for each delay and plotted in the three histograms represented on the right. MRT = microbeam radiation therapy.

drugs to the tumor core. Adjuvant chemotherapy would be justified by the fact that in previous studies, MRT did not sterilize intracerebral 9LGS, a highly resistant gliosarcoma model, even when adequate irradiation configurations and valley doses were used (45Gy 36Gy) (15, 17). In the present experiment, tumor growth was inhibited during several weeks after MRT in association with reduced proportions of proliferative Ki67-positive tumor cells, starting on $D_{15}T_5$. Two weeks after MRT, large necrotic regions were detected in the tumor core. The presence of proliferative cells at the tumor periphery may indicate tumor recurrence.

Because several rats survived for a long period after MRT for 9LGS in other experiments (5, 16), despite the presence of ~2% surviving clonogenic 9LGS cells in the tumor (5), it was suggested that tumor ablation was due to the preferential effect of MRT on tumor blood vessels resulting in ischemic necrosis of the tumor. However, in this study, morphometric parameters of the vascular network were not affected shortly after MRT, *i.e.*, between $D_{12}T_2$ and $D_{18}T_8$. Indeed, we observed no difference in BVf and VSI values between irradiated and nonirradiated tumors. Conversely, during this period, RECA-1 labeled endothelia were not detected in all Type IV collagen–positive vascular structures of irradiated tumors, whereas their vascular counterparts in the time-matched nonirradiated tumors exhibited obvious double staining. Loss of RECA-1 immunoreactivity indicates a loss of endothelial cells. Alternatively, some vessels might have been occluded by thrombosis or following endothelial denudation. However, BVf and VSI values measured by MRI after intravenous Sinerem injection did not indicate a decreased tumor perfusion after irradiation. Thus, the loss of endothelial cells might not have measurably impaired tumor blood supply after MRT. Loops of extracellular matrix, devoid of endothelia, seem able to irrigate tumors with blood temporarily (18). Such C_{IV}-positive vessel-like structures lacking immunoreactive endotheliocytes, might thus permit a transitory perfusion of 9GLS; the parameters showing the evolving perfusion after irradiation in the same animal support this interpretation (Fig. 1A): after $D_{18}T_8$, tumor size reduction until $D_{25}T_{15}$ correlates with the significant decrease in TBVf and in VSI (–24.6%, <0.05 and –23.8%, p <0.01, respectively). Conversely, BVf and VSI values in the normal brain parts exposed to cross-fired arrays, remained unchanged during the same period. These data persuasively support the existence of a preferential damaging effect of MRT on tumor vessels. During the second week after treatment, tumor necrosis can be associated with the delayed decrease in TBVf and VSI.

The use of 50-μm-wide microbeams significantly improved the MSTs for rats with 9LGS in our laboratory (15, 17), notably in this study. This particularly radioresistant tumor requires high radiation dose deposition for palliation or even ablation; a 40-Gy radiosurgical dose controlled only 50% of 9LGS (19). Tumor responses to MRT on $D_{55}T_{45}$ in our study were markedly heterogeneous. Indeed, two of five rats did not exhibit tumors, two animals showed

well-delimited small tumors, and 1 rat had a large tumor invading the whole hemisphere. The cause for these different responses is not understood, but these five rats displayed a common change in MRI, a cerebral edema in parts of the ipsilateral hemisphere exposed to both intersecting arrays. These results were supported by demonstration of infiltrates of monocytes/macrophages (Supplement 1, Fig. e1) and of a strong disorganization and remodeling of the normal vascular network at this site. Normal vessels appeared tortuous and larger, an observation consistent with the significant increase in VSI at $D_{55}T_{45}$ (+9.8%). Thin matricial entities, probably not perfused, were commonly observed. RECA-1 labeling was inhomogeneous.

A gradual increase in VEGF expression was detected in tumoral and normal tissues. However, the kinetics and the amount of the protein produced seemed to depend on the radiation dose (exposure to uni- or bidirectional irradiation) and the status of the tissue (normal or tumoral). VEGF, secreted, *e.g.*, in ischemia, stroke, and after irradiation (20, 21), is commonly induced in presence of hypoxia; changes in tumoral and normal brain oxygen saturation after MRT should thus be evaluated. VEGF in the ipsilateral hemisphere was detectable from the second day after MRT and reached levels comparable to those measured in nonirradiated tumors. Thus, VEGF is implied in cerebral response in the early phase after MRT, but its role is not defined. The overexpression of VEGF after MRT could have increased blood vessel permeability and led to severe brain edema. Because the size of the tumors did not change significantly between $D_{25}T_{15}$ and $D_{55}T_{45}$, we assume that MRT-induced brain edema in the cross-fired regions was the main cause of animal deaths in our study. These qualitative findings are consistent with observations (16) that major histopathologic brain and vascular damage was confined to MRT beam-crossing regions, whereas only minor damage was apparent in zones of the brain irradiated unidirectionally (16). A comprehensive and detailed quantitative brain damage index for our study was not established. However, the histopathologic findings were comparable, despite the different irradiation modalities.

Cross-fired MRT, particularly efficient for tumor control, may require corticosteroid injections (22) to control ensuing brain edema. Furthermore, recovery from radiation injury may be influenced by growth factors involved in cell renewal and differentiation of neural tissue, *e.g.*, by VEGF. Thus, brief therapy with VEGF can prevent or delay radiation myelopathy after spinal cord injury in rats (23). Experimentally, inhibition of VEGF may increase local tumor control after irradiation, possibly by preventing tumor angiogenesis (21).

The preferential effect of MRT on tumor vasculature may lead to further improvements. Most important, the tumor targeting for MRT used preclinically must be improved and adapted to clinical standards. Irradiation fields must be limited to the tumor; image-guided, non-coplanar irradiation methods that limit normal tissue damage should be adopted (15, 24).

REFERENCES

1. Jain RK, di Tomaso E, Duda DG, *et al*. Angiogenesis in brain tumours. *Nat Rev Neurosci* 2007;8:610–622.
2. Slatkin DN, Spanne P, Dilmanian FA, *et al*. Subacute neuropathological effects of microplanar beams of x-rays from a synchrotron wiggler. *Proc Natl Acad Sci U S A* 1995;92: 8783–8787.
3. Bräuer-Krisch E, Serduc R, Siegbahn EA, *et al*. Effects of pulsed, spatially fractionated, microscopic synchrotron X-ray beams on normal and tumoral brain tissue. *Mutat Res* 2010; 704:160–166.
4. Laissue JA, Blattmann H, Wagner HP, *et al*. Prospects for microbeam radiation therapy of brain tumours in children to reduce neurological sequelae. *Dev Med Child Neurol* 2007;49:577–581.
5. Dilmanian FA, Button TM, Le Duc G, *et al*. Response of rat intracranial 9L gliosarcoma to microbeam radiation therapy. *Neuro-oncol* 2002;4:26–38.
6. Serduc R, van de Looij Y, Francony G, *et al*. Characterization and quantification of cerebral edema induced by synchrotron x-ray microbeam radiation therapy. *Phys Med Biol* 2008;53: 1153–1166.
7. Serduc R, Vérant P, Vial JC, *et al*. In vivo two-photon microscopy study of short-term effects of microbeam irradiation on normal mouse brain microvasculature. *Int J Radiat Oncol Biol Phys* 2006;64:1519–1527.
8. Van der Sanden B, Bräuer-Krisch E, Siegbahn EA, *et al*. Tolerance of arteries to microplanar x-ray beams. *Int J Radiat Oncol Biol Phys*. 2010;1545–1552.
9. Serduc R, Christen T, Laissue J, *et al*. Brain tumor vessel response to synchrotron microbeam radiation therapy: A short-term in vivo study. *Phys Med Biol* 2008;53:3609–3622.
10. Serduc R, Bouchet A, Brauer-Krisch E, *et al*. Synchrotron microbeam radiation therapy for rat brain tumor palliation-influence of the microbeam width at constant valley dose. *Phys Med Biol* 2009;54:6711–6724.
11. Bräuer-Krisch E, Requardt H, Brochard T, *et al*. New technology enables precision multislit collimators for microbeam radiation therapy. *Rev Sci Instrum* 2009;80:074301
12. Siegbahn EA, Stepanek J, Bräuer-Krisch E, *et al*. Determination of dosimetrical quantities used in microbeam radiation therapy (MRT) with Monte Carlo simulations. *Med Phys* 2006;33: 3248–3259.
13. Troprés I, Grimault S, Vaeth A, *et al*. Vessel size imaging. *Magn Reson Med* 2001;45:397–408.
14. Troprés I, Lamalle L, Péoc M, *et al*. In vivo assessment of tumoral angiogenesis. *Magn Reson Med* 2004;51:533–541.
15. Serduc R, Bräuer-Krisch E, Bouchet A, *et al*. First trial of spatial and temporal fractionations of the delivered dose using synchrotron microbeam radiation therapy. *J Synchrotron Radiat* 2009; 16:587–590.
16. Laissue JA, Geiser G, Spanne PO, *et al*. Neuropathology of ablation of rat gliosarcomas and contiguous brain tissues using a microplanar beam of synchrotron-wiggler-generated X rays. *Int J Cancer* 1998;78:654–660.
17. Serduc R, Bouchet A, Bräuer-Krisch E, *et al*. Synchrotron microbeam radiation therapy for rat brain tumor palliation-influence of the microbeam width at constant valley dose. *Phys Med Biol* 2009;54:6711–6724.
18. Maniotis AJ, Folberg R, Hess A, *et al*. Vascular channel formation by human melanoma cells in vivo and in vitro: Vasculogenic mimicry. *Amer J Pathol* 1999;155:739–752.

19. Kim JH, Khil MS, Kolozsvary A, *et al*. Fractionated radiosurgery for 9L gliosarcoma in the rat brain. *Int J Radiat Oncol Biol Phys* 1999;45:1035–1040.
20. Kim JH, Chung YG, Kim CY, *et al*. Upregulation of VEGF and FGF2 in normal rat brain after experimental intraoperative radiation therapy. *J Korean Med Sci* 2004;19:879–886.
21. Verhoeff JJ, Stalpers LJ, Claes A, *et al*. Tumour control by whole brain irradiation of anti-VEGF-treated mice bearing intracerebral glioma. *Eur J Cancer*.
22. Piette C, Munaut C, Foidart JM, *et al*. Treating gliomas with glucocorticoids: From bedside to bench. *Acta Neuropathol* 2006;112:651–664.
23. Andratschke NH, Nieder C, Price RE, *et al*. Potential role of growth factors in diminishing radiation therapy neural tissue injury. *Semin Oncol* 2005;32:S67–70.
24. Serduc R, Bräuer-Krisch E, Siegbahn EA, *et al*. High-precision radiosurgical dose delivery by interlaced microbeam arrays of high-flux low-energy synchrotron X-rays. *PLoS One* 2010;5:e9028.

Références bibliographiques

Altafaj, X., W. Cheng, et al. (2005). "Maurocalcine and domain A of the II-III loop of the dihydropyridine receptor Cav 1.1 subunit share common binding sites on the skeletal ryanodine receptor." J Biol Chem **280**(6): 4013-4016.

Alves, I. D., N. Goasdoue, et al. (2008). "Membrane interaction and perturbation mechanisms induced by two cationic cell penetrating peptides with distinct charge distribution." Biochim Biophys Acta **1780**(7-8): 948-959.

Alves, I. D., C. Y. Jiao, et al. "Cell biology meets biophysics to unveil the different mechanisms of penetratin internalization in cells." Biochim Biophys Acta.

Anderson, R. G. and K. Jacobson (2002). "A role for lipid shells in targeting proteins to caveolae, rafts, and other lipid domains." Science **296**(5574): 1821-1825.

Aoshiba, K., N. Yokohori, et al. (2003). "Alveolar wall apoptosis causes lung destruction and emphysematous changes." Am J Respir Cell Mol Biol **28**(5): 555-562.

Aroui, S. (2009). "Maurocalcine as a non toxic drug carrier overcomes doxorubicin resistance in the cancer cell line MDA-MB 231." pharmaceutical research.

Aroui, S., D. Mili, et al. "Doxorubicin coupled to penetratin promotes apoptosis in CHO cells by a mechanism involving c-Jun NH2-terminal kinase." Biochem Biophys Res Commun **396**(4): 908-914.

Aroui, S., N. Ram, et al. (2009). "Maurocalcine as a non toxic drug carrier overcomes doxorubicin resistance in the cancer cell line MDA-MB 231." Pharm Res **26**(4): 836-845.

Arya, S. K., C. Guo, et al. (1985). "Trans-activator gene of human T-lymphotropic virus type III (HTLV-III)." Science **229**(4708): 69-73.

Barany-Wallje, E., J. Gaur, et al. (2007). "Differential membrane perturbation caused by the cell penetrating peptide Tp10 depending on attached cargo." FEBS Lett **581**(13): 2389-2393.

Bates, E., C. Bode, et al. (2008). "Intracoronary KAI-9803 as an adjunct to primary percutaneous coronary intervention for acute ST-segment elevation myocardial infarction." Circulation **117**(7): 886-896.

Beauvais, D. M. and A. C. Rapraeger (2004). "Syndecans in tumor cell adhesion and signaling." Reprod Biol Endocrinol **2**: 3.

Benmerah, A. and C. Lamaze (2002). "Endocytose: chaque voie compte!" medecine/sciences **18**(11): 1126-1136.

Berlose, J. P., O. Convert, et al. (1996). "Conformational and associative behaviours of the third helix of antennapedia homeodomain in membrane-mimetic environments." Eur J Biochem **242**(2): 372-386.

Bhorade, R., R. Weissleder, et al. (2000). "Macrocyclic chelators with paramagnetic cations are internalized into mammalian cells via a HIV-tat derived membrane translocation peptide." Bioconjug Chem **11**(3): 301-305.

Binder, H. and G. Lindblom (2003). "Charge-dependent translocation of the Trojan peptide penetratin across lipid membranes." Biophys J **85**(2): 982-995.

Bjorklund, J., H. Biverstahl, et al. (2006). "Real-time transmembrane translocation of penetratin driven by light-generated proton pumping." Biophys J **91**(4): L29-31.

Boni-Mitake, M., H. Costa, et al. (2006). "Distribution of (125)I-labeled crotamine in mice tissues." Toxicon **48**(5): 550-555.

Brasseur, R. and G. Divita "Happy birthday cell penetrating peptides: Already 20years." Biochim Biophys Acta **1798**(12): 2177-2181.

Breau, W. C., W. J. Atwood, et al. (1992). "Class I major histocompatibility proteins are an essential component of the simian virus 40 receptor." J Virol **66**(4): 2037-2045.

Breukink, E. and B. De Kruijff (1999). "The lantibiotic nisin, a special case or not?" Biochimica et Biophysica Acta: 223-234.

Brooks, H., B. Lebleu, et al. (2005). "Tat peptide-mediated cellular delivery: back to basics." Adv Drug Deliv Rev **57**(4): 559-577.

Cahill, K. (2009). "Simple model of the transduction of cell-penetrating peptides." IET Syst Biol **3**(5): 300-306.

Cai, B., Y. Lin, et al. (2010). "TAT-mediated delivery of neuroglobin protects against focal cerebral ischemia in mice." Exp Neurol **227**(1): 224-231.

Cantelmo, A. R., R. Cammarota, et al. (2010). "Cell delivery of Met docking site peptides inhibit angiogenesis and vascular tumor growth." Oncogene **29**(38): 5286-5298.

Catterall, W. A. (1980). "Neurotoxins that act on voltage-sensitive sodium channels in excitable membranes." Annu Rev Pharmacol Toxicol **20**: 15-43.

Chaubey, B., S. Tripathi, et al. (2005). "A PNA-transportan conjugate targeted to the TAR region of the HIV-1 genome exhibits both antiviral and virucidal properties." Virology **331**(2): 418-428.

Chen, B., Q. Liu, et al. (2008). "Transmembrane delivery of the cell-penetrating peptide conjugated semiconductor quantum dots." Langmuir **24**(20): 11866-11871.

Chen, L., E. Esteve, et al. (2003). "Maurocalcine and peptide A stabilize distinct subconductance states of ryanodine receptor type 1, revealing a proportional gating mechanism." J Biol Chem **278**(18): 16095-16106.

Choi, Y.-S., J. Y. Lee, et al. "The systemic delivery of siRNAs by a cell penetrating peptide, low molecular weight protamine." Biomaterials **In Press, Corrected Proof**.

Choi, Y.-S., J. Y. Lee, et al. "The systemic delivery of siRNAs by a cell penetrating peptide, low molecular weight protamine." Biomaterials **31**(6): 1429-1443.

Christiaens, B., J. Grooten, et al. (2004). "Membrane interaction and cellular internalization of penetratin peptides." Eur J Biochem **271**(6): 1187-1197.

Chugh, A. and F. Eudes (2008). "Cellular uptake of cell-penetrating peptides pVEC and transportan in plants." J Pept Sci **14**(4): 477-481.

Conner, S. D. and S. L. Schmid (2003). "Regulated portals of entry into the cell." Nature **422**(6927): 37-44.

Console, S., C. Marty, et al. (2003). "Antennapedia and HIV transactivator of transcription (TAT) "protein transduction domains" promote endocytosis of high molecular weight cargo upon binding to cell surface glycosaminoglycans." J Biol Chem **278**(37): 35109-35114.

Couchman, J. R. (2003). "Syndecans: proteoglycan regulators of cell-surface microdomains?" Nat Rev Mol Cell Biol **4**(12): 926-937.

Crombez, L., G. Aldrian-Herrada, et al. (2009). "A new potent secondary amphipathic cell-penetrating peptide for siRNA delivery into mammalian cells." Mol Ther **17**(1): 95-103.

Crombez, L., A. Charnet, et al. (2007). "A non-covalent peptide-based strategy for siRNA delivery." Biochem Soc Trans **35**(Pt 1): 44-46.

Crombez, L., M. C. Morris, et al. (2009). "Targeting cyclin B1 through peptide-based delivery of siRNA prevents tumour growth." Nucleic Acids Res **37**(14): 4559-4569.

Damm, E. M., L. Pelkmans, et al. (2005). "Clathrin- and caveolin-1-independent endocytosis: entry of simian virus 40 into cells devoid of caveolae." J Cell Biol **168**(3): 477-488.

Davidson, T. J., S. Harel, et al. (2004). "Highly efficient small interfering RNA delivery to primary mammalian neurons induces MicroRNA-like effects before mRNA degradation." J Neurosci **24**(45): 10040-10046.

Delehanty, J. B., C. E. Bradburne, et al. (2010). "Delivering quantum dot-peptide bioconjugates to the cellular cytosol: escaping from the endolysosomal system." Integr Biol (Camb) **2**(5-6): 265-277.

Derossi, D., S. Calvet, et al. (1996). "Cell internalization of the third helix of the Antennapedia homeodomain is receptor-independent." J Biol Chem **271**(30): 18188-18193.

Derossi, D., A. H. Joliot, et al. (1994). "The third helix of the Antennapedia homeodomain translocates through biological membranes." J Biol Chem **269**(14): 10444-10450.

Deshayes, S., T. Plenat, et al. (2006). "Formation of transmembrane ionic channels of primary amphipathic cell-penetrating peptides. Consequences on the mechanism of cell penetration." Biochim Biophys Acta **1758**(11): 1846-1851.

Desjardins, M. (2003). "ER-mediated phagocytosis: a new membrane for new functions." Nat Rev Immunol **3**(4): 280-291.

Duchardt, F., M. Fotin-Mleczek, et al. (2007). "A comprehensive model for the cellular uptake of cationic cell-penetrating peptides." Traffic **8**(7): 848-866.

Dupont, E., A. Prochiantz, et al. "Penetratin story: an overview." Methods Mol Biol **683**: 21-29.

Dupont, E., A. Prochiantz, et al. (2007). "Identification of a signal peptide for unconventional secretion." J Biol Chem **282**(12): 8994-9000.

Edidin, M. (2001). "Shrinking patches and slippery rafts: scales of domains in the plasma membrane." Trends Cell Biol **11**(12): 492-496.

Ehrenstein, G. and H. Lecar (1977). "Electrically gated ionic channels in lipid bilayers." Q Rev Biophys **10**(1): 1-34.

Elbashir, S. M., J. Harborth, et al. (2001). "Duplexes of 21-nucleotide RNAs mediate RNA interference in cultured mammalian cells." Nature **411**(6836): 494-498.

Endoh, T. and T. Ohtsuki (2009). "Cellular siRNA delivery using cell-penetrating peptides modified for endosomal escape." Adv Drug Deliv Rev **61**(9): 704-709.

Endoh, T., M. Sisido, et al. (2008). "Cellular siRNA delivery mediated by a cell-permeant RNA-binding protein and photoinduced RNA interference." Bioconjug Chem **19**(5): 1017-1024.

Esbjorner, E. K., P. Lincoln, et al. (2007). "Counterion-mediated membrane penetration: cationic cell-penetrating peptides overcome Born energy barrier by ion-pairing with phospholipids." Biochim Biophys Acta **1768**(6): 1550-1558.

Escoubas, P. and G. F. King (2009). "Venomics as a drug discovery platform." Expert Rev Proteomics **6**(3): 221-224.

Esteve, E., K. Mabrouk, et al. (2005). "Transduction of the scorpion toxin maurocalcine into cells. Evidence that the toxin crosses the plasma membrane." J Biol Chem **280**(13): 12833-12839.

Esteve, E., S. Smida-Rezgui, et al. (2003). "Critical amino acid residues determine the binding affinity and the Ca2+ release efficacy of maurocalcine in skeletal muscle cells." J Biol Chem **278**(39): 37822-37831.

Evangelou, A., C. Zikos, et al. (2009). "In vitro binding and in vivo biodistribution studies of the neuroprotective peptide humanin using [125I]humanin derivatives." Peptides **30**(12): 2409-2417.

Fajloun, Z., R. Kharrat, et al. (2000). "Chemical synthesis and characterization of maurocalcine, a scorpion toxin that activates Ca(2+) release channel/ryanodine receptors." FEBS Lett **469**(2-3): 179-185.

Fawell, S., J. Seery, et al. (1994). "Tat-mediated delivery of heterologous proteins into cells." Proc Natl Acad Sci U S A **91**(2): 664-668.

Fischer, R., M. Fotin-Mleczek, et al. (2005). "Break on through to the other side-biophysics and cell biology shed light on cell-penetrating peptides." Chembiochem **6**(12): 2126-2142.

Fischer, R., K. Kohler, et al. (2004). "A stepwise dissection of the intracellular fate of cationic cell-penetrating peptides." J Biol Chem **279**(13): 12625-12635.

Fittipaldi, A., A. Ferrari, et al. (2003). "Cell membrane lipid rafts mediate caveolar endocytosis of HIV-1 Tat fusion proteins." J Biol Chem **278**(36): 34141-34149.

Fossat, P., E. Dobremez, et al. (2010). "Knockdown of L calcium channel subtypes: differential effects in neuropathic pain." J Neurosci **30**(3): 1073-1085.

Fragneto, G., E. Bellet-Amalric, et al. (2000). "Neutron and X-Ray reflectivity studies at solid-liquid interfaces: the interaction of a peptide with model membranes." Physica 501-502.

Fragneto, G., F. Graner, et al. (2000). "Interaction of the Third Helix of Antennapedia Homeodomain with a Deposited Phospholipid Bilayer: A Neutron Reflectivity Structural Study." Langmuir **16**: 4581-4588.

Frost, S. C. and M. D. Lane (1985). "Evidence for the involvement of vicinal sulfhydryl groups in insulin-activated hexose transport by 3T3-L1 adipocytes." J Biol Chem **260**(5): 2646-2652.

Fu, S. W., L. Chen, et al. (2011). "miRNA Biomarkers in Breast Cancer Detection and Management." J Cancer **2**: 116-122.

Galbiati, F., B. Razani, et al. (2001). "Emerging themes in lipid rafts and caveolae." Cell **106**(4): 403-411.

Gammon, S. T., V. M. Villalobos, et al. (2003). "Quantitative analysis of permeation peptide complexes labeled with Technetium-99m: chiral and sequence-specific effects on net cell uptake." Bioconjug Chem **14**(2): 368-376.

Garibotto, F. M., A. D. Garro, et al. "Penetratin analogues acting as antifungal agents." Eur J Med Chem **46**(1): 370-377.

Gerbal-Chaloin, S., C. Gondeau, et al. (2007). "First step of the cell-penetrating peptide mechanism involves Rac1 GTPase-dependent actin-network remodelling." Biol Cell **99**(4): 223-238.

Ghibaudi, E., B. Boscolo, et al. (2005). "The interaction of the cell-penetrating peptide penetratin with heparin, heparansulfates and phospholipid vesicles investigated by ESR spectroscopy." J Pept Sci **11**(7): 401-409.

Gilquin, B., M. Bourgoin, et al. (2003). "Motions and structural variability within toxins: implication for their use as scaffolds for protein engineering." Protein Sci **12**(2): 266-277.

Glebov, O. O., N. A. Bright, et al. (2006). "Flotillin-1 defines a clathrin-independent endocytic pathway in mammalian cells." Nat Cell Biol **8**(1): 46-54.

Gold, S., P. Monaghan, et al. "A clathrin independent macropinocytosis-like entry mechanism used by bluetongue virus-1 during infection of BHK cells." PLoS One **5**(6): e11360.

Goun, E. A., T. H. Pillow, et al. (2006). "Molecular transporters: synthesis of oligoguanidinium transporters and their application to drug delivery and real-time imaging." Chembiochem **7**(10): 1497-1515.

Gump, J. M., R. K. June, et al. "Revised role of glycosaminoglycans in TAT protein transduction domain-mediated cellular transduction." J Biol Chem **285**(2): 1500-1507.

Gwee, M. C., S. Nirthanan, et al. (2002). "Autonomic effects of some scorpion venoms and toxins." Clin Exp Pharmacol Physiol **29**(9): 795-801.

Hallbrink, M., A. Floren, et al. (2001). "Cargo delivery kinetics of cell-penetrating peptides." Biochim Biophys Acta **1515**(2): 101-109.

Hampton, M. B., A. J. Kettle, et al. (1998). "Inside the neutrophil phagosome: oxidants, myeloperoxidase, and bacterial killing." Blood **92**(9): 3007-3017.

Hancock, R. E. (1997). "Peptide antibiotics." Lancet **349**(9049): 418-422.

Hancock, R. E. and A. Patrzykat (2002). "Clinical development of cationic antimicrobial peptides: from natural to novel antibiotics." Curr Drug Targets Infect Disord **2**(1): 79-83.

Hansen, C. G., N. A. Bright, et al. (2009). "SDPR induces membrane curvature and functions in the formation of caveolae." Nat Cell Biol **11**(7): 807-814.

Hara, T., Y. Mitani, et al. (2001). "Heterodimer formation between the antimicrobial peptides magainin 2 and PGLa in lipid bilayers: a cross-linking study." Biochemistry **40**(41): 12395-12399.

Heitz, F., M. C. Morris, et al. (2009). "Twenty years of cell-penetrating peptides: from molecular mechanisms to therapeutics." Br J Pharmacol **157**(2): 195-206.

Hemler, M. E. (2005). "Tetraspanin functions and associated microdomains." Nat Rev Mol Cell Biol **6**(10): 801-811.

Henriques, S. T. and M. A. Castanho (2004). "Consequences of nonlytic membrane perturbation to the translocation of the cell penetrating peptide pep-1 in lipidic vesicles." Biochemistry **43**(30): 9716-9724.

Herbig, M. E., K. Weller, et al. (2005). "Membrane surface-associated helices promote lipid interactions and cellular uptake of human calcitonin-derived cell penetrating peptides." Biophys J **89**(6): 4056-4066.

Herreros, J., T. Ng, et al. (2001). "Lipid rafts act as specialized domains for tetanus toxin binding and internalization into neurons." Mol Biol Cell **12**(10): 2947-2960.

Heuser, J. E. and R. G. Anderson (1989). "Hypertonic media inhibit receptor-mediated endocytosis by blocking clathrin-coated pit formation." J Cell Biol **108**(2): 389-400.

Hill, M. M., M. Bastiani, et al. (2008). "PTRF-Cavin, a conserved cytoplasmic protein required for caveola formation and function." Cell **132**(1): 113-124.

Holm, T., S. E. Andaloussi, et al. (2011). "Comparison of CPP uptake methods." Methods Mol Biol **683**: 207-217.

Inagaki, K., L. Chen, et al. (2003). "Inhibition of delta-protein kinase C protects against reperfusion injury of the ischemic heart in vivo." Circulation **108**(19): 2304-2307.

Jayagopal, A., Y. R. Su, et al. (2009). "Quantum dot mediated imaging of atherosclerosis." Nanotechnology **20**(16): 165102.

Jiao, C. Y., D. Delaroche, et al. (2009). "Translocation and endocytosis for cell-penetrating peptide internalization." J Biol Chem **284**(49): 33957-33965.

Johnson, J. L., B. C. Lowell, et al. "TAT-Mediated Delivery of a DNA Repair Enzyme to Skin Cells Rapidly Initiates Repair of UV-Induced DNA Damage." J Invest Dermatol.

Johnson, J. L., B. C. Lowell, et al. (2010). "TAT-Mediated Delivery of a DNA Repair Enzyme to Skin Cells Rapidly Initiates Repair of UV-Induced DNA Damage." J Invest Dermatol **131**(3): 753-761.

Johnson, R. M., S. D. Harrison, et al. (2011). "Therapeutic applications of cell-penetrating peptides." Methods Mol Biol **683**: 535-551.

Joliot, A., C. Pernelle, et al. (1991). "Antennapedia homeobox peptide regulates neural morphogenesis." Proc Natl Acad Sci U S A **88**(5): 1864-1868.

Josephson, L., C. H. Tung, et al. (1999). "High-efficiency intracellular magnetic labeling with novel superparamagnetic-Tat peptide conjugates." Bioconjug Chem **10**(2): 186-191.

Kanjhan, R. and M. C. Bellingham "Penetratin Peptide Potentiates Endogenous Calcium-Activated Chloride Currents in Xenopus oocytes." J Membr Biol.

Kaplan, I. M., J. S. Wadia, et al. (2005). "Cationic TAT peptide transduction domain enters cells by macropinocytosis." J Control Release **102**(1): 247-253.

Kerkis, A., I. Kerkis, et al. (2004). "Crotamine is a novel cell-penetrating protein from the venom of rattlesnake Crotalus durissus terrificus." FASEB J **18**(12): 1407-1409.

Kerkis, I., S. Silva Fde, et al. (2010). "Biological versatility of crotamine - a cationic peptide from the venom of a South American rattlesnake." Expert Opin Investig Drugs **19**(12): 1515-1525.

Kerr, M. C. and R. D. Teasdale (2009). "Defining macropinocytosis." Traffic **10**(4): 364-371.

Kersemans, V., K. Kersemans, et al. (2008). "Cell penetrating peptides for in vivo molecular imaging applications." Curr Pharm Des **14**(24): 2415-2447.

Khafagy el, S., M. Morishita, et al. (2009). "Efficiency of cell-penetrating peptides on the nasal and intestinal absorption of therapeutic peptides and proteins." Int J Pharm **381**(1): 49-55.

Khafagy el, S., M. Morishita, et al. "The role of intermolecular interactions with penetratin and its analogue on the enhancement of absorption of nasal therapeutic peptides." Int J Pharm **388**(1-2): 209-212.

Kilk, K., A. Elmquist, et al. (2004). "Targeting of antisense PNA oligomers to human galanin receptor type 1 mRNA." Neuropeptides **38**(5): 316-324.

Kim, D. W., H. J. Jeong, et al. (2009). "Transduced human PEP-1-catalase fusion protein attenuates ischemic neuronal damage." Free Radic Biol Med **47**(7): 941-952.

Kim, M. J., D. W. Kim, et al. "Protective effects of transduced PEP-1-Frataxin protein on oxidative stress-induced neuronal cell death." J Neurol Sci **298**(1-2): 64-69.

Kinchen, J. M. and K. S. Ravichandran (2008). "Phagosome maturation: going through the acid test." Nat Rev Mol Cell Biol **9**(10): 781-795.

Kiss, A. L. and E. Botos (2009). "Endocytosis via caveolae: alternative pathway with distinct cellular compartments to avoid lysosomal degradation?" J Cell Mol Med **13**(7): 1228-1237.

Konate, K., L. Crombez, et al. "Insight into the cellular uptake mechanism of a secondary amphipathic cell-penetrating peptide for siRNA delivery." Biochemistry **49**(16): 3393-3402.

Kumari, S., S. Mg, et al. (2010). "Endocytosis unplugged: multiple ways to enter the cell." Cell Res **20**(3): 256-275.

Lajoie, P. and I. R. Nabi (2010). "Lipid rafts, caveolae, and their endocytosis." Int Rev Cell Mol Biol **282**: 135-163.

Lamaziere, A., F. Burlina, et al. (2007). "Non-metabolic membrane tubulation and permeability induced by bioactive peptides." PLoS One **2**(2): e201.

Lamaziere, A., O. Maniti, et al. "Lipid domain separation, bilayer thickening and pearling induced by the cell penetrating peptide penetratin." Biochim Biophys Acta **1798**(12): 2223-2230.

Le Roux, I., A. H. Joliot, et al. (1993). "Neurotrophic activity of the Antennapedia homeodomain depends on its specific DNA-binding properties." Proc Natl Acad Sci U S A **90**(19): 9120-9124.

Lecomte, C., J. M. Sabatier, et al. (1998). "Synthetic peptides as tools to investigate the structure and pharmacology of potassium channel-acting short-chain scorpion toxins." Biochimie **80**(2): 151-154.

Legros, C., B. Ceard, et al. (1998). "Evidence for a new class of scorpion toxins active against K+ channels." FEBS Lett **431**(3): 375-380.

Letoha, T., S. Gaal, et al. (2003). "Membrane translocation of penetratin and its derivatives in different cell lines." J Mol Recognit **16**(5): 272-279.

Liang, J. F. and V. C. Yang (2005). "Synthesis of doxorubicin-peptide conjugate with multidrug resistant tumor cell killing activity." Bioorg Med Chem Lett **15**(22): 5071-5075.

Lindgren, M., K. Rosenthal-Aizman, et al. (2006). "Overcoming methotrexate resistance in breast cancer tumour cells by the use of a new cell-penetrating peptide." Biochem Pharmacol **71**(4): 416-425.

Lindgren, M. E., M. M. Hallbrink, et al. (2004). "Passage of cell-penetrating peptides across a human epithelial cell layer in vitro." Biochem J **377**(Pt 1): 69-76.

Liu, X. J., J. R. Gingrich, et al. (2008). "Treatment of inflammatory and neuropathic pain by uncoupling Src from the NMDA receptor complex." Nat Med **14**(12): 1325-1332.

Lundberg, P., S. El-Andaloussi, et al. (2007). "Delivery of short interfering RNA using endosomolytic cell-penetrating peptides." FASEB J **21**(11): 2664-2671.

Lundberg, P. and U. Langel (2003). "A brief introduction to cell-penetrating peptides." J Mol Recognit **16**(5): 227-233.

Lundin, P., S. E. Andaloussi, et al. (2011). "Toxicity methods for CPPs." Methods Mol Biol **683**: 195-205.

Mabrouk, K., N. Ram, et al. (2007). "Critical amino acid residues of maurocalcine involved in pharmacology, lipid interaction and cell penetration." Biochim Biophys Acta **1768**(10): 2528-2540.

Magzoub, M., L. E. Eriksson, et al. (2003). "Comparison of the interaction, positioning, structure induction and membrane perturbation of cell-penetrating peptides and non-translocating variants with phospholipid vesicles." Biophys Chem **103**(3): 271-288.

Magzoub, M., K. Oglecka, et al. (2005). "Membrane perturbation effects of peptides derived from the N-termini of unprocessed prion proteins." Biochim Biophys Acta **1716**(2): 126-136.

Magzoub, M., A. Pramanik, et al. (2005). "Modeling the endosomal escape of cell-penetrating peptides: transmembrane pH gradient driven translocation across phospholipid bilayers." Biochemistry **44**(45): 14890-14897.

Maiolo, J. R., M. Ferrer, et al. (2005). "Effects of cargo molecules on the cellular uptake of arginine-rich cell-penetrating peptides." Biochim Biophys Acta **1712**(2): 161-172.

Mamelak, A. N. and D. B. Jacoby (2007). "Targeted delivery of antitumoral therapy to glioma and other malignancies with synthetic chlorotoxin (TM-601)." Expert Opin Drug Deliv **4**(2): 175-186.

Martin-Eauclaire, M.-F. and P.-E. Bougis (2007). "Les toxines des venins de scorpion." Biofutur **280**: 35-39.

Martin, I., M. Teixido, et al. (2011). "Design, Synthesis and Characterization of a New Anionic Cell-Penetrating Peptide: SAP(E)." Chembiochem **12**(6): 896-903.

Masman, M. F., A. M. Rodriguez, et al. (2009). "Penetratin and derivatives acting as antifungal agents." Eur J Med Chem **44**(1): 212-228.

Meade, B. R. and S. F. Dowdy (2007). "Exogenous siRNA delivery using peptide transduction domains/cell penetrating peptides." Adv Drug Deliv Rev **59**(2-3): 134-140.

Mebs, D. (2002). "Scorpions and snakes, such as cobras, mambas and vipers made the African continent famous for venomous animals." Bull Soc Pathol Exot **95**(3): 131.

Medarova, Z., W. Pham, et al. (2007). "In vivo imaging of siRNA delivery and silencing in tumors." Nat Med **13**(3): 372-377.

Mercer, J. and A. Helenius (2009). "Virus entry by macropinocytosis." Nat Cell Biol **11**(5): 510-520.

Mishra, R., W. Su, et al. (2009). "Cell-Penetrating Peptides and Peptide Nucleic Acid-Coupled MRI Contrast Agents: Evaluation of Cellular Delivery and Target Binding." Bioconjug Chem.

Morris, M. C., J. Depollier, et al. (2001). "A peptide carrier for the delivery of biologically active proteins into mammalian cells." Nat Biotechnol **19**(12): 1173-1176.

Morris, M. C., P. Vidal, et al. (1997). "A new peptide vector for efficient delivery of oligonucleotides into mammalian cells." Nucleic Acids Res **25**(14): 2730-2736.

Mosbah, A., R. Kharrat, et al. (2000). "A new fold in the scorpion toxin family, associated with an activity on a ryanodine-sensitive calcium channel." Proteins **40**(3): 436-442.

Moschos, S. A., A. E. Williams, et al. (2007). "Cell-penetrating-peptide-mediated siRNA lung delivery." Biochem Soc Trans **35**(Pt 4): 807-810.

Mueller, J., I. Kretzschmar, et al. (2008). "Comparison of cellular uptake using 22 CPPs in 4 different cell lines." Bioconjug Chem **19**(12): 2363-2374.

Muratovska, A. and M. R. Eccles (2004). "Conjugate for efficient delivery of short interfering RNA (siRNA) into mammalian cells." FEBS Lett **558**(1-3): 63-68.

Murriel, C. L. and S. F. Dowdy (2006). "Influence of protein transduction domains on intracellular delivery of macromolecules." Expert Opin Drug Deliv **3**(6): 739-746.

Nakase, I., M. Niwa, et al. (2004). "Cellular uptake of arginine-rich peptides: roles for macropinocytosis and actin rearrangement." Mol Ther **10**(6): 1011-1022.

Nakase, I., A. Tadokoro, et al. (2007). "Interaction of arginine-rich peptides with membrane-associated proteoglycans is crucial for induction of actin organization and macropinocytosis." Biochemistry **46**(2): 492-501.

Nascimento, F. D., M. A. Hayashi, et al. (2007). "Crotamine mediates gene delivery into cells through the binding to heparan sulfate proteoglycans." J Biol Chem **282**(29): 21349-21360.

Nguyen, Q. T., E. S. Olson, et al. "Surgery with molecular fluorescence imaging using activatable cell-penetrating peptides decreases residual cancer and improves survival." Proc Natl Acad Sci U S A **107**(9): 4317-4322.

Niu, R., P. Zhao, et al. "Preparation, characterization, and antitumor activity of paclitaxel-loaded folic acid modified and TAT peptide conjugated PEGylated polymeric liposomes." J Drug Target.

Oh, S. Y., Y. Ju, et al. (2010). "PNA-based antisense oligonucleotides for micrornas inhibition in the absence of a transfection reagent." Oligonucleotides **20**(5): 225-230.

Olson, E. S., T. Jiang, et al. "Activatable cell penetrating peptides linked to nanoparticles as dual probes for in vivo fluorescence and MR imaging of proteases." Proc Natl Acad Sci U S A **107**(9): 4311-4316.

Padari, K., P. Saalik, et al. (2005). "Cell transduction pathways of transportans." Bioconjug Chem **16**(6): 1399-1410.

Palm-Apergi, C., A. Lorents, et al. (2009). "The membrane repair response masks membrane disturbances caused by cell-penetrating peptide uptake." FASEB J **23**(1): 214-223.

Palm, C., M. Jayamanne, et al. (2007). "Peptide degradation is a critical determinant for cell-penetrating peptide uptake." Biochim Biophys Acta **1768**(7): 1769-1776.

Parkar, N. S., B. S. Akpa, et al. (2009). "Vesicle formation and endocytosis: function, machinery, mechanisms, and modeling." Antioxid Redox Signal **11**(6): 1301-1312.

Pelkmans, L. and A. Helenius (2002). "Endocytosis via caveolae." Traffic **3**(5): 311-320.

Pelkmans, L., J. Kartenbeck, et al. (2001). "Caveolar endocytosis of simian virus 40 reveals a new two-step vesicular-transport pathway to the ER." Nat Cell Biol **3**(5): 473-483.

Perea, S. E., O. Reyes, et al. (2004). "Antitumor effect of a novel proapoptotic peptide that impairs the phosphorylation by the protein kinase 2 (casein kinase 2)." Cancer Res **64**(19): 7127-7129.

Petricevich, V. L. (2010). "Scorpion venom and the inflammatory response." Mediators Inflamm **2010**: 903295.

Poillot, C., K. Dridi, et al. "D-maurocalcine, a pharmacologically-inert efficient cell penetrating peptide analogue." J Biol Chem.

Pooga, M., M. Hallbrink, et al. (1998). "Cell penetration by transportan." FASEB J **12**(1): 67-77.

Pooga, M., C. Kut, et al. (2001). "Cellular translocation of proteins by transportan." FASEB J **15**(8): 1451-1453.

Potocky, T. B., A. K. Menon, et al. (2003). "Cytoplasmic and nuclear delivery of a TAT-derived peptide and a beta-peptide after endocytic uptake into HeLa cells." J Biol Chem **278**(50): 50188-50194.

Poungpair, O., A. Pootong, et al. (2010). "A human single chain transbody specific to matrix protein (M1) interferes with the replication of influenza A virus." Bioconjug Chem **21**(7): 1134-1141.

Pujals, S., J. Fernandez-Carneado, et al. (2008). "D-SAP: a new, noncytotoxic, and fully protease resistant cell-penetrating peptide." ChemMedChem **3**(2): 296-301.

Pust, S., A. B. Dyve, et al. (2010). "Interplay between toxin transport and flotillin localization." PLoS One **5**(1): e8844.

Qian, Y. Q., M. Billeter, et al. (1989). "The structure of the Antennapedia homeodomain determined by NMR spectroscopy in solution: comparison with prokaryotic repressors." Cell **59**(3): 573-580.

Radis-Baptista, G., B. G. de la Torre, et al. (2008). "A novel cell-penetrating peptide sequence derived by structural minimization of a snake toxin exhibits preferential nucleolar localization." J Med Chem **51**(22): 7041-7044.

Rajendran, L., S. Le Lay, et al. (2007). "Raft association and lipid droplet targeting of flotillins are independent of caveolin." Biol Chem **388**(3): 307-314.

Ram, N., S. Aroui, et al. (2008). "Direct peptide interaction with surface glycosaminoglycans contributes to the cell penetration of maurocalcine." J Biol Chem **283**(35): 24274-24284.

Ram, N., N. Weiss, et al. (2008). "Design of a disulfide-less, pharmacologically inert, and chemically competent analog of maurocalcine for the efficient transport of impermeant compounds into cells." J Biol Chem **283**(40): 27048-27056.

Rao, K. S., M. K. Reddy, et al. (2008). "TAT-conjugated nanoparticles for the CNS delivery of anti-HIV drugs." Biomaterials **29**(33): 4429-4438.

Rennert, R., C. Wespe, et al. (2006). "Developing novel hCT derived cell-penetrating peptides with improved metabolic stability." Biochim Biophys Acta **1758**(3): 347-354.

Richard, J. P., K. Melikov, et al. (2005). "Cellular uptake of unconjugated TAT peptide involves clathrin-dependent endocytosis and heparan sulfate receptors." J Biol Chem **280**(15): 15300-15306.

Rothberg, K. G., Y. S. Ying, et al. (1990). "The glycophospholipid-linked folate receptor internalizes folate without entering the clathrin-coated pit endocytic pathway." J Cell Biol **110**(3): 637-649.

Ruan, G., A. Agrawal, et al. (2007). "Imaging and tracking of tat peptide-conjugated quantum dots in living cells: new insights into nanoparticle uptake, intracellular transport, and vesicle shedding." J Am Chem Soc **129**(47): 14759-14766.

Rusnati, M., D. Coltrini, et al. (1997). "Interaction of HIV-1 Tat protein with heparin. Role of the backbone structure, sulfation, and size." J Biol Chem **272**(17): 11313-11320.

Rusnati, M., G. Tulipano, et al. (1999). "Multiple interactions of HIV-I Tat protein with size-defined heparin oligosaccharides." J Biol Chem **274**(40): 28198-28205.

Saalik, P., A. Elmquist, et al. (2004). "Protein cargo delivery properties of cell-penetrating peptides. A comparative study." Bioconjug Chem **15**(6): 1246-1253.

Saar, K., M. Lindgren, et al. (2005). "Cell-penetrating peptides: a comparative membrane toxicity study." Anal Biochem **345**(1): 55-65.

Sahay, G., D. Y. Alakhova, et al. (2010). "Endocytosis of nanomedicines." J Control Release **145**(3): 182-195.

Said Hassane, F., A. F. Saleh, et al. "Cell penetrating peptides: overview and applications to the delivery of oligonucleotides." Cell Mol Life Sci **67**(5): 715-726.

Sakaue, Y., J. Kim, et al. (2010). "Effects of TAT-conjugated platinum nanoparticles on lifespan of mitochondrial electron transport complex I-deficient Caenorhabditis elegans, nuo-1." Int J Nanomedicine **5**: 687-695.

Santra, S., H. Yang, et al. (2005). "Rapid and effective labeling of brain tissue using TAT-conjugated CdS:Mn/ZnS quantum dots." Chem Commun (Camb)(25): 3144-3146.

Sato, A. K., M. Viswanathan, et al. (2006). "Therapeutic peptides: technological advances driving peptides into development." Curr Opin Biotechnol **17**(6): 638-642.

Sawant, R. R. and V. P. Torchilin (2009). "Enhanced cytotoxicity of TATp-bearing paclitaxel-loaded micelles in vitro and in vivo." Int J Pharm **374**(1-2): 114-118.

Sawicka, M., M. Kalinowska, et al. (2004). "A review of selected anti-tumour therapeutic agents and reasons for multidrug resistance occurrence." J Pharm Pharmacol **56**(9): 1067-1081.

Schnitzer, J. E., P. Oh, et al. (1994). "Filipin-sensitive caveolae-mediated transport in endothelium: reduced transcytosis, scavenger endocytosis, and capillary permeability of select macromolecules." J Cell Biol **127**(5): 1217-1232.

Segal, A. W. (2005). "How neutrophils kill microbes." Annu Rev Immunol **23**: 197-223.

Shai, Y. and Z. Oren (2001). "From "carpet" mechanism to de-novo designed diastereomeric cell-selective antimicrobial peptides." Peptides **22**(10): 1629-1641.

Shaw, P. A., I. R. Catchpole, et al. (2008). "Comparison of protein transduction domains in mediating cell delivery of a secreted CRE protein." Biochemistry **47**(4): 1157-1166.

Sherr, C. J. and F. McCormick (2002). "The RB and p53 pathways in cancer." Cancer Cell **2**(2): 103-112.

Shogomori, H. and A. H. Futerman (2001). "Cholera toxin is found in detergent-insoluble rafts/domains at the cell surface of hippocampal neurons but is internalized via a raft-independent mechanism." J Biol Chem **276**(12): 9182-9188.

Sieczkarski, S. B. and G. R. Whittaker (2002). "Dissecting virus entry via endocytosis." J Gen Virol **83**(Pt 7): 1535-1545.

Silva, E., H. W. Au-Yeung, et al. (2007). "Requirement for a Drosophila E3-ubiquitin ligase in phagocytosis of apoptotic cells." Immunity **27**(4): 585-596.

Simeoni, F., M. C. Morris, et al. (2003). "Insight into the mechanism of the peptide-based gene delivery system MPG: implications for delivery of siRNA into mammalian cells." Nucleic Acids Res **31**(11): 2717-2724.

Simeoni, F., M. C. Morris, et al. (2005). "Peptide-based strategy for siRNA delivery into mammalian cells." Methods Mol Biol **309**: 251-260.

Snyder, E. L., B. R. Meade, et al. (2004). "Treatment of terminal peritoneal carcinomatosis by a transducible p53-activating peptide." PLoS Biol **2**(2): E36.

Sodroski, J., R. Patarca, et al. (1985). "Location of the trans-activating region on the genome of human T-cell lymphotropic virus type III." Science **229**(4708): 74-77.

Spoden, G., K. Freitag, et al. (2008). "Clathrin- and caveolin-independent entry of human papillomavirus type 16--involvement of tetraspanin-enriched microdomains (TEMs)." PLoS One **3**(10): e3313.

Srinivasan, K. N., P. Gopalakrishnakone, et al. (2002). "SCORPION, a molecular database of scorpion toxins." Toxicon **40**(1): 23-31.

Su, W., R. Mishra, et al. (2007). "Synthesis and cellular uptake of a MR contrast agent coupled to an antisense peptide nucleic acid--cell- penetrating peptide conjugate." Contrast Media Mol Imaging **2**(1): 42-49.

Swanson, J. A. (2008). "Shaping cups into phagosomes and macropinosomes." Nat Rev Mol Cell Biol **9**(8): 639-649.

Swanson, J. A. and C. Watts (1995). "Macropinocytosis." Trends Cell Biol **5**(11): 424-428.

Temsamani, J. and P. Vidal (2004). "The use of cell-penetrating peptides for drug delivery." Drug Discov Today **9**(23): 1012-1019.

Thoren, P. E., D. Persson, et al. (2000). "The antennapedia peptide penetratin translocates across lipid bilayers - the first direct observation." FEBS Lett **482**(3): 265-268.

Thoren, P. E., D. Persson, et al. (2005). "Membrane destabilizing properties of cell-penetrating peptides." Biophys Chem **114**(2-3): 169-179.

Tollis, S., A. E. Dart, et al. "The zipper mechanism in phagocytosis: energetic requirements and variability in phagocytic cup shape." BMC Syst Biol **4**: 149.

Trehin, R., H. M. Nielsen, et al. (2004). "Metabolic cleavage of cell-penetrating peptides in contact with epithelial models: human calcitonin (hCT)-derived peptides, Tat(47-57) and penetratin(43-58)." Biochem J **382**(Pt 3): 945-956.

Tyagi, M., M. Rusnati, et al. (2001). "Internalization of HIV-1 tat requires cell surface heparan sulfate proteoglycans." J Biol Chem **276**(5): 3254-3261.

Tytgat, J., K. G. Chandy, et al. (1999). "A unified nomenclature for short-chain peptides isolated from scorpion venoms: alpha-KTx molecular subfamilies." Trends Pharmacol Sci **20**(11): 444-447.

Tytgat, J., T. Debont, et al. (1998). "Purification and partial characterization of a 'short' insectotoxin-like peptide from the venom of the scorpion Parabuthus schlechteri." FEBS Lett **441**(3): 387-391.

Uematsu, N. and K. Matsuzaki (2000). "Polar angle as a determinant of amphipathic alpha-helix-lipid interactions: a model peptide study." Biophys J **79**(4): 2075-2083.

Valdivia, H. H., M. S. Kirby, et al. (1992). "Scorpion toxins targeted against the sarcoplasmic reticulum Ca(2+)-release channel of skeletal and cardiac muscle." Proc Natl Acad Sci U S A **89**(24): 12185-12189.

Veldhoen, S., S. D. Laufer, et al. (2006). "Cellular delivery of small interfering RNA by a non-covalently attached cell-penetrating peptide: quantitative analysis of uptake and biological effect." Nucleic Acids Res **34**(22): 6561-6573.

Vendeville, A., F. Rayne, et al. (2004). "HIV-1 Tat enters T cells using coated pits before translocating from acidified endosomes and eliciting biological responses." Mol Biol Cell **15**(5): 2347-2360.

Vercauteren, D., M. Piest, et al. "Flotillin-dependent endocytosis and a phagocytosis-like mechanism for cellular internalization of disulfide-based poly(amido amine)/DNA polyplexes." Biomaterials **32**(11): 3072-3084.

Vives, E., P. Brodin, et al. (1997). "A truncated HIV-1 Tat protein basic domain rapidly translocates through the plasma membrane and accumulates in the cell nucleus." J Biol Chem **272**(25): 16010-16017.

Vives, E., C. Granier, et al. (1997). "Structure-activity relationship study of the plasma membrane translocating potential of a short peptide from HIV-1 Tat protein." Letters in Peptide Science **4**: 429-436.

Vives, E., J. P. Richard, et al. (2003). "TAT peptide internalization: seeking the mechanism of entry." Curr Protein Pept Sci **4**(2): 125-132.

Vives, E., J. Schmidt, et al. (2008). "Cell-penetrating and cell-targeting peptides in drug delivery." Biochim Biophys Acta **1786**(2): 126-138.

Wadia, J. S., R. V. Stan, et al. (2004). "Transducible TAT-HA fusogenic peptide enhances escape of TAT-fusion proteins after lipid raft macropinocytosis." Nat Med **10**(3): 310-315.

Walum, E. and A. Peterson (1982). "Tritiated 2-deoxy-D-glucose as a probe for cell membrane permeability studies." Anal Biochem **120**(1): 8-11.

Watkins, C. L., D. Schmaljohann, et al. (2009). "Low concentration thresholds of plasma membranes for rapid energy-independent translocation of a cell-penetrating peptide." Biochem J **420**(2): 179-189.

Wilson, R. (2010). "The extracellular matrix: an underexplored but important proteome." Expert Rev Proteomics **7**(6): 803-806.

Wright, L. R., J. B. Rothbard, et al. (2003). "Guanidinium rich peptide transporters and drug delivery." Curr Protein Pept Sci **4**(2): 105-124.

Xue, F. L., J. Y. Chen, et al. (2007). "Enhancement of intracellular delivery of CdTe quantum dots (QDs) to living cells by Tat conjugation." J Fluoresc **17**(2): 149-154.

Yanagishita, M., K. A. Podyma-Inoue, et al. (2009). "Extraction and separation of proteoglycans." Glycoconj J **26**(8): 953-959.

Yanez-Mo, M., O. Barreiro, et al. (2009). "Tetraspanin-enriched microdomains: a functional unit in cell plasma membranes." Trends Cell Biol **19**(9): 434-446.

Yang, H., S. Liu, et al. "Chondroitin sulfate as a molecular portal that preferentially mediates the apoptotic killing of tumor cells by penetratin-directed mitochondria-disrupting peptides." J Biol Chem **285**(33): 25666-25676.

Yang, L., T. A. Harroun, et al. (2001). "Barrel-stave model or toroidal model? A case study on melittin pores." Biophys J **81**(3): 1475-1485.

Yeaman, M. R. and N. Y. Yount (2003). "Mechanisms of antimicrobial peptide action and resistance." Pharmacol Rev **55**(1): 27-55.

Yoo, J. S., C. M. Kim, et al. (2009). "Inhibition of Japanese encephalitis virus replication by peptide nucleic acids targeting cis-acting elements on the plus- and minus-strands of viral RNA." Antiviral Res **82**(3): 122-133.

Yu, X., N. Lu, et al. (2008). "Phagocytic receptor CED-1 initiates a signaling pathway for degrading engulfed apoptotic cells." PLoS Biol **6**(3): e61.

Zaro, J. L., T. E. Rajapaksa, et al. (2006). "Membrane transduction of oligoarginine in HeLa cells is not mediated by macropinocytosis." Mol Pharm **3**(2): 181-186.

Zaro, J. L. and W. C. Shen (2003). "Quantitative comparison of membrane transduction and endocytosis of oligopeptides." Biochem Biophys Res Commun **307**(2): 241-247.

Zhang, C., N. Tang, et al. (2006). "siRNA-containing liposomes modified with polyarginine effectively silence the targeted gene." J Control Release **112**(2): 229-239.

Zhang, W. and S. O. Smith (2005). "Mechanism of penetration of Antp(43-58) into membrane bilayers." Biochemistry **44**(30): 10110-10118.

Zhao, P., H. Wang, et al. "Paclitaxel-loaded, folic-acid-targeted and TAT-peptide-conjugated polymeric liposomes: in vitro and in vivo evaluation." Pharm Res **27**(9): 1914-1926.

Zhao, Y., S. Wu, et al. (2011). "Introduction of hypoxia-targeting p53 fusion protein for the selective therapy of non-small cell lung cancer." Cancer Biol Ther **11**(1): 95-107.

Zhou, Q. and G. N. Verne (2011). "miRNA-based therapies for the irritable bowel syndrome." Expert Opin Biol Ther.

Ziegler, A. and J. Seelig (2004). "Interaction of the protein transduction domain of HIV-1 TAT with heparan sulfate: binding mechanism and thermodynamic parameters." Biophys J **86**(1 Pt 1): 254-263.